Université de Montréal

Stimulateur cardiaque biologique: effets de la répartition spatiale des cardiomyocytes avec activité spontanée et de l'étirement uniaxial.

par

James Elber Duverger

Institut de Génie Biomédical

Faculté de Médecine

Thèse présentée à la Faculté de médecine en vue de l'obtention du grade de PhD en Génie Biomédical

Juillet, 2017

RÉSUMÉ

La bradycardie est une maladie caractérisée par un rythme cardiaque trop lent. L'implantation définitive d'un stimulateur cardiaque électronique (SCE) est souvent envisagée dans le cadre du traitement. Cet appareil réduit la morbidité et la mortalité chez certains patients, mais présente de nombreux inconvénients, notamment la durée limitée de la batterie, l'inflammation et le remodelage tissulaire. Le stimulateur cardiaque biologique (SCB) est possiblement une alternative thérapeutique au SCE. Il est développé *in vivo* à partir de la manipulation de canaux ioniques, d'injection de cellules souches ou de reprogrammation somatique. La plupart de ces méthodes ne tiennent compte ni de la répartition spatiale aléatoire des cardiomyocytes avec activité spontanée, ni du couplage mécano-électrique. L'objectif de la thèse est d'investiguer en quoi ces deux phénomènes pourraient influencer l'activité spontanée du SCB. La première étude, théorique, démontre que la répartition spatiale aléatoire des cardiomyocytes avec activité spontanée, *a priori* inconnue, pourrait induire une variabilité intrinsèque non négligeable de l'activité spontanée du SCB. La variabilité intrinsèque, définie comme la différence de performance observée expérimentalement entre des SCB développés dans les mêmes conditions, peut affecter négativement le taux de succès des implantations chez le patient. La deuxième étude, également théorique, démontre que la force de l'automaticité (i.e. la capacité du cardiomyocyte autonome à dépolariser ses voisins non autonomes) et l'anisotropie structurelle linéaire pourraient moduler la variabilité intrinsèque du SCB, sans toutefois l'éliminer. La dernière étude, expérimentale, caractérise les effets de l’étirement uniaxial chez les SCB en monocouche de culture, et met en lumière le double rôle de stabilisateur temporel et

spatial de ce type de stimulus mécanique. Collectivement, ces études démontrent que la répartition spatiale des cardiomyocytes avec activité spontanée et le couplage mécano-électrique sont des phénomènes important dont il faudrait tenir compte avant l'implantation du SCB au patient.

Mots clés:

Automaticité cardiaque

Bradycardie

Stimulateur cardiaque électronique

Stimulateur cardiaque biologique

Cardiomyocyte avec activité spontanée

Répartition spatiale

Force de l'automaticité

Anisotropie

Modélisation cardiaque

Étirement uniaxial

ABSTRACT

Bradycardia refers to pathologically slow heart rhythm. Implantation of an electronic pacemaker (EP) is a standard treatment. Despite reducing morbidity and mortality in appropriate patients, EPs display many shortcomings, notably limited lifespan of the battery, inflammation and tissue remodeling. Biological pacemakers (BPs) may be a therapeutic alternative to EPs. They are created *in vivo* via ionic channels manipulation, stem cells injection or somatic reprogramming. Those methods usually ignore the random spatial disposition of spontaneous cardiomyocytes and mechano-electric coupling. This thesis aims to investigate the effects of those two phenomena on the spontaneous activity of the BP. Our first project, a theoretical study, demonstrated that random spatial disposition of spontaneous cardiomyocytes, *a priori* unknown, may induce non negligible intrinsic variability in the BP's spontaneous activity. Intrinsic variability, defined as performance disparities experimentally observed among BPs created under the same protocol, may compromise success rate of implantations to the patient. Our second project, another theoretical study, demonstrated that automaticity strength (the autonomous cardiomyocyte’s ability to drive its quiescent neighbors) and linear structural anisotropy may modulate but not eliminate intrinsic variability. Our last project, an experimental study, characterized effects of uniaxial stretch in BP monolayer cultures, and revealed both temporal and spatial stabilizing roles of that type of mechanical stimulus. Together, those studies stress that random spatial disposition of spontaneous cardiomyocytes and cardiac mechano-electric coupling are important phenomena that most be taken into account before BP's implantation to the patient.

Key words:

Cardiac automaticity

Bradycardia

Electronic pacemaker

Biological pacemaker

Spontaneous cardiomyocyte

Spatial disposition

Automaticity strength

Anisotropy

Cardiac modeling

Uniaxial stretch

TABLE DES MATIÈRES

LISTE DES TABLEAUX

Chapitre 1. Introduction

Chapitre 3. Deuxième étude

Chapitre 4. Troisième étude

LISTE DES FIGURES

Chapitre 1. Introduction

Chapitre 2. Première Étude

Chapitre 3. Deuxième étude

Chapitre 4. Troisième étude

LISTE DES ACRONYMES

2D: deux dimensions

AV: auriculo-ventriculaire

$[Ca^{2+}]_i$: concentration intracellulaire de calcium

Cav: canal ionique calcique

CEC: couplage excitation-contraction

CME: couplage mécano-électrique

CSE_K : canal ionique sensible à l'étirement, et sélectif vis-à-vis des ions K^+

CSE_{NS} : canal ionique sensible à l'étirement et non-sélectif vis-à-vis des ions monovalents

CSV: canaux ioniques sensibles au volume

DDL: dépolarisation diastolique lente

ECG: électrocardiogramme

HCN: *Hyperpolarisation-activated Cyclic-Nucleotid modulated Cation Non-selective Channel*

I_f : courant pacemaker

I_{K1} : courant potassique rectifiant entrant

I_{Kr} , I_{Ks} : courants potassiques à rectification retardée

I_{NaK}: courant généré par la pompe NaK

I_{NCX}: courant généré par la pompe NCX

K_{ATP} : canal potassique sensible à l'adénosine triphosphate

KCl: chlorure de potassium

Kv: canal ionique potassique

LR1: modèle de Luo-Rudy de 1ère génération

MFS: mécanisme de Frank-Starling

NaK: pompe sodium-potassium

Nav: canal ionique sodique

NCX: échangeur sodium-calcium

NKX2-5: *homeobox protein Nkx-2.5 encoding gene*

PA: potentiel d'action

PDM: potentiel diastolique minimum

RyR: récepteur à ryanodine

SA: sino-auriculaire

SCB: stimulateur cardiaque biologique

SCN5A: gène codant la sous-unité alpha d'un canal sodique

SCE: stimulateur cardiaque électronique

SR: réticulum sarcoplasmique

Tbx5, Tbx18: groupe de gènes impliqué dans la formation du tissu et des organes durant le développement embryonnaire

Je dédie cette thèse à tous mes bienfaiteurs,

à tous ceux et celles qui m'ont supporté quand j'étais dans le besoin,

et protégé quand j'étais vulnérable.

Ils se reconnaîtront.

Votre frêle oisillon est désormais un aigle féroce.

Vos efforts n'auront pas été vains.

Je veillerai à ce que votre opportune générosité

rejaillisse doublement sur vous.

REMERCIEMENTS

Je tiens d’abord à remercier les membres de mon jury. De bon cœur, vous avez accepté de vous pencher sur mon ouvrage et de le commenter. Vos opinions scientifiques comptent pour moi, et me permettront certainement de m’améliorer et d’améliorer ma thèse.

Un grand merci à mon directeur de recherche, le Dr Philippe Comtois. Merci Philippe d’avoir laissé la chance au coureur, et de m’avoir ouvert toutes les portes. Je te serai toujours reconnaissant pour nos discussions, les conférences auxquelles j’ai pu assister, les stagiaires que j’ai pu former, et les laboratoires et entreprises avec lesquels j’ai pu collaborer. Merci pour ton ouverture d’esprit, qui a permis à mon autonomie et à ma passion pour le traitement de signal de s’épanouir. Je suis venu les mains vides et je quitte le CV bien rempli, grâce à ton laboratoire où j’ai tout appris.

À mes collègues Alireza Aghighi et Antoine Belzil, et à mes anciens collègues: Mohamed Mourchid Adegbindin, Garance Vinson, Alassane Maiga, Minh Duc Le, William Lembe Titti, Issoufou Ide Nouhou, Feng Xiong, Jonathan Boudreau-Béland, et Yashar Alami Alamdari. La plupart d’entre vous sont devenus des amis personnels. Merci pour nos échanges, notre solidarité, nos plaisanteries et nos fous rires.

Merci à mes anciens stagiaires: Marwann Abaki, Fanny Todd, Weiting Xiong et Paul Coudert. J’ai autant appris à votre contact que vous au mien.

Merci à toute la sympathique équipe de l’Institut de Cardiologie de Montréal, notamment les membres du département de génie biomédical et du laboratoire du Dr Stanley Nattel, Louis Villeneuve et Michèle Plante. Votre disponibilité, patience et bonne humeur m’ont beaucoup aidé.

Je remercie les Dr Ange Maguy, Patrice Naud, Vincent Jacquemet et Alain Vinet pour leurs précieux conseils tout au long de mon parcours.

J’aimerais du fond cœur remercier mes parents Bérel et Alerte, ma grande sœur Cyntia et ma tante Perpétue pour leur soutien inconditionnel et à tous les niveaux. Sans vous mon parcours aurait été tout autre.

Enfin, je tiens à remercier tout particulièrement mon épouse, Phydeline. *Ma première fan, mon roc, the one keeping the lights on*. Déjà 10 ans que nous partageons nos vies avec beaucoup de complicité. Tu sais mieux que nul autre à quel point mes hauts sont hauts et mes bas vraiment très bas. Tu as toujours su célébrer mes hauts et tenir bon à mes côtés dans mes bas. Merci de ton fidèle dévouement et de la fierté que je lis si souvent dans tes yeux. Je suis heureux et comblé de pouvoir te dire enfin que mes études sont terminées. *Ti amo mia bellissima*.

CHAPITRE 1 : INTRODUCTION

1.1. L'automaticité cardiaque: les origines ioniques

Le cœur est le premier organe fonctionnel du corps humain. Il pompe du sang après seulement quelques semaines de gestation, et assumera sa fonction tout au long de l'existence humaine, soit 2 à 3 milliards de battements pour une durée de vie normale. Les contractions du cœur sont provoquées par les excitations électriques provenant du nœud sino-auriculaire (SA), une petite région spécialisée de l'oreillette droite. Les impulsions électriques du nœud SA vont d'abord se propager à l'oreillette droite, et par le faisceau de Bachmann à l'oreillette gauche, pour ensuite atteindre les deux ventricules en passant par la jonction auriculo-ventriculaire (AV), le faisceau de His et les fibres de Purkinje (Fig. 1). Les cellules du nœud SA et de la jonction AV sont excitables et oscillatoires, contrairement à celles des oreillettes et des ventricules qui sont seulement excitables. La découverte du nœud SA en 1907 [1] a ouvert la voie à tout un champ d'étude sur les origines du battement cardiaque.

À l'échelle cellulaire, l'automaticité cardiaque repose sur la lente dépolarisation de la membrane durant la diastole, mécanisme qui élève le potentiel membranaire jusqu'au seuil (~-40mV) et génère un potentiel d'action (PA). La dépolarisation diastolique lente (DDL), cyclique et persistante, est le phénomène de base derrière l'automaticité cardiaque, et ses processus sous-jacents sont les cibles de choix de la plupart des études sur ce sujet. La DDL provient de la combinaison de différents mécanismes ioniques (Fig. 1) historiquement nommés *horloges*. Notons principalement la synergie des courants traversant la membrane (*horloge membranaire*) et les oscillations de la concentration intracellulaire de Ca^{2+} (*horloge calcique*). Ces deux *horloges* sont intimement interreliées et, de nos jours, leur clivage conceptuel ne repose plus

sur aucun fondement. Au sens large donc, les mécanismes de l'automaticité comprennent tout mouvement d'ions qui: (a) crée en amont des conditions favorables à l'activation, (b) contribue à la DDL, ou (c) stabilise le rythme en aval, i.e. l'empêche de devenir trop lent ou trop rapide. Les principaux contributeurs sont décrits ci-après (Fig. 2).

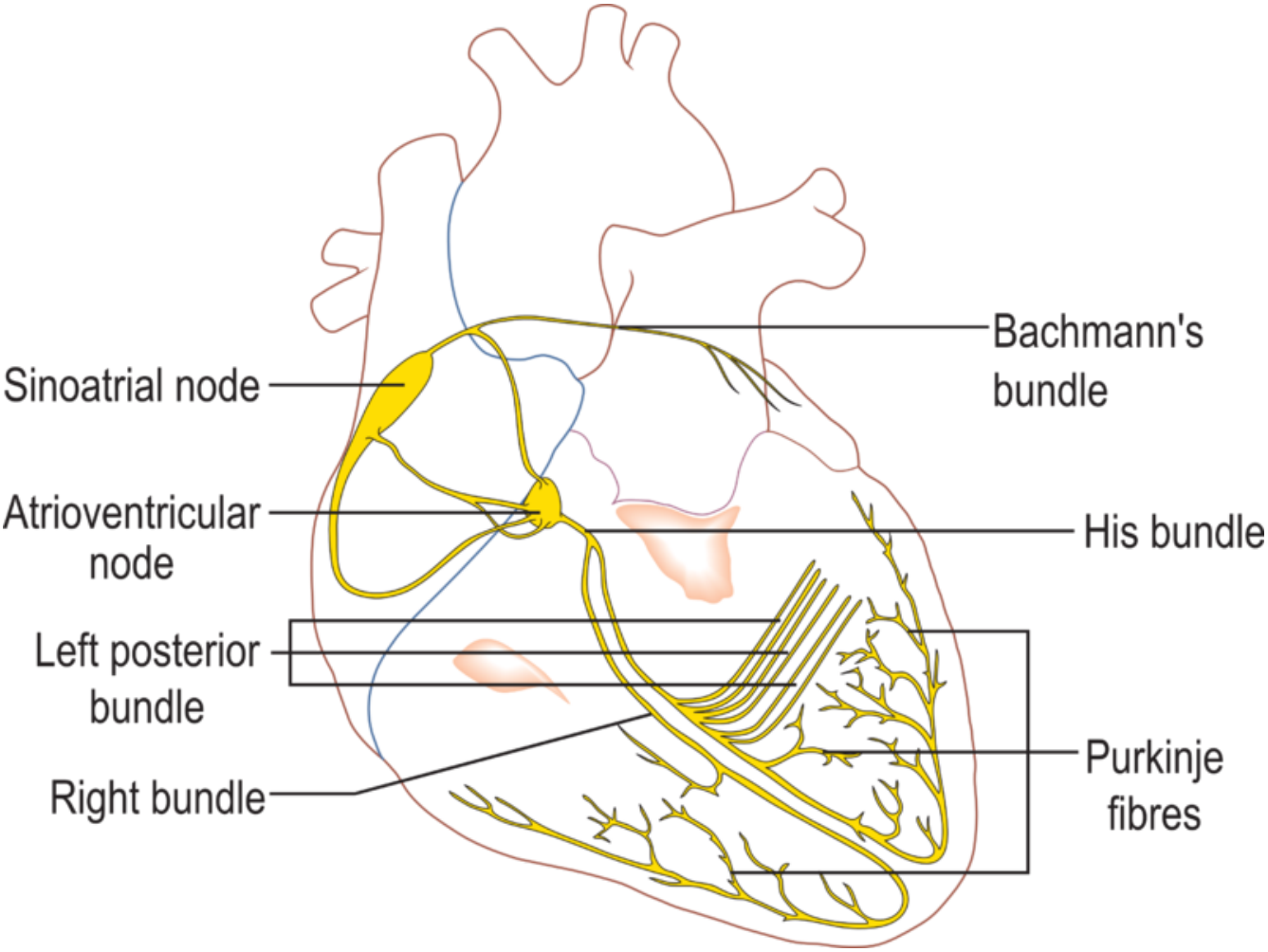

Figure 1. Système de conduction électrique du cœur. L'impulsion provenant du nœud sinusal se répand dans l'oreillette droite, et par le faisceau de Bachmann dans l'oreillette gauche. Le signal transite ensuite par le nœud AV, puis bifurque au niveau du faisceau de His pour rejoindre les deux réseaux de fibres de Purkinje. Figure tirée de [2].

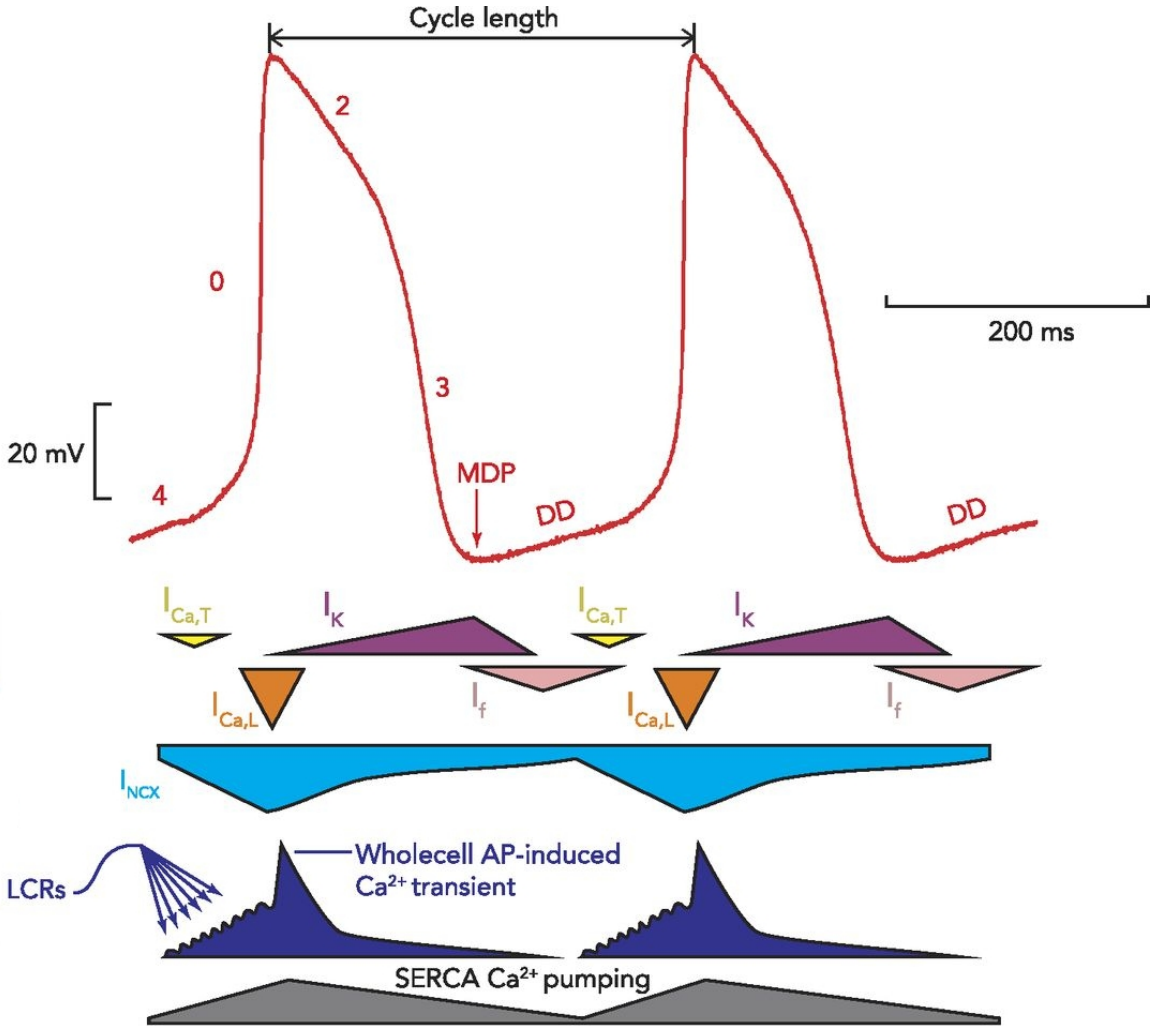

Figure 2. Mécanismes ioniques de l'automaticité cardiaque. Durant la diastole le courant I_f entre dans la cellules et les RyR relâchent spontanément du calcium, ce qui a pour effet d'élever le potentiel membranaire. Au contact du calcium, l'échangeur NCX active le courant entrant I_{NCX} et à -60mV le courant I_{CaT} entre dans la cellule. Ces deux courants élèvent encore le potentiel membranaire. À -50mV le courant entrant I_{CaL} prend le relai: il amène le voltage membranaire au seuil de ~ -40mV et provoque la phase de dépolarisation rapide. Figure modifiée de [3].

Courant pacemaker I_f. Le courant pacemaker I_f, composé à la fois de Na^+ et de K^+, s'active et entre dans la cellule si le potentiel membranaire devient inférieur -65mV [4], [5]. En plus de contribuer à la DDL [6], il protège la cellule autonome de l'hyperpolarisation excessive [7], [8] évitant ainsi un rythme trop lent (bradycardie). L'inhibition du courant I_f (notamment par l'ivabradine) cause en effet une augmentation de la longueur du cycle autonome de 5 à 20% [9]–[11].

Courant I_{NaK}. La pompe sodium-potassium (NaK) échange activement, i.e. contre leur gradient de concentration, trois ions Na^+ du milieu intracellulaire contre deux ions K^+ du milieu extracellulaire. Le courant I_{NaK} qui en résulte est donc un courant sortant qui hyperpolarise la membrane. Ce courant ralentit l'automaticité [10] et contribue au maintien du potentiel diastolique minimum [12].

Courants calciques I_{CaT},I_{CaL}. Le courant calcique I_{CaT} s'active autour de -60mV [13] et contribue à la DDL. L'inhibition du courant I_{CaT} ralentit le rythme autonome [14] . Son cousin I_{CaL} , qui s'active entre -50 et -40mV [14], [15], contribue à la fois à la DDL et à la phase de dépolarisation rapide du PA. En effet, les canaux calciques de type L forment une famille à plusieurs branches. La branche $Ca_v1.3$ est impliquée dans la DDL et la branche $Ca_v1.2$ dans la phase de dépolarisation rapide du PA [16], [17]. Le courant I_{CaL} joue ainsi le rôle du courant sodique rapide I_{Na}, absent dans les cellules centrales du nœud SA. Le blocage de I_{CaL} par la nifédipine chez les cellules sinusales centrales suppriment l'automaticité [18]. Le même protocole appliqué chez les cellules sinusales périphériques ralentit mais ne supprime pas l'activité spontanée grâce à présence de I_{Na} [18].

RyR et courant I_{NCX}. Dans des conditions basales, les récepteurs à ryanodine (RyR) du

réticulum sarcoplasmique (SR) relâchent spontanément des ions Ca^{2+} [19], [20]. Ce phénomène est cyclique (1 – 5Hz) et essentiellement indépendant de l'activité ou même de l'intégrité membranaire [21]–[23]. Le calcium relâché par les RyR active l'échangeur sodium-calcium (NCX) [24], qui génère le courant entrant I_{NCX} en important trois ions Na^+ pour chaque ion Ca^{2+} transporté hors de la cellule. La dynamique de NCX ne dépend pas du temps, mais réagit immédiatement à son exposition au calcium intracellulaire. L'inhibition de I_{NCX} cause un arrêt complet de l'automaticité [25]. L'invalidation des RyR ou la chélation du Ca^{2+} intracellulaire affecte l'amplitude de I_{NCX} et atténue grandement ou abolit l'automaticité [26].

Courants potassiques I_{K1}, I_{Kr}, I_{Ks}. Au-delà de la repolarisation de la membrane, les courants potassiques participent aussi à l'établissement et au maintien du potentiel diastolique minimum (PDM). Leurs rôles spécifiques dans l'automaticité varient en fonction du type cellulaire considéré. Les cardiomyocytes néonataux ont un courant I_{K1} plus faible que leurs équivalents adulte [27]. Dans ces cellules, le courant I_{K1} ne contribue pas à la DDL, mais facilite l'automaticité en rendant le potentiel diastolique minimal moins négatif et donc plus proche du seuil de ~-40mV. Ce fait est très connu, et l'inhibition de I_{K1} dans des cardiomyocytes adultes a été utilisée pour induire de l'automaticité (voir section 1.3). Les cellules du nœud SA n'ont par contre pas de courant I_{K1}. Dépendamment des espèces, I_{K1} est remplacé par une combinaison de I_{Kr} et I_{Ks} (ou seulement I_{Ks}, notamment chez le porc [10]). Le principe d'action est le même que pour I_{K1}, mais l'inhibition de I_{Kr}/I_{Ks} a des effets délétères sur l'activité spontanée. En effet, l'élévation démesurée du potentiel membranaire (par exemple en ajoutant du KCl dans la solution extracellulaire) supprime l'automaticité chez les cellules sinusales [10] et non chez les cardiomyocytes embryonnaires ou néonataux [28], [29]. Les cellules sinusales ont donc besoin

de leurs canaux ioniques voltage-dépendants pour générer de l'automaticité. C'est donc sans surprise que l'inhibition partielle ou totale du courant I_{Kr} (chez le lapin et les rongeurs) ou I_{Ks} (chez le porc) ralentit ou supprime [30]–[33].

Courant I_{Na}. La lenteur de la dépolarisation diastolique a longtemps établi l'idée de la primauté de I_{CaL} par rapport à I_{Na} dans l'activation autonome. Ceci dit, I_{Na} est bien présent et actif dans certaines cellules sinusales. Une variante de I_{Na} sensible à tétrodoxine (TTX), I_{NaTTX} [34]–[37], contribue à l'automaticité chez les lapins néonataux [34], et chez la souris adulte [36], [37]. Son rôle semble être de raccourcir la DDL et rendre le seuil d'activation plus négatif. En effet, l'application de TTX aux cellules sinusales de lapins néonataux ralentit la DDL et augmente le seuil d'activation, ce qui a pour effet de ralentir l'activité autonome [34]. De même, l'injection de lidocaïne pour inhiber le courant sodique chez la souris adulte ralentit le rythme [38]. Le cœur *ex vivo* sous perfusion de Lagendorff ralentit également après exposition à la TTX [37].

En règle générale, l'existence de la DDL nécessite un débalancement ionique entre les courants entrants et sortants, dont la résultante est un flux ionique net entrant qui dépolarise la cellule. Ce débalancement, variable en fonction du type cellulaire ou de l'espèce, provient de l'augmentation de certains courants entrants et de la diminution de certains courants sortants. C'est un processus extrêmement complexe qui doit être facilité en amont et stabilisé en aval. La défaillance de la génération de l'automaticité, ou de sa propagation une fois générée, est en partie à la base des troubles du rythme cardiaque.

1.2. La bradycardie: pathophysiologie et prise en charge via stimulateur cardiaque

électronique

Une fois son développement complété, la capacité du cœur à se régénérer suite à dommages et maladies devient minimale. Le cœur est de fait l'organe qui se régénère le moins [39] et son dysfonctionnement demeure la plus grande cause de mortalité à travers la planète [40], [41]. Suite à des conditions défavorables, le cœur peut développer une arythmie; la fréquence cardiaque devient trop rapide, trop lente ou irrégulière. La bradycardie est une arythmie caractérisée par un rythme trop lent par rapport à la normale (inférieur à 50 battements/minute pour un adulte au repos, qui est éveillé et qui n'est pas un sportif). C'est la pathologie ciblée par la présente thèse.

1.2.1. Pathophysiologie de la bradycardie

Les symptômes communs liés à la bradycardie incluent la fatigue, l'intolérance à l'exercice et, dans les cas plus sévères, l'effondrement hémodynamique suivi de syncope ou de décès [42]. Les causes associées sont multiples, mais les 2 principales restent la dysfonction sinusale et le bloc AV.

La dysfonction sinusale est une anomalie de la formation du pulse cardiaque, ou une difficulté du pulse formé à se propager au-delà du nœud SA. En conséquence, le rythme auriculaire ne parvient plus à répondre aux besoins physiologiques de l'organisme. La dysfonction sinusale inclut un large éventail de problèmes du rythme, allant de la lenteur persistante du nœud sinusale à son arrêt complet (avec remplacement de sa fonction par l'échappement ventriculaire), en passant par l'incompétence chronotrope, i.e. l'incapacité du cœur à augmenter

son rythme quand c'est nécessaire [43]–[48]. Les origines de cette maladie peuvent être intrinsèques au nœud SA. Par exemple, un défaut génétique altérant la fonction de certains canaux ioniques représente une cause fréquente de cette dysfonction [44], [49]–[52]. Le nœud SA peut aussi subir du remodelage tissulaire qui survient après un infarctus [44], [53], [54] ou suite à d'autres maladies telles que: l'amylose, la connectivite, l'hémochromatose et la sarcoïdose [55]. Il existe aussi des origines extrinsèques à la dysfonction sinusale, qui l'imitent ou l'exacerbent. C'est le cas notamment de certaines anomalies électrolytiques (hypocalcémie, hypo- ou hyperkaliémie), l'hyperthyroïdie, l'hypoxie, l'hypothermie et certaines toxines (par exemple la TTX). Sont aussi impliquées certaines médications comme le lithium, les antiarythmiques, les inhibiteurs calciques et les bêta-bloquants [55], [56].

Quand une impulsion électrique provenant du nœud SA transite par le nœud AV, un délai de conduction physiologique est appliqué afin de permettre aux ventricules de récupérer de la précédente impulsion. Quand ce délai devient trop long, nous parlons de bloc AV [57]. L'intervalle PR, i.e. la durée entre l'onde P et pic R de l'électrocardiogramme (ECG) de surface, est la mesure utilisée pour quantifier le délai de conduction. Il existe trois degrés de bloc AV, en fonction de la gravité de la pathologie. Pour un bloc AV du 1er degré, chaque impulsion non-prématurée du nœud SA transite par le nœud AV mais l'intervalle PR est supérieur à 0.2s. Le bloc AV du 2^{e} degré existe sous deux formes: le type 1 et le type 2. Le bloc AV du 2^{e} degré de type 1 est caractérisé notamment par un allongement graduel l'intervalle PR jusqu'à l'atteinte d'un défaut de conduction où un battement des oreillettes n'est pas suivi de battement des ventricules. Sur l'ECG, ce phénomène est reconnaissable à une onde P non suivi du complexe QRS. Le bloc AV du 2^{e} degré de type 2 est un défaut abrupt de conduction, non précédé de

l'allongement de l'intervalle PR. Ce défaut est temporaire ou intermittent; par exemple le nœud AV peut laisser passer une impulsion sinusale non-prématurée sur deux. Le bloc AV du 3e degré correspond à un défaut de conduction qui est total et permanent. Le nœud SA n'entraîne plus les ventricules; sa fonction est remplacée par l'échappement ventriculaire. Les activités auriculaires et ventriculaires sont désormais totalement dissociées. Les causes du bloc AV sont extrêmement variées. Elles peuvent être génétiques, comme par exemple une mutation délétère du gène SCN5A relié aux canaux sodiques [58], ou une mutation au niveau des gènes Tbx5 ou NKX2-5, jouant un rôle capital dans le développement normal du système de conduction [57]. Cette maladie peut aussi être une conséquence de l'ischémie myocardique ou de la fibrose post-infarctus. Dysfonction sinusale et bloc AV se rapprochent sur certaines causes communes, notamment la fibrose dégénérative, l'amylose, la sarcoïdose et certaines médications (antiarythmiques, inhibiteurs calciques, bêta-bloquants).

1.2.2. Prise en charge par le stimulateur cardiaque électronique

Quand la bradycardie devient chronique et que la pharmacothérapie ne parvient pas à élever le rythme cardiaque de manière sécuritaire et durable, l'implantation définitive d'un stimulateur cardiaque électronique (SCE) est souvent envisagée [59]. Le SCE est un petit appareil (moins de 5 cm de longueur) composé d'un boîtier relié une ou plusieurs sondes (Fig. 3). Le boîtier est implanté chirurgicalement sous la clavicule, en face d'un muscle pectoral. Les sondes conductrices unipolaires ou bipolaires, souples et recouvertes d'une gaine isolantes, sont introduites dans le cœur par voie veineuse.

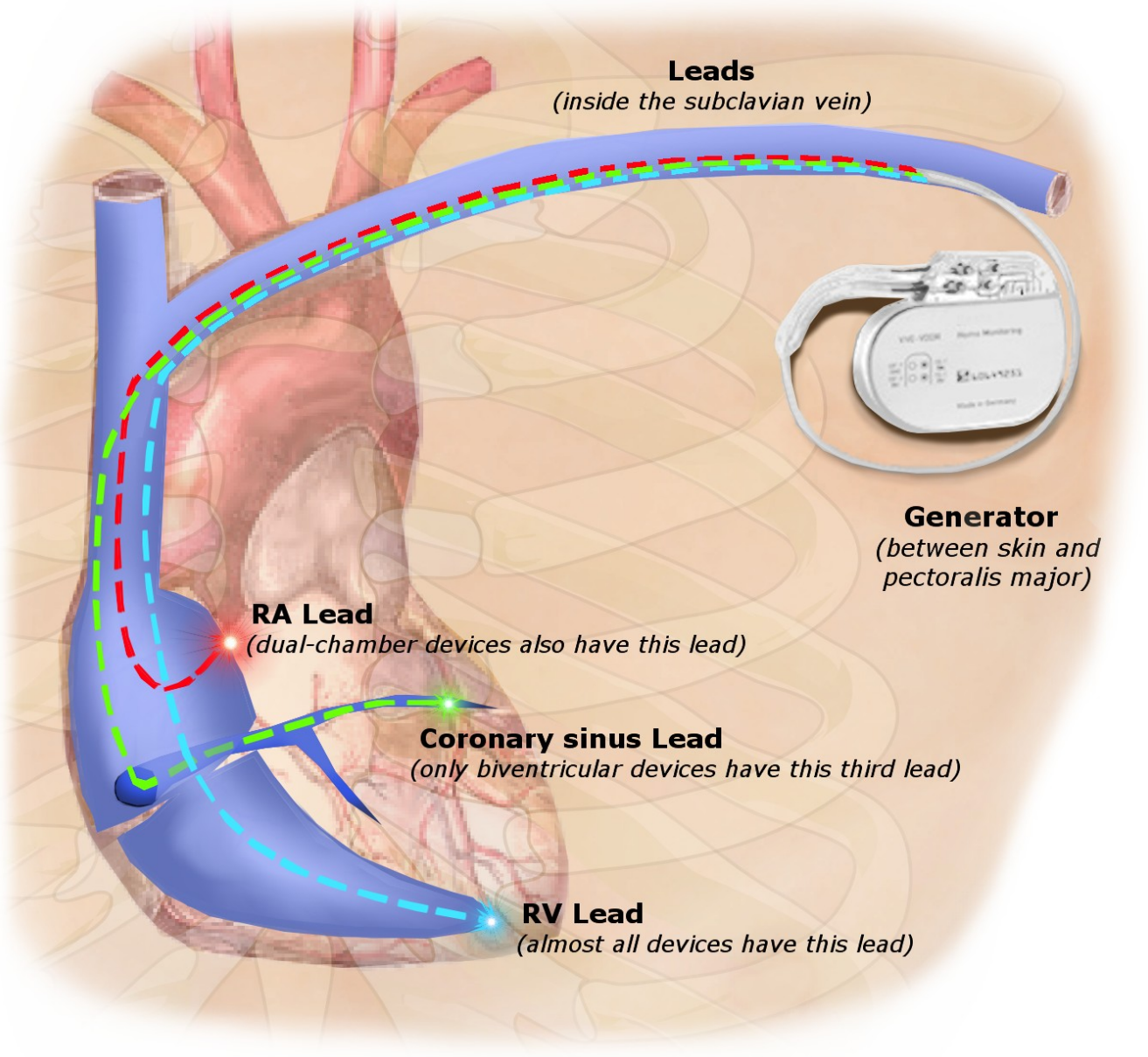

Figure 3. Stimulateur cardiaque électronique. Une chirurgie permet d'implanter le stimulateur sous la clavicule, en face d'un muscle pectoral. Dépendamment de la thérapie du patient, le stimulateur est relié à une ou plusieurs sondes. Dans l'oreillette droite, l'électrode au bout de la sonde est accrochée au niveau de l'appendice. Le point d'accrochage est l'apex pour le ventricule droit, et le sinus coronarien pour le ventricule gauche. Figure tirée de [60].

Les SCE simple-chambre comprennent une seule sonde reliée à l'oreillette droite (au niveau de

l'appendice) ou au ventricule droit (au niveau de l'apex). Les SCE double-chambre sont munis de deux sondes reliées à la fois à l'oreillette droite et au ventricule droit. Les SCE destinés à la resynchronisation ventriculaire comprennent une troisième sonde destinés au ventricule gauche via le sinus coronaire. Le boîtier contient la pile et le circuit électronique. Le circuit est composé de plusieurs sous-étages dédiés. La liste suivante, certainement non exhaustive compte tenu de la diversité des modèles, contient les principales fonctions des sous-étages dédiés.

(a) Les circuits de mesure de paramètres physiologiques du patient. Il s'agit notamment de la détection d'événements cardiaques auriculaires et/ou ventriculaires, comme l'occurrence d'une activation, ou la présence d'une arythmie en analysant la fréquence cardiaque en fonction du temps. Beaucoup d'autres capteurs ont été développés pour asservir la réponse du SCE à l'effort et aux demandes métaboliques du patient, comme par exemple l'accéléromètre et détecteur de ventilation [61].

(b) Les circuits d'application de la stimulation électrique selon différents modes.

* Dans le mode *inhibition* (inhibition) l'application de la stimulation dans l'oreillette ou dans ventricule peut respectivement être inhibée par la détection d'un événement dans l'oreillette ou dans le ventricule. En d'autres termes, le SCE applique le pulse uniquement quand l'oreillette ou le ventricule ne présente aucune activation intrinsèque.

* Dans le mode *trigger* (déclenchement), après l'activation de l'oreillette (intrinsèque ou stimulée), un pulse est appliqué au ventricule en l'absence d'activation intrinsèque.

* Le mode *dual* (inhibition et déclenchement) est une combinaison des deux modes précédents.

(c) Les circuits de mesure des paramètres techniques reliés au SCE et à son fonctionnement: le

niveau de charge de la pile et l'impédance de stimulation (représentant tout ce qui résiste au passage du courant de stimulation) par exemple.

(d) Le stockage de données et la transmission d'information via une antenne radio-fréquence.

Une séquence de lettres (actuellement 5) décrivant les fonctions du SCE a été établie, et est entretenue depuis 1974 par un comité conjoint entre la NASPE et le BPEG. Cette séquence est aujourd'hui composée de 5 lettres dont la description détaillée se trouve dans le Tableau 1. Par exemple, VVIRO signifie: (a) la stimulation a lieu dans le ventricule; (b) la détection a lieu dans le ventricule; (c) la stimulation est en mode inhibition et (d) est asservie au rythme cardiaque; (e) il n'y a qu'un seul site de stimulation par carvité cardiaque. Il est à noter que les O à la fin sont en général omis, i.e. VVIRO s'écrit dans les faits VVIR.

Tableau 1. Fonctions du stimulateur cardiaque électronique.

I	**II**	**III**	**IV**	**V**
Cavité cardiaque stimulée	Cavité cardiaque détectée	Mode de stimulation	Modulation du rythme	Stimulation multisite
O = *none* (aucun)	O = *none* (aucun)	O = *none* (aucun)	O = *none* (aucun)	O = *none* (aucun)
A = *Atrium* (oreillette)	A = *Atrium* (oreillette)	T = *Triggered* (déclenché)	R = Rate Modulation (asservi au rythme cardiaque)	A = *Atrium* (oreillette)
V = *Ventricle* (ventricule)	V = *Ventricle* (ventricule)	I = *Inhibited* (inhibé)		V = *Ventricle* (ventricule)
D = *Dual* (A+V)	D = *Dual* (A+V)	D = *Dual* (T+I)		D = *Dual* (A+V)
* NASPE: North American Society of Pacing and Electrophysiology * BPEG: British Pacing and Electrophysiology Group * Stimulation multisite: présence de plus d'un site de stimulation dans une cavité cardiaque donnée.				

Le SCE réduit la morbidité et la mortalité chez des patients bradycardiques soigneusement sélectionnés. Typiquement, il est implanté chez les malades qui ont: (a) une dysfonction sinusale avérée et symptomatique, incluant l'incompétence chronotrope [43], [62]–[66], (b) un rythme cardiaque diurne inférieur à 40 battements/min avec des symptômes intermittents de bradycardie, même minimaux [43], [62]–[66], (c) des syncopes idiopathiques avec une quelconque anomalie sinusale détectée ou provoquée par des tests médicaux [43], [62]–[66], et (d) un bloc AV de 3^{e} degré ou de 2^{e} degré type II [43], [62], [67]–[71]. Il n'y a pas de consensus définitif sur le mode de stimulation à appliquer dépendamment des causes de la bradycardie, mais les lignes suivantes sont souvent appliquées: (a) AAIR pour la dysfonction sinusale sans bloc AV; (b) DDD pour le bloc AV sans dysfonction sinusale; (c) DDDR pour la dysfonction sinusale associée au bloc AV [59].

La dysfonction sinusale représente à elle seule la moitié des cas d'implantation de SCE [44], [46], [72]; et vu la tendance des patients atteints de cette dysfonction à développer par la suite le bloc AV, la stimulation à double chambre est souvent appliquée [43], [73]–[79].

Longtemps décriés pour les nombreuses complications qu'il implique, le SCE a au fil du temps profité de conséquentes améliorations, notamment une batterie à durée de vie étendue, une électrode minimisant l'inflammation et le remodelage tissulaire, et des algorithmes facilitant l'adéquation entre le rythme cardiaque et les exercices physiques [42]. Il demeure cependant incapable d'assumer toutes les fonctions du nœud sinusal natif, comme la réponse aux émotions et aux exercices isométriques ou très intenses [80]. De plus, il est contre-indiqué dans certaines situations cliniques spécifiques. Par exemple, en cas d'antibiothérapie suite à une infection liée

au SCE, l'appareil doit être enlevé pour la durée du traitement [81]; l'utilisation d'un SCE d'appoint, quoique nécessaire pour les patients totalement dépendants, n'est pas souhaitable puisque le nouveau corps étranger risque de recréer les conditions de l'infection. Finalement, même si le SCE réduit la morbidité, il n'augmente le taux de survie que chez les patients présentant un bloc AV, le taux de mortalité restant inchangé pour ceux souffrant de dysfonction sinusale [82]. Le SCE est un palliatif et non une cure.

1.3. Le stimulateur cardiaque biologique: alternative au stimulateur cardiaque électronique

Le développement du SCB s'appuie sur plusieurs motivations dont la capacité d'avoir une activité autonome plus physiologique (comme la variation diurne/nocturne du rythme et la réponse aux stimulations adrénergiques) et la possibilité de s’accommoder à la croissance de son porteur (une optique très favorable aux patients pédiatriques) [42]. Les efforts s'appuient sur trois familles d'approches générales: (a) la manipulation de canaux ioniques; (b) l’injection dans le myocarde de cellules souches/pluripotentes/néonatales destinées à devenir des cardiomyocytes autonomes; (c) la reprogrammation somatique d'un sous-ensemble de cellules du myocarde en cardiomyocytes autonomes.

1.3.1. Approche par manipulation de canaux ioniques

Les premiers travaux en vue de la création du SCB ont fait usage de transfert par adénovirus de matériel génétique exprimant ou modifiant l'expression de canaux ioniques. Le gène mutant

négatif dominant Kir2.1, injecté dans le ventricule gauche de cochons d'Inde, induit de l'activité ectopique en supprimant le courant potassique I_{K1}, qui joue un rôle important dans le maintien du potentiel diastolique [83]. D'autres études sont parvenues au même résultat en injectant le gène exprimant un canal mutant HCN2, relié au courant pacemaker I_f, dans le myocarde de chiens [84], [85]. Les approches basées sur les canaux ioniques présentent souvent le désavantage de ne pas tenir compte des propriétés non encore caractérisées de l'automaticité cardiaque [42].

1.3.2. Approche par cellules souches/pluripotentes/néonatales

Des cellules fœtales d'oreillette et de nœud sinusal, injectées dans le ventricule gauche de chiens chez qui un bloc AV total a ensuite été provoqué trois semaines après, génèrent un échappement ventriculaire de 70 battements/min [86]. Ces cellules fœtales étaient électriquement couplées entre elles et avec les cardiomyocytes du myocarde par des jonctions communicantes. Une expérience similaire, effectuée chez le chien avec des cellules souches mésenchymateuses humaines exprimant HCN2, a démontré que le rythme autonome augmentait suite à l'infusion d'épinéphrine et que les cellules pouvaient survivre jusqu'à six semaines sans être immunosupprimées [87]. Les thérapies à base de cellules souches/pluripotentes ont toutefois un potentiel tératogène et la population de cellules différenciées qui en résulte est très hétérogène [42]. De plus, des expériences à succès chez les petits animaux [88], une fois reprises sur les primates, ont provoqué des arythmies ventriculaires [89].

1.3.3. Approche par reprogrammation somatique

La transdifférentiation, permettant de convertir une cellule mature quelconque en un autre cellule mature sans passer par la phase intermédiaire pluripotente, a ouvert une nouvelle voie [90]. Mais cette méthode est encore inefficiente, comme en témoignent des études où des fibroblastes de souris et d'humain ont été transdifférentiés en cellules s'apparentant à des cardiomyocytes [91], [92]. Par contre, la conversion d'un type de cellules cardiaques à un autre (par exemple de ventriculaire à sinusale) a rencontré plus de succès, *in vitro* et *in vivo* [93], [94]. Le principe consiste à réactiver certaines voies développementales dans des cellules cardiaques matures afin de les transformer, et les cellules nouvellement reprogrammées n'auront plus besoin de l'expression du gène ayant provoqué le changement de phénotype. Le facteur de transcription Tbx18 (jouant un rôle dans le développement embryonnaire) a notamment été utilisé pour reprogrammer *in vivo* des cellules ventriculaires en cellules sinusales et générer plus ou moins durablement (14 jours) de l'activité autonome [95]. Malgré tous ces espoirs, la méthode par reprogrammation somatique n'est pas sans risque: l'absence d'infection ou de fibrose au niveau du site d'injection de l'adénovirus et l'innocuité à long terme des mini-infections observées dans d'autres organes comme les poumons et la rate, n'ont pas encore été démontrés [42]. De plus il difficile d'évaluer si la dispersion virale peut provoquer plusieurs site d'initiation de l'activité autonome (phénomène très arythmogène) et si Tbx18, qui est pléiotrope, n'a pas provoqué la génération d'autres types cellulaires potentiellement dangereux [42].

Tous les SCB créés à ce jour ont un caractère transitoire. Vraisemblablement, les gènes injectés sont supprimés, et les cellules souches ou infectées prises en charge par le système immunitaire

[80].

1.4. Modélisation mathématique du stimulateur cardiaque biologique

Le cœur n'est pas uniquement un organe; c'est aussi un conducteur électrique et une pompe mécanique. De ce fait, il a été l'objet d'intenses investigations mathématiques, et de nombreux progrès ont préparé l'avènement de la modélisation du SCB, tel qu'on le connaît aujourd'hui. Ce qui suit en est un bref historique, avec une emphase particulière sur les aspects qui seront considérés pour les études réalisées dans le cadre de cette thèse.

1.4.1. Le potentiel de Nernst

La membrane cellulaire est une bicouche lipidique perméable à certains ions. Quand la concentration extérieure (c_e) et la concentration intérieure (c_i) d'un type spécifique d'ion (par exemple Na^+) diffèrent, il est possible de se baser sur l'équation thermodynamique de Boltzmann pour définir le potentiel de Nernst développé de part et d'autre de la membrane:

$$E = -\frac{RT}{zF} \ln\frac{c_i}{c_e} \quad (1)$$

E: potentiel de Nernst (mV)

R: constante universelle des gaz parfaits (8.3144621 $J.mol^{-1}\cdot K^{-1}$)

z: charge de l'ion

F: constante de Faraday (96,485 $C\cdot mol^{-1}$)

1.4.2. Le modèle de Hodgkin-Huxley

Le potentiel de Nernst sera repris dans le modèle de Hodgkin-Huxley [96], qui est le premier à fournir une compréhension fondamentale quantitative sur les mécanismes derrière le potentiel d'action (PA) des cellules excitables, tout en étant déterminant dans la découverte des canaux ioniques [97]. Ce modèle de PA d'axone géant de calmar part d'une élégante analogie avec des circuits électriques simples, où la membrane cellulaire est représentée par un condensateur et les canaux ioniques par des conductances variables (voir Fig. 4). La relation entre la capacité membranaire, la somme des courants ioniques et la différence de potentiel de part et d'autre de la membrane a été établie comme suit:

$$C_m \frac{dV}{dt} = -I_{ion} \quad (2)$$

V: potentiel membranaire (mV)

C_m: capacité membranaire ($\mu F/cm^2$)

I_{ion}: somme des courants ioniques (pA)

La formule (2) est l'équation fondamentale de l'électrophysiologie. Des expériences réalisées sur l'axone géant de calmar ont permis d'établir l'existence des courants sodique (I_{Na}) et potassique (I_K) qui génèrent le PA, et un courant chlorure ou courant de fuite (I_L) responsable du potentiel de repos. Le courant I_{ion} de la formule (2) est ainsi défini de manière détaillée:

$$\begin{aligned} I_{ion} &= I_{Na} + I_K + I_L \\ I_{Na} &= g_{Na}(V - E_{Na}) \\ I_K &= g_K(V - E_K) \\ I_L &= g_L(V - E_L) \end{aligned} \quad (3)$$

I_{Na}, I_K, I_L : courants sodique, potassique et de fuite (pA)

E_{Na}, E_K, E_L : potentiels de Nernst (mV)

g_{Na}, g_K : conductances variables dépendant de V (nS)

g_L: conductance constante (nS)

Pour chaque type d'ions, le sens du courant est déterminé par (V – E). Un courant négatif est entrant et un courant positif est sortant.

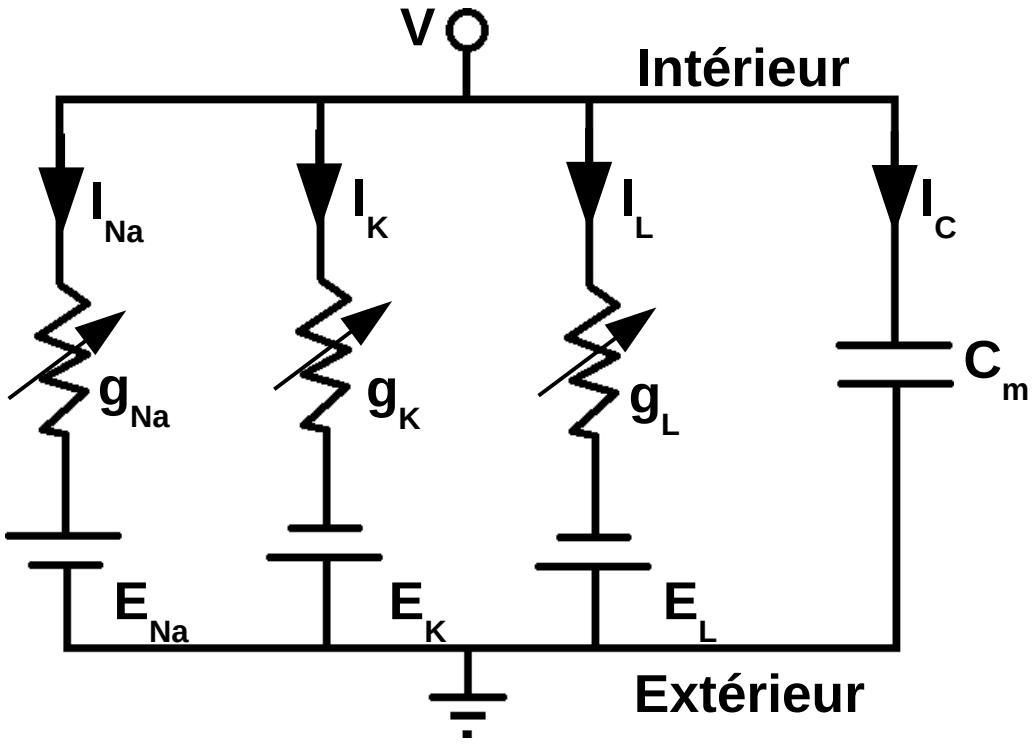

Figure 4. Modèle de Hodgkin-Huxley. La membrane est représentée par une capacité et les canaux ioniques par des conductances variables. Le potentiel de Nernst associé à chaque type d'ion est représenté par une source constante de voltage en série avec la conductance respective. Le potentiel membranaire est la différence de voltage entre l'intérieur et l'extérieur de la cellule.

1.4.3. Le modèle de FitzHugh-Nagumo

Les travaux de Richard FitzHugh [98], [99] proposent en 1961 une simplification du modèle de Hodgkin-Huxley, fortement non-linéaire, complexe, et ne pouvant être résolu que numériquement. L'équation différentielle de second ordre de van der Pol [100] a d'abord été transformée en un système de deux équations différentielles de premier ordre, puis modifiée comme suit:

$$\begin{aligned} \frac{dv}{dt} &= \kappa \left(v - \frac{1}{3}v^3 - w \right) \\ \frac{dw}{dt} &= v - \gamma w + \beta \end{aligned} \qquad (4)$$

v : variable d'activation (similaire au potentiel membranaire)

w : variable d'inactivation (ramenant le potentiel membranaire au repos)

α, β, ε : paramètres constants

J. Nagumo [101] réalise en 1962 le circuit équivalent du système de FitzHugh (Fig. 5). Le modèle de FitzHugh-Nagumo a été utilisé dans notre première étude.

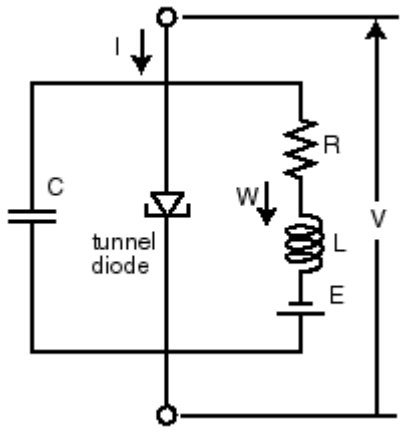

Figure 5. Circuit équivalent du système de R. FitzHugh. Figure tirée de [98].

1.4.4. Modélisation du potentiel d'action cardiaque

La stratégie utilisée pour Hodgkin-Huxley a été reprise pour modéliser le PA cardiaque. Depuis le premier résultat présenté en 1962 par Denis Noble [102], plus d'une centaine de modèles ont été développés [103]. Au fil du temps, ils n'ont cessé de se complexifier et couvrent désormais un large éventails de cellules (ex.: sinusale [104], Purkinje [102], auriculaire [105], ventriculaire [106]) pour des espèces de plus en plus nombreuses (ex.: chien [107], cochon d'Inde [108], humain [109], lapin [110], rat [111], souris [112]). Ces modèles peuvent être classés en trois générations de complexité croissante.

Les modèles de 1ère génération comportent typiquement 10 équations différentielles ou moins. Le nombre de courants ioniques est limité (Na^+, Ca^{2+}, K^+). Les concentrations intracellulaires de Na^+ et K^+ sont fixes. Abstraction est faite de la dynamique calcique et la concentration intracellulaire de Ca^{2+} est définie uniquement par le courant calcique. Beeler-Reuter [106] et Luo-Rudy I (LR1) [108] sont les principaux représentants de cette génération. Le modèle LR1 a été utilisé dans notre deuxième étude.

Les modèles de 2e génération comportent entre 20 et 40 équations différentielles. Ils contiennent entre 10 et 20 courants ioniques, et prennent en charge la dynamique calcique et la régulation des concentrations intracellulaires de Na^+ et K^+. La formulation mathématique des courant ioniques est beaucoup plus détaillée, avec l'introduction des transitions de Markov [113], pour préciser l'ouverture et la fermeture de canaux ioniques, et de la signalisation cellulaire [114], [115]. Le modèle de Luo-Rudy II [116] est un représentant phare de cette

génération.

La 3e génération de modèles, en cours de développement, met notamment en avant la distribution des canaux ioniques dans la membrane cellulaire et les caractéristiques spatiales de la dynamique calcique [117]. Le niveau de complexité atteint est inégalé.

1.4.5. Modélisation de la conduction électrique dans la monocouche cardiaque

Les modèles cités précédemment décrivent l'excitabilité cardiaque à l'échelle cellulaire. D'autres travaux ont permis de décrire la propagation du PA à l'échelle tissulaire. Seul le tissu cardiaque 2D (monocouche) sera considéré dans les études qui constituent cette thèse. Il existe différents paradigmes pour modéliser la conduction électrique dans la monocouche cardiaque: le paradigme discret et le paradigme continu.

Dans le paradigme discret, chaque cellule est explicitement représentée. Les premiers représentants majeurs de ce paradigme sont les automates cellulaires. Les automates sont conceptuellement des «cellules» pouvant adopter un nombre finis d'états; elles sont interconnectées et réparties sur une grille régulière. À chaque pas de temps, l'état de chaque «cellule» évolue en fonction de l'état précédent et de l'état des «cellules» voisines. Ces systèmes, d'une remarquable simplicité, ont permis de formuler mathématiquement la propagation du potentiel d'action [118] et de mener à bien des les premières simulations numériques de propagation [119]. Les automates cellulaires se prêtent bien à l'étude des effets de la courbure de propagation [120], [121], de l'anisotropie [122], et des ondes en spirale dans les tissus cardiaques hétérogènes [119], [120], [123], [124]. Ces modèles réclament généralement peu de ressources informatiques, mais manquent de réalisme pour les

phénomènes dépendant du rythme. Et c'est à ce niveau qu'interviennent les seconds représentants majeurs du paradigme discret, où chaque cellule de la monocouche est représentée par un système d'équations différentielles ordinaires décrivant sa dynamique. Les cellules cardiaques de ce réseau 2D sont reliées à leurs voisines par des jonctions communicantes. Ces jonctions sont des canaux ioniques qui, conformément à la loi d'Ohm, laissent passer les ions de la cellule au potentiel le plus élevé vers la ou les cellules connectées au potentiel plus bas. Ce transfert d'ions permet la propagation du PA d'une cellule à l'autre. L'équation (2) est redéfinie pour tenir compte du courant ionique circulant d'une cellule i donnée à ces voisines:

$$C_m(i)\,\frac{dV(i)}{dt} = -I_{ion}(i) + \sum_{k=1}^{N} g_j(k)\,[V(k) - V(i)] \quad (5)$$

$C_m(i)$: capacité membranaire de la i^e cellule de la monocouche ($\mu F/cm^2$)

$V(i)$: potentiel membranaire de la i^e cellule (mV)

$I_{ion}(i)$: somme des courants ioniques entrant et sortant de la i^e cellule, à l'exception des courants circulant à travers les jonctions communicantes (pA)

$g_j(k)$: conductance de la jonction communicante de la k^e voisine de la i^e cellule (nS)

$V(k)$: potentiel membranaire de la k^e voisine de la i^e cellule (mV)

N: nombre de voisine de la i^e cellule

La composante ajoutée à droite de l'équation utilise la loi d'Ohm pour quantifier la quantité totale de courant qui passe de la i^e cellule à l'ensemble de ses voisines. Il est à noter que la conductance g_j peut varier d'une voisine à l'autre, permettant ainsi de simuler une monocouche hétérogène, composée de divers types de cellules. Ces modèles ont été utilisés pour l'étude des

effets des jonctions communicantes, ainsi que l'anisotropie [125]–[128]. Ils permettent une description très détaillée de l'architecture du tissu, mais peuvent se révéler très coûteux du point vue des ressources informatiques [129] et réclament une quantité prohibitive de données physiologiques sur chaque cellule (taille et capacité membranaire), chaque jonction communicante (positions et conductance) et le milieu extracellulaire (composition).

Le paradigme continu réclame moins de données physiologiques et est moins coûteux en puissance de calcul. Dans ce paradigme, le tissu 2D est vue comme un milieu continu ou syncytium. Une équation classique de réaction-diffusion décrit alors la propagation du voltage dans l'espace:

$$\frac{\partial V}{\partial t} = -\frac{I_{ion}}{C_m} + D_x \frac{\partial^2 V}{\partial x^2} + D_y \frac{\partial^2 V}{\partial y^2} \quad (6)$$

V: potentiel membranaire (mV)

I_{ion}: somme des courants ioniques (pA)

C_m: capacité membranaire ($\mu F/cm^2$)

D_x, D_y: constantes de diffusion longitudinale et transversale (cm^2/s)

Les constantes de diffusion longitudinale et transversale sont définies comme suit:

$$D_x = \frac{1}{C_m \rho_x \chi} \quad \text{et} \quad D_y = \frac{1}{C_m \rho_y \chi} \quad (7)$$

ρ_x, ρ_y: résistivité dans les directions longitudinale et transversale ($k\Omega.cm$)

χ: ration surface/volume du cardiomyocyte (cm^{-1})

Si la monocouche est isotrope et électriquement homogène, les constantes de diffusion longitudinale et transversale sont égales et la formule (6) est simplifiée:

$$\frac{\partial V}{\partial t} = -\frac{I_{ion}}{C_m} + D\left(\frac{\partial^2 V}{\partial x^2} + \frac{\partial^2 V}{\partial y^2}\right) \quad (8)$$

D: constante de diffusion $D = D_x, = D_y$ (cm^2/s)

Le paradigme du domaine continu a aussi été utilisé avec beaucoup de succès pour des modèles plus simples comme celui de FitzHugh-Nagumo, précédemment présenté:

$$\begin{aligned} \frac{dv}{dt} &= \kappa\left(v - \frac{1}{3}v^3 - w\right) + D_x \frac{\partial^2 v}{\partial x^2} + D_y \frac{\partial^2 v}{\partial y^2} \\ \frac{dw}{dt} &= v - \gamma w + \beta \end{aligned} \quad (9)$$

Le modèle 2D de FitzHugh-Nagumo a historiquement joué un rôle déterminant dans la compréhension de la dynamique du milieu excitable, i.e. la manière dont les ondes se propagent dans un réseau de cellules excitables interconnectées.

Les équations (6) et (9) ne considèrent que la conduction par les jonctions communicantes et ignorent l'espace extracellulaire. Les modèles décrits par ces équations sont dit monodomaines. Dans les tissus cardiaques réels, la conduction électrique a également lieu dans l'espace extracellulaire, peut avoir une conductance et un ratio anisotrope qui diffèrent de l'espace intracellulaire. Si un courant est injecté dans l'espace extracellulaire [130], [131] (défibrillation par exemple), il devient important d'utiliser des modèles dit bidomaines [132]–[134] :

$$\begin{aligned} \chi\left(C_m \frac{\partial V}{\partial t} + I_{ion}\right) &= \nabla.(\vec{\sigma}_i \nabla V) + \nabla.(\vec{\sigma}_i \nabla \phi_e) \\ \nabla.[(\vec{\sigma}_i + \vec{\sigma}_e)\nabla \phi_e] &= -\nabla.(\vec{\sigma}_i \nabla V) \end{aligned} \quad (10)$$

ϕ_i , ϕ_e : potentiels intra- et extracellulaire, avec $V = \phi_i - \phi_e$.

σ_i , σ_e : tenseurs de conductivité intra- et extracellulaire.

1.5. Les motivations derrière la thèse

En général, les méthodes de création du SCB ne tiennent pas compte des aspects post-implantation, notamment: (a) la répartition spatiale des cardiomyocytes avec activité spontanée au sein du SCB et (b) les effets des contraintes mécaniques.

1.5.1. Répartition spatiale des cardiomyocytes avec activité spontanée

Dans cette thèse, la répartition spatiale est un terme parapluie qui regroupe au fait deux variables distinctes et complémentaires: la densité et la distribution spatiale. La densité réfère au nombre de cardiomyocytes avec activité spontanée par rapport au nombre total de cardiomyocytes présents dans le SCB. La distribution spatiale décrit l'homogénéité de la dispersion des cardiomyocytes avec activité spontanée au sein du SCB. La répartition spatiale *in situ* des cardiomyocytes avec activité spontanée est *a priori* inconnue dans la plupart des méthodes de développement du SCB.

L'architecture du nœud SA natif démontre pourtant l'importance capitale des caractéristiques spatiales. Le bon fonctionnement du nœud SA repose effectivement sur une collection hétérogène de cellules dont la répartition spatiale permet un équilibre électrotonique entre les cellules sinusales (conceptuellement vues comme des sources de charges) et les cardiomyocytes excitables mais sans automaticité (vus comme des puits de charges) [135]. Tout d'abord, le nœud dans son ensemble est fonctionnellement isolé de l'oreillette, à l'exception de certaines voies de sortie, par du tissu connectif [136]–[139] ou une redistribution adaptée des

jonctions communicantes [140], [141]. Cet isolement est électrotoniquement important puisque la fréquence du nœud sinusal augmente substantiellement quand il est détaché du tissu auriculaire [142]. Ensuite, la distribution spatiale des cellules à l'intérieur du nœud sinusal favorise une transition graduelle des propriétés du PA, du centre vers la périphérie [143]. La distribution spatiale exacte en question fait encore l'objet d'une controverse, les points de vue étant divisés entre: (a) le modèle «gradient», qui propose que les propriétés électrophysiologiques des cellules sinusales changent graduellement du centre vers la périphérie, et (b) le modèle «mosaïque» qui avance que c'est plutôt la densité des cellules sinusales qui fait la différence entre le centre et la périphérie [144].

L'importance de la répartition spatiale commence partiellement à émerger dans les études sur le SCB. Par exemple, pour assurer la fonction spontanée dans le cœur canin, il a été établi que le fluide injecté dans le ventriculaire gauche devait contenir au minimum 280,000 cellules avec activité autonome [87]. Ce fait est une claire indication des effets de la densité *in situ*. Les limitations techniques ne permettant pas une caractérisation plus précise, ce sont les modèles mathématiques qui prennent le relais dans la quête de compréhension du phénomène. Cependant, la plupart des études théoriques sur le sujet ne s'intéressent pas directement à la distribution spatiale des cardiomyocytes avec activité autonome, mais plutôt aux propriétés des canaux ioniques [145], [146], à la connectivité intercellulaire [120], [147], [148], et à la présence de cellules non-excitables et/ou d'espaces non-conducteurs [149]–[152].

La compréhension de la nature et des effets de la répartition spatiale des cardiomyocytes avec activité spontanée représente donc un vide immense à combler. Les deux premières études de la thèse seront consacrées à ce sujet.

1.5.2. Le couplage mécano-électrique du stimulateur cardiaque biologique

Contrairement à la répartition spatiale des cardiomyocytes autonomes, les effets du couplage mécano-électrique sur l'activité spontanée sont expérimentalement très étudiés.

Le couplage excitation-contraction (CEC) est le phénomène par lequel l'activité électrique du cœur pilote son comportement mécanique, notamment sa contraction [153]. Par rétroaction, les contraintes mécaniques que subit le cœur peuvent aussi avoir un effet sur son activité électrique. Cette rétroaction est nommée couplage mécano-électrique (CME) [154]. Le CME peut être chronique ou aigu; c'est l'aspect aigu qui est visé dans la thèse.

Le CME aigu peut se manifester à l'échelle systémique dans des conditions tout à fait physiologiques, par exemple au début d'un exercice d'aérobie. En effet, la contraction des muscles squelettiques cause une augmentation soudaine du retour veineux; la surcharge hémodynamique qui en résulte va aboutir à la dilation des chambres cardiaques, et un étirement aigu du myocarde [155]. L'augmentation de la pression diastolique provoque immédiatement une augmentation de la force de contraction et conséquemment une augmentation du volume d'éjection systolique, réaction connue sous le nom de mécanisme de Frank-Starling [156], [157]. Cet exemple où une contrainte mécanique (augmentation de la pression diastolique) provoque une réponse électrique (activation du CEC pour augmenter la force de contraction) illustre bien le fonctionnement du CME. Ce phénomène est le principe derrière certaines pratiques sauvant des vies, comme le coup de poing sternal [158] qui, en cas d'arrêt cardio-respiratoire, peut dans certains cas relancer l'activité cardiaque. Il peut aussi être létal, notamment en cas de *commotio cordis* [159], [160], où une mort subite survient des suites d'un

tachycardie ventriculaire provoquée par un choc sur la poitrine.

La réponse électrique à une contrainte mécanique implique l'existence de nombreux récepteurs mécaniques au niveau cellulaire, notamment les canaux ioniques sensibles au volume (CSV) et les canaux ioniques sensibles à l'étirement (CSE). Le terme générique “étirement” inclut non seulement l'élongation axiale, mais aussi la compression latérale, le changement de courbure de la cellule et toute déformation locale de la membrane. Compte tenu du délai de réponse (pouvant atteindre plusieurs minutes) des CSV, ce sont surtout les CSE [161] qui sont impliqués dans la réponse aigüe aux contraintes mécaniques. Les CSE membranaires peuvent être non-sélectifs vis-à-vis des ions monovalent en général (CSE_{NS}), ou être sélectifs aux ions K^+ en particulier (CSE_K). Ils peuvent simultanément être sensibles au voltage et à certains ligands, de même qu'éventuellement certains canaux ioniques spécialisés dans d'autres stimuli sont aussi sensibles à l'étirement (notamment HCN [162], K_{ATP} [163], [164] , Kv [165], Cav [166], [167] ou Nav [168]).

Des données semblent indiquer que les CSE (ou autres mécanismes sensibles à l'étirement) ne seraient pas uniquement situés au niveau de la membrane cellulaire. Il a été démontré à de nombreuses reprises que l'étirement pouvait modifier la gestion du calcium intracellulaire [169]–[171]. En effet, la fréquence des relâches spontanées de calcium du SR augmente en présence d'étirement axial aigu [172], [173], même chez des cardiomyocytes au repos et en absence de calcium et de sodium extracellulaires [174]. La réponse chronotrope positive de la fréquence de l'activité autonome à l'étirement est réduite en abaissant la quantité de Ca^{2+} contenue dans le SR (blocage de la pompe SERCA) ou en diminuant les relâches calciques des RyR (interférence dans l'activité de ces récepteurs) [175]. La fréquence des relâches de calcium

des mitochondries augmente aussi quand des cardiomyocytes sont pressurés par de petits jets de fluide [176]. L'étirement module l'affinité de la troponine C au Ca^{2+} [177], ce qui modifie $[Ca^{2+}]_i$ par effet tampon, et qui ultimement affecte la fréquence autonome [178]. Enfin, la connexine 46, non cardiaque, est sensible aux contraintes mécaniques [179]; peut-être est-ce aussi le cas pour son isoforme cardiaque la connexine 43. Les mécanismes exacts de l'activation due à l'étirement ne sont pas totalement établis, mais impliquerait une augmentation latérale (dans le sens de l'étirement) de la circonférence du canal et un amincissement transversal (dans le sens orthogonal à l'étirement) de son épaisseur [180].

À l'échelle macroscopique, une corrélation positive entre la charge volumique auriculaire et la fréquence cardiaque a été démontrée chez le chien par Francis Arthur Bainbridge en 1915 [181]. De fait, tout changement dans le retour veineux (par la respiration, la toux, la posture ou la défécation) aura un impact sur la charge volumique auriculaire et donc sur le rythme cardiaque [182]. Cette réponse chronotrope positive de la fréquence cardiaque à l'étirement a été redémontrée sur le cœur [183], l'oreillette [183]–[185] et le nœud SA isolés [186]–[189]. Elle est inversement proportionnelle au rythme basal (i.e. avant étirement) [186] et coïncide avec une augmentation du PDM [186], [190]. L'augmentation du PDM obtenue en maintenant un étirement physiologique constant du nœud sinusal isolé peut régulariser l'activité autonome [187]. Un étirement non physiologique augmente la variabilité [187] et introduit la compétition entre plusieurs site d'initiation de l'activité autonome [191].

Au niveau cellulaire, l'étirement affecte d'abord la durée du PA pour les amplitudes modérées, et ensuite le potentiel diastolique pour les amplitudes plus sévères [192]. Un étirement suffisant durant la diastole cause généralement une dépolarisation de la membrane, alors que

les effets durant le PA sont plus diverses: augmentation de la durée du PA, retard ou perturbation de la repolarisation [192]. La figure 6 résume quelques effets connus de l'étirement sur le potentiel d'action de la cellule sinusale.

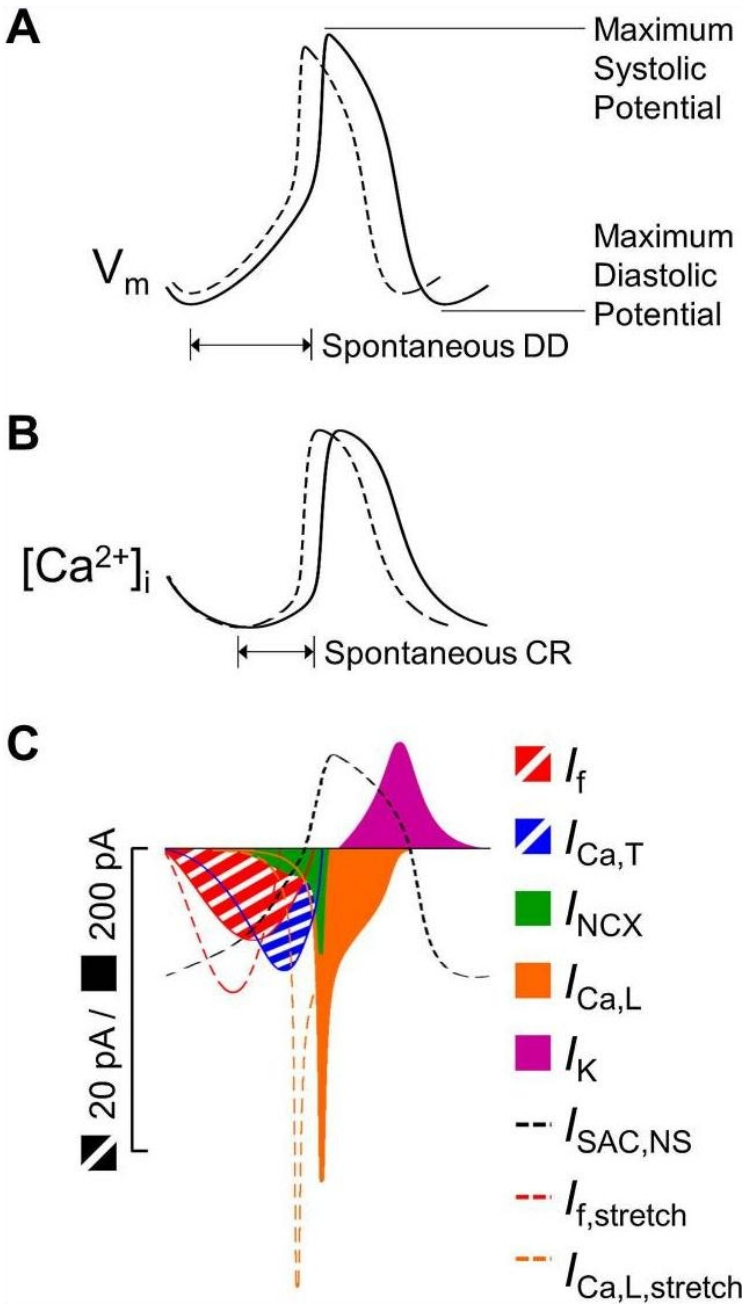

Figure 6. Effets de l'étirement sur le potentiel d'action de la cellule sinusale. Tous les tracés

en ligne discontinue indique la présence de l'étirement. (A) L'étirement augmente le potentiel diastolique minimum, accélère la dépolarisation diastolique et raccourcit le potentiel d'action. (B) La phase montante de la transitoire calcique est également accélérée et sa durée se raccourcit. (C) L'étirement augmente l'amplitude du courant I_f et du courant I_{CaL}. Figure tirée [182].

La réponse à l'étirement des cellules du nœud SA implique principalement les CSE_{NS} [193], qui ont un potentiel d'inversion $E_{CSE,NS}$ entre -25 et 0 mV [161], [194]. L'étirement accélère la DDL et la phase initiale de repolarisation, et décélère l'activation et la phase retardée de repolarisation se trouvant en dessous de $E_{CSE,NS}$; en d'autres termes, il accélère tous les changements de potentiel s'approchant de $E_{CSE,NS}$ et décélère tous les changements de potentiel s'éloignant de $E_{CSE,NS}$ [182] (voir Fig. 7).

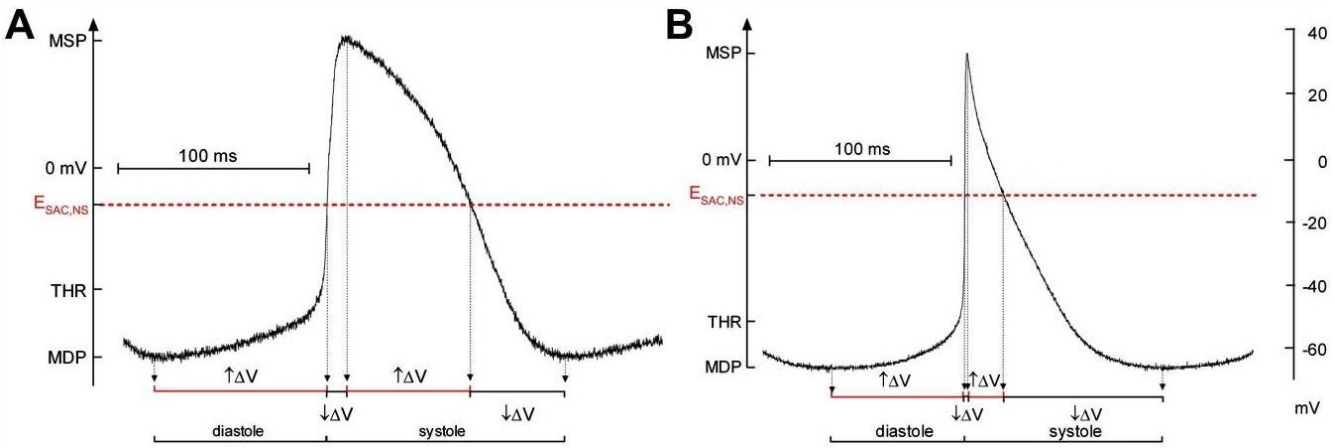

Figure 7. Effet de l'étirement sur le potentiel d'action en fonction de l'espèce. (A) Lapin. (B) Muriné. Le taux de changement du potentiel d'action ΔV augmente (flèche vers le haut) quand le potentiel se rapproche de $E_{CSE,NS}$ et diminue quand le potentiel s'en éloigne. La morphologie du potentiel d'action peut donc expliquer en partie que l'effet chronotrope de

l'étirement sur les cellules du nœud SA varie en fonction des espèces. Figure tirée [182].

L'effet chronotrope de l'étirement dépend ainsi du rapport entre le pourcentage du cycle du PA s'approchant de $E_{CSE,NS}$ et le pourcentage qui s'en éloigne [192]. Par exemple, 54% du cycle du PA se rapproche du potentiel d'inversion chez le lapin contre 29% chez le muriné; d'où une augmentation du rythme chez l'un et une diminution chez l'autre [195]. Ce phénomène peut expliquer en partie que l'effet chronotrope de l'étirement sur les cellules du nœud SA varie en fonction des espèces, avec apparemment une augmentation de la fréquence chez les “gros” et “moyens” animaux (comme les cochons d'Inde, les chiens ou les humains, qui ont un rythme basal lent) et une diminution chez les “petits” animaux (comme les murinés, qui ont un rythme basal élevé). Cette différence trouve probablement sa source dans la morphologie du PA, comme expliqué à la figure 7.

1.6. Les objectifs de la thèse

L’objectif général de la thèse est de quantifier les effets de deux phénomènes sur l’activité spontanée du SCB en monocouche: (a) la répartition spatiale des cardiomyocytes autonomes et (b) l’étirement uniaxial.

Chaque phénomène sera étudié différemment. Une approche théorique sera privilégiée pour la répartition spatiale des cardiomyocytes autonomes afin de mener à bien des investigations et des caractérisations microstructurelles qui seraient impossibles avec les moyens techniques

actuels. Une approche expérimentale sera par contre utilisée pour l'étirement uniaxial, en continuité avec ce qui a été réalisé dans d'autres travaux de recherche.

L'évaluation des effets de la répartition spatiale des cardiomyocytes autonomes se déclinera en deux études aux objectifs distincts mais complémentaires.

Les objectifs de la première étude sont:

(1) Définir et caractériser mathématiquement, au sein d'une monocouche cardiaque, la répartition spatiale aléatoire des cardiomyocytes autonomes, en tenant compte à la fois de la densité globale et de l'homogénéité de la dispersion spatiale (densité locale).

(2) Établir les effets de la répartition spatiale aléatoire des cardiomyocytes autonomes sur l'occurrence de l'automaticité, la période autonome (effet temporel) et les délais d'activation (effet spatial).

Les objectifs de la deuxième étude sont:

(1) Introduire la force de l'automaticité (i.e. la capacité du cardiomyocyte autonome à dépolariser ses voisins non autonomes) et l'anisotropie structurelle linéaire dans le cadre théorique de la première étude.

(2) Déterminer si la force de l'automaticité et/ou l'anisotropie structurelle linéaire peut moduler ou éliminer les effets de la répartition spatiale aléatoire des cardiomyocytes autonomes sur l'occurrence de l'automaticité, la période autonome (effet temporel) et les délais d'activation (effet spatial).

L'évaluation des effets de l'étirement uniaxial se déclinera en une seule étude sont les objectifs

sont:

(1) Cultiver un SCB en monocouche sur un substrat élastique et transparent.

(2) Appliquer un étirement uniaxial, avec ou sans stimulation électrique, au SCB.

(3) Enregistrer la réponse aigüe de l'activité spontanée du SCB à l'étirement uniaxial, en utilisant une approche par fluorescence.

(4) Concevoir et implémenter des algorithmes caractérisant, dans les domaines temporel et spatial, la réponse aigüe de l'activité spontanée du SCB à l'étirement uniaxial.

CHAPITRE 2 – AUTOMATICITÉ MULTICELLULAIRE DES MONOCOUCHES DE CELLULES CARDIAQUES : EFFET DE LA DENSITÉ ET DE LA DISTRIBUTION SPATIALE DES CELLULES AVEC ACTIVITÉ SPONTANÉE

Multicellular automaticity of cardiac cell monolayers: effects of density and spatial distribution of pacemaker cells

James Elber Duverger[1,2], Jonathan B. Béland[1,2], Minh Duc Le[1], and Philippe Comtois[1,2,*]

[1]Research Centre, Montreal Heart Institute, 5000 Belanger Street, Montreal, Quebec, Canada H1T 1C8.
[2]Department of Cellular and Integrative Physiology / Institute of Biomedical Engineering, Université de Montréal, C.P. 6128, Succursale Centre-Ville, Montreal, Quebec, Canada H3C 3J7

E-mail: philippe.comtois@umontreal.ca

Received: June 23, 2014
Revised: September 29, 2014
Accepted for publication: October 6, 2014
Published: November 20, 2014
New Journal of Physics 16 (2014) 113046
doi:10.1088/1367-2630/16/11/113046

Short title: Global automaticity from spatially distributed pacemakers

Classification scheme: PACS

Classification numbers: 87.18.-h, 87.18.Hf, 05.40.-a, 87.19.Hh, 05.45.Xt

*Author to whom any correspondence should be addressed.

Abstract

Self-organization of pacemaker (PM) activity of interconnected elements is important to the general theory of reaction–diffusion systems as well as for applications such as PM activity in cardiac tissue to initiate beating of the heart. Monolayer cultures of neonatal rat ventricular myocytes (NRVMs) are often used as experimental models in studies on cardiac electrophysiology. These monolayers exhibit automaticity (spontaneous activation) of their electrical activity. At low plated density, cells usually show a heterogeneous population consisting of PM and quiescent excitable cells (QECs). It is therefore highly probable that monolayers of NRVMs consist of a heterogeneous network of the two cell types. However, the effects of density and spatial distribution of the PM cells on spontaneous activity of monolayers remain unknown. Thus, a simple stochastic pattern formation algorithm was implemented to distribute PM and QECs in a binary-like 2D network. A FitzHugh–Nagumo excitable medium was used to simulate electrical spontaneous and propagating activity. Simulations showed a clear nonlinear dependency of spontaneous activity (occurrence and amplitude of spontaneous period) on the spatial patterns of PM cells. In most simulations, the first initiation sites were found to be located near the substrate boundaries. Comparison with experimental data obtained from cardiomyocyte monolayers shows important similarities in the position of initiation site activity. However, limitations in the model that do not reflect the complex beat-to-beat variation found in experiments indicate the need for a more realistic cardiomyocyte representation.

Keywords: automaticity, excitable medium, stochastic model, pattern formation, multicellular monolayer

2.1. Introduction

The study of collective behaviour of interconnected elements is important to the general theory of reaction–diffusion systems and is applicable to different areas of science from physics to physiology [1–4]. Diverse behaviours can be observed in networks of connected elements including a variety of synchronous regimes, pattern formation, spiral wave propagation, and spatio–temporal chaos. An example of a physiologically-relevant system is the monolayer cultures of neonatal rat ventricular myocytes (NRVMs) that is often used as experimental models in studies on multicellular cardiac electrophysiology [5–8]. These monolayers usually exhibit electrical automaticity [9–11], defined as the ability to generate action potentials without external (electrical, mechanical, or chemical) stimulations. Primary cultures of isolated NRVMs revealed the existence of pacemaker (PM) cells and quiescent excitable cells (QECs) [12]. Thus, it is highly probable that monolayers of NRVMs are heterogeneous networks of these two cell types. The spontaneous beating rate in these cultures is reportedly modulated by plating density [13]; however, the specific effects of PM cell density and spatial distribution on confluent monolayer spontaneous frequency are still unknown.

Understanding the impact of density and spatial distribution of PM cells on automaticity of the global cardiac network is highly relevant for several clinical situations, such as the reliability of heart activation by the sinoatrial node (SAN) and the initiation of arrhythmias by cells susceptible to delayed afterdepolarisations (DADs). When the heart is being activated, the SAN

PM cells act as initial depolarizing current sources and the surrounding myocardial cells as related sinks. Considering the electrotonic depression of the SAN by electrical connection with the myocardium, the number of PM cells must be large enough to initiate this activation. As a matter of fact, the spontaneous rate and minimum diastolic potential of the SAN dramatically increase when it is isolated from atrial tissue [14]. This knowledge is exploited in the process of creating biological PMs, an alternative to electronic PMs in the treatment of bradycardia [15]. Indeed, to create a sustained PM function in canine ventricle, xenografted cell-containing fluid injected in the left ventricular myocardium must contain at least 700 000 adult human mesenchymal stem cells, and consist of ∼40% PM cells [16]. This is clear example of where the number of PM cells is important, and must be locally increased to activate the surrounding tissue. On the other hand, the presence of PM cells is also linked to arrhythmia initiation. Premature ventricular complexes, for example, can occur when a group of cells with DADs manage to initiate ectopic electrical propagation. These pathological cells act as secondary PM cells competing with the leading SAN. Since a ventricular cell is on average connected to 11 other cardiomyocytes [17], there must be a sufficient number of connected cells simultaneously generating DADs to overcome the electrotonic source–sink mismatch and initiate propagation [18].

Monolayer cultures of NRVMs may provide a useful biological tool to investigate the role of PM-cell–cluster patterns on automaticity and therefore gain better understanding of clinical issues, including creation of biopacemakers [19]. However, the seeding process is usually random and the final spatial distribution of the two cell types unknown. Experimental

assessment of density and spatial distribution of PM cells within a monolayer remains an unsolved problem.

Mathematical modelling may help gain insight into the complex source–sink mechanism behind the effects of PM cell clusters on the spontaneous behaviour of the 2D network. Rather than concentrating on PM cell aggregate spatial characteristics, simulation studies on monolayers of excitable cells have predominantly focussed on ion channel properties [20, 21], effects of coexistence of non-excitable cells [11, 22, 23], intercellular electrical connectivity [24–26], or sink (cells clamped at steady state potential) and break (regions with no conductivity) densities [27]. Theoretical studies on the spatial–temporal behaviour of random mixtures of excitable and oscillating cells have been performed. One notable study was performed by Kanako *et al* [28], who demonstrated the importance of diffusion constant on global activation pattern on a lattice. However, the specific issue of the impact of spatial distribution structure of PM cells on monolayer activity remains to be evaluated. To fill this gap, the present study aims to theoretically assess the effects of spatial distribution and density of PM cells on global automaticity of the cardiac monolayer.

Here, we hypothesized that:

(a) The monolayer is a binary network of interconnected PMs and QECs (passive cells and cleft spaces were not included).

(b) The diffusion is isotropic, since the gap junctions of NRVMs are evenly distributed [29].

(c) The spatial distribution and density of PM cells and QECs (independent variables) influence

automaticity via modulation of spontaneous frequency and electrical propagation properties (dependent variables).

Based on these hypotheses, we created different 2D networks of PM cells and QECs. PM cells were spatially distributed using a stochastic model allowing the variation of aggregation (PM cells connecting to other PM cells) and nucleation (PM cells forming new clusters). The modulation of spontaneous frequency and electrical activation by PM cell spatial distribution and density was then studied with a FitzHugh–Nagumo (FHN)-type model of excitable media [30]. Simulations showed a clear nonlinear dependency of spontaneous activity (occurrence and amplitude of spontaneous period) on the spatial patterns of PM cells. In most simulations, the first initiation sites were found to be located near the substrate boundaries. Data were compared to fluorescence recordings of calcium waves in NRVM monolayers to highlight similarities and limitations of the model.

2.2. Methodology

2.2.1 Generation of spatial patterns for PM cells

Patterns were created assuming the existence of only two types of NRVMs (PM cells and QECs) and this led to a binary 2D network. Each PM cell made connections with all its neighbours (the eight nearest cells in a square lattice). The spatial pattern formation algorithm randomly determined the positions of PM cells, and QECs filled the remaining available space.

The algorithm is presented in figure 1(a) and is summarized as follows. The starting point was an empty square lattice of dimension $N \times N$. For the first iteration, an initial PM cell was randomly seeded in one of the N^2 available sites. The status of a place containing an autonomous cell was referred to as the *autonomous site* (‘aut’ site). During the second iteration, a random number p ($0 \leqslant p \leqslant 1$) was drawn from a uniform distribution and compared with a user-defined iteration-independent parameter p_{thr} ($0 \leqslant p_{thr} \leqslant 1$) that decided whether the new PM cell would or would not be in contact with an existing cluster (a group of one or more interconnected PM cells).

If $p \leqslant p_{thr}$, then the new cell would not contact any existing cluster and would be randomly deposited in a free site from the M_2 set (blue available sites in figure 1(b)). Inversely, if $p > p_{thr}$, then the new cell would be part of the M_1 set (red available sites in figure 1(b) corresponding to the 8-connected free neighbourhood). Repeating this procedure for n iterations increased the density of autonomous cells (D_{aut} = number of PM cells/N^2) to the desired level. There was a D_{aut} limit ($D_{aut} > D_{aut,max}(p_{thr})$) beyond which no new sites could be added to the lattice without converging on an existing cluster. In summary, spatial distribution was modulated by parameter p_{thr} while the density was modulated by the number n of iterations.

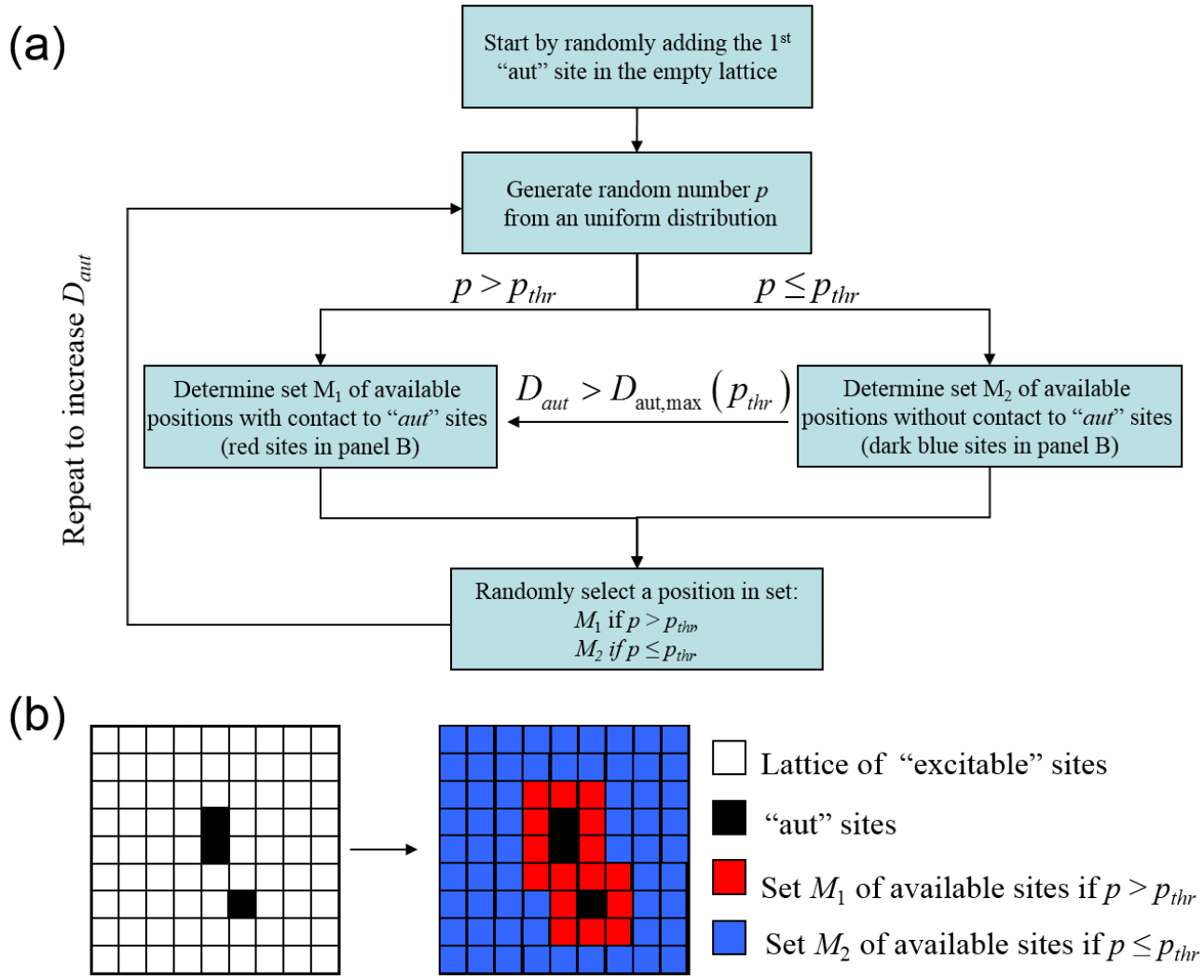

Figure 1. Algorithm for spatial distribution. (a) Algorithm for the stochastic model based on the threshold parameter p_{thr} and random number p generated from a uniform distribution. (b) Left panel: a schematic showing the pattern after three iterations of the model with 'aut' sites (black squares). Right panel: the positions in set M_1 (red squares, available sites if $p > p_{thr}$) and set M_2 (blue squares, available sites if $p \leqslant p_{thr}$) available for the subsequent iteration.

2.2.2 Mathematical model of autonomous cells and QECs

Modelling could be performed with various types of excitable representations ranging from the simplest FHN model to cardiac realistic ionic models [31, 32]. Here, we selected a simple

modified FHN model of PM cells integrated into a 2D excitable network similar to cultured monolayers. The model was described previously by Borek et al [30]:

$$\frac{\partial V}{\partial t} = \frac{1}{\kappa}\left(V - \frac{V^3}{3} - w\right) + I_P + \left(D_x \frac{\partial^2 V}{\partial x^2} + D_y \frac{\partial^2 V}{\partial y^2}\right),$$
$$\frac{\partial w}{\partial t} = \kappa(V + \beta - \gamma w)\left(\frac{w_h - w_l}{1 + e^{-4V}} + w_l\right), \quad (1)$$

where V and w represent the activation (similar to the transmembrane voltage) and inhibition variables, respectively. The parameter values were fixed to obtain an excitable but non-autonomous medium: diffusion coefficient $D_x = D_y = 0.2$, $\kappa = 0.6$, $\beta = 0.7$, $w_h = w_l = 0.1$, $I_P = 0$. A PM current $I_P = 1$ was applied to achieve autonomous activity. Spatial distribution of the autonomous cell was thus implemented by setting $I_P = 1$ in 'aut' sites (all the locations occupied by an autonomous cell) of the lattice built with the stochastic model described in section 2.2.1. The model was solved on the N^2 lattice ($N = 200$, unless stated otherwise in the text) using an Euler forward finite difference in time ($\Delta t = 0.001$) coupled with a central difference in space of $\Delta x = \Delta y = 0.05$ and no-flux boundary conditions applied to the four sides of the lattice. The estimated space constant of the system with the above parameters was greater than $10\Delta x$. Initial conditions were the resting state for QECs and the state of minimum V for PM cells. All PM cells were set to the same phase in this study for simplicity.

2.2.3 Experiments with NRVMs monolayer cultures

All animal handling procedures were concordant with the Canadian Council on Animal Care guidelines and were approved by the Montreal Heart Institute Animal Research Ethics

Committee. Sprague-Dawley rats aged 1–3 days were sacrificed by decapitation. Beating hearts were removed immediately and kept in cold Ca^{2+}- and Mg^{2+}-free Hank's balanced salt solution. Ventricular muscle was excised and tissue was minced on ice into 1–3 mm^3 pieces. The mixture was subjected to purified enzymatic digestion using a Neonatal Cardiomyocytes Isolation System (Worthington Biochemical, Lakewood, NJ). Isolated cells (enriched cardiomyocytes) were counted and seeded at a density of 1 × 106 cells mL^{-1} in 29 mm diameter glass-bottom culture dishes (D29-20-0-N, In vitro Scientific, Sunnyvale, CA) pre-coated with 0.2% gelatine and 0.001 25% fibronectin solution. Cells were grown in an incubator (37 °C, 5% CO_2) for 48 h in phenol-free Dulbecco's modified Eagle's medium (DMEM, 319-050-CL, Wisent, St-Bruno, Canada) with 1% penicillin/streptomycin (P/S, 450-201-EL, Wisent). For the first 24 h of incubation, 5% foetal bovine serum (FBS, SH30396.03, Fisher Scientific) was added to the culture medium.

The calcium-sensitive dye Fluo-4 AM (F-14201, Life Technologies, Carlsbad, CA) was used to stain cells for fluorescence imaging experiments. To prepare the solution, 50 μg of Fluo-4 AM was dissolved in 18 μL of pure dimethyl sulfoxide (DMSO, 4-X-5, ATCC, Manassas, VA). The dissolved dye was added to 4.5 mL DMEM (without FBS and P/S) containing 4.5 μL of 2% DMSO-dissolved pluronic acid (F-127, Life Technologies). Post-cultured monolayers were loaded with 300 μL/dish of staining solution and incubated for 30 min. The dye was then washed out twice with DMEM and replaced with 1.5 mL fresh DMEM (without FBS and P/S). A 15 min equilibration period was allowed for the de-esterification process of Fluo-4 AM to occur before initiating acquisitions.

Mapping experiments were performed with a setup developed in-house using a high-speed CCD camera system (80 × 80 pixels, RedShirtImaging, LLC, Decatur, GA). The dye was excited with a quartz tungsten halogen lamp (Oriel Instruments, Stratford, CT). The filters used for excitation and emission were $\lambda_{excitation} \approx 480 \pm 20$ nm (Chroma Technology, Bellows Falls, VT) and $\lambda_{emission} \approx 535 \pm 25$ nm (Semrock, Rochester, NY), respectively. The system was set to image a field of view of 1.38 cm^2 and the acquisition frame rate was 125 Hz for all experiments. Signals were filtered and analysed using a program developed in-house using Matlab software (R2008, MathWorks, Natick, MA). In summary, raw acquisitions were normalized by the minimum fluorescence for each pixel and the *dF/dt* (the first time derivative of fluorescence) was approximated using a finite difference approach. The resulting signals were then spatially filtered using a Gaussian kernel (5 × 5 pixels with $\sigma = 1.5$) followed by a temporal moving average with a 2-sample window.

2.3. Results

2.3.1. Characterization of the spatial distribution of autonomous cells based on the stochastic model

Patterns of PM cells obtained by simulating the stochastic model are shown in figure 2 for $D_{aut} = 0.35$ corresponding to 35% occupation of the lattice by PM cells.

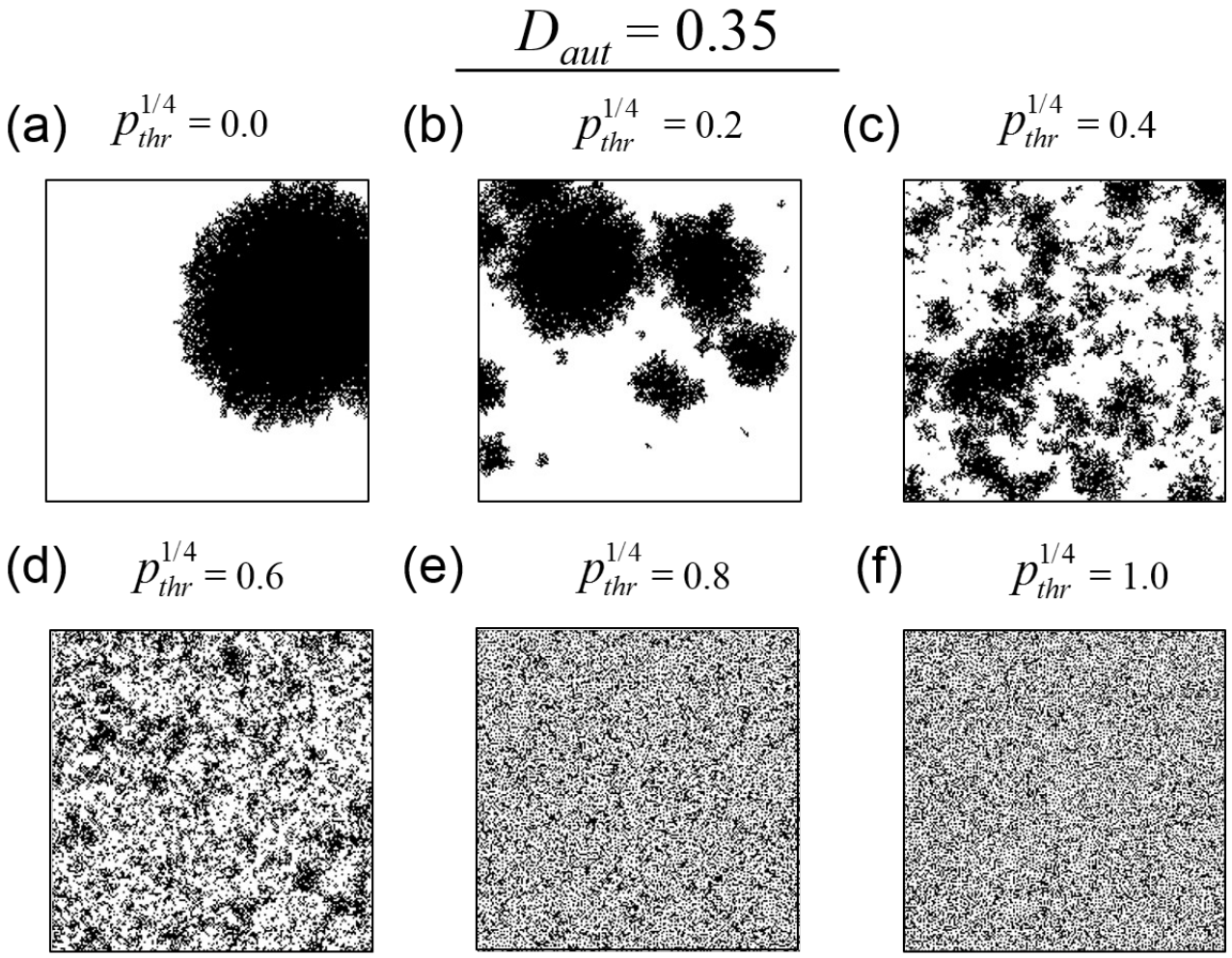

Figure 2. Examples of patterns. Examples of patterns with N = 500 at D_{aut} = 0.35 obtained for a set of $p_{thr} \in [0,1]$ (indicated on top of each panel) increasing from 0 (panel (a)) to 1 (panel (f)).

When p_{thr} = 0, only a single cluster (normalized area of 0.35) is created by aggregation of the new PM cells around the initial random seeding. All patterns obtained with p_{thr} = 0 have a single Eden-like cluster and are thus similar to the example presented in panel (a). For this special case, the only difference between created patterns stems predominantly from the initial random seeding around which the aggregation process occurs. Patterns in figure 2 were

obtained with $p_{thr} > 0$ and resulted in a higher number of clusters (B, 72; C, 1020; D, 5400; E, 14015; F, 14602); thus, decreasing the mean normalized area per cluster (B, 486.1×10^{-5} ; C, 34.3×10^{-5} ; D, 6.5×10^{-5} ; E, 2.5×10^{-5} ; F, 2.4×10^{-5}).

As D_{aut} increases when building patterns, the number of positions in set M_2, i.e. sites not touching an existing cluster, decreases such that there exists a limit for each pattern when M_2 is empty and $D_{aut} < 1$. Except for p $p_{thr} = 0$ for which the limit is $D_{aut} = 1$, the limit is represented by a distribution of $D_{aut,max}(p_{thr})$ corresponding to the distribution of maximum D_{aut} for individual patterns. This limit is shown in figure 3(a) as three curves representing the 5th percentile line (bottom curve), median (middle curve), and 95th percentile (top curves) obtained for a set of 1000 patterns per (p_{thr},D_{aut}) pair. The result is shown with scaling of p_{thr} ($p_{thr}^{1/4}$) to facilitate viewing since most of variations occurred at low pthr. Median $D_{aut,max}(p_{thr})$ decreases with increasing p_{thr}. The interval between the 5th and 95th percentiles of $D_{aut,max}(p_{thr})$ is not constant as a function of $p_{thr}^{1/4}$. It is narrow for $p_{thr}^{1/4}$ close to zero, widest around $p_{thr}^{1/4} \approx 0.3$, and slowly decreases towards $p_{thr}^{1/4} = 1$.

The average number of clusters ($N_{clusters}$) obtained for dimension $N = 100$ and 1000 samples per (p_{thr}, D_{aut}) pair is shown in figure 3(b). Two general results can be stated. Firstly, for a given $p_{thr} > 0$, the number of clusters increases and then decreases with D_{aut} in a biphasic manner, as long as $D_{aut} < D_{aut,max}(p_{thr})$ (the median shown by a white line in the figure). Secondly, for a given D_{aut}, the number of clusters is higher, again with greater p_{thr}, as long as $D_{aut} < D_{aut,max}(p_{thr})$. Thus,

the maximum Nclusters is found for p_{thr} = 1 and D_{aut} immediately below $D_{aut,max}(1)$.

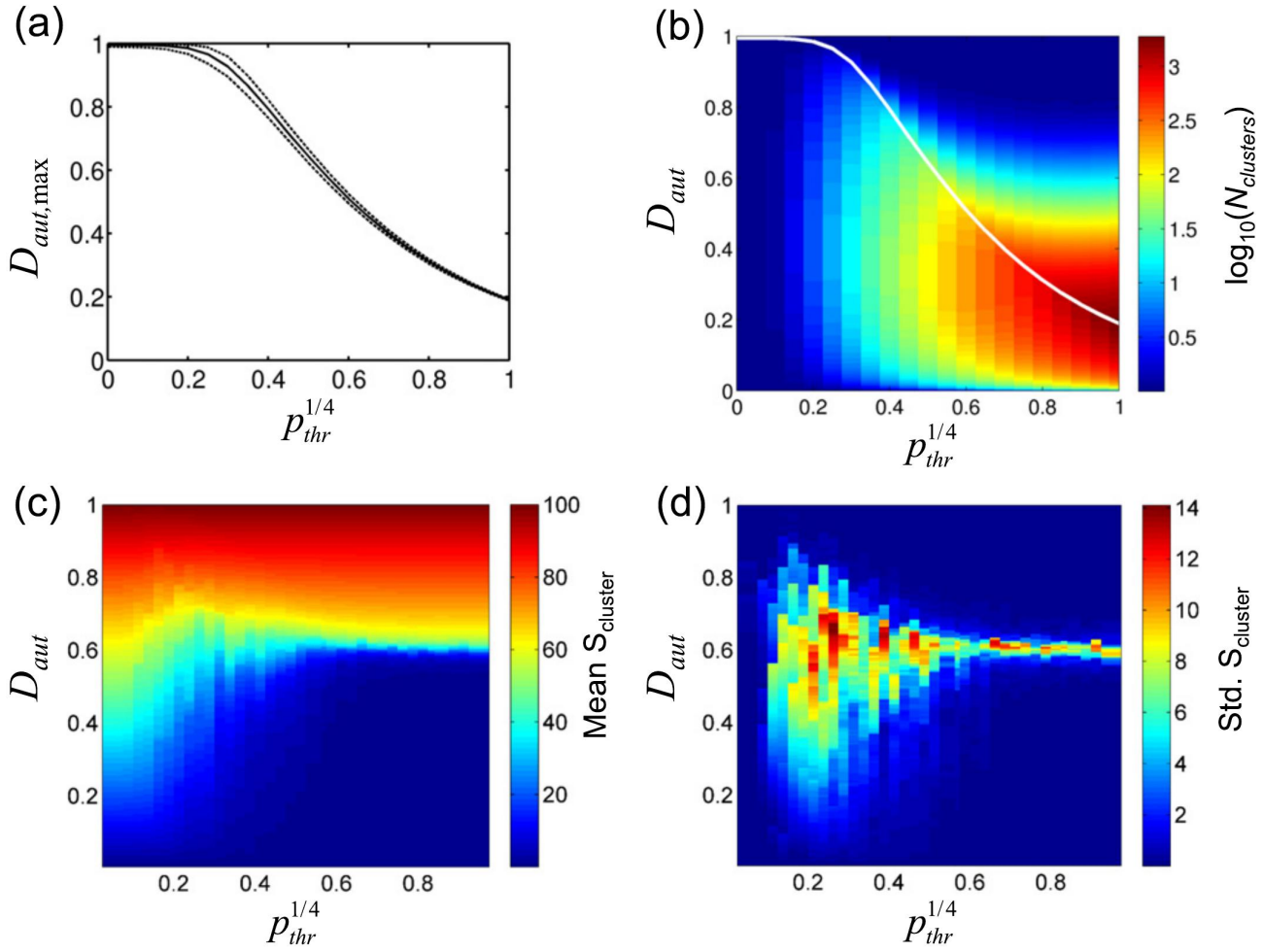

Figure 3. Spatial characterization. (a) A maximum D_{aut} ($D_{aut,max}$) exists for each substrate corresponding to the situation where M_2 is empty (see figure 1, available positions on the lattice without contact to an 'aut' site). $D_{aut,max}$ for a set of N = 1000 simulations is shown by a set of percentile curves (bottom: 5%, mid: 50%, and upper: 95%). (b) The number of clusters ($N_{clusters}$) is plotted using a colour scale as a function of p_{thr} and D_{aut}. (c) Variation in the mean cluster maximum area (mean $S_{cluster}$) as a function of $p_{thr}^{1/4}$ and D_{aut}. As expected, increasing D_{aut} yields a higher area. However, the increase is more linear for low $p_{thr}^{1/4}$, while high $p_{thr}^{1/4}$ shows minimal area until $D_{aut} \approx 0.6$ where a rapid transition occurs due to aggregation of individual

clusters. Note that there is a slight shift to higher D_{aut} for mean $S_{cluster}$ around 60 for $p_{thr}^{1/4}$ between 0.2 and 0.4. (d) Standard deviation of the maximum cluster area (std.$S_{cluster}$) showing that intrinsic variation between generated patterns occurs over a different range of Daut as a function of $p_{thr}^{1/4}$. The maximum range with higher variation is found for $p_{thr}^{1/4}$ between 0.2 and 0.4.

The average maximum cluster area (mean $S_{cluster}$) was calculated from the set of maximum cluster area for each simulated patterns and is shown in figure 3(c). $p_{thr}^{1/4}$ = 0 is a special case where all clusters consist of a single site. Otherwise, increasing D_{aut} resulted in higher mean $S_{cluster}$ independent of $p_{thr}^{1/4}$. However, a difference was observed in the slope for increasing D_{aut}. Indeed, for low $p_{thr}^{1/4}$ the increase is more linear and starts at low D_{aut} while the transition to high-area cluster occurs at high D_{aut} (around 0.6) with a rapid augmentation. Interestingly, for a given D_{aut}, increasing $p_{thr}^{1/4}$ results in a decrease of mean Scluster. However, biphasic variation occurs for D_{aut} between 0.6 and 0.8. This is also the region of greatest variability between samples as highlighted by the higher standard deviation in the maximum cluster size (std.$S_{cluster}$) depicted in figure 3(d).

2.3.2. Analysis of the stochastic model

The parameter p_{thr} in the model represents the threshold in the interval [0, 1] selected between creating a new cluster (nucleation) and adding an autonomous site to an existing cluster (aggregation). Thus, the probability for a new cluster to be created should be equal to p_{thr} as

long as $D_{aut} < D_{aut,max}(p_{thr})$. The average creation rate estimated by the mean change in the number of clusters per iteration is depicted for three increasing D_{aut} intervals in figure 4(a).

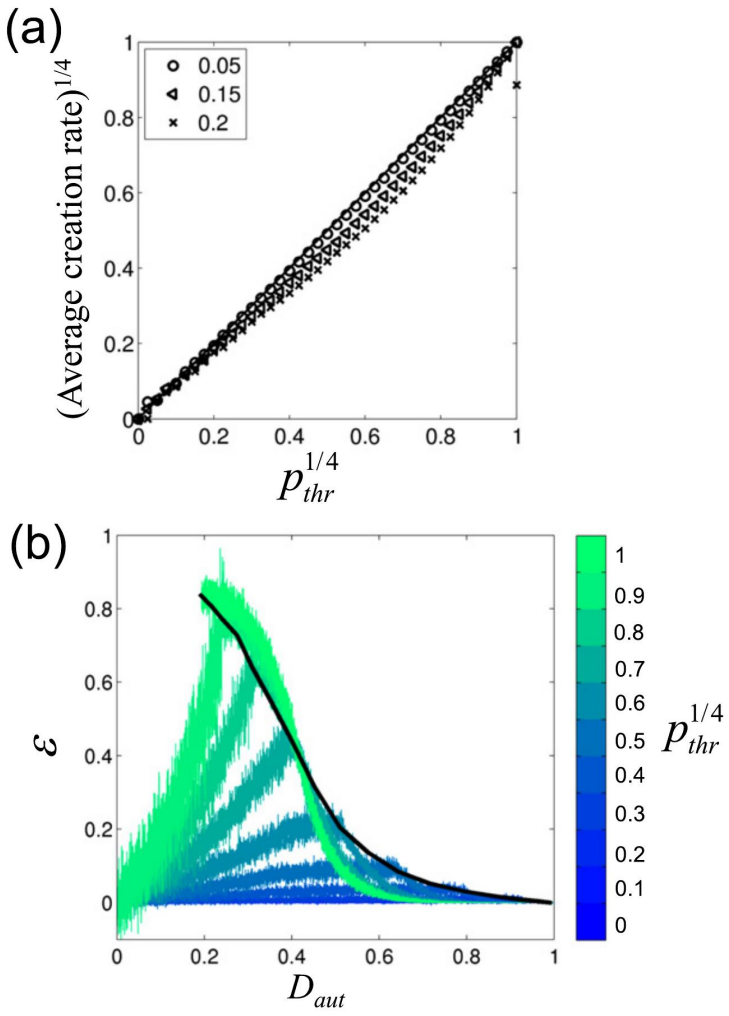

Figure 4. Analysis of the stochastic model. (a) Average cluster creation rate calculated as a function of p_{thr} as the mean change in the number of clusters per iteration over the interval $[D_{aut,upper} - D_{aut,upper}]$, where $D_{aut,upper} \in \{0.05,0.15,0.2\}$ (corresponding to the markers shown in the legend). The results show linear correspondence at low $D_{aut,upper}$ but increased deviation from the line of identity with increased $D_{aut,upper}$. (b) The probability of cluster fusion (ε) as a function of D_{aut} for $p_{thr} \in [0,1]$ exhibiting biphasic variation with an initial increase followed by a decrease for $D_{aut} > D_{aut,max}(p_{thr})$. The black line represents the median of $D_{aut,max}(p_{thr})$.

As expected, the average creation rate correlates almost perfectly with p_{thr} for small D_{aut} (black circles, $D_{aut,upper}$ = 0.05). However, as the number of iterations increases to achieve higher D_{aut} (from $D_{aut,upper}$ = 0.15 to 0.2), the average rate remains strictly below the line of identity with a maximum deflection for $p_{thr}^{1/4} \approx 0.65$. Thus, on average, the total number of clusters are less than the value predicted by p_{thr}.

The decrease in the average creation rate can be explained from the following model. Starting from the initial single autonomous site in an empty square lattice, the number of clusters (n) at time zero is equal to 1 (n_0 = 1). The change in average number of clusters at iteration i + 1 (n_{i+1}), can then be approximated by:

$$n_{i+1} - n_i = \begin{cases} p_{\text{thr}} - \varepsilon\left(p_{\text{thr}}, D_{\text{aut}}\right)\left[1 - p_{\text{thr}}\right] & \text{if } D_{\text{aut}} < D_{\text{aut, max}}\left(p_{\text{thr}}\right), \\ -\varepsilon\left(p_{\text{thr}}, D_{\text{aut}}\right) & \text{if } D_{\text{aut}} \geqslant D_{\text{aut, max}}\left(p_{\text{thr}}\right). \end{cases} \quad (2)$$

Here $\varepsilon(p_{thr}, D_{aut})$ represents the probability that adding the new site results in the merger or aggregation of two or more clusters. The average of $\varepsilon(p_{thr}, D_{aut})$ obtained for 1000 simulations per pair of parameters are plotted in figure 4(b). At low D_{aut}, $\varepsilon(p_{thr}, D_{aut}) \rightarrow 0$ adding a new autonomous site to an existing cluster should not connect to existing clusters because the number of clusters is small compared to the distance between clusters. As D_{aut} increases, so does $\varepsilon(p_{thr}, D_{aut})$ since the average distance between neighbouring clusters decreases. Finally, $\varepsilon(p_{thr}, D_{aut}) \rightarrow 0$ with increasing D_{aut} as the number of clusters decreases to a single cluster because of aggregation. The variation in $\varepsilon(p_{thr}, D_{aut})$ with p_{thr} is shown in figure 4(b) with values

increasing as p_{thr} increases. For the special case of $p_{thr} = 1$, $\varepsilon(p_{thr}, D_{aut})$ is not defined for $D_{aut} < D_{aut,max}(p_{thr})$ because of the impossibility of adding an autonomous site to an already existing cluster.

It is still possible to estimate the average total number of clusters for this model. For example, for $p_{thr} = 0$, $\varepsilon = 0$ since there is a single cluster and no new cluster is created on every iteration (see figure 2 with $D_{aut} = 0.35$). In contrast, for $p_{thr} = 1$, the added new site will never come into contact with an existing cluster as long as $D_{aut} < D_{aut,max}(1)$. We can deduce from equation (2) that the average number of clusters should be:

$$N_{\text{clusters}}\left(D_{\text{aut}}, N^2\right) - 1 = \begin{cases} p_{\text{thr}} D_{\text{aut}} N^2 - \left(1 - p_{\text{thr}}\right) \sum_{i=1}^{N^2} \varepsilon\left(p_{\text{thr}}, i/N^2\right) \\ \quad \text{if } D_{\text{aut}} \leqslant D_{\text{aut, max}}\left(p_{\text{thr}}\right), \\ p_{\text{thr}} D_{\text{aut, max}}\left(p_{\text{thr}}\right) N^2 \\ \quad - \left(1 - p_{\text{thr}}\right) \sum_{i=1}^{N^2} \varepsilon\left(p_{\text{thr}}, i/N^2\right) \\ \quad \text{if } D_{\text{aut}} > D_{\text{aut, max}}\left(p_{\text{thr}}\right), \end{cases} \tag{3}$$

where the first term corresponds to the average number of clusters created for the density D_{aut} in a medium with N^2 sites and the second term corresponds to the total loss (over the addition process from 0 to D_{aut}) of clusters caused by cluster aggregation or fusion.

2.3.3. Modulation of the autonomous period by PM cell density in simulations

The period of activity (normalized to the single-cell period) is increased in a heterogeneous

spatially extended system compared to single-cell autonomous activity of the FHN for equation (1) with I_P = 1. The change in period when simulating a circular patch with increasing radius is depicted in figure 5(a). Two main characteristics can be found: (1) there is a minimal radius for automaticity occurrence, and (2) the normalized period is increased by ∼32% when automaticity starts to occur and decreases asymptotically to the period of the single-cell model.

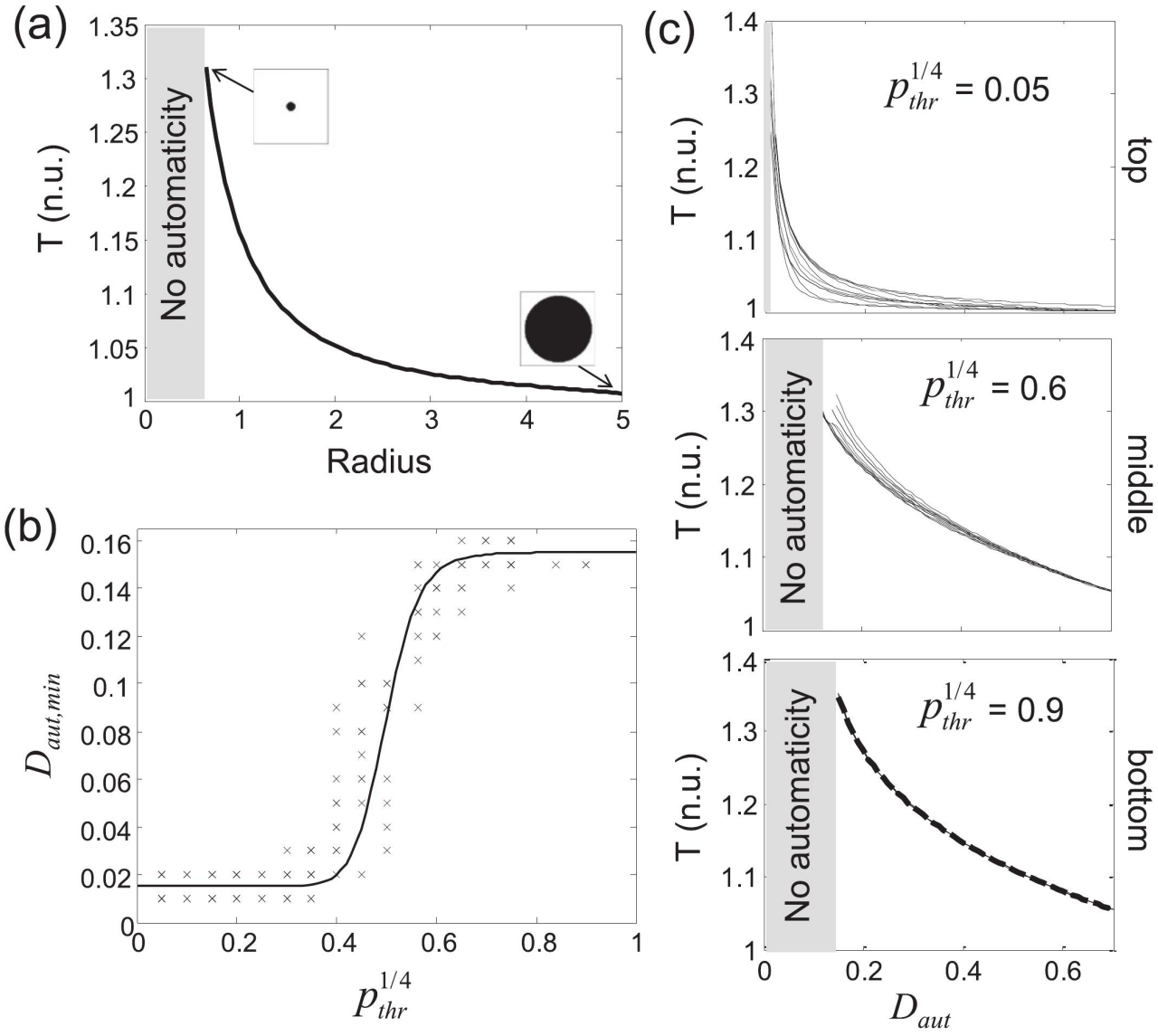

Figure 5. Autonomous periods. (a) Simulation results of the effects of a centred circular zone

of autonomous cells with a set of excitable cells on the normalized period of activity (normalized to the period of an autonomous cell for the parameters presented in section 2.2.2). It clearly shows that a minimum cluster area is needed to drive the monolayer (highlighted by the grey area labelled no automaticity). While a small cluster yielded ∼32% slowing, increasing the cluster area decreased the period towards the isolated cell period (T = 1). (b) Minimum D_{aut} ($D_{aut,min}$) as a function of $p_{thr}^{1/4}$ is presented. A clear transition between low $D_{aut,min}$ close to 0.015 is found for $p_{thr}^{1/4}$ < 0.4 and rapid transition to values around 0.15 for $p_{thr}^{1/4}$ > 0.6. A sigmoidal fit with $p_{thr}^{1/4}$ at half value of 0.5 is superimposed (black line). (c) Normalized period of activity (T) for three $p_{thr}^{1/4}$ values is shown where a faster decrease in T is found for $p_{thr}^{1/4}$ = 0.05 (top) compared with $p_{thr}^{1/4}$ = 0.6 (middle) and $p_{thr}^{1/4}$ = 0.9 (bottom). In addition, variability between samples occurs over a larger D_{aut} interval for smaller $p_{thr}^{1/4}$.

We then asked what effects stochastic patterns would have on the minimum density of autonomous sites ($D_{aut,min}$) for autonomous activity to occur. Simulation results are shown in figure 5(b) where a clear transition between low $D_{aut,min}$ and high $D_{aut,min}$ is found with ∼10 times larger density needed for high $p_{thr}^{1/4}$ ($D_{aut,min}$ = 0.015 for $p_{thr}^{1/4}$ close to zero and $D_{aut,min}$ = 0.155 for $p_{thr}^{1/4}$ close to 1). The transition occurs around $p_{thr}^{1/4}$ = 0.5 as estimated by fitting a sigmoidal function (black curve).

Low density of autonomous cells also always results in longer periods of activity. Simulation results for $p_{thr}^{1/4} \in \{0.05,0.6,0.9\}$ are shown in figure 5(c). The period T decreases rapidly after starting at low D_{aut} with important variability for D_{aut} < 0.4 at low $p_{thr}^{1/4}$ (top panel). In

comparison, for $p_{thr}^{1/4}$ = 0.6 (middle panel), the decrease in period is slower. While some variability in period is detected between samples, the level seems to be less and restricted to lower D_{aut}. A high $p_{thr}^{1/4}$ of 0.9 results in a slow decrease in period T, but also negligible variability between samples, a hallmark of the low variability observed in the maximum cluster area (as seen in figure 3(d)). In all cases of figure 5(c), a greater minimum density is required to generate spontaneous activity. Global mean of the period (mean T) of activity is presented as a function of $p_{thr}^{1/4}$ and D_{aut} in figure 6(a) and the corresponding standard deviation of the period (std.T) in figure 6(b). A closer look at the results in figure 6(a) shows that a given delay occurs at a small D_{aut} for small $p_{thr}^{1/4}$ while more PM cells are needed to obtain a similar rate for high $p_{thr}^{1/4}$. For example for T = 1.15 (black curve), D_{aut} is around 0.03 for $p_{thr}^{1/4}$ = 0.1 compared to 0.39 for $p_{thr}^{1/4}$ = 0.9; thus, giving rise to a 36% difference in cell density. As T approaches unity, the difference increases such that for T = 1.10 (white curve), the difference in cell density is 49%. In most of the parameters space, the transition from low to high D_{aut} occurs within the interval 0.2 < $p_{thr}^{1/4}$ < 0.6 where patterns consist of a combination of small and large clusters (see figure 2(c)). As expected, the variability between results is generally higher at low D_{aut} followed by a monotone decrease with increasing density. However, the change in variability as a function of $p_{thr}^{1/4}$ for a given D_{aut} has biphasic variation within the same interval 0.2 < $p_{thr}^{1/4}$ < 0.6 . This indicates an instability in the generated patterns, and a correlation between variability and increased sensitivity of the period to changes in $p_{thr}^{1/4}$.

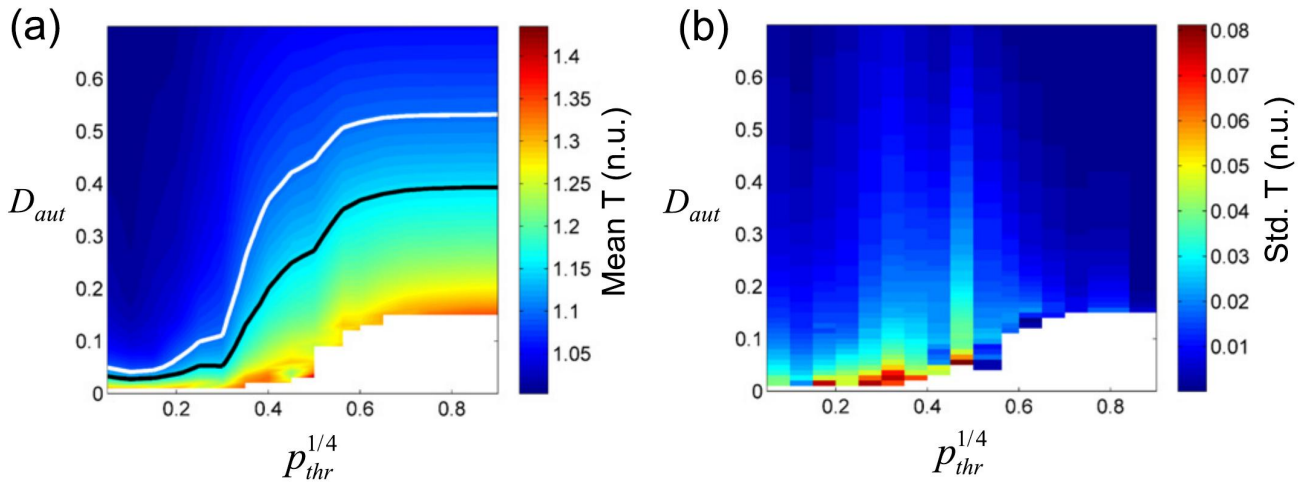

Figure 6. Autonomous periods : complete overview. (a) Mean normalized periods (mean T) and (b) standard deviation of normalized periods (std.T) are shown for the set of simulations from patterns obtained for $0 < p_{thr}^{1/4} < 1$ and $0.01 < D_{aut} < 0.7$. The curves added in panel (a) correspond to isovalues of period for T = 1.1 (white curve) and T = 1.15 (black curve).

2.3.4. Impact of the spatial distribution of autonomous cells on synchronous activation

The simulations were analysed and the total activation time ($t_{act,tot}$) for the last simulated beat calculated. For a specific beat, the total activation time is the activation delay between the first and last nodes and represents the time required for the initial activation to fully propagate in the monolayer. It is calculated as *time of the last activation – time of the first activation* for the same beat. Mean $t_{act,tot}$ (figure 7(a)) and the standard deviation of $t_{act,tot}$ (std.$t_{act,tot}$, figure 7(b)) show a variation as a function of $p_{thr}^{1/4}$ and D_{aut}. Small $p_{thr}^{1/4}$ yields the largest delay (example for D_{aut} = 0.25 with $t_{act,tot}$ = 0.37 is shown in the top panel of figure 7(c)). The delay decreases with increasing $p_{thr}^{1/4}$ (examples with $t_{act,tot}$ = 0.26 for $p_{thr}^{1/4}$ = 0.5 and 0.035 for $p_{thr}^{1/4}$ = 0.9).

Thus, while large clusters of autonomous cells yield the smaller period of activity for a given density, the activity is less synchronous and more dependent on propagation. On the other hand, a more uniform distribution of autonomous cells (as created with large $p_{thr}^{1/4}$) is slower, being more affected by electrotonic effect; however, it yields a more synchronized activation. Importantly, as depicted in figure 7(d), the normalized period of activity T shows no interbeat variation regardless of pattern type (e.g. $p_{thr}^{1/4}$ values).

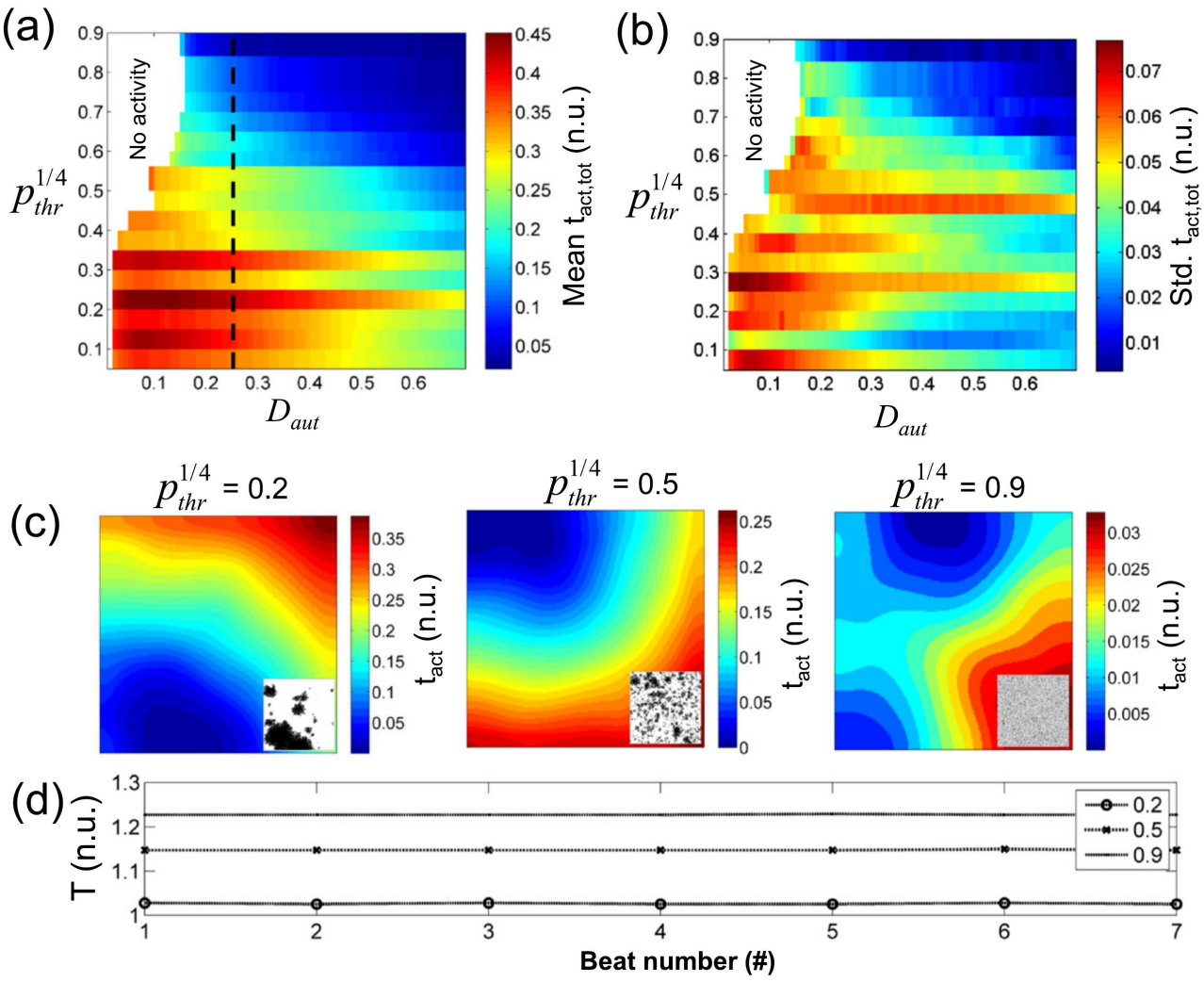

Figure 7. Synchronicity of activation. (a) Effects of autonomous cell spatial distribution on synchronicity of activation. (a) Mean of total activation time (mean $t_{act,tot}$) obtained as a function of $p_{thr}^{1/4}$ and D_{aut} shows a clear dependence on the density of autonomous cells. This becomes increasingly important for $p_{thr}^{1/4}$ > 0.6, where mean $t_{act,tot}$ is minimal and lower than 0.1. (b) Same as (a) except that the standard deviation of total activation time is shown. (c) Examples of activation maps with D_{aut} = 0.25 are presented for three patterns (shown in inserts of each example). In all three examples, activation starts close to a boundary (dark blue colour on the maps). For $p_{thr}^{1/4}$ = 0.2 (top panel), activation starts at the bottom (where the largest cluster of autonomous cells is located in the insert) and ends ∼0.37 normalized time later. Increasing $p_{thr}^{1/4}$ to 0.5 (middle panel) decreases $t_{act,tot}$ to ∼0.26 with initial activation near the top boundary. A large $p_{thr}^{1/4}$ of 0.9 (bottom panel) where autonomous cells are distributed homogeneously within the substrate yields the lowest $t_{act,tot}$ of ∼0.035; this finding is 10-times smaller than the value generated for $p_{thr}^{1/4}$ = 0.2 (top panel). Note that the site of first initiation is close to the top boundary followed by a second region in the bottom left corner. (d) T for the last seven simulation beats for the three examples presented in panel (c).

2.3.5. Localization of the first activation sites

Another interesting result can be seen in figure 7(c), which shows that the sites where activation starts (site of first activation, dark blue from the colour scale) are located close to the boundaries. Indeed, the example for $p_{thr}^{1/4}$ = 0.2 (top panel of figure 7(c)) and $p_{thr}^{1/4}$ = 0.5 (middle panel) show a single first activation site respectively located at the bottom and top of the substrate. Although only a single first activation site is observed for the example with $p_{thr}^{1/4}$ = 0.9 (bottom panel), a second region starts to activate rapidly at the bottom left corner.

Pooling and plotting the first activation sites of the last three activations of each simulation (all $D_{aut} < 0.35$ and $p_{thr}^{1/4}$) yields figure 8(a).

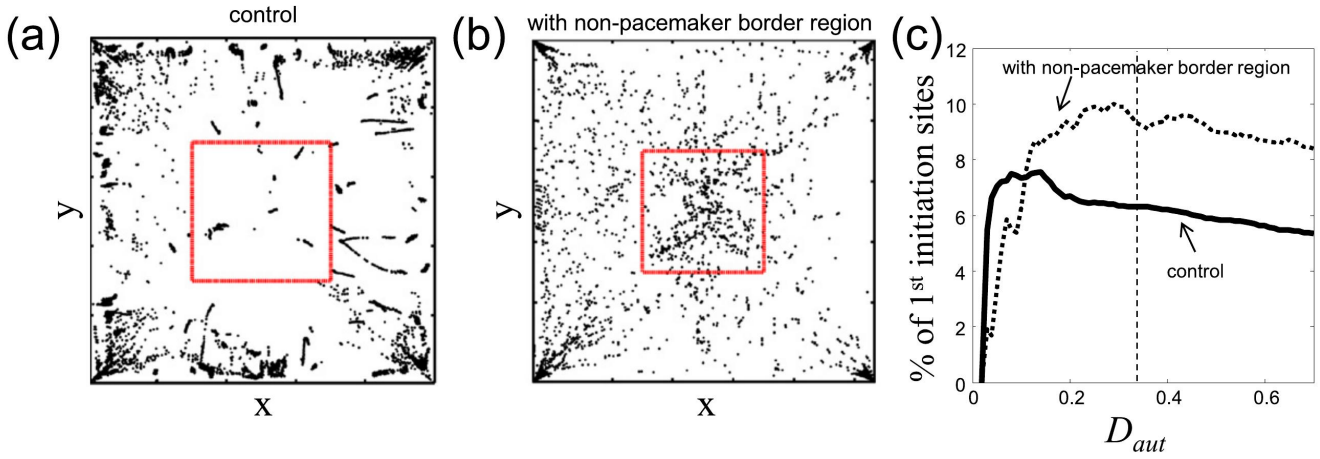

Figure 8. First initiation sites. (a) Spatial distribution of first initiation sites of the last three autonomous activations of all simulations for $D_{aut} < 0.35$. Although some sites are found in the middle of the substrate (6.3% of sites within the red square), most sites are found close to the boundaries (with no-flux condition). (b) In comparison, adding a layer of excitable but non-pacemaker cells around the patterns simulated in (a) yielded a more homogeneous distribution of sites with 9.2% of sites inside the red square. (c) Evolution of the percentage of sites inside the centred red square in (a) and (b) as a function of D_{aut} for the two sets of simulations. While the number of first initiation sites increases more rapidly in our control sets, adding the border of excitable cells yielded around 50% more sites inside the region delimited by the red square for $D_{aut} > 0.1$.

Clearly, the vast majority of the first activation sites is found close to the boundaries. Indeed only 6.3% of sites are located within the red square. Simulations with the spatial patterns of autonomous cells were repeated after adding a border of excitable cells (with a layer of 0.65 cm). The distribution of the first activation sites is displayed in figure 8(b), which shows a more

homogeneous distribution of sites. By adding the excitable layer around the pattern of autonomous cells (width of 13 sites all around the previously simulated distribution patterns), the proportion of sites within the red square increased to 9.2% (corresponding to an increase of 46% compared with control conditions in panel (a)). A comparison of the density of first initiation sites in the red square was made between these two sets of simulations at cumulative D_{aut}. The result is shown in figure 8(c) and indicates that the presence of no-flux boundary conditions near autonomous cells favour their activation by constraining local diffusion; thus, decreasing the electrotonic effect on spontaneous activity.

2.3.6. Complex dynamic behaviour: insights from experimental data

A typical post-culture recording of calcium waves is shown in figure 9. In this example, three different initiation sites were identified and located at the bottom right (panel (a)), upper right (panel (b)), and bottom left (panel (c)) corners of calculated activation maps, similar to what is shown in our simulations. However, contrary to the simulations, the pacemaking loci compete with each other. During transitions between first activation sites, some beats show multiloci quasi-simultaneous activation (panel (b)). In panel (d), the initiation site of each beat is specified with a coloured star on a single-pixel signal. Large beat-to-beat variations are observed in the dynamics, such as the interbeat interval and the position of the initiation site. The complex dynamical behaviour in autonomous activity is clear when looking at the interbeat sequence (panel (e)), which displays a large variation in intervals, ranging from 664 to 1392 ms.

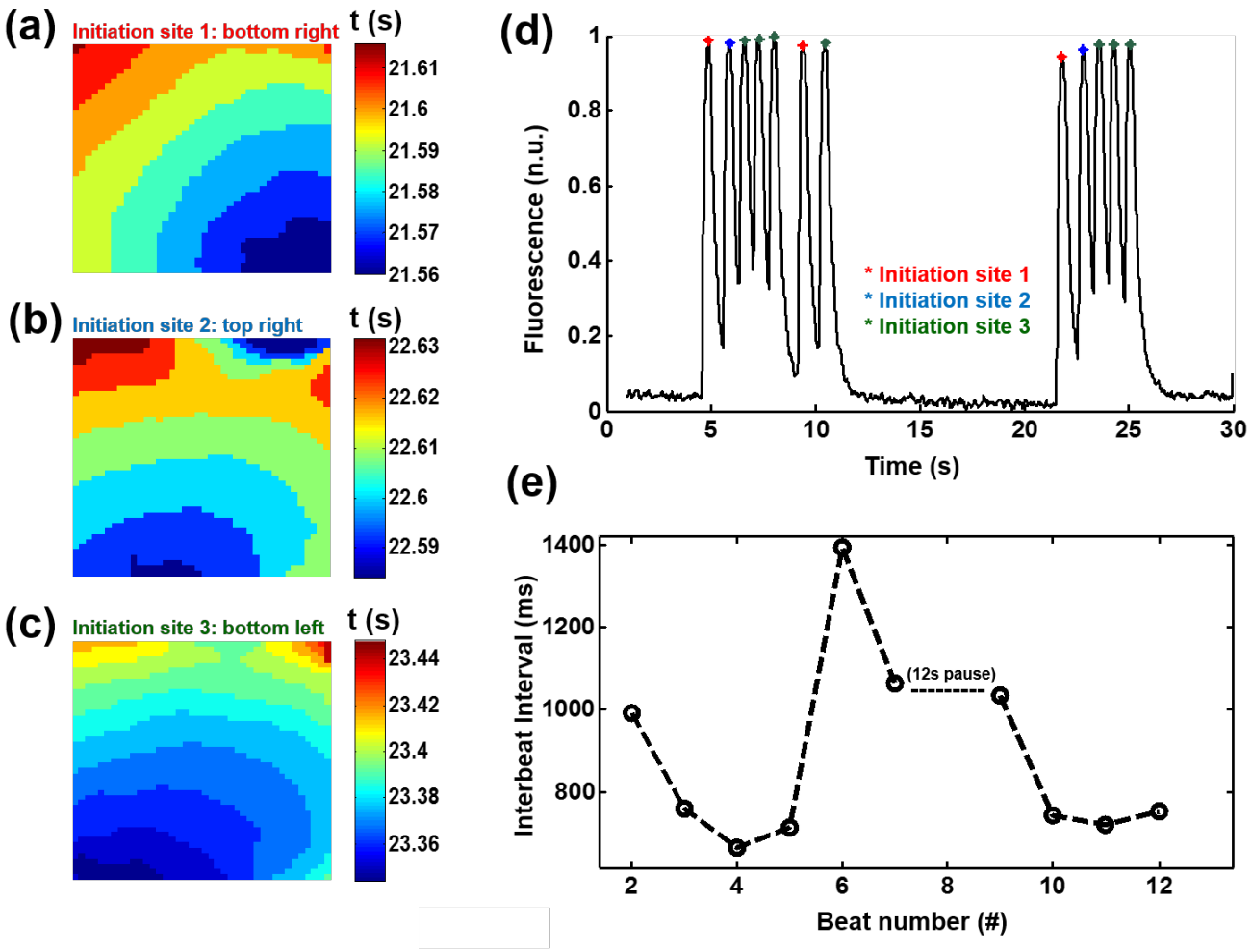

Figure 9. Experimental autonomous activity obtained in cultured neonatal ventricular cardiomyocytes. Three competing initiation sites are found with activation patterns presented in panels (a)–(c). (d) The calcium signal acquired for 30 s shows a series of events corresponding to transition between initiation sites (labelled with a coloured asterisk). The activation maps (panels (a)–(c)) correspond to the first three beats after a 12 s pause. (e) Interbeat intervals of the signal presented in panel (d) show a large variation in rhythm.

2.4. Discussion and conclusion

In the present study we proposed, to the best of our knowledge, the first theoretical study assessing the effects of spatial distribution and density of PM cells on the global automaticity of the strongly-coupled cardiac monolayer.

The spatial distribution of PM cells on a N × N lattice was generated by a very simple stochastic model (depicted in figure 1), with a single parameter p_{thr} determining the rate of nucleation (formation of new clusters) and aggregation (growth of existing clusters). Using this model, we were able to obtain various spatial distributions of PM cells. The remaining available sites of the lattice where filled with excitable but resting cells, to form a 100% confluent monolayer. The spatial distribution homogeneity is modulated by p_{thr} and the density by the number n of iterations. It is important to note that the algorithm is based on an 8-neighbour rule. Using a 4-neighbour rule would affect the spatial characteristics of PM cell distribution. Furthermore, this rule may impact pacemaking activity with increasing D_{aut}, which is a subject of a future study. The pattern formation model shows similarity to other models for cooperative sequential adsorption [33], invader–resident competition [34], and reaction-diffusion controlled cluster–cluster aggregation [35].

With this approach to build spatially distributed patterns, the number and size of PM cell aggregates can be varied while still mimicking the random nature of the spatial distribution and density of PM cells in experimental cardiomyocyte monolayers. Created patterns demonstrate

complex and nonlinear changes in the number and spatial dispersion of PM cell clusters as a function of the parameter p_{thr} (figure 2). The main interest of this pattern formation method is that it easily permits the effects of spatial patterns of PM cells to be studied within an excitable but resting lattice. Currently, this question cannot be easily addressed with available experimental techniques.

A previous study showed that a random distribution of PM cells with varying frequencies coupled to excitable cells exhibit from incoherent behaviour to global synchronization with increasing coupling between cells [28]. Here, we were interested at looking at the effects of having different spatial correlations in PM clusters in a condition of highly-coupled cells where global synchronisation is favoured. Thus, we found in our simulations (and similarly in experiments) all or none spontaneous activity of the monolayer but no asynchronous or reentrant activity as seen in monolayers with lower intercellular coupling [23, 25, 28, 36, 37]. Patterns obtained with our stochastic model confirmed the existence of a pattern-dependent minimum PM cluster size to generate automaticity (figure 5(a)). This was observed even for the simplest FHN excitable tissue where the PM cluster must contain a sufficiently large number of PM cells to initiate electrical activation of the monolayer. Indeed, around 280 000 PM cells are necessary for a biological PM to drive a canine ventricle [16]. Early-after depolarisations (EADs), which underlie abnormal ectopic activity, have been found to be electrotonically suppressed in well-connected networks of NRVMs [38]. Propagation cannot be initiated when EAD-susceptible cells are connected with too many non-EAD-susceptible myocytes, because the transmembrane voltage gradient generating the diffusion current becomes too low to rapidly

depolarize above threshold in non-EAD cardiomyocytes.

For our model, a smaller density is required to generate automaticity (figure 5(b)) with large aggregates of PM cells (low p_{thr}). This result emphasizes the importance of the granularity (local density) of PM spatial distribution on spontaneous activity, a crucial aspect to take into account in regenerative cardiology for in vivo cell injection procedures as that large aggregates of injected cells prone to spontaneous activity could induce tissue activity. A similar condition determines the capacity of DAD-susceptible foci to initiate an activation wave that can propagate throughout the tissue [18] and highlights the impact of non-excitable cells on silencing of spontaneous activity [23]. The sigmoid-like variation in the minimum density for spontaneous activity to occur ($D_{aut,min}$) and the spatial distribution correlation through the parameter p_{thr} remains a key result emphasizing the nonlinear relation between cluster spatial characteristics and intercellular interaction to overcome the electrotonic effect. Unsurprisingly, the period of spontaneous activity always decreases for increasing PM cell density (figure 5(c)). However, a clear p_{thr}-dependent decay rate in period is accompanied by a change in variability between samples. This result requires further experimental validation. For a given plating density (same D_{aut}), the variation with patterns obtained for different p_{thr} can have a strong effect on autonomous activity (notably the period) of the monolayer (figure 6). This result may explain, at least in part, the variability in spontaneous behaviour observed experimentally among NRVM monolayers with identical plating densities and similar culture conditions. This knowledge could be important in the process of creating biological PMs, an alternative to electronic PMs in the treatment of bradycardia [15].

Interestingly, simulations revealed that the initiation sites of spontaneous activity are mostly located at the edge of the monolayer (figure 7(c)) compared with ∼20% in experiments from a previous study [21]. This finding may be explained by a source–sink mechanism [18, 39]. At the edge, which has no-flux boundary conditions, PM aggregates are effectively connected with fewer QECs; as such, they are less electrotonically depressed and possess increased capacity to initiate activation. It is also particularly interesting to note that seemingly competing initiation sites appear when PM cells are distributed in a large number of small clusters (large values of p_{thr}). This result shows some similarities with experimental results (figure 9) that demonstrate the existence of localized PM foci and a tendency for the first initiation sites to be located at the boundary of the culture dish where sink effects would be decreased. As mechanical effects have shown to induce spontaneous activity at a certain distance of the boundaries [40], how spatially-distributed PM cells in an electrical–mechanical model would modify this property.

However, a major difference between experimental and modelling results exists in the temporal behaviour where, for the same acquisition, experimental data show complex competition between PM loci. No simulations with the FHN model, a simple excitable model, exhibited the complex sequence of activation depicted in figure 9. In simulations, there is no beat-to-beat variability in autonomous frequency and initiation site position for a given PM cell pattern as depicted in figure 7(d). However, experimentally, three initiation sites competed. Furthermore, the fastest locus seemed to experience fatigue, occasionally leaving the competition open to the two slower loci. Similar complex behaviour has also been documented by others [21]. The

dynamical behaviour highlights limitations of the FHN model and the need to develop and study the behaviour in monolayers with a more realistic NRVM ionic model. However, the level of model and its characteristics needed to reproduce this results is unknown since comparison between the FHN and Luo-Rudy models (a more realistic cardiac model) showed qualitatively similar results [23]. In the present study, the focus has been placed on the effect of the spatial structure of PM cells on electrical activity. However, this activity also relies on the excitability of the membrane, which depends on the properties of ion channels; these are not well represented by FHN-like models and have important effects on propagation [41]. A quiescent version of the NRVM ionic model has been published [42] and could be modified to exhibit spontaneous activity more similar to real cardiomyocytes in culture with complex spontaneous activity [43].

In the present study, monolayers were modelled as a 100% confluent and isotropic network composed solely of two types of cardiomyocytes (quiescent and PM cells) identically connected with strong coupling between cells. It is clear that experimental frequencies of activity will vary between PM cells [12], a factor that was not taken into account in this study, but this has been carefully studied previously for random distributions [28]. Such variation in intrinsic frequencies may have a physiological role even for cardiomyocyte monolayers. For example, to perform normal PM function, the SAN is known to require a heterogeneous architecture that involves multiple cell types with a gradient of cellular and intercellular characteristics [44]. Also, more realistic spatial characteristics of monolayers of cardiomyocytes have been shown to affect global electrophysiological behaviour [45]. The

spatial characteristics not included in our model include cell shape, cell-to-cell coupling, and degree of cleft space. The simplifications (single diffusion coefficient, identical number of neighbours, single-frequency PM cells with identical initial conditions) were performed to isolate the specific effects of spatial distribution of PM cells. It remains to be seen how inclusion of these more realistic characteristics of monolayers would influence monolayer spontaneous activity as a function of spatial distribution of PM cells. Such future studies will undoubtedly improve our understanding of the complex temporal behaviour found in experiments and will help in the development of biopacemakers as a cardiac therapy.

Acknowledgments

Supported by the Natural Science and Engineering Research Council of Canada, the Mitacs Network, and the Fonds de Recherche du Québec—Santé and ‘Réseau ThéCell’ of the Fonds de Recherche-Santé du Québec (FRQ-S).

2.5. References

[1] Haken H 1983 Advanced Synergetics: Instability Hierarchies of Self-Organizing Systems and Devices vol 20 (Berlin: Springer)

[2] Kuramoto Y 1984 Chemical Oscillations, Waves, and Turbulence vol 19 (Berlin: Springer)

[3] Winfree A T 1987 When Time Breaks Down: The Three-Dimensional Dynamics of Electrochemical Waves and Cardiac Arrhythmias (Princeton, NJ: Princeton University Press)

[4] Tass P A 1999 Phase Resetting in Medicine and Biology: Stochastic Modelling and Data Analysis (Berlin: Springer)

[5] Chlopcikova S, Psotova J and Miketova P 2001 Neonatal rat cardiomyocytes—a model for the study of morphological, biochemical and electrophysiological characteristics of the heart Biomed. Pap. Med. Fac. Univ. Palacky Olomouc Czech. Repub. 145 49–55

[6] Bursac N et al 1999 Cardiac muscle tissue engineering: toward an in vitro model for electrophysiological studies Am. J. Physiol. 277 H433–44

[7] Bursac N, Parker K K, Iravanian S and Tung L 2002 Cardiomyocyte cultures with controlled macroscopic anisotropy: a model for functional electrophysiological studies of cardiac muscle Circ. Res. 91 e45–54

[8] Badie N, Scull J A, Klinger R Y, Krol A and Bursac N 2012 Conduction block in micropatterned cardiomyocyte cultures replicating the structure of ventricular cross-sections Cardiovasc. Res. 93 263–71

[9] Mark G E and Strasser F F 1966 Pacemaker activity and mitosis in cultures of newborn rat heart ventricle cells Exp. Cell Res. 44 217–33

[10] Vink M J et al 2004 Alterations of intercellular communication in neonatal cardiac myocytes from connexin43 null mice Cardiovasc. Res. 62 397–406

[11] Fahrenbach J P, Mejia-Alvarez R and Banach K 2007 The relevance of non-excitable cells for cardiac pacemaker function J. Physiol. 585 565–78

[12] Guo W, Kamiya K, Cheng J and Toyama J 1996 Changes in action potentials and ion currents in long-term cultured neonatal rat ventricular cells Am. J. Physiol. 271 93–102 [13] Orita H, Fukasawa M, Hirooka S, Uchino H, Fukui K and Washio M 1993 Modulation of cardiac myocyte beating rate and hypertrophy by cardiac fibroblasts isolated from neonatal rat ventricle Japan. Circ. J. 57 912–20

[14] Kirchhof C J, Bonke F I, Allessie M A and Lammers W J 1987 The influence of the atrial myocardium on impulse formation in the rabbit sinus node Pflugers Arch. 410 198–203 [15] Morikawa K et al 2010 Identification, isolation and characterization of HCN4-positive pacemaking cells derived from murine embryonic stem cells during cardiac differentiation Pacing Clin. Electrophysiol. 33 290–303

[16] Plotnikov A N et al 2007 Xenografted adult human mesenchymal stem cells provide a platform for sustained biological pacemaker function in canine heart Circulation 116 706-13

[17] Hoyt R H, Cohen M L and Saffitz J E 1989 Distribution and three-dimensional structure of intercellular junctions in canine myocardium Circ. Res. 64 563–74

[18] Xie Y, Sato D, Garfinkel A, Qu Z and Weiss J N 2010 So little source, so much sink: requirements for afterdepolarizations to propagate in tissue Biophys. J. 99 1408–15 [19] Morris G M and Boyett M R 2009 Perspectives—biological pacing, a clinical reality? Ther. Adv. Cardiovasc. Dis. 3 479–83

[20] Masumiya H, Oku Y and Okada Y 2009 Inhomogeneous distribution of action potential characteristics in the rabbit sino-atrial node revealed by voltage imaging J. Physiol. Sci. 59 227–41

[21] Ponard J G, Kondratyev A A and Kucera J P 2007 Mechanisms of intrinsic beating variability in cardiac cell cultures and model pacemaker networks Biophys. J. 92 3734–52

[22] Zlochiver S, Munoz V, Vikstrom K L, Taffet S M, Berenfeld O and Jalife J 2008 Electrotonic myofibroblast-to-myocyte coupling increases propensity to reentrant arrhythmias in two-dimensional cardiac monolayers Biophys. J. 95 4469–80

[23] Kryukov A K et al 2008 Synchronization phenomena in mixed media of passive, excitable,

and oscillatory cells Chaos 18 037129

[24] Kuklik P and Zebrowski J J 2005 Reentry wave formation in excitable media with stochastically generated inhomogeneities Chaos 15 33301

[25] Bub G, Shrier A and Glass L 2002 Spiral wave generation in heterogeneous excitable media Phys. Rev. Lett. 88 058101

[26] Rohr S, Kucera J P, Fast V G and Kleber A G 1997 Paradoxical improvement of impulse conduction in cardiac tissue by partial cellular uncoupling Science 275 841–4

[27] Shajahan T K, Borek B, Shrier A and Glass L 2011 Scaling properties of conduction velocity in heterogeneous excitable media Phys. Rev. E 84 046208

[28] Kanakov O I, Osipov G V, Chan C K and Kurths J 2007 Cluster synchronization and spatio–temporal dynamics in networks of oscillatory and excitable Luo–Rudy cells Chaos 17 015111

[29] Fast V G and Kleber A G 1994 Anisotropic conduction in monolayers of neonatal rat heart cells cultured on collagen substrate Circ. Res. 75 591–5

[30] Borek B, Shajahan T K, Gabriels J, Hodge A, Glass L and Shrier A 2012 Pacemaker interactions induce reentrant wave dynamics in engineered cardiac culture Chaos 22 033132

[31] Comtois P and Nattel S 2011 Impact of tissue geometry on simulated cholinergic atrial fibrillation: a modeling study Chaos 21 013108

[32] Aguilar-Shardonofsky M, Vigmond E J, Nattel S and Comtois P 2012 In silico optimization of atrial fibrillation-selective sodium channel blocker pharmacodynamics Biophys. J. 102 951–60

[33] Evans J W 1993 Random and cooperative sequential adsorption Rev. Mod. Phys. 65 1281–

329

[34] Korniss G and Caraco T 2005 Spatial dynamics of invasion: the geometry of introduced species J. Theor. Biol. 233 137–50

[35] Family F, Meakin P and Vicsek T 1985 Cluster size distribution in chemically controlled cluster–cluster aggregation J. Chem. Phys. 83 4144–50

[36] Bub G, Shrier A and Glass L 2005 Global organization of dynamics in oscillatory heterogeneous excitable media Phys. Rev. Lett. 94 028105

[37] Steinberg B E, Glass L, Shrier A and Bub G 2006 The role of heterogeneities and intercellular coupling in wave propagation in cardiac tissue Philos. Trans. A 364 1299–311 [38] Himel H D et al 2013 Electrotonic suppression of early afterdepolarizations in the neonatal rat ventricular myocyte monolayer J. Physiol. 591 5357–64

[39] Comtois P and Vinet A 1999 Curvature effects on activation speed and repolarization in an ionic model of cardiac myocytes Phys. Rev. E 60 4619–28

[40] Panfilov A V, Keldermann R H and Nash M P 2005 Self-organized pacemakers in a coupled reaction–diffusion-mechanics system Phys. Rev. Lett. 95 258104

[41] Biktashev V N 2002 Dissipation of the excitation wave fronts Phys. Rev. Lett. 89 168102

[42] Korhonen T, Hanninen S L and Tavi P 2009 Model of excitation–contraction coupling of rat neonatal ventricular myocytes Biophys. J. 96 1189–209

[43] Glynn P, Onal B and Hund T J 2014 Cycle length restitution in sinoatrial node cells: a theory for understanding spontaneous action potential dynamics PLoS One 9 e89049

[44] Boyett M R, Dobrzynski H, Lancaster M K, Jones S A, Honjo H and Kodama I 2003 Sophisticated architecture is required for the sinoatrial node to perform its normal pacemaker

function J. Cardiovasc. Electrophysiol. 14 104–6

[45] Kim J M, Bursac N and Henriquez C S 2010 A computer model of engineered cardiac monolayers Biophys. J. 98 1762–71

CHAPITRE 3 – ÉTUDE IN SILICO DE L'AUTOMATICITÉ MULTICELLULAIRE CHEZ LES MONOCOUCHES HÉTÉROGÈNES DE CELLULES CARDIAQUES : EFFETS DE LA FORCE DE L'AUTOMATICITÉ ET DE L'ANISOTROPIE STRUCTURELLE LINÉAIRE

In silico study of multicellular automaticity of heterogeneous cardiac cell monolayers: Effects of automaticity strength and structural linear anisotropy

Automaticity strength, anisotropy, and cardiac spontaneous activity

James Elber Duverger[1,2], Vincent Jacquemet[2,3], Alain Vinet[2,3], Philippe Comtois[1,2]

[1]Research Centre, Montreal Heart Institute, Montreal, Quebec, Canada
[2]Department of Pharmacology and Physiology / Institute of Biomedical Engineering, Université de Montréal, Montreal, Quebec, Canada
[3]Research Centre, Hôpital du Sacré-Coeur de Montréal, Montreal, Quebec, Canada

Email: philippe.comtois@umontreal.ca (PC)

Received: August 21, 2017
Accepted: January 9, 2018
Published: March 12, 2018
PLoS Comput Biol. 2018 Mar 12;14(3):e1005978
doi:https://doi.org/10.1371/journal.pcbi.1005978

Abstract. The biological pacemaker approach is an alternative to cardiac electronic pacemakers. Its main objective is to create pacemaking activity from added or modified distribution of spontaneous cells in the myocardium. This paper aims to assess how automaticity strength of pacemaker cells (i.e. their ability to maintain robust spontaneous activity with fast rate and to drive neighboring quiescent cells) and structural linear anisotropy,

combined with density and spatial distribution of pacemaker cells, may affect the macroscopic behavior of the biological pacemaker. A stochastic algorithm was used to randomly distribute pacemaker cells, with various densities and spatial distributions, in a semi-continuous mathematical model. Simulations of the model showed that stronger automaticity allows onset of spontaneous activity for lower densities and more homogeneous spatial distributions, displayed more central foci, less variability in cycle lengths and synchronization of electrical activation for similar spatial patterns, but more variability in those same variables for dissimilar spatial patterns. Compared to their isotropic counterparts, *in silico* anisotropic monolayers had less central foci and displayed more variability in cycle lengths and synchronization of electrical activation for both similar and dissimilar spatial patterns. The present study established a link between microscopic structure and macroscopic behavior of the biological pacemaker, and may provide crucial information for optimized biological pacemaker therapies.

Author summary. Implantation of electronic pacemakers is a standard treatment to pathologically slow heart rhythm. Despite improving quality of life, those devices display many shortcomings. Bioengineered tissue pacemakers may be a therapeutic alternative, but associated design methods usually lack control of the way cells with spontaneous activity are scattered throughout the tissue. Our study is the first to use a mathematical model to rigorously define and thoroughly characterize how pacemaker cells scattering at the microscopic level may affect macroscopic behaviors of the bioengineered tissue pacemaker. Automaticity strength (ability of pacemaker cell to drive its non-pacemaker neighbors) and anisotropy (preferential orientation of cell shape) are also implemented and give unparalleled insights on

how effects of uncontrollable scattered pacemaker cells may be modulated by available experimental techniques. Our model is a powerful tool to aid in optimized bioengineered pacemaker therapies.

3.1. Introduction

Oscillating, autonomous or spontaneous electrical activity is the basis of normal heart physiology [1], as well as some impaired rhythms triggered by ectopic activity [2]. Two oscillating mechanisms or clocks, the membrane and calcium clocks, are hypothesized to control the sinoatrial node (SAN) isolated cellular rate [3–5]. Membrane clock refers to the synergy of transmembrane ionic currents [6,7], and calcium clock to the oscillations of intracellular calcium concentration [8]. Developmental variations may change magnitudes of the respective clock components [9]. Interplay between these two strongly coupled mechanisms may be responsible for spontaneous activity and temporal fluctuation in heart rate [10]. At the cellular level, the clocks basically create an ionic imbalance during the diastolic period, leading to a net inward flux of ionic current that slowly increases membrane potential until the threshold (~ −40 mV) to fire an action potential is reached. Inducing this net inward flux of ionic current during the diastole can actually generate automaticity in otherwise quiescent cardiomyocytes (CMs). This principle has been exploited in the design of biological pacemakers (BPs), a therapeutic alternative to overcome the shortcomings of cardiac electronic pacemakers [11] in the treatment of bradycardia. Different procedures have been proposed, including injection-based gene [12] and cell therapy [13], that locally modify cardiomyocyte

phenotype or bring differentiated cells in the myocardium.

These concepts are limited by the lack of control on the spatial distribution and phenotype of pacemaker (PM) cells within the resting but excitable cellular network of the myocardium. We have shown that density and spatial distribution of PM cells can alter significantly the emergence and characteristics of multicellular spontaneous activity [14]. In fact, density and spatial distribution of PM cells, *a priori* unknown in BPs, may lead to a non-negligible intrinsic variability in the spontaneous activity of the overall network. Intrinsic variability is defined as behavioral discrepancies among BP samples that had undergone the exact same protocol. This phenomenon could eventually compromise the success of BP implantation in patients, and is observed even in *in vitro* BP models like monolayer cultures of neonatal rat ventricular myocytes (NRVMs), which are also heterogeneous network of autonomous and quiescent cardiomyocytes [15].

In the present simulation study, besides density and spatial distribution of PM cells, we introduce two additional variables: (a) automaticity strength and (b) anisotropy. Automaticity strength is defined as the ability of a pacemaker cell to maintain robust spontaneous activity with fast rate and to drive neighboring quiescent cells. It is strongly related to the amplitude of the net inward ionic current into the PM cell during the late diastolic period and the rising phase of the action potential (AP). For example, adding fetal bovine serum to monolayer cultures of NRVMs “strengthens” automaticity, i.e. favors higher firing rate, by upregulating inward long-lasting activation calcium current I_{CaL} [16]. Early versions of engineered BPs have been created from quiescent monolayer cultures or quiescent *in vivo* CMs via the use of different techniques to upregulate inward pacemaking current I_f [17]. The second newly

introduced variable, anisotropy, can be created in cultures of NRVMs via several methods, notably by patterning the culture substrate [18,19] or directly seeding the cell into a thin slice of decellularized cardiac tissue [20]. These methods usually lead to functional cardiac network with elongated cell and faster propagation in the longitudinal direction [20]. It has been proposed that linear anisotropy could facilitate BP function [21]. However, the underlying mechanism remains unclear since most studies do not assess specific effects of anisotropy on spontaneous activity but instead focus on contractile function [20], electrical activation [22], or orientation-related response to stretch [23].

This study aims to assess modulation effects of automaticity strength and anisotropy on the spontaneous activity of cardiac monolayers with various densities and spatial distributions. The non-linear relationship between those two variables and automaticity will be characterized with simulation methods and discussed in details.

3.2. Methods

3.2.1. Cardiac network model

Semi-discrete microstructure models are more suitable than continuous models when individual cell sizes, shapes and orientations are variables under investigation [24,25]. For this reason, a previously described semi-discrete microstructure model [26] was used to simulate two 2D network geometries corresponding to isotropic and anisotropic monolayers. The two network geometries were identical in all aspects, except: (a) aspect ratio of cells (AR, length divided by width of the cell), and (b) distribution of gap junctions. As summarized in Table 1, a grid of 920

x 920 nodes was created with 6 μm resolution, and assigned to 42,642 CMs to create a 5.5 mm x 5.5 mm monolayer.

Table 1. Characterization of the monolayers: isotropic vs. anisotropic. Isotropic and anisotropic monolayers are identical for most of the features. The cells differ only in aspect ratio and intercellular conductivities.

	Isotropic	**Anisotropic**
Total number of nodes (#)	920 x 920	920 x 920
Resolution (μm)	6	6
Length of monolayer (mm)	5.5	5.5
Width of monolayer (mm)	5.5	5.5
Area of monolayer (mm^2)	30.5	30.5
Total number of cells (#)	42642	42642
Number of nodes per cell (# nodes)	20 ± 4	20 ± 3
Number of neighbors (#)	6 ± 1	6 ± 1
Aspect ratio of cell (n.u.)	1.02 ± 0.26	2.92 ± 0.62
Length of cells (μm)	31.4 ± 5.3	53.6 ± 6.5
Width of cells (μm)	31.5 ± 5.2	18.9 ± 3.0
Intracellular resistivity (Ω·cm)	200	200
Longitudinal intercellular conductivity (nS)	0.04	0.062
Transverse intercellular conductivity (nS)	0.04	0.034
Longitudinal conduction velocity (cm/s)	15.0	24.3
Transverse conduction velocity (cm/s)	15.2	10.4

Each cell included ~20 nodes. CMs for anisotropic geometry had an average AR of 3 compared to 1 for isotropic geometry. Longitudinal and transverse intercellular conductivities were adjusted to fit experimental conduction velocities found in NRVMs monolayer cultures [18]. The experimental isotropic conduction velocity was reported to be 16.8 ± 2.1 cm/s in all directions; and for anisotropic monolayer cultures, the longitudinal and transverse conduction

velocities were 20.8 ± 3.2 cm/s and 10.9 ± 2.9 cm/s respectively. Intercellular coupling was set to 0.04 nS per 6 μm border length for CMs in isotropic network, and 0.062 nS and 0.034 nS per 6 μm border length respectively along longitudinal and transverse borders of CMs in anisotropic network.

The Luo-Rudy Phase 1 (LR1) mathematical model of ventricular cell [27] was used to represent the CMs, with the application of a constant inward bias current (I_{bias}) to generate spontaneous activity [28,29]. The LR1 model is simulated at every node of each cell, and examples of APs and total ionic currents obtained in a single cell with I_{bias} = 2.6 μA/cm² and I_{bias} = 3.5 μA/cm² are illustrated in Fig 1a and Fig 1b respectively.

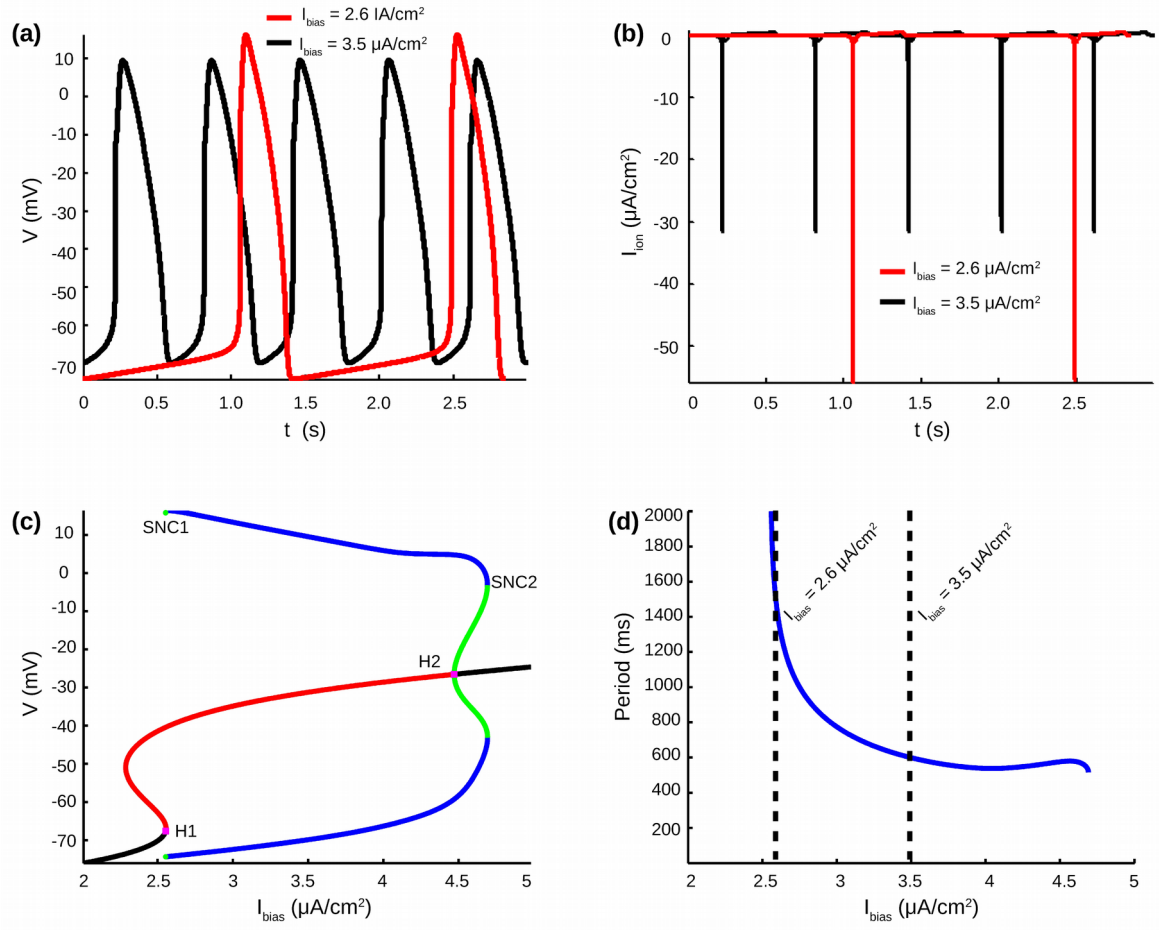

Fig 1. Cardiac monolayer model. (**a**) Example of spontaneous APs obtained for I_{bias} = 2.6 μA/cm^2 and I_{bias} = 3.5 μA/cm^2. (**b**) Total ionic currents corresponding to AP traces in panel a. (**c**) Stable and unstable fixed points (black and red line respectively), with subcritical Hopf bifurcations H1 and H2 (magenta squares, I_{bias} = 2.554 and 4.470 μA/cm^2). Maximum and minimum membrane potential V values of the stable and unstable cycles (blue and green lines respectively). The stable cycles exists between the two cycle saddle nodes bifurcation SNC1 and SNC2 (I_{bias} = 2.553 and 4.691 μA/cm^2). (**d**) Autonomous cycle lengths as a function of I_{bias} (stable cycles only). Dashed lines display cycle length for I_{bias} = 2.6 μA/cm^2 and I_{bias} = 3.5 μA/cm^2, corresponding to AP traces in panel a.

This cell model was chosen because its bifurcation structure related to oscillatory behavior has been fully characterized. Indeed, bifurcation analysis undertaken with AUTO continuation software [30] is displayed in Fig 1c. The S-shape curve of fixed points has a lower and upper branch connected by an intermediate branch of unstable fixed points. Both the lower and upper branches change stability through subcritical Hopf Bifurcations (H1 and H2, magenta square). Stable cycle exist in between the two Cycle Saddle nodes bifurcation (blue lines from SNC1 and SNC2). At high I_{bias}, the branch of unstable cycles created at SNC2 (green line) connect the Hopf bifurcation H2. The branch of unstable cycles created at SNC2 exist only on a small interval of I_{bias} and ends through a Homoclinic bifurcation with the intermediate branch of fixed point. Similarly, the branch of unstable cycles created at H1 exist on a tiny interval of I_{bias} and also disappears through a Homoclinic bifurcation with the intermediate branch of fixed point. The cycle length of stable spontaneous activity decreased with I_{bias} and ranged from 1989 ms to 516 ms (Fig 1d).

3.2.2. Stochastic distribution of pacemaker cells

The 2D cardiac network was assumed to contain two populations of cells: PM (I_{bias} = 2.6 μA/cm² or I_{bias} = 3.5 μA/cm²) and quiescent (I_{bias} = 0 μA/cm²) excitable cells. The density of pacemaker cells ($D_{aut} \in [0,1]$) was defined as the percentage of PM cells within the network. The spatial distribution was dependent on a variable ($p_{thr} \in [0,1]$) determining how homogeneous PM cells were spread in the network. Fig 2 provides intuitive disambiguation between density and spatial distribution. Density described the total number of PM cells in the network, regardless of their scattering within the network.

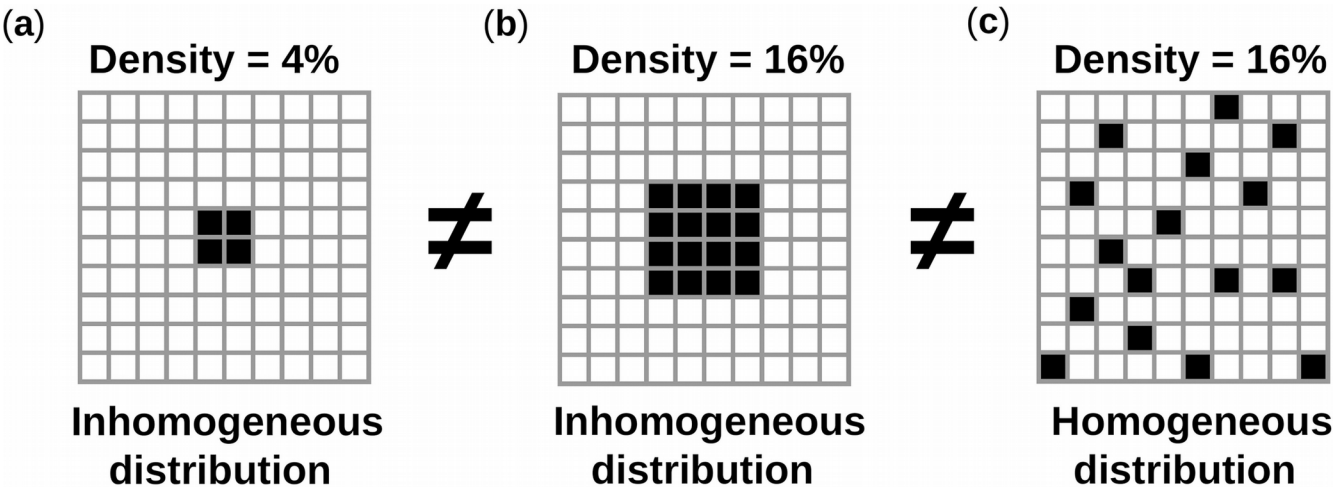

Fig 2. Disambiguation: density vs. spatial distribution. (**a**) Density of 4% with inhomogeneous distribution. (**b**) Density of 16% with inhomogeneous distribution. (**c**) Density of 16% with homogeneous distribution.

Spatial distribution described the scattering of PM cells, and hence completed the spatial information from the overall density. Both variables were required to fully specify a spatial

pattern. Two networks might have the same density of PM cells but different spatial distributions, or conversely they might share similar spatial distribution of PM cells but had different densities. Higher values of D_{aut} and p_{thr} correlate with higher percentage and more homogeneous spatial distribution of PM cells respectively. A previously described stochastic algorithm [14] was modified and implemented to randomly attribute positions to PM cells in the isotropic and anisotropic networks. Aggregation occurred when a PM cell was placed in the immediate neighborhood of another PM cell. Otherwise nucleation was said to occur, i.e. the PM cell occupied a position where only quiescent CMs were in its immediate neighborhood. Any random process of the algorithm followed continuous uniform probability distribution. For each pair (D_{aut}, p_{thr}), the algorithm worked as stated below and as illustrated in Fig 3:

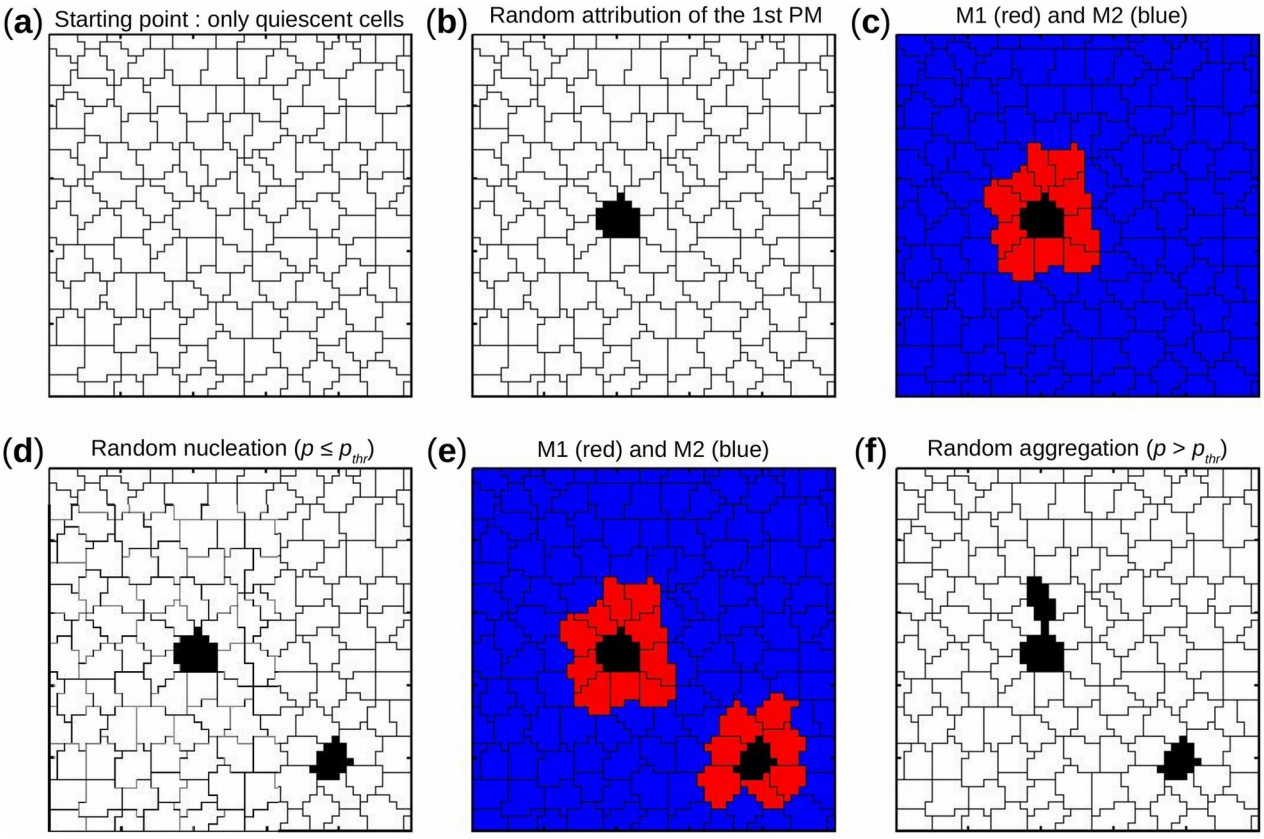

Fig 3. Stochastic algorithm governing density and spatial distribution of pacemaker cells: an illustration. (**a**) Blank geometry where all cells are quiescent. (**b**) Random attribution of the 1st pacemaker cell. (**c**) Determination of M_1 available sites for aggregation and M_2 available sites for nucleation in red and blue respectively. (**d**) Random nucleation of the 2nd pacemaker cell in M_2 eventually because $p \leq p_{thr}$. (**e**) Determination of M_1 and M_2. (**f**) Random aggregation of the 3rd pacemaker cell in M_1 eventually because $p > p_{thr}$.

Step 1: randomly place the 1st PM cell in the network (equal probability for each cell of the network);

Step 2: determine M_1 (aggregation available sites) and M_2 (nucleation available sites);

Step 3: randomly generate decision number $p \in [0,1]$;

Step 4: perform aggregation in M_1 (if $p > p_{thr}$) or nucleation in M_2 (if $p \leq p_{thr}$);

Step 5: perform aggregation in M_1 (if M_2 is empty);

Step 6: repeat steps 2 to 5 until the required D_{aut} is reached.

Default I_{bias} value for all cells was 0, i.e. all cells are quiescent unless set otherwise. Placing a PM cell consisted in setting I_{bias} for all nodes of a cell to a single non-zero value inside the interval [2.6 – 4.7] μA/cm². The same procedure was used to distribute spontaneous cells in the isotropic and anisotropic cell layouts.

In Fig 4 are presented the first 50 x 50 nodes of two geometries. Cells in network with isotropic geometry demonstrated no preferential orientation compared to cells in network with anisotropic geometry which are clearly oriented along the longitudinal axis.

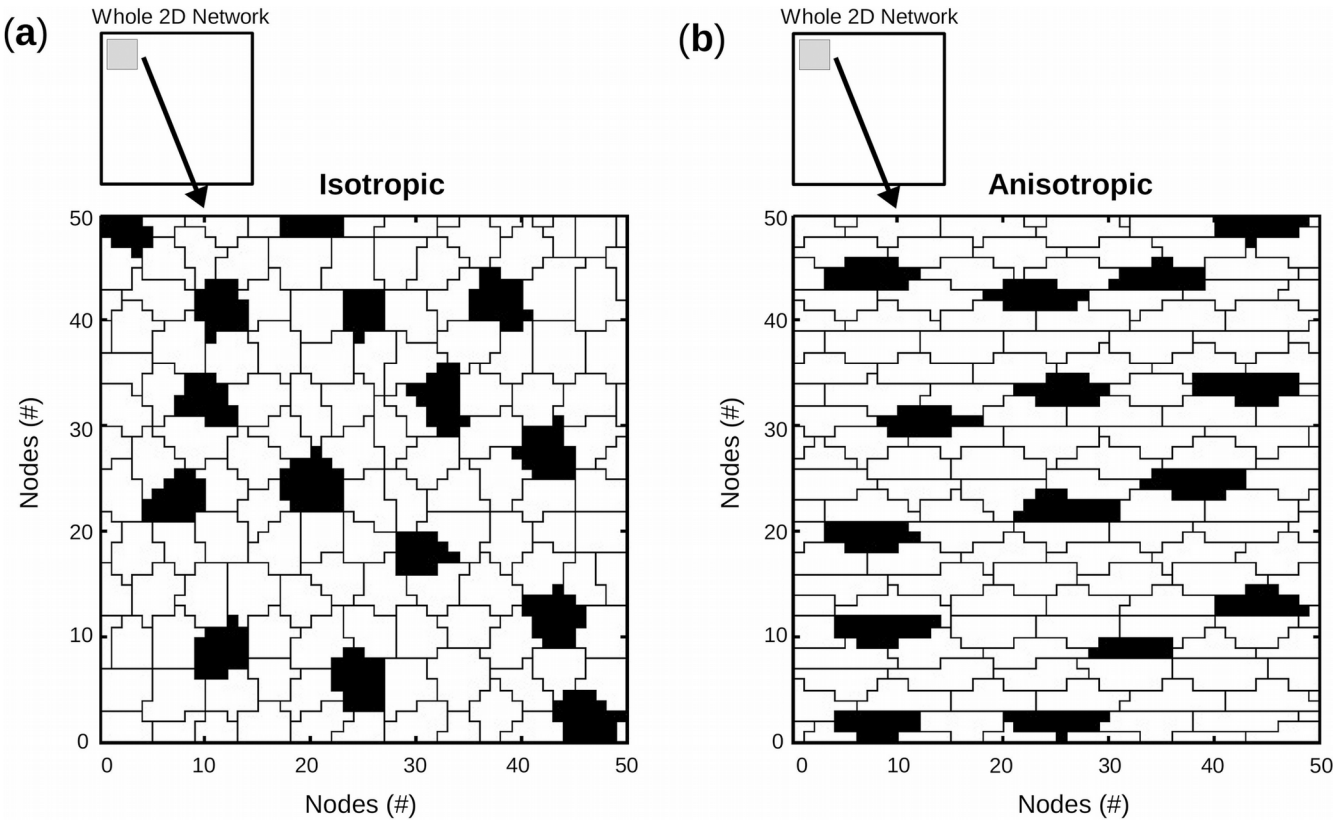

Fig 4. Network geometry: isotropic vs. anisotropic. Illustration of the 50 x 50 first nodes of 2 monolayers, with pacemaker cells in black and quiescent cells in white. (**a**) Isotropic monolayer where cells display no preferential orientation. (**b**) Anisotropic monolayer where cells display preferential orientation along the longitudinal/horizontal axis.

Within the cardiac 2D network, a PM cluster was a subgroup of interconnected PM cells. Two PM cells were considered interconnected if they shared gap junctions. The size of a PM cluster was the number of PM cells in that cluster, and the maximum PM cluster size $S_{cluster}$ was the size of the network's biggest PM cluster. Porosity was the fraction of quiescent cells in a PM cluster. In fact, any subgroup of interconnected PM cells was a PM cluster, but quiescent cells might also be enclosed within the cluster, i.e. totally surrounded by the cluster's PM cells. Given $\overline{S}_{Tcluster}$, the average of maximum PM cluster size including both PM and quiescent cells,

porosity was defined as follows:

$$Porosity = 1 - \frac{\overline{S}_{cluster}}{\overline{S}_{Tcluster}} \quad (12)$$

with

Porosity: average fraction of quiescent cells in the largest PM cluster

$\overline{S}_{cluster}$: average of maximum PM cluster size, counting only PM cells

$\overline{S}_{Tcluster}$: average of maximum PM cluster size, counting both PM and quiescent cells

3.2.3. Simulation protocols and data analysis

As previously described [26], a 2D monodomain approximation with fine discretization was used to formulate the microstructure model. No-flux boundary conditions were applied to the four sides of the network. Initial conditions for all cells corresponded to the resting state of quiescent cells. The total simulation duration was 10 s, and the steady-state behaviors were reached rapidly within two to three autonomous period for most spontaneous cases, the longest transient behaviors found at the transition between non-autonomous to autonomous multicellular activity. Analysis was done on simulations after removing the first action potential thus including the time from the 2nd action potential up until 10 s. Simulations were performed to study the effect of D_{aut} and p_{thr} on the spontaneous activity of 4 groups:

* ISO-2.6 – networks with isotropic geometry and weak automaticity (I_{bias} = 2.6 µA/cm² for all PM cells)

* ISO-3.5 – networks with isotropic geometry and strong automaticity (I_{bias} = 3.5

μA/cm² for all PM cells)

* ANISO-2.6 – networks with anisotropic geometry and weak automaticity (I_{bias} = 2.6 μA/cm² for all PM cells)

* ANISO-3.5 – networks with anisotropic geometry and strong automaticity (I_{bias} = 3.5 μA/cm² for all PM cells)

400 pairs (D_{aut}, p_{thr}) were drawn from 20 values of $D_{aut} \in \{0.05, 0.1, \ldots, 0.95\}$ and 20 values of scaled $p_{thr}^{1/4} \in \{0.05, 0.1, \ldots, 1\}$. We used non-regular spacing for p_{thr} due to its nonlinear effect on cell distribution. Eight random realizations of the networks were generated for each pair (D_{aut},p_{thr}) and for each group, generating 4 groups x 8 networks x 400 (D_{aut},p_{thr}) = 12,800 simulations, as detailed below:

* ISO-2.6: 8 isotropic networks with weak automaticity × 400 (D_{aut},p_{thr}) = 3,200 simulations

* ISO-3.5: 8 isotropic network with strong automaticity × 400 (D_{aut},p_{thr}) = 3,200 simulations

* ANISO-2.6: 8 anisotropic network with weak automaticity × 400 (D_{aut},p_{thr}) = 3,200 simulations

* ANISO-3.5: 8 anisotropic network with strong automaticity × 400 (D_{aut},p_{thr}) = 3,200 simulations

Post-simulation analysis was performed in Matlab (The Mathworks, Natick, MA). The network was said to have spontaneous activity if two complete activations or more were detected during 10 s of simulation. Conversely, the simulation was labeled as non-automatic if a single AP or

no activation was detected. The activation time of an action potential (AP) was defined as the time when the transmembrane voltage depolarizes beyond -40 mV. For the i^{th} AP of a given simulation, the activation map ($M_{tact,i}$ in ms) was a matrix constructed from detected activation times for all nodes.

A first set of measures was computed for each 10 s simulation with spontaneous activity.

* Normalized activation map ($M_{ntact,i}$ in ms) for the i^{th} AP was obtained as follows:

$$M_{ntact,i} = M_{tact,i} - \min\left[M_{tact,i}\right] \quad (1)$$

* Spontaneous cycle length map ($\Delta M_{tact,i}$ in ms) for the i^{th} AP was defined as:

$$\Delta M_{tact,i} = M_{tact,i} - M_{tact,i-1} \quad (2)$$

The spontaneous cycle length value ($\Delta t_{act,i}$ in ms) for that map was:

$$\Delta t_{act,i} = \text{median}\left[\Delta M_{tact,i}\right] \quad (3)$$

And the average spontaneous cycle length ($\Delta t_{act,i}$ in ms) for the series of N APs was:

$$\overline{\Delta t}_{act} = \frac{1}{N-1}\sum_{i=2}^{N} \Delta t_{act,i} \quad (4)$$

* The map of synchronization times ($M_{\tau sync,i}$ in s/cm) for the i^{th} AP was the inverse of conduction velocities, calculated from the spatial gradient of $M_{tact,i}$ using a previously described method [31]. It quantified activation delays between cells. If all cells were synchronized, meaning they activated at the same time, $M_{\tau sync,i}$ would be zero for each position on the lattice. The average synchronization time for N APs was:

$$\bar{\tau}_{sync} = \frac{1}{N}\sum_{i=1}^{N} \text{median}\left[M_{\tau sync,i}\right] \quad (5)$$

A second set of measures were defined for each pair (D_{aut},p_{thr}) to assess how spontaneous activity behaves for similar spatial patterns and hence the variability between realizations of the same random process of pattern generation. In fact, as previously stated, eight monolayers have been produced for every pairs (D_{aut},p_{thr}). The monolayers produced with the same (D_{aut},p_{thr}) had similar spatial patterns, compared to monolayers produced with different (D_{aut},p_{thr}) which had dissimilar spatial patterns.

* For each pair (D_{aut},p_{thr}), given n simulations (up to 8) with spontaneous activity, average and standard deviation of spontaneous cycle length for similar spatial patterns were defined as:

$$\overline{\Delta T}_{act} = \frac{1}{n}\sum_{j=1}^{n} \overline{\Delta t}_{act,j} \tag{6}$$

$$\sigma_{\Delta Tact} = \sqrt{\frac{1}{(n-1)}\sum_{j=1}^{n} \left(\overline{\Delta t}_{act,j} - \overline{\Delta T}_{act}\right)^2} \tag{7}$$

$\overline{\Delta T}_{act}$: average cycle length over n simulations for a pair (D_{aut}, p_{thr})

$\sigma_{\Delta Tact}$: standard deviation of cycle length over n simulations for a pair (D_{aut}, p_{thr})

$\overline{\Delta t}_{act,j}$: cycle length for the j^{th} simulation, as stated in equation (4)

* For each pair (D_{aut},p_{thr}), average and standard deviation of synchronization time for similar spatial patterns were defined as:

$$\overline{T}_{sync} = \frac{1}{n}\sum_{j=1}^{n} \overline{\tau}_{sync,j} \tag{8}$$

$$\sigma_{TSync} = \sqrt{\frac{1}{(n-1)}\sum_{j=1}^{n} \left(\overline{\tau}_{sync,j} - \overline{T}_{sync}\right)^2} \tag{9}$$

$\overline{T}_{sync}$: average synchronization time over n simulations for a pair (D_{aut}, p_{thr})

σ_{TSync} : standard deviation of synchronization time over n simulations for a pair (D_{aut}, p_{thr})

$\tau_{sync,j}$: synchronization time for the j^{th} simulation, as stated in equation (5)

The same process is used to calculate $\overline{T}_{sync,x}$, $\overline{T}_{sync,y}$, longitudinal and transverse components of $\overline{T}_{sync}$.

The third set of measures were defined for dissimilar spatial patterns, i.e. monolayers with different values of (D_{aut},p_{thr}).

* The cycle length range for dissimilar patterns was defined as the percentage variation between the minimum and maximum values of $\overline{\Delta T}_{act}$ over all pairs of (D_{aut},p_{thr}):

$$Range\left[\overline{\Delta T}_{act}\right] = 100 \text{ x } \frac{\max\left[\overline{\Delta T}_{act}\right] - \min\left[\overline{\Delta T}_{act}\right]}{\min\left[\overline{\Delta T}_{act}\right]} \quad (10)$$

$\overline{\Delta T}_{act}$: average cycle length over n simulations for a pair (D_{aut}, p_{thr}), as stated in equation (6)

* The synchronization time range for dissimilar patterns was defined as the percentage variation between the minimum and maximum values of $\overline{T}_{sync}$ over all pairs of (D_{aut},p_{thr}):

$$Range\left[\overline{T}_{sync}\right] = 100 \text{ x } \frac{\max\left[\overline{T}_{sync}\right] - \min\left[\overline{T}_{sync}\right]}{\min\left[\overline{T}_{sync}\right]} \quad (11)$$

$\overline{T}_{sync}$: average synchronization time over n simulations for a pair (D_{aut}, p_{thr}), as stated in equation (8)

Furthermore, each monolayer was divided in two areas separated by a square of 2.75 mm side (half of the side of the monolayer) to distinguish between border and central foci (first initiation

site of AP). Border foci behavior was assessed by anisotropy ratio. The border foci anisotropy ratio (r) was defined as:

$$r = \frac{\eta_L}{\eta_T} \tag{13}$$

η_L: number of border foci in longitudinal x-direction (anisotropy direction)

η_T: number of border foci in transverse y-direction

3.3. Results

3.3.1. Characterization of the cardiac 2D network

$\overline{S}_{cluster}$, average of $S_{cluster}$ over 8 monolayers for each pair (D_{aut},p_{thr}), increased with D_{aut}, independently of $p_{thr}^{1/4}$, with a transition from below 10,000 PM cells to over 30,000 PM cells around D_{aut} = 0.5 (Fig 5a and 5d).

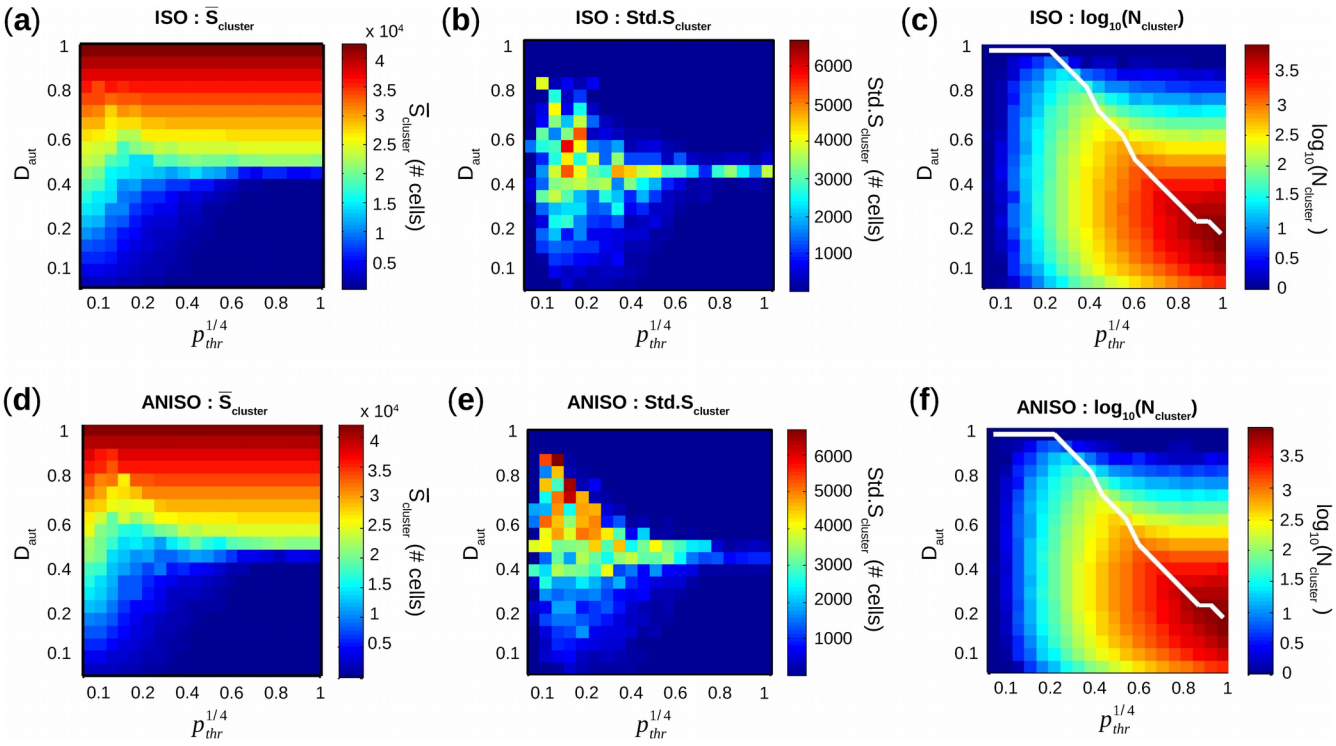

Fig 5. Characterization of the stochastic algorithm governing density and spatial distribution of pacemaker cells. (**a**,**d**) Average of maximum cluster size $\overline{S}_{cluster}$ in color scale map as a function of D_{aut} and $p_{thr}^{1/4}$, for monolayers with isotropic and anisotropic geometries. The size of a cluster is the actual number of pacemaker cells in that cluster. (**b**,**e**) Standard deviation of $S_{cluster}$ vs. D_{aut} and $p_{thr}^{1/4}$. (**c**,**f**) Log_{10} of number of clusters $N_{cluster}$ vs. D_{aut} and $p_{thr}^{1/4}$. Solid white line is $D_{aut,max}$ (see definition in text) as a function of $p_{thr}^{1/4}$.

The extent of the transition phase, i.e. the number of pairs (D_{aut},p_{thr}) with $\overline{S}_{cluster}$ between 10,000 and 30,000 PM cells, correlated with increased standard deviation of $S_{cluster}$ (Std.$S_{cluster}$). In fact, Std.$S_{cluster}$ (Fig 5b and 5e) was below 1,000 PM cells for all pairs (D_{aut},p_{thr}) except for the transition phase where Std.$S_{cluster}$ > 2,000 PM cells. As shown in Fig 5c and 5f, the number of clusters ($N_{clusters}$) increased with D_{aut} as long as $D_{aut} \leq D_{aut,max}$ (white solid line), and then decreased for $D_{aut} > D_{aut,max}$. For each $p_{thr}^{1/4}$, $D_{aut,max}$ was the maximum D_{aut} beyond which M_2

became empty, i.e. there was no more available site to perform cluster nucleation during the creation of the spatial distribution of PM cells. Thus, once $D_{aut,max}$ has been reached, only aggregation was possible for increasing D_{aut}. In Fig 6, a relationship was established between the transition in $\overline{S}_{cluster}$ and $D_{aut,max}$.

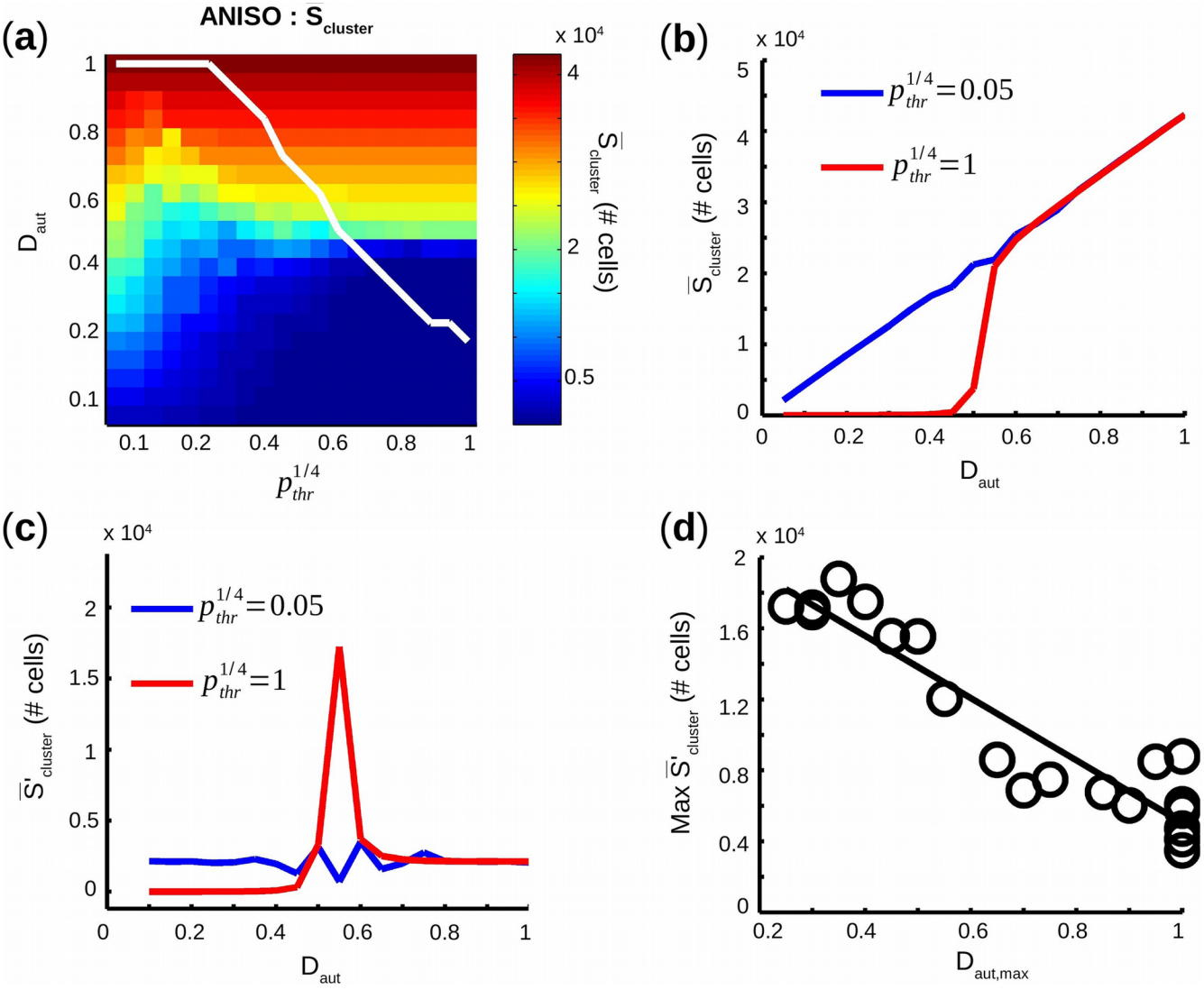

Fig 6. Relationship between cluster size transition and cluster fusion. (**a**) $\overline{S}_{cluster}$ (average of maximum cluster size) in color scale map as a function a function of D_{aut} and $p_{thr}^{1/4}$, for anisotropic networks. Solid white line is $D_{aut,max}$ as a function of $p_{thr}^{1/4}$. (**b**) $\overline{S}_{cluster}$ as a function of

D_{aut}, for first and last $p_{thr}^{1/4}$. (**c**) $\overline{S}'_{cluster}$ (first derivative of $\overline{S}_{cluster}$) as a function of D_{aut}, for first and last $p_{thr}^{1/4}$. (**d**) Maximum of $\overline{S}'_{cluster}$ vs. D_{aut} and for all $p_{thr}^{1/4}$, plotted as a function $D_{aut,max}$.

The maximum of the derivative of $\overline{S}_{cluster}$ as a function of D_{aut}, i.e. $\max[\overline{S}'_{cluster}] = \max[\Delta\overline{S}_{cluster}/\Delta D_{aut}]$, representing the sharpness of the transition of $\overline{S}_{cluster}$ from below 10,000 PM cells to over 30,000 PM cells, was calculated for all $p_{thr}^{1/4}$ and plotted against $D_{aut,max}$. The sharpness of the transition was inversely proportional to $D_{aut,max}$ (Fig 6d). Differences between isotropic and anisotropic geometries were unsurprisingly negligible for $\overline{S}_{cluster}$, $N_{clusters}$, and $D_{aut,max}$, since the number of neighbors was approximately the same for both geometries. As such, spatial distribution of spontaneous cells created by our aggregation and nucleation process are not affected by cell preferential orientation.

3.3.2. Occurrence of spontaneous activity

In general, 2D cardiac networks with isotropic geometry demonstrated circular-shaped electrical activation, as illustrated in Fig 7b for the pattern shown in panel a. Networks with the anisotropic geometry typically had ellipse-shape electrical activation (Fig 7d for the pattern in panel c).

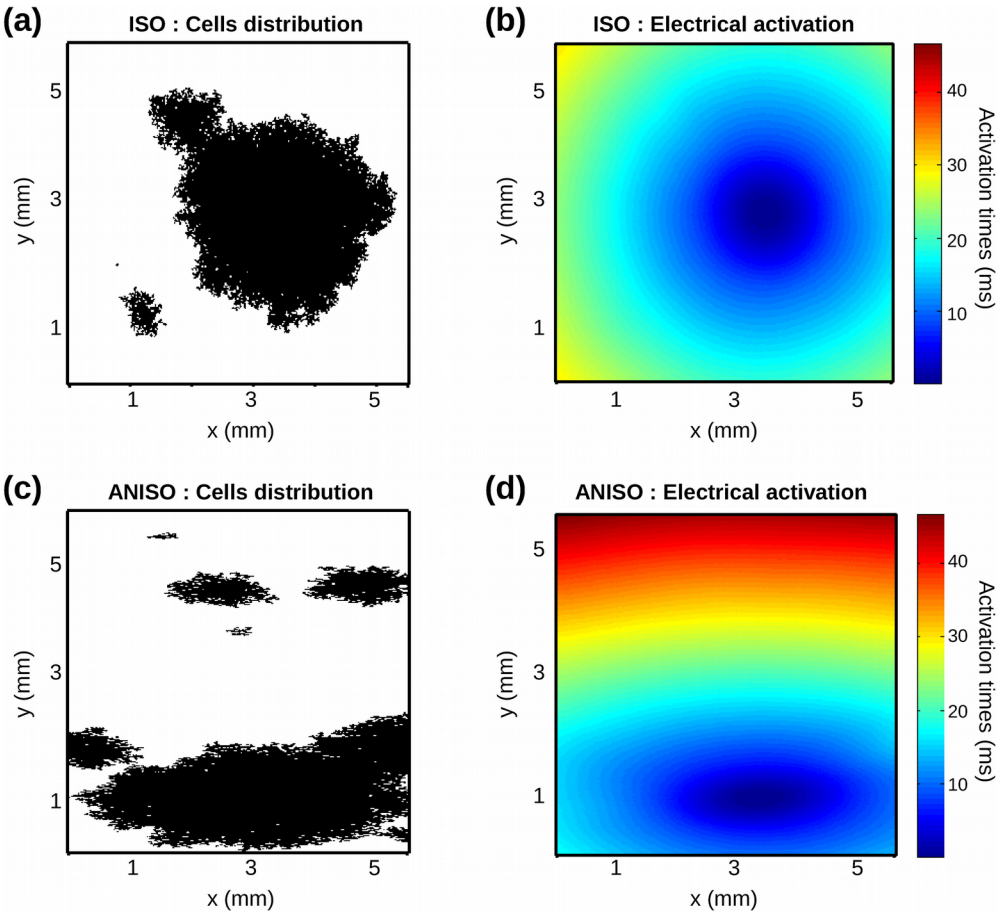

Fig 7. Electrical activation: isotropic vs. anisotropic. (**a**) Isotropic monolayer with D_{aut} = 0.3 and $p_{thr}^{1/4}$ = 0.10. (**b**) Electrical activation times (ms) color scale map as a function of node positions for the previously described isotropic monolayer. (**c**) Anisotropic monolayer with D_{aut} = 0.3 et $p_{thr}^{1/4}$ = 0.15. (**d**) Electrical activation times (ms) for the anisotropic monolayer.

For a specific pair (D_{aut}, p_{thr}), given n the number of simulations with automaticity: (a) [n=8] meant automaticity occurred for all 8 simulations, (b) [0<n<8] for 1 to 7 simulations, and (c) [n=0] for no simulation with automaticity. As shown in Fig 8, autonomous activity occurs more often in ISO-3.5 and ANISO-3.5 compared to ISO-2.6 and ANISO-2.6 over all pairs pairs (D_{aut}, p_{thr}).

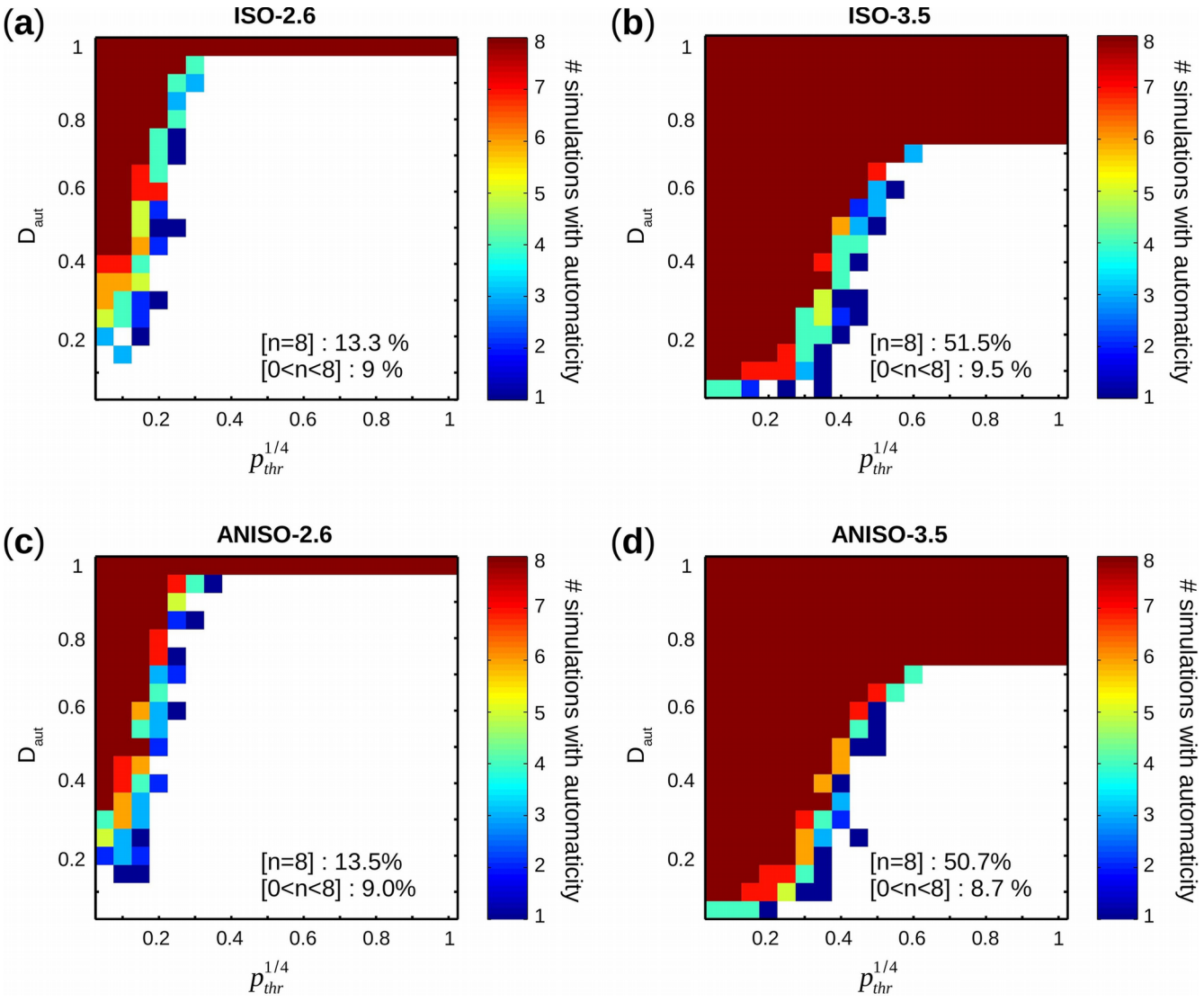

Fig 8. Occurrence of automaticity. (**a-d**) For each group, number n of simulations with automaticity is displayed in color scale map as a function D_{aut} and $p_{thr}^{1/4}$. White spots correspond to [n=0]. Proportions of pairs (D_{aut},p_{thr}) with [n = 8] and [0<n<8] are also indicated.

For example, 51.5% of pairs (D_{aut},p_{thr}) demonstrated [n=8] in ISO-3.5 versus 13.3% in ISO-2.6. Interestingly, proportions of pairs (D_{aut},p_{thr}) with [0<n<8] were very similar for all four groups (~9%). Automaticity was thus more likely to be observed for higher values of D_{aut} and lower

values of $p_{thr}^{1/4}$, and no difference in occurrence of autonomous activity was found between isotropic and anisotropic geometries.

A transition curve from [n=0] to [0<n<8] was the line drawn by the minimum D_{aut} required for each $p_{thr}^{1/4}$ to transition from [n=0] to [0<n<8]. Similarly, the transition curve from [0<n<8] to [n=8] was the line drawn by the minimum D_{aut} required for each $p_{thr}^{1/4}$ to transition from [0<n<8] to [n=8]. In Fig 9a-d, transition curves from [n=0] to [0<n<8] (solid line) and from [0<n<8] to [n=8] (dashed line) were superimposed to the color scale map of $\overline{S}_{cluster}$ and porosity, for isotropic and anisotropic networks.

$\overline{S}_{cluster}$ combined with porosity offered crucial insights on the morphology of the transition curves. Typically, automaticity did not appear when $\overline{S}_{cluster}$ was below 5,000 PM cells and when porosity was over 0.35. The higher $p_{thr}^{1/4}$ was, the greater $\overline{S}_{cluster}$ had to be to generate automaticity. In all groups, larger $\overline{S}_{cluster}$ was required to reach [n=8] versus [0<n<8]. Networks with strong automaticity displayed spontaneous activity at smaller values of $\overline{S}_{cluster}$ and higher porosity.

For all 4 groups, transition curves to [0<n<8] were subtracted from transition curves to [n=8], and the differences were displayed in Fig 9e and 9f. Peak differences were higher for ISO-2.6 (0.50) and ANISO-2.6 (0.45) compared to ISO-3.5 (0.35) and ANISO-3.5 (0.40) respectively. Furthermore peak differences occurred for lower $p_{thr}^{1/4}$ for ISO-2.6 and ANISO-2.6 (~0.2) compared to ISO-3.5 and ANISO-3.5 (~0.40).

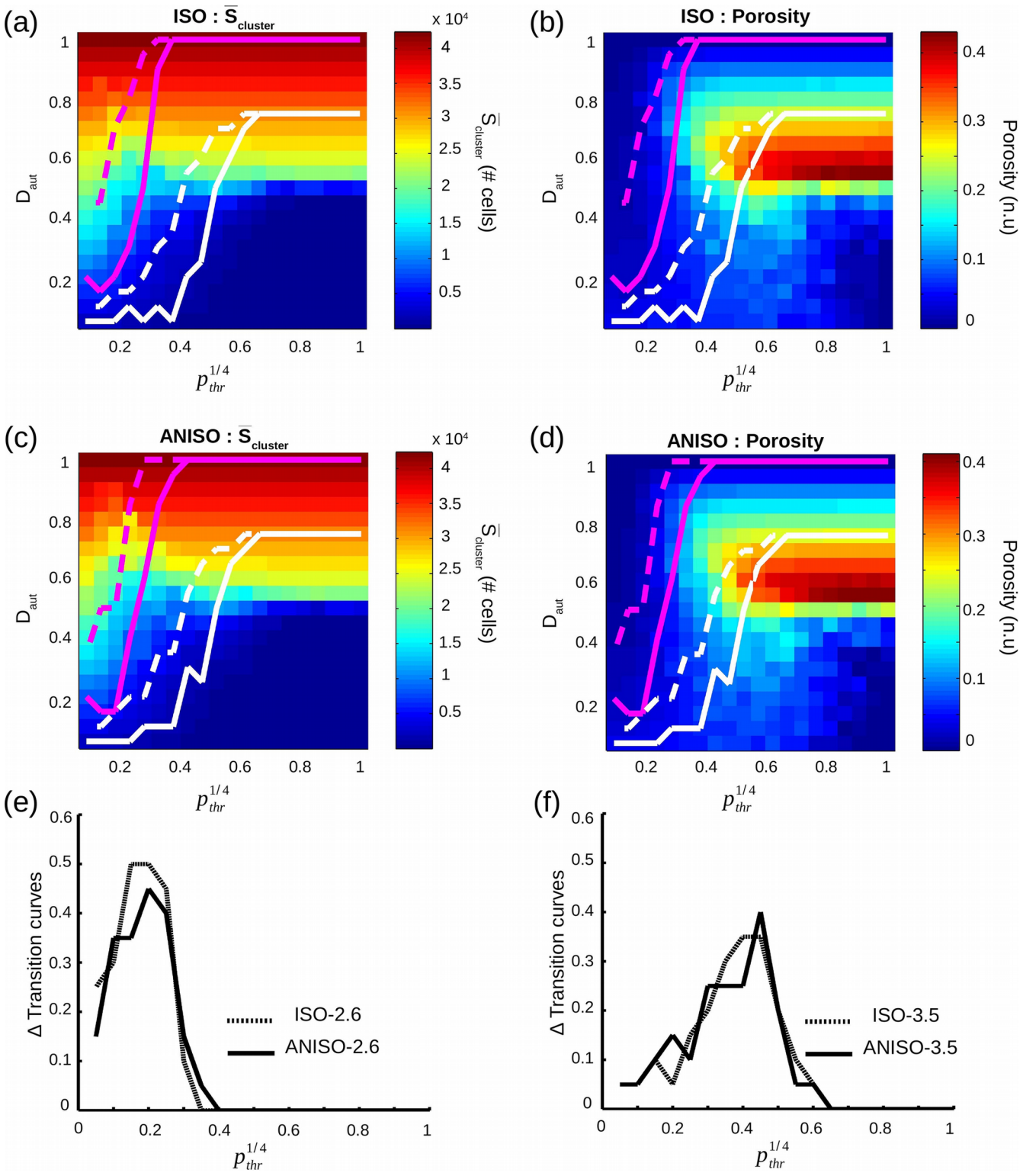

Fig 9. Transition curves. (**a-d**) Transition curves from [n=0] to [0<n<8] (solid line) and from [0<n<8] to [n=8] (dashed line) are displayed in magenta for ISO-2.6 and ANISO-2.6, and in white for ISO-3.5 and ANISO-3.5. In background is color scale map of either $\overline{S}_{cluster}$ or porosity,

both against D_{aut} and $p_{thr}^{1/4}$. (**e**,**f**) For each group, transition curve to [0<n<8] is subtracted to transition curve to [n=8].

3.3.3. Rate of spontaneous activity

In Fig 10a-d, $\overline{\Delta T}_{act}$ was calculated for each pair (D_{aut},p_{thr}) with [n=8] and displayed as color scale map vs. D_{aut} and $p_{thr}^{1/4}$.

Independently of groups and for any given $p_{thr}^{1/4}$, $\overline{\Delta T}_{act}$ decreased with increasing D_{aut}. And ranges, i.e. intrinsic variability for dissimilar patterns, of $\overline{\Delta T}_{act}$ for ISO-2.6 (16.19%) and ANISO-2.6 (14.56%) were much smaller than ISO-3.5 (98.86%) and ANISO-3.5 (100.96%).

In Fig 10e is presented mean[$\overline{\Delta T}_{act}$], calculated as the average $\overline{\Delta T}_{act}$ over all pairs (D_{aut},p_{thr}) with [n=8] shown in Fig 10a-d. Detailed values can be found in Table 2.

Mean[$\overline{\Delta T}_{act}$] for ISO-2.6 and ANISO-2.6 were respectively 110.26% and 110.96% higher compared to those of ISO-3.5 and ANISO-3.5. This behavior was not surprising, considering the difference observed in single cell simulations (1428 ms for I_{bias} = 2.6 μA/cm^2 compared to 599 ms for I_{bias} = 3.5 μA/cm^2, in Fig 1d). Besides, it is important to notice that, for a given I_{bias} value, single pacemaker cells always display lower cycle length than monolayers. No difference in mean[$\overline{\Delta T}_{act}$] was found between isotropic and anisotropic geometries for [n=8], but focusing on the set with [0<n<8] yielded interesting results. Pooling together all pairs (D_{aut}, p_{thr}) satisfying the condition [0<n<8] (Table 2), there was a higher mean[$\overline{\Delta T}_{act}$] ANISO-2.6 versus ISO-2.6 (3.08%), and ANISO-3.5 versus ISO-3.5 (5.50%).

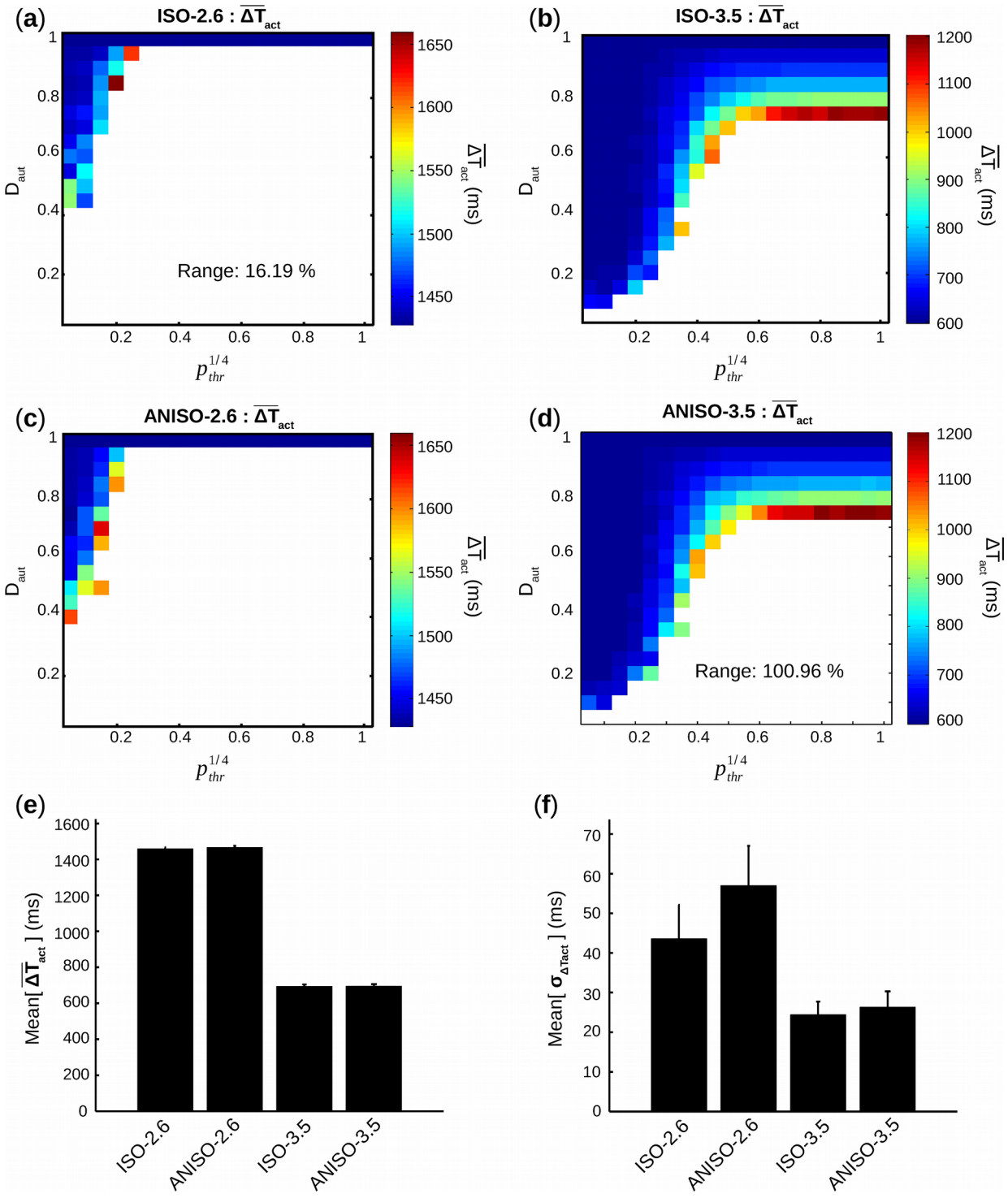

Fig 10. Rate of spontaneous activity. (**a-d**) For all groups, average cycle length $\overline{\Delta T}_{act}$ is calculated for each pair (D_{aut},p_{thr}) with [n=8] and displayed as a color scale map. The corresponding percentage range between the minimum and the maximum values of the $\overline{\Delta T}_{act}$ map is also displayed. (**e**) For each group, mean and s.e.m of values in $\overline{\Delta T}_{act}$ map are calculated.

(**f**) For each group, mean and s.e.m of values in Std cycle length $\sigma_{\Delta Tact}$ map (obtained following the same process than $\overline{\Delta T}_{act}$) are calculated.

Table 2. Summary of simulation results.

	ISO 2.6	**ANISO 2.6**	**ISO 3.5**	**ANISO 3.5**
Range[$\overline{\mathbf{\Delta T}}_{\mathbf{act}}$] (%) [n=8]	16.2	14.6	98.9	101.0
Mean[$\overline{\mathbf{\Delta T}}_{\mathbf{act}}$] (ms) [n=8]	1460 ± 6	1467 ± 8	694 ± 10	696 ± 10
Mean[$\boldsymbol{\sigma}_{\mathbf{\Delta Tact}}$] (ms) [n=8]	44 ± 9	57 ± 10	24 ± 3	26 ± 4
Mean[$\overline{\mathbf{\Delta T}}_{\mathbf{act}}$] (ms) [0<n<8]	1702± 25	1754± 28	1078± 39	1137± 49
Mean[$\boldsymbol{\sigma}_{\mathbf{\Delta Tact}}$] (ms) [0<n<8]	120± 10	175± 21	193± 27	208± 19
Central foci (%) [n=8]	8.33	2.57	21.7	12.8
Central foci (%) [0<n<8]	1.42	0.775	16.2	12.6
r [n=8]	1.28	1.62	0.93	2.82
r [0<n<8]	1.26	5	1	2.19
Range[$\overline{\mathbf{T}}_{\mathbf{Sync}}$] (%) [n=8]	6.5	16.9	414.0	484.7
Mean[$\overline{\mathbf{T}}_{\mathbf{Sync}}$] (s/cm) [n=8]	$0.0665 \pm 2\times10^{-4}$	$0.0876 \pm 6\times10^{-4}$	$0.0640 \pm 6\times10^{-4}$	$0.0811 \pm 10\times10^{-4}$
Mean[$\boldsymbol{\sigma}_{\mathbf{TSync}}$] (s/cm) [n=8]	$0.00094 \pm 2\times10^{-4}$	$0.0047 \pm 3\times10^{-4}$	$0.0020 \pm 2\times10^{-4}$	$0.0064 \pm 3\times10^{-4}$
Mean [$\overline{\mathbf{T}}_{\mathbf{sync,x}}$] (s/cm) [n=8]	$0.0436 \pm 7\times10^{-4}$	$0.0131 \pm 9\times10^{-4}$	$0.0404 \pm 6\times10^{-4}$	$0.0160 \pm 3\times10^{-4}$
Mean [$\overline{\mathbf{T}}_{\mathbf{sync,y}}$] (s/cm) [n=8]	$0.0433 \pm 7\times10^{-4}$	$0.0857 \pm 8\times10^{-4}$	$0.0418 \pm 6\times10^{-4}$	$0.0781 \pm 10\times10^{-4}$

Similarly to $\overline{\Delta T}_{act}$, $\sigma_{\Delta Tact}$ was calculated for each pair (D_{aut},p_{thr}) with [n=8]. Mean[$\sigma_{\Delta Tact}$], the average value of $\sigma_{\Delta Tact}$ over all pairs (D_{aut},p_{thr}) with [n=8] is also shown in Fig 10f and Table 2 for all groups. Mean[$\sigma_{\Delta Tact}$] was a measure of intrinsic variability between monolayers with similar spatial patterns of PM cells. Mean[$\sigma_{\Delta Tact}$] for ISO-2.6 and ANISO-2.6 were respectively 78.52% and 116.68% higher compared ISO-3.5 and ANISO-3.5. A difference between isotropic and anisotropic geometries was found where mean[$\sigma_{\Delta Tact}$] in ANISO-2.6 was 30% higher vs. ISO-2.6, while a more limited increase of 8% was found for ANISO-3.5 compared to ISO-3.5.

3.3.4. Spatial characteristics of spontaneous activity

Difference in spatial characteristics of spontaneous activity between isotropic and anisotropic geometry was evaluated. The position of foci (i.e. first initiation sites of electrical activation) was estimated to determine if differences existed between the two network geometries. Independently of geometry, focal activation was highly stable in time for a given spatial pattern of spontaneous cells, demonstrating no beat-to-beat variability. For direct comparison between geometries, the focal position of the last simulated spontaneous beat was selected for all simulations with automaticity (i.e. [n>0]). Pooled positions were plotted in Fig11a-d.

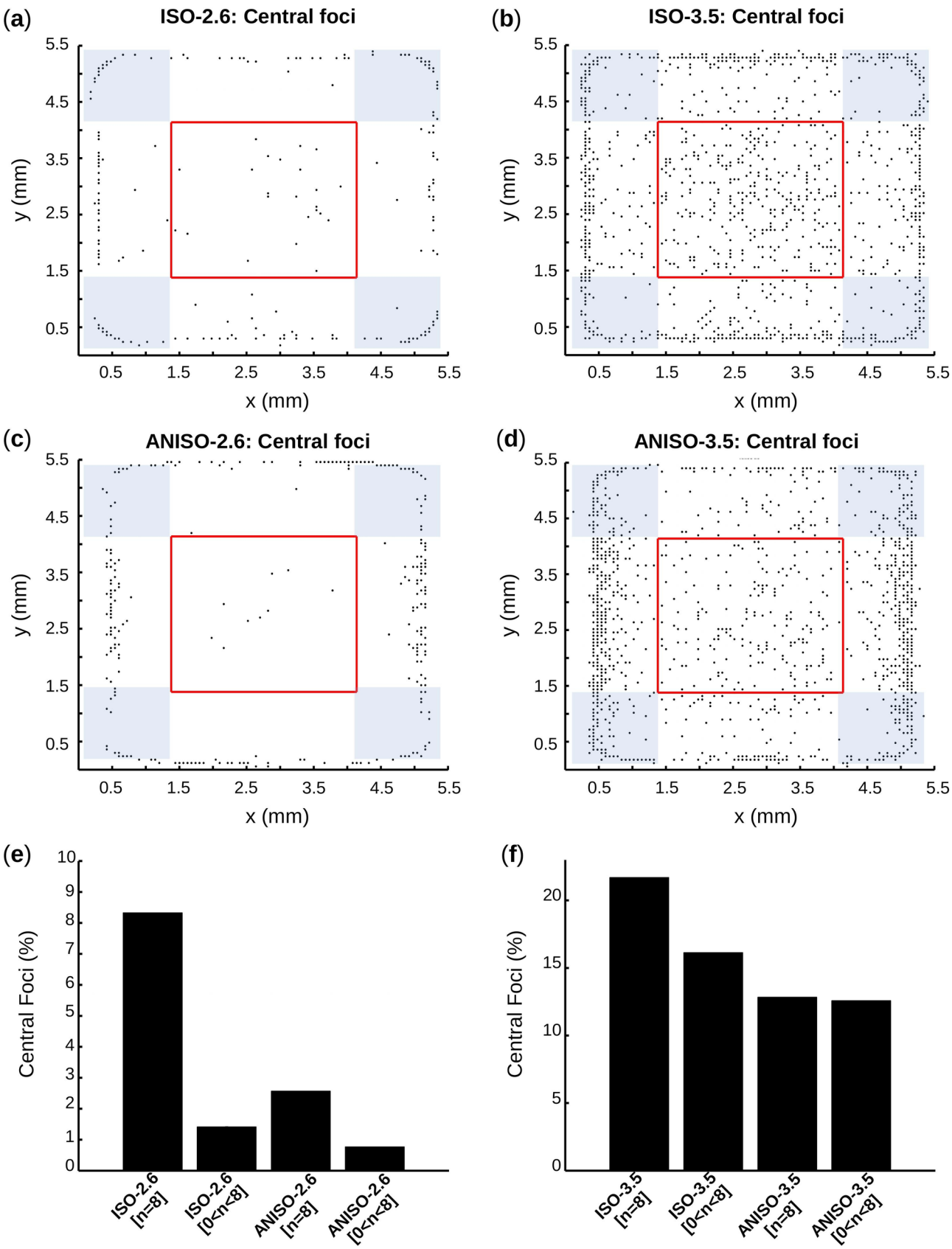
(a)
ISO-2.6: Central foci
(b)
ISO-3.5: Central foci
(c)
ANISO-2.6: Central foci
(d)
ANISO-3.5: Central foci
y (mm)
x (mm)
0.5
1.5
2.5
3.5
4.5
5.5
(e)
Central Foci (%)
0
1
2
3
4
5
6
7
8
9
10
ISO-2.6 [n=8]
ISO-2.6 [0<n<8]
ANISO-2.6 [n=8]
ANISO-2.6 [0<n<8]
(f)
Central Foci (%)
0
5
10
15
20
ISO-3.5 [n=8]
ISO-3.5 [0<n<8]
ANISO-3.5 [n=8]
ANISO-3.5 [0<n<8]

Fig 11. Foci positions: central vs. border. (**a**-**d**) For each group, and for [n>0], focal position of the last activation is plotted. Central foci are inside the red square, whose side is 50% of the monolayer side. The border foci in the longitudinal x-direction are the foci located outside the red box, exclusively to the left and to the right. The border foci in the transverse y-direction are exclusively at the top and the bottom. Non exclusive border foci at the corners, i.e. foci that are common to longitudinal and transverse direction are in the blue areas and are not considered in the calculation of border foci anisotropy ratio (r) in equation (13). (**e**,**f**) Proportions of central focals for [n=8] and [0<n<8].

The proportion of central foci over all foci is shown in Fig 11e and 11f and Table 2 for pairs of (D_{aut},p_{thr}) with [n=8] and pairs (D_{aut},p_{thr}) with [0<n<8]. Anisotropic geometries demonstrated fewer central foci, independently of I_{bias} or n values. For pairs (D_{aut},p_{thr}) with [n=8], proportions of central foci decreased by 69.11% from ISO-2.6 to ANISO-2.6, and by 40.84% from ISO-3.5 to ANISO-3.5. The drop was less important for pairs of (D_{aut},p_{thr}) with [0<n<8] case, where proportions of central foci fell by 45.35% from ISO-2.6 to ANISO-2.6, and by 22.05% from ISO-3.5 to ANISO-3.5. It was also interesting to observe that cases with [0<n<8] demonstrated fewer central foci than cases with [n=8], independently of I_{bias} value or geometry. In fact, in ISO-2.6 and ANISO-2.6, proportions of central foci respectively fell by 83% and 69.9% from [n=8] to [0<n<8]. The difference between pairs of (D_{aut},p_{thr}) with [n=8] and [0<n<8] was less important when I_{bias} = 3.5 μA/cm^2. As a matter of fact, the drop of central foci proportions from [n=8] to [0<n<8] was 25.58% in ISO-3.5 and 1.94% in ANISO-3.5.

The border foci in the longitudinal x-direction were the foci located outside the red box, exclusively to the left and to the right. The border foci in the transverse y-direction were the

foci located outside the red box, exclusively at the top and the bottom. Non exclusive border foci at the corners, i.e. foci that are common to longitudinal and transverse directions (blue areas in Fig 11a-d), were not considered in the calculations. Ratio with values greater than one suggested that there were more border foci in the longitudinal direction compared to the transverse direction. Values of *r* were calculated for [n=8] and [0<n<8] and are presented in Table 2. Interestingly, *r* in anisotropic geometry are consistently greater than one and always higher compared to the value obtained in isotropic geometry. In fact, for [n=8] case, *r* raised by 27% from ISO-2.6 to ANISO-2.6, and by 204% from ISO-3.5 to ANISO-3.5. For [0<n<8], *r* raised by 297% from ISO-2.6 to ANISO-2.6, and by 119% from ISO-3.5 to ANISO-3.5. No clear preference in border foci position was found for the isotropic network.

Synchronization of electrical activation is an important marker of spontaneously beating multicellular monolayer, either *in silico* or *in vitro*. $\overline{T}_{sync}$ was displayed as color map vs. D_{aut} and $p_{thr}^{1/4}$ for each pair (D_{aut},p_{thr}) with [n=8] in Fig 12a-d.

No particular tendencies were observed in $\overline{T}_{sync}$ map for ISO-2.6 and ANISO-2.6. For ISO-3.5 and ANISO-3.5, and for $D_{aut} \geq 0.8$, $\overline{T}_{sync}$ increased and then decreased as a function of $p_{thr}^{1/4}$. I_{bias} = 3.5 μA/cm^2 led to much higher ranges compared to I_{bias} = 2.6 μA/cm^2. Indeed, range[$\overline{T}_{sync}$] for ISO-2.6 (6.5%) and ANISO-2.6 (16.9%) were much smaller than ISO-3.5 (414%) and ANISO-3.5 (485%). Moreover, the increase in ranges could be noticed in anisotropic geometries versus isotropic geometries: 160% increase from ISO-2.6 to ANISO-2.6 and more moderate 17.15% increase from ISO-3.5 to ANISO-3.5.

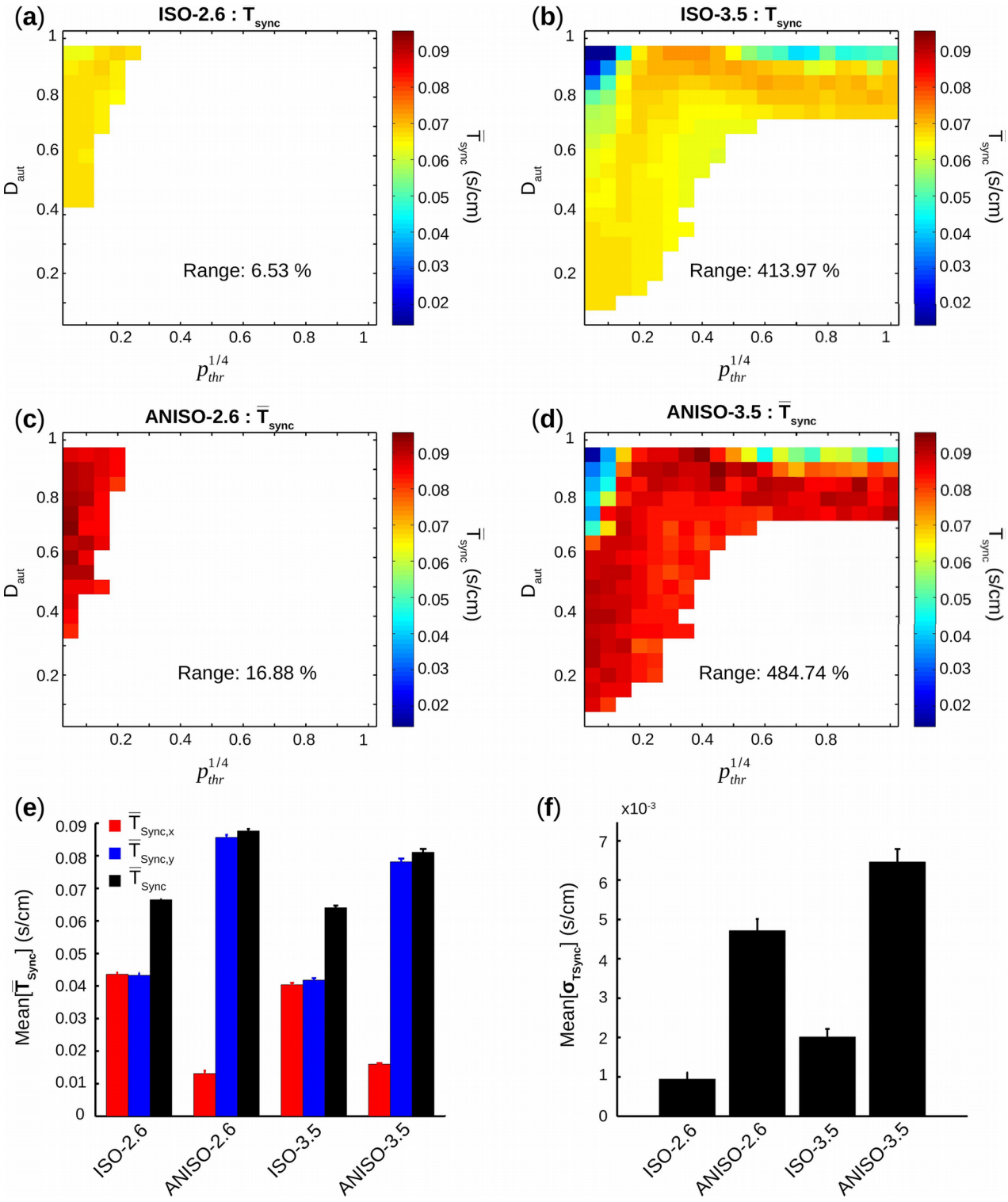
(a)
ISO-2.6 : T sync
Range: 6.53 %
(b)
ISO-3.5 : T sync
Range: 413.97 %
(c)
ANISO-2.6 : T sync
Range: 16.88 %
(d)
ANISO-3.5 : T sync
Range: 484.74 %
D aut
p thr 1/4
T sync (s/cm)
(e)
T Sync,x
T Sync,y
T Sync
Mean[T Sync] (s/cm)
ISO-2.6
ANISO-2.6
ISO-3.5
ANISO-3.5
(f)
x10-3
Mean[σ TSync] (s/cm)
ISO-2.6
ANISO-2.6
ISO-3.5
ANISO-3.5

Fig 12. Synchronization times. (**a-d**) For all groups, average synchronization time $\overline{T}_{sync}$ is calculated for each pair (D_{aut},p_{thr}) with [n=8] and displayed as a color scale map. The corresponding percentage range between the minimum and the maximum values of the $\overline{T}_{sync}$ map is also displayed.(**e**) For each group, mean and s.e.m of values in $\overline{T}_{sync,x}$, $\overline{T}_{sync,y}$, $\overline{T}_{sync}$ map are calculated. (**f**) For each group, mean and s.e.m of values in Std synchronization time σ_{TSync} map (obtained following the same process than $\overline{T}_{sync}$) are calculated.

Anisotropy consistently yielded higher synchronization times. Mean[$\overline{T}_{sync}$] rose by 31.87% from ISO-2.6 to ANISO-2.6 and by 26.64% from ISO-3.5 to ANISO-3.5. Mean[$\overline{T}_{sync,y}$] obviously played an important role in that increase. In fact, the unsurprising decrease of synchronization times in the direction of anisotropy mean[$\overline{T}_{sync,x}$] was associated with a dramatic increase of mean[$\overline{T}_{sync,y}$], leading to a higher resultant mean[$\overline{T}_{sync}$].

3.4. Discussion & Conclusion

To our knowledge, this paper presents the first *in silico* study in a microstructure model describing how automaticity strength and structural linear anisotropy may modulate the effects of density and spatial distribution of PM cells on the spontaneous activity of the BP.

Our previous study [14] demonstrated that not only the density but also the spatial distribution of PM cells may induce important intrinsic variability in the BP dynamical behavior. The study focused on a simple continuous and isotropic 2D substrate with a single period of activity for the autonomous cells. These results quickly raised a very important question: can this intrinsic variability be limited despite the lack of control on density and spatial distribution of

autonomous cells? Two straightforward solutions may be considered: (a) either the BP is tested ex vivo and then implanted into the myocardium, or (b) the current methods are combined with new processes intended to minimize the intrinsic variability. Investigating the second candidate solution is the main motivation behind the mathematical modeling optimization process that is underway. Here, we studied how different automaticity strengths and structural linear anisotropy can influence the spatial-temporal activity of the BP.

The main new contributions are described as follows:

(1) Spatial patterns of PM cells were mathematically defined and characterized within a semi-discrete 2D model, describing both automaticity strength and structural linear anisotropy.

(2) Automaticity strength enhanced occurrence of spontaneous activity, decreased variability in cycle length $\overline{\Delta T}_{act}$ and synchronization time $\overline{T}_{sync}$ for similar spatial patterns of PM cells, but increased the number of central foci, and the variability of $\overline{\Delta T}_{act}$ and $\overline{T}_{sync}$ for dissimilar spatial patterns PM cells.

(3) Structural linear anisotropy had no important effect on occurrence of spontaneous activity, increased variability in $\overline{\Delta T}_{act}$ and $\overline{T}_{sync}$ for both similar and dissimilar spatial patterns of PM cells, and decreased the proportion of central foci.

(4) Intrinsic variability was modulated but not eliminated by neither automaticity strength nor structural linear anisotropy, since there was still a proportion of pairs (D_{aut},p_{thr}) with no spontaneous activity and important performance discrepancies notably for dissimilar spatial patterns of PM cells.

PM cells were randomly placed in a semi-discrete 2D microstructure via a stochastic algorithm with a parameter D_{aut} controlling density and a parameter $p_{thr}^{1/4}$ determining homogeneity of

spatial distribution. Two levels of automaticity strength (weak and strong) were achieved by two different values of I_{bias} (2.6 μA/cm² and 3.5 μA/cm²). Linear anisotropy was structurally created by: (1) geometrically increasing aspect ratio of cells from one to three, and (2) fitting longitudinal and transverse gap junctions distribution to published conduction velocities from anisotropic monolayer cultures of NRVMs [18].

Isolated PM cell dynamics were described by LR1 cardiac ventricle myocyte model [27], with a constant inward bias current to generate automaticity, as described elsewhere [28,29]. More complex ionic models (for example the published NRVM ionic model [32] or a mathematical models representing stem cell-derived human cardiomyocytes [33]) were not used: (1) to avoid important computational cost because of the associated long transient dynamics and (2) because increasing dimensions of mathematical ionic models does not necessarily lead to more predictive power. As a matter of fact, in many high dimension models very different set of parameters can lead to the same AP; in this case the model is said to have identifiability issue, a major flaw to predictive reliability [34]. The LR1 model obviously does not include the detailed ionic currents of cardiomyocytes (pacemaking and resting) nor can it reproduce the intricate interaction between the membrane/voltage clocks [6,28]. However it remains an appropriate trade-off option since it is identifiable [34] and can reproduce the basic physiological behaviors considered in the present study, namely automaticity and AP propagation.

To avoid confounding effects, some simplifications were made:

(1) We considered only two populations of cells: PM and quiescent excitable cells. Other types of heterogeneities such as sinks (spots with voltage fixed at resting potential like

fibroblasts) and breaks (spots with no conduction, like monolayer damage) were not considered although they may have had an effect on conduction [35].

(2) I_{bias} was the same for all PM cells of a specific monolayers, i.e. all PM cells were identical. All cells had the same initial conditions and no time delay. It is important to notice however that clinical BPs with all identical PM cells would lack robustness to external perturbations. For example they may completely stop firing after acetylcholine stimulation. Cellular diversity is indeed an important aspect to preserve robustness in the native sinus node [36].

(3) The number of neighbors was approximately the same for each cell. Different number of neighbors could create electrotonic disparities between PM clusters and induce confusion with effects of porosity on occurrence of automaticity.

No reentry or asynchronous activation was detected in the simulations; this fact is an indication of strong intercellular coupling [28,29,37–39] but also may be limited by the homogeneous initial conditions used in the simulations. But the strongest coupling is not necessarily the best for clinical *in situ* BPs, without no-flux boundary conditions. In fact, to maintain source-sink balance with the atrium, native SAN cells are coupled with low conductance connexins (Cx-45) instead of high conductance Cx-43 [40]. There is indeed an inverse proportional relationship between coupling strength and the safety factor of propagation [41].

$\overline{S}_{cluster}$ and $N_{cluster}$ as a function of D_{aut} and $p_{thr}^{1/4}$ displayed remarkable similarities with our previous study [14], despite different model structure and different number of neighbors. In fact, average of the maximum PM cluster size $\overline{S}_{cluster}$ monotonically increased with D_{aut}, with a transition around D_{aut} = 0.5 (Fig 5). However, in this study we brought deeper spatial

characterizations compared to the previous one. For example, the sharpness of this transition was demonstrated to be inversely proportional to $D_{aut,max}$ (Fig 6). The sharpness of the transition relied on two related phenomena: aggregation of clusters at low $p_{thr}^{1/4}$ and «fusion» [14] of clusters at high $p_{thr}^{1/4}$. For low $p_{thr}^{1/4}$ (heterogeneous spatial distribution of PM cells) $\overline{S}_{cluster}$ grew mainly because of aggregation and was proportional to D_{aut} which increased linearly, hence showing a smooth transition. For higher $p_{thr}^{1/4}$ (homogeneous spatial distribution) $\overline{S}_{cluster}$ grew mainly because of «fusion» since there was more nucleation and less aggregation. In fact, as D_{aut} increases, clusters start having common neighboring available sites. When a PM cell is placed on one of those sites, previously separated clusters «fuse» into one bigger cluster. Decrease of $N_{cluster}$ indicates a start in the «fusion» process, systematically above $D_{aut,max}$. So $\overline{S}_{cluster}$ started growing slowly for high $p_{thr}^{1/4}$ and low D_{aut} because there was almost no aggregation and no «fusion». Once $D_{aut,max}$ was reached, «fusion» process provoked a sharp increase of $S_{cluster}$ and hence a sharp transition.

Higher D_{aut} and lower $p_{thr}^{1/4}$ led to more chance of having automaticity ([n>0]) (**Fig 8**). Even higher D_{aut} and lower $p_{thr}^{1/4}$ were necessary for all simulations to show automaticity ([n=8]). The lower $p_{thr}^{1/4}$ was, the lower D_{aut} was required to generate automaticity.

The transition curves are also a major characterization improvement, compared to our previous study [14]. Superimposing transition curves over $\overline{S}_{cluster}$ and porosity color scale maps (Fig 9) gave crucial information about relationship between the monolayer microstructure organization and occurrence of automaticity. It was really interesting to observe that small $\overline{S}_{cluster}$ at low $p_{thr}^{1/4}$

could generate spontaneous activity while large $\overline{S}_{cluster}$ at high $p_{thr}^{1/4}$ could not. A big cluster at high $p_{thr}^{1/4}$ may contain too much inside spots with quiescent cells and not be able to fire an AP, while a small cluster at low $p_{thr}^{1/4}$ containing no inside quiescent spot at all will be able to do it. This is where porosity remarkably came into play. Porosity established the importance of electrotonic source-sink balance inside the PM cluster itself.

Spontaneous activity occurs more often with strong automaticity (I_{bias} = 2.6 μA/cm^2). Basically, lower $\overline{S}_{cluster}$ was needed and higher porosity was tolerated for automaticity with stronger PM cells to be observed.

For each $p_{thr}^{1/4}$ value, average autonomous cycle length $\overline{\Delta T}_{act}$ decreased with increasing D_{aut} (Fig 10) since bigger clusters (with reasonably low porosity) have more electrotonic driving force. Unsurprisingly, strong automaticity brought smaller period of activity (lower $\overline{\Delta T}_{act}$), but also resulted in higher ranges of $\overline{\Delta T}_{act}$, i.e. more intrinsic variability for dissimilar spatial patterns. Stronger automaticity allowed occurrence of spontaneous activity in more difficult conditions (lower $\overline{S}_{cluster}$, and higher porosity), but the resulting periods would be noticeably higher compared to more favorable conditions. On a clinical point of view, this result means that creating BPs with stronger automaticity would not solve the problem of not having control over the fate of the PM cells *in situ* (intrinsic variability). The generated BP may have better chance to display automaticity, but would have very disparate performances from one patient to another. The best way to bypass the problem is to create multiple BPs *ex vivo*, pick the cultured BP with the targeted performance and then graft it to the patient myocardium.

In accordance with the literature [14,42,43], foci were usually located at the border (Fig 11)

since, with no-flux boundary condition, border clusters had less cells to depolarize. Strong PM cells led to more central foci because more clusters had enough electrotonic driving force to depolarize neighboring cells without interacting with the no-flux boundary condition. It was interesting to notice that anisotropy yielded more border foci in the longitudinal direction compared to the transverse direction. In fact, because of the aspect ratio, there were actually more cells at the two longitudinal borders and thus more chance of having a sufficiently bigger $\overline{S}_{cluster}$ to fire an AP.

Electrical activations were less synchronous in anisotropic monolayers (Fig 12). Very low $\overline{T}_{sync}$ in the longitudinal direction were hindered by very high $\overline{T}_{sync}$ in the transverse direction, leading to an electrical activation that was globally less synchronous. The evolution of $\overline{T}_{sync}$ as a function of $p_{thr}^{1/4}$ for $D_{aut} \geq 0.8$ is very interesting and requires further investigations. Further investigations are also needed to explain how structural linear anisotropy consistently induced more intrinsic variability for both similar and dissimilar spatial patterns. Anisotropy had also limited effect on occurrence of automaticity and $\overline{\Delta T}_{act}$, compared to strength of automaticity. If there was indeed an effect, it eventually happened below the 5% resolution of D_{aut} and $p_{thr}^{1/4}$. Automaticity strength and anisotropy may not be as independent as displayed in this study. Anisotropy has been shown to induce changes in intracellular calcium transients ($[Ca^{2+}]_i$) dynamics, decreasing the diastolic $[Ca^{2+}]_i$ levels and increasing $[Ca^{2+}]_i$ influx per cardiac cycle [44]. Anisotropy may also alter the properties of voltage-gated ion channels, notably expression and regulatory properties of voltage-gated calcium channels [45]. So, on a strict structural point of view (i.e. aspect ratio and distribution of gap junctions), anisotropy may not have an impact,

but it may indirectly affect automaticity strength, which then will have an effect on spontaneous activity. As such, even if linear structural anisotropy does not increase occurrence of automaticity and does not decrease intrinsic variability, it may still be clinically interesting.

This study offered crucial insights on the relationships between the microstructure of the BP and its macroscopic behavior. Automaticity strength and structural linear anisotropy may modulate effects of density and spatial distribution of PM cells on the spontaneous activity of the BP, but will probably not eliminate intrinsic variability among BPs. Therapeutic procedures that do not take characteristics of spatial distribution into account (eg. cell and gene therapies) may end up with a non-negligible intrinsic variability, despite standardized protocols. Increasing the number of pacemaker cells may not solve the issue. As a matter of fact, the native SAN tissue exhibits a specific architecture with gradual transition of intermediate cells and gradually decreasing density of pacemaker cells from the center to the periphery. That spatial arrangement promotes automaticity by maintaining the delicate balance in the source-sink relationship between the SAN and the surrounding atrial tissue [36]. With an unknown spatial arrangement, that balance may randomly be compromised, hence the intrinsic variability. Furthermore, unlike the SAN which is electrically isolated from the rest of the atrium with the exception of few exit pathways, BPs lack electrotonic barrier at the macroscopic level, another challenge to their performance. All those facts stress the importance of *ex vivo* design and performance assessments on BPs in bioreactors before implantation to patients.

A sheet-based BP as a replacement to the normal sinus node has important intrinsic differences with the physiological structure. The normal pacemaker is a compact node of heterogeneous

spontaneous cells believed to be connected at specific exit points thus limiting contact to a restricted number of atrial cells [46]. The simulated BP in this study are very different where a population of autonomous cells are connected to resting ventricular myocytes, both having similar morphology and dimensions. Cell dimensions and morphologies vary between pacemaker cells (assuming spindle-like cell morphology as in the sinus node) and resting but excitable cardiomyocyte (with also differences between atrial and ventricular cells). Cardiomyocyte dimensions is well known to affect electrical propagation [47]. Thus, important work is still needed to study the differences in spontaneous activity of BP monolayer when considering morphological differences between cell types although the differences between cell types (sinus node cell, atrial and ventricular-like derived cardiomyocytes) for derived cardiomyocytes may not be as important as in adult hearts. More importantly, BP activity when electrically coupled to myocardium in order to drive the tissue will be depressed by the electrotonic effect [48] and biomimetism of the sinus node coupling structure to the atria may need to be considered for coupling the BP to the myocardium.

In summary, a pure change from isotropic to anisotropic substrate modelled by an elongated cell shape and anisotropic intercellular conductivity without modifications of ion channel expression nor spatial distribution has limited effects on spontaneous activity. However, increasing the intrinsic rate of autonomous cells has a much stronger effects. Although the two were studied together and independently, it is of importance to note that there is a strong possibility that both changes (anisotropy and autonomous strength) could be coupled [44]. Further work is thus needed to uncover this importance of the interaction (and by how much

methods to induce cellular anisotropy can increase the cellular automaticity strength) and to elucidate how it could favor the BP development.

Acknowledgements

This work was supported by the Natural Sciences and Engineering Research Council of Canada, the Montreal Heart Institute Foundation and by the Réseau ThéCell du Fonds de recherche du Québec –Santé (FRQS). Computations were made on the supercomputer Cottos from Université de Montréal, managed by Calcul Québec and Compute Canada. The operation of this supercomputer is funded by the Canada Foundation for Innovation (CFI), the ministère de l'Économie, de la science et de l'innovation du Québec (MESI) and the Fonds de recherche du Québec - Nature et technologies (FRQ-NT).

3.5. References

References

1. Mangoni ME, Nargeot J. Genesis and Regulation of the Heart Automaticity. Physiol Rev. 2008;88: 919–982. doi:10.1152/physrev.00018.2007

2. Rozanski GJ, Lipsius SL. Electrophysiology of functional subsidiary pacemakers in canine right atrium. Am J Physiol. 1985;249: H594-603.

3. Monfredi O, Maltsev VA, Lakatta EG. Modern Concepts Concerning the Origin of the Heartbeat. Physiology. 2013;28: 74–92. doi:10.1152/physiol.00054.2012

4. Maltsev VA, Lakatta EG. Dynamic interactions of an intracellular Ca2+ clock and membrane ion channel clock underlie robust initiation and regulation of cardiac pacemaker function.

Cardiovasc Res. 2008;77: 274–284. doi:10.1093/cvr/cvm058

5. Maltsev VA, Vinogradova TM, Lakatta EG. The Emergence of a General Theory of the Initiation and Strength of the Heartbeat. J Pharmacol Sci. 2006;100: 338–369. doi:10.1254/jphs.CR0060018

6. Severi S, Fantini M, Charawi LA, DiFrancesco D. An updated computational model of rabbit sinoatrial action potential to investigate the mechanisms of heart rate modulation. J Physiol. 2012;590: 4483–4499. doi:10.1113/jphysiol.2012.229435

7. DiFrancesco D. The Role of the Funny Current in Pacemaker Activity. Circ Res. 2010;106: 434–446. doi:10.1161/CIRCRESAHA.109.208041

8. Stern MD, Maltseva LA, Juhaszova M, Sollott SJ, Lakatta EG, Maltsev VA. Hierarchical clustering of ryanodine receptors enables emergence of a calcium clock in sinoatrial node cells. J Gen Physiol. 2014;143: 577–604. doi:10.1085/jgp.201311123

9. Sasse P, Zhang J, Cleemann L, Morad M, Hescheler J, Fleischmann BK. Intracellular Ca2+ Oscillations, a Potential Pacemaking Mechanism in Early Embryonic Heart Cells. J Gen Physiol. 2007;130: 133–144. doi:10.1085/jgp.200609575

10. Zaniboni M, Cacciani F, Lux RL. Beat-to-Beat Cycle Length Variability of Spontaneously Beating Guinea Pig Sinoatrial Cells: Relative Contributions of the Membrane and Calcium Clocks. PLOS ONE. 2014;9: e100242. doi:10.1371/journal.pone.0100242

11. Munshi NV, Olson EN. Improving cardiac rhythm with a biological pacemaker. Science. 2014;345: 268–269. doi:10.1126/science.1257976

12. Hu Y-F, Dawkins JF, Cho HC, Marbán E, Cingolani E. Biological pacemaker created by minimally invasive somatic reprogramming in pigs with complete heart block. Sci Transl Med.

2014;6: 245ra94. doi:10.1126/scitranslmed.3008681

13. Cai J, Lin G, Jiang H, Yang B, Jiang X, Yu Q, et al. Transplanted neonatal cardiomyocytes as a potential biological pacemaker in pigs with complete atrioventricular block. Transplantation. 2006;81: 1022–1026. doi:10.1097/01.tp.0000214954.09515.51

14. Duverger JE, Boudreau-Béland J, Le MD, Comtois P. Multicellular automaticity of cardiac cell monolayers: effects of density and spatial distribution of pacemaker cells. New J Phys. 2014;16: 113046. doi:10.1088/1367-2630/16/11/113046

15. Guo W, Kamiya K, Cheng J, Toyama J. Changes in action potentials and ion currents in long-term cultured neonatal rat ventricular cells. Am J Physiol. 1996;271: C93-102.

16. Gomez JP, Potreau D, Branka JE, Raymond G. Developmental changes in Ca2+ currents from newborn rat cardiomyocytes in primary culture. Pflugers Arch. 1994;428: 241–249.

17. Boink GJJ, Christoffels VM, Robinson RB, Tan HL. The past, present, and future of pacemaker therapies. Trends Cardiovasc Med. 2015;25: 661–673. doi:10.1016/j.tcm.2015.02.005

18. Bursac N, Parker KK, Iravanian S, Tung L. Cardiomyocyte Cultures With Controlled Macroscopic Anisotropy. Circ Res. 2002;91: e45–e54. doi:10.1161/01.RES.0000047530.88338.EB

19. Liau B, Christoforou N, Leong K, Bursac N. Pluripotent Stem Cell-derived Cardiac Tissue Patch with Advanced Structure and Function. Biomaterials. 2011;32: 9180–9187. doi:10.1016/j.biomaterials.2011.08.050

20. Blazeski A, Kostecki GM, Tung L. Engineered heart slices for electrophysiological and contractile studies. Biomaterials. 2015;55: 119–128. doi:10.1016/j.biomaterials.2015.03.026

21. Campbell PH, Feinberg AW, Goss JA, Parker KK, Ripplinger CM. Anisotropic biological pacemakers and av bypasses [Internet]. WO2012048242 A1, 2012. Available: http://www.google.ca/patents/WO2012048242A1

22. Diego C de, Chen F, Xie Y, Pai RK, Slavin L, Parker J, et al. Anisotropic conduction block and reentry in neonatal rat ventricular myocyte monolayers. Am J Physiol - Heart Circ Physiol. 2011;300: H271–H278. doi:10.1152/ajpheart.00758.2009

23. Schwan J, Kwaczala AT, Ryan TJ, Bartulos O, Ren Y, Sewanan LR, et al. Anisotropic engineered heart tissue made from laser-cut decellularized myocardium. Sci Rep. 2016;6. doi:10.1038/srep32068

24. Spach MS, Heidlage JF, Barr RC, Dolber PC. Cell size and communication: role in structural and electrical development and remodeling of the heart. Heart Rhythm. 2004;1: 500–515. doi:10.1016/j.hrthm.2004.06.010

25. Kim JM, Bursac N, Henriquez CS. A computer model of engineered cardiac monolayers. Biophys J. 2010;98: 1762–1771. doi:10.1016/j.bpj.2010.01.008

26. Jacquemet V, Henriquez CS. Loading effect of fibroblast-myocyte coupling on resting potential, impulse propagation, and repolarization: insights from a microstructure model. Am J Physiol - Heart Circ Physiol. 2008;294: H2040–H2052. doi:10.1152/ajpheart.01298.2007

27. Luo CH, Rudy Y. A model of the ventricular cardiac action potential. Depolarization, repolarization, and their interaction. Circ Res. 1991;68: 1501–1526. doi:10.1161/01.RES.68.6.1501

28. Kanakov OI, Osipov GV, Chan C-K, Kurths J. Cluster synchronization and spatio-temporal dynamics in networks of oscillatory and excitable Luo-Rudy cells. Chaos Woodbury N.

2007;17: 015111. doi:10.1063/1.2437581

29. Kryukov AK, Petrov VS, Averyanova LS, Osipov GV, Chen W, Drugova O, et al. Synchronization phenomena in mixed media of passive, excitable, and oscillatory cells. Chaos Interdiscip J Nonlinear Sci. 2008;18: 037129. doi:10.1063/1.2956985

30. AUTO [Internet]. [cited 12 Jul 2017]. Available: http://indy.cs.concordia.ca/auto/

31. Bayly PV, KenKnight BH, Rogers JM, Hillsley RE, Ideker RE, Smith WM. Estimation of conduction velocity vector fields from epicardial mapping data. IEEE Trans Biomed Eng. 1998;45: 563–571. doi:10.1109/10.668746

32. Korhonen T, Hänninen SL, Tavi P. Model of Excitation-Contraction Coupling of Rat Neonatal Ventricular Myocytes. Biophys J. 2009;96: 1189–1209. doi:10.1016/j.bpj.2008.10.026

33. Paci M, Hyttinen J, Aalto-Setälä K, Severi S. Computational models of ventricular- and atrial-like human induced pluripotent stem cell derived cardiomyocytes. Ann Biomed Eng. 2013;41: 2334–2348. doi:10.1007/s10439-013-0833-3

34. Hui BBCB, Dokos S, Lovell NH. Parameter Identifiability of Cardiac Ionic Models Using a Novel CellML Least Squares Optimization Tool. 2007 29th Annual International Conference of the IEEE Engineering in Medicine and Biology Society. 2007. pp. 5307–5310. doi:10.1109/IEMBS.2007.4353539

35. Shajahan TK, Borek B, Shrier A, Glass L. Scaling properties of conduction velocity in heterogeneous excitable media. Phys Rev E Stat Nonlin Soft Matter Phys. 2011;84: 046208. doi:10.1103/PhysRevE.84.046208

36. Unudurthi SD, Wolf RM, Hund TJ. Role of sinoatrial node architecture in maintaining a balanced source-sink relationship and synchronous cardiac pacemaking. Front Physiol. 2014;5.

doi:10.3389/fphys.2014.00446

37. Bub G, Shrier A, Glass L. Global organization of dynamics in oscillatory heterogeneous excitable media. Phys Rev Lett. 2005;94: 028105. doi:10.1103/PhysRevLett.94.028105

38. Bub G, Shrier A, Glass L. Spiral wave generation in heterogeneous excitable media. Phys Rev Lett. 2002;88: 058101. doi:10.1103/PhysRevLett.88.058101

39. Steinberg BE, Glass L, Shrier A, Bub G. The role of heterogeneities and intercellular coupling in wave propagation in cardiac tissue. Philos Trans R Soc Lond Math Phys Eng Sci. 2006;364: 1299–1311. doi:10.1098/rsta.2006.1771

40. Boyett MR, Inada S, Yoo S, Li J, Liu J, Tellez J, et al. Connexins in the sinoatrial and atrioventricular nodes. Adv Cardiol. 2006;42: 175–197. doi:10.1159/000092569

41. Kleber AG, Saffitz JE. Role of the intercalated disc in cardiac propagation and arrhythmogenesis. Front Physiol. 2014;5. doi:10.3389/fphys.2014.00404

42. Boudreau-Béland J, Duverger JE, Petitjean E, Maguy A, Ledoux J, Comtois P. Spatiotemporal Stability of Neonatal Rat Cardiomyocyte Monolayers Spontaneous Activity Is Dependent on the Culture Substrate. PLoS ONE. 2015;10. doi:10.1371/journal.pone.0127977

43. Ponard JGC, Kondratyev AA, Kucera JP. Mechanisms of Intrinsic Beating Variability in Cardiac Cell Cultures and Model Pacemaker Networks. Biophys J. 2007;92: 3734–3752. doi:10.1529/biophysj.106.091892

44. Pong T, Adams WJ, Bray M-A, Feinberg AW, Sheehy SP, Werdich AA, et al. Hierarchical architecture influences calcium dynamics in engineered cardiac muscle. Exp Biol Med Maywood NJ. 2011;236: 366–373. doi:10.1258/ebm.2010.010239

45. Walsh KB, Parks GE. Changes in cardiac myocyte morphology alter the properties of

voltage-gated ion channels. Cardiovasc Res. 2002;55: 64–75.

46. Li N, Hansen BJ, Csepe TA, Zhao J, Ignozzi AJ, Sul LV, et al. Redundant and diverse intranodal pacemakers and conduction pathways protect the human sinoatrial node from failure. Sci Transl Med. 2017;9. doi:10.1126/scitranslmed.aam5607

47. Spach MS, Heidlage JF, Dolber PC, Barr RC. Electrophysiological Effects of Remodeling Cardiac Gap Junctions and Cell Size. Circ Res. 2000;86: 302–311. doi:10.1161/01.RES.86.3.302

48. Xie Y, Sato D, Garfinkel A, Qu Z, Weiss JN. So Little Source, So Much Sink: Requirements for Afterdepolarizations to Propagate in Tissue. Biophys J. 2010;99: 1408–1415. doi:10.1016/j.bpj.2010.06.042

CHAPITRE 4 – COUPLAGE MÉCANO-ÉLECTRIQUE ET STIMULATEUR CARDIAQUE BIOLOGIQUE : MÉTHODE CARACTÉRISANT LES EFFETS SPATIO-TEMPORELS DE L'ÉTIREMENT UNIAXIAL SUR L'ACTIVITÉ SPONTANÉE DE MONOCOUCHES CARDIAQUES EN CULTURE

Cardiac mechano-electric coupling and the biological pacemaker: method to characterize spatiotemporal effects of uniaxial stretch on the spontaneous activity of beating cardiac monolayers

James Elber Duverger[1,2], Yashar Alami Alamdari[1,2], Jonathan Boudreau-Béland[1,2], Paul Coudert[1], Patrice Naud[1,2], Alexandre Blanchette[1], Philippe Comtois[1,2]

[1]Research Centre, Montreal Heart Institute, 5000 Belanger Street, Montreal, Quebec, H1T1C8, Canada

[2]Department of Molecular and Integrative Physiology/Institute of Biomedical Engineering, Université de Montréal, C.P. 6128, Succursale Centre-Ville, Montreal, Quebec, H3C3J7, Canada

E-mail: philippe.comtois@umontreal.ca

Abstract. The biological pacemaker, a therapeutic alternative to electronic pacemakers, may take the form of a cultured patch of spontaneously beating cardiac cells grafted to the myocardium. Once implanted *in vivo*, the patch would undergo mechanical constraint affecting its dynamics through the mechano-electric coupling. This project aims to develop a method characterizing acute spatiotemporal effects of physiological uniaxial stretch on the spontaneous activity of the biological pacemaker. To validate the approach, neonatal rat ventricular myocytes are cultured on a rectangular, elastic, and clear silicone membrane. Five days post-culture, cells are stained with a voltage sensitive dye and then the membrane is attached to a pair of 3D printed plastic holders coupled to a motorized uniaxial stretching device. Electrical

activity observed from the change in fluorescence level of the patch is recorded with an EMCCD camera. Electrical stimulation protocols are implemented by the application of an electric field between two parallel carbon electrodes supplied with amplified voltage from a digital-to-analog converter. A remapping algorithm has been developed to rescale post-stretch to pre-stretch dimensions and consequently allow, for the first time, direct spatial comparison between the two conditions. Compared to pre-stretch state, static 20% uniaxial stretch resulted in: (1) enhanced occurrence of spontaneous activity, (2) increased autonomous rate (3) reduced beat-to-beat variability of autonomous rate and focal positions, (4) reduced recovery delay to resume spontaneous activity after electrical stimulation, and (5) induced anisotropic conduction slowing. The method replicates previously established time-dependent effects of stretch in different SAN cell and tissue preparations and thoroughly quantifies, for the first time, the spatial effect of stretch on the spontaneous activity of the biological pacemaker.

4.1. Introduction

In case of bradycardia, mainly due to sinoatrial node (SAN) dysfunction [1], [2] or atrioventricular (AV) node block [3], the standard treatment is the implantation of an electronic pacemaker [4] (EP), which reduces mortality and morbidity in carefully selected patients [5]. However, EPs also present several shortcomings, notably a limited duration of the battery, possible occurrence of infection and lead fracture, tissue remodeling including fibrosis and cardiomyocytes disarray leading to ventricular function impairment [6]. Despite remarkable improvements including leadless devices [7] and secondary batteries [8], functional

replacement of the native SAN remains unreached, notably about the response to stressors including exercise [9]. Furthermore, EPs reduce mortality rate only for patients with AV node block and not for patients with SAN dysfonction [10], [11].

The biological pacemaker (BP) stands out as an interesting alternative therapy. Several approaches have been considered to date. For example, gene therapy can perform somatic reprogramming of a subset of cardiomyocytes by viral injection into the myocardium to change the original phenotype into an SAN cell-like one [12]–[14]. Cell therapy has also been proposed, and consists of direct injection of fetal or pluripotent stem cells derived SAN-like cells into the myocardium, initiating spontaneous localized activity [15], [16]. Although promising, both of these methods lack control on the final distribution of spontaneous cells and, thus, functional properties of the BP once created *in situ*. Such limitations could results in high variability between patients as highlighted in our previous modeling study [17]. For this reason, we believe that a two-step workflow where the BP is first cultured and tested *in vitro* before being implanted to the patient's heart would be preferable. This method would thus allow *in vitro* performance assessments and optimization before implantation to the myocardium.

Once implanted in situ, the BP patch will undergo mechanical constraint that could affect its electrical activity because of the mechano-electric coupling (MEC) [18]. So the observed *in vitro* behavior of BP patch may no longer apply once grafted into the heart.

Mechano-electric coupling is a very complex phenomenon. Literature on different cardiac cells and tissues have shown that MEC effects can not only be through the activation of stretch-activated channels (SACs), but also through calcium-dependent (endothelin and angiotensin pathways) and cGMP-dependent pathways (cardiac natriuretic hormones and nitric oxide) [19].

Mechanical constraints applied to cardiac cells have diverse origins, including but not limited to: intracellular volume increase, shear stress, compression and stretch. For purpose of simplicity, only acute stretch will be considered in this study.

Cardiac response to acute stretch is highly nonlinear. In fact, under 6% static stretch, sarcomeric length in single neonatal rat cardiomyocytes stays elongated for approximately 40 minutes and then is gradually restored to the original position over an hour [20]. Electrophysiological changes induced by acute stretch depends on many intricate factors. Among them are species [21] and even the type of experimental preparations. For example, stretch-induced increase in beat rate (BR) of isolated rabbit atrium (+15% to +40%) [22] is bigger than that observed in single rabbit SAN cells (+5%) [23]. The type of stretch also has an impact on the BR response. Indeed, on one hand, axial stretch has a lesser increase on BR than concentric stretch (+9% vs. 16%) in isolated sinus node [24]. Gradual increase of stretch (i.e. applied over a period of 1 to 5 minutes) of canine SAN region by 50 grams load leads to smaller BR increase than rapid stretch (i.e. in less than 1 minute), with (+5% vs. +28%) or without vagal stimulation (+14% vs. +18%) [25]. Beyond preparations and stimuli type, stretch-induced BR response varies with samples pre-stretch state. In isolated rat right atrium, lower BR in unstretched state correlated to greater chronotropic response with stretch: from 160 to 470 beats per minute (bpm) of unstretched BR, the percentage change in atrial rate goes from +24% to -5% [26]. Apart from the BR, acute stretch influences several other physiological measures. In cat isolated SAN, stretch induces upward shift in minimum diastolic potential (MDP), initiates spontaneous activity in quiescent preparations, and restores regular activity in preparations with irregular activity [27]. In micropatterned mouse cardiomyocytes culture, 14%

longitudinal stretch increased cell membrane capacitance by 98% (that will later influence cell membrane charging and spontaneous activity) and decreased conduction velocity by 26% [28]. Determining the acute effects of stretch on the BP patch is thus of high importance. As such, this project aims to develop a method to evaluate both time-dependent and spatial effects of acute uniaxial stretch on the autonomous activity of a patch-like BP. The specific goals are stated as follows: (1) culture of a BP monolayer patch on an elastic and clear-bottom substrate; (2) apply acute uniaxial stretch to the BP patch, with or without electrical stimulation; (3) record the acute response of the BP patch due to uniaxial stretch, using a fast-fluorescence voltage imaging approach; and (4) design and implement algorithms to characterize time-dependent and spatial effects of uniaxial stretch on the BP patch. This paper will explain the rationale and *modus operandi* behind each step of the methodology, and discuss experimental results, notably the stabilization effect of physiological stretch.

4.2. Methods

4.2.1. Membrane fabrication and preparation for cell culture

Elastic and clear substrates were fabricated to culture the BP patch (Fig. 1a,b). The mold was designed on FreeCAD (open-source 3D CAD software) [29] and machined in polycarbonate (Lexan, Sabic inc.) with a 3-axis micromilling CNC machine (Roland iModela iM-01, TechSoft UK Limited) with 1 mm tip high hook slot drill (TA-SDEA-1, TechSoft UK Limited). A thin plastic spacer was glued to the top of the mold to fix the bottom thickness (278 μm) of the

culture well.

Polydimethylsiloxane (PDMS, Dow Corning) with 20:1 silicone to curing agent ratio (Young's modulus of ~ 87 kPa [30]), was poured into the mold, covered, and left to cure at room temperature for 24 hours. The process resulted in a biocompatible, elastic, and clear PDMS membrane, with a centered 6 mm x 6 mm x 1 mm well that can then be prepared for cell culture. Since PDMS is hydrophobic [31], a 60 seconds air plasma treatment (PDC-32G, Harrick Plasma Inc) was required to improve hydrophilicity of the membrane. The culture well was then pre-treated with a 0,007% fibronectin solution in pure water and left at 37 °C for 3 hours before rinsing to favor cell adhesion [32].

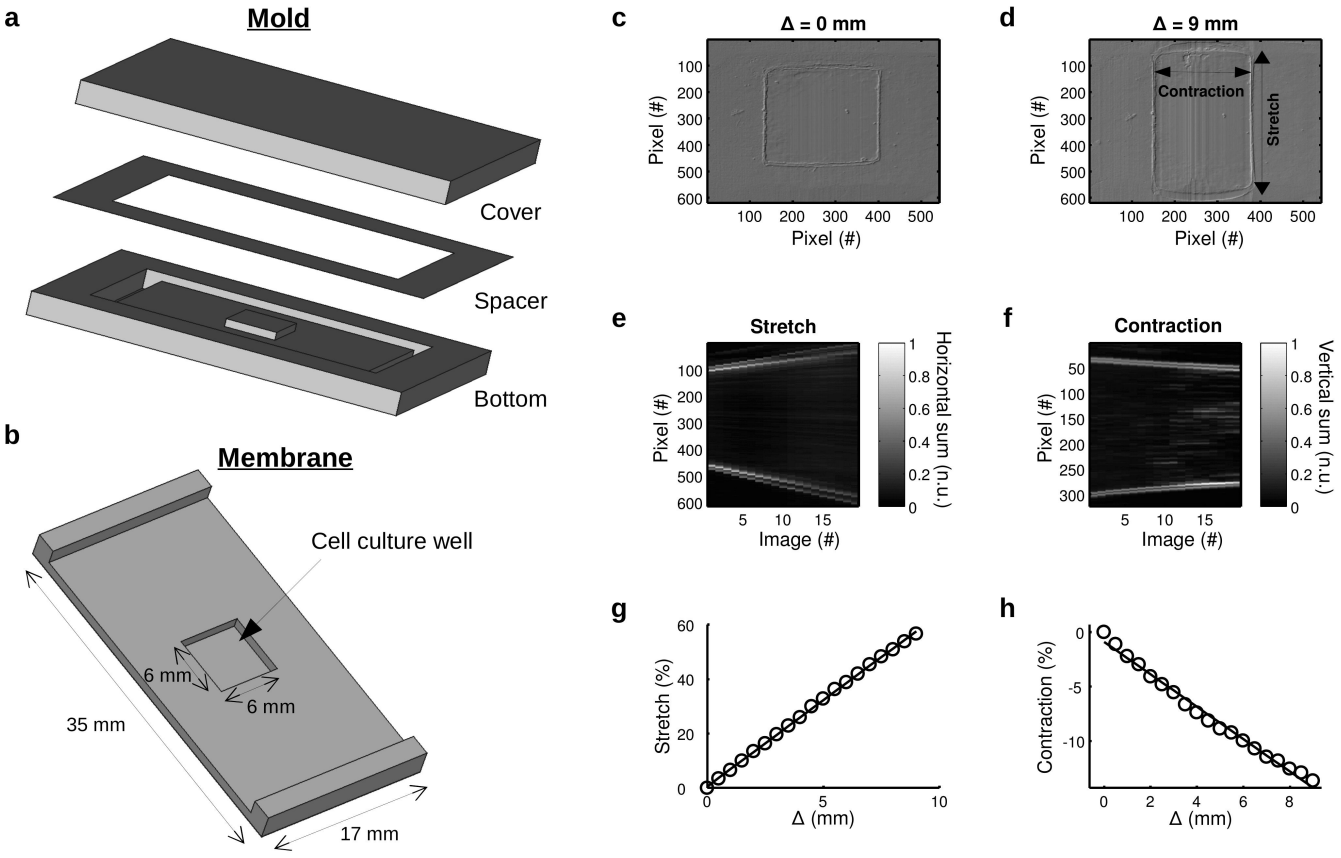

Figure 1. Membrane for cell culture: molding and characterization. a, 3D model of the mold, with spacer and cover. The mold was machined in polycarbonate using a 3-axis milling

CNC machine. A thin plastic spacer is glued to the top of the mold to fix the thickness (278 μm) of the bottom of the culture well. After PDMS was poured in the mold, the top cover is put in place for curing at room temperature for 24 hours. **b,** 3D model of the membrane. The molded membrane has the following characteristics: 35 mm long, 17 mm large, and 1.278 mm thick. At the center is a 6mm × 6mm × 1mm well, whose bottom thickness is 278 μm. In the longitudinal/stretch direction, both ends of the membrane are 1 mm thicker to facilitate the grip on the stretcher. **c,d,** First (**c**) and last (**d**) post-processed top-view pictures of a series of 19, taken at different elongation levels (0 to 9 mm, with a step of 0.5 mm). **e,f,** Each of the 19 vertical lines respectively represents horizontal (**e**) and vertical (**f**) summation of pixel intensities for the 19 post-processed pictures. **g,h,** The distance between the 2 maximum intensities of each vertical lines in (**e**) and (**f**) are edges the culture well and allow the calculation of stretch (**g**) and stretch-induced contraction (**h**) respectively (circles). Linear regressions (solid lines) establish the affine relationship between elongation (in mm) applied by motors and the actual stretch (in %) and stretch-induced contraction (in %) of the central culture well.

4.2.2. Stretcher device and electrical stimulator

A previously described [33] computer-controlled stretcher device has been improved to apply uniaxial stretch to the BP (Fig. 2). The PDMS membrane was attached to two custom made c-shape-ended plastic holders both coupled to a linear guide (i.e. carriage sliding on a rail, Igus inc). Deformation of the membrane was imposed by the displacement of two linear stepper motors (28000 series size 11 miniature stepper motor non-captive linear actuator, 28F4(7)-12V, Haydon Kerk Motion Solutions). Motion control was achieved with a stepper motor driver carrier chip (A4988, Pololu Robotics & Electronics). A custom Matlab (R2008A, The MatWorks) routine drove a multifunction digital acquisition module (NI USB-6221 DAQ,

National Instruments Corp.) controlling the A4988 chip to set the motor displacement direction (TTL signal) and speed (clock signal). Details about the driving method and description of the electronic chip can be found in Supplementary Fig. 1 and Supplementary Table 1 respectively. The BP patch could be electrically field stimulated with the application of a voltage difference between 2 parallel carbon plate electrodes (SK-05 ISO Graphite Plates, Industrial Graphite Sales LLC) supplied with post-amplified voltage signal from a digital-to-analog converter of the DAQ module, as depicted in Supplementary Fig. 2.

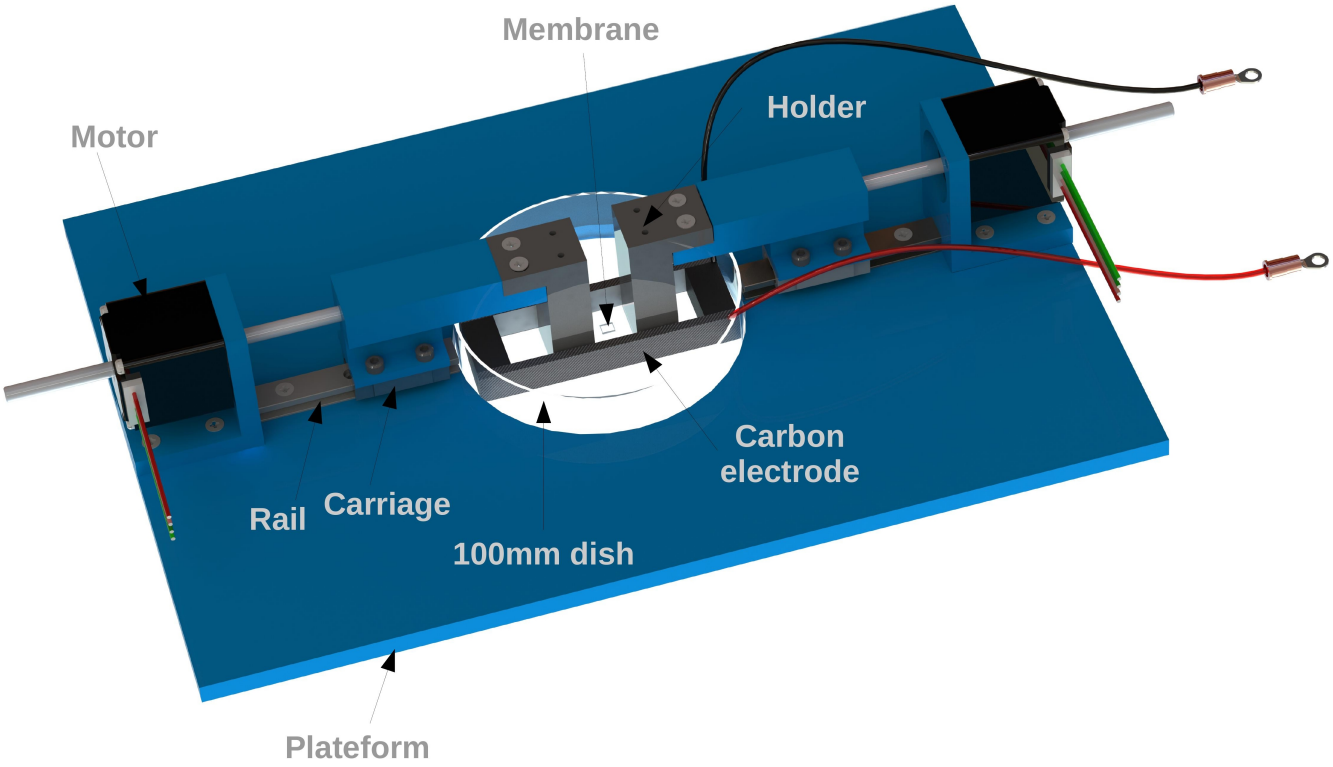

Figure 2. Stretcher device with electrodes for electrical stimulation. A 100 mm plastic petri dish is inserted in a 100 mm hole cut in the center of a 29 × 20 × 6.35 mm rectangular polycarbonate platform. Two 60 mm rails are screwed at each side of the center hole, on the diameter following the longitudinal direction of the platform. A carriage slides on each rail to make a linear guide. Each thick end of the membrane is laterally inserted in a c-shape-ended

plastic holder which is screwed to a custom plastic piece linking the carriage of the linear guide to the shaft of the motor. Two carbon plate electrodes (80 mm length, 6 mm height, 4 mm thick) are attached to 2 plastic custom pieces to form a setup whose internal width is 22 mm, letting room for the free displacement of the membrane.

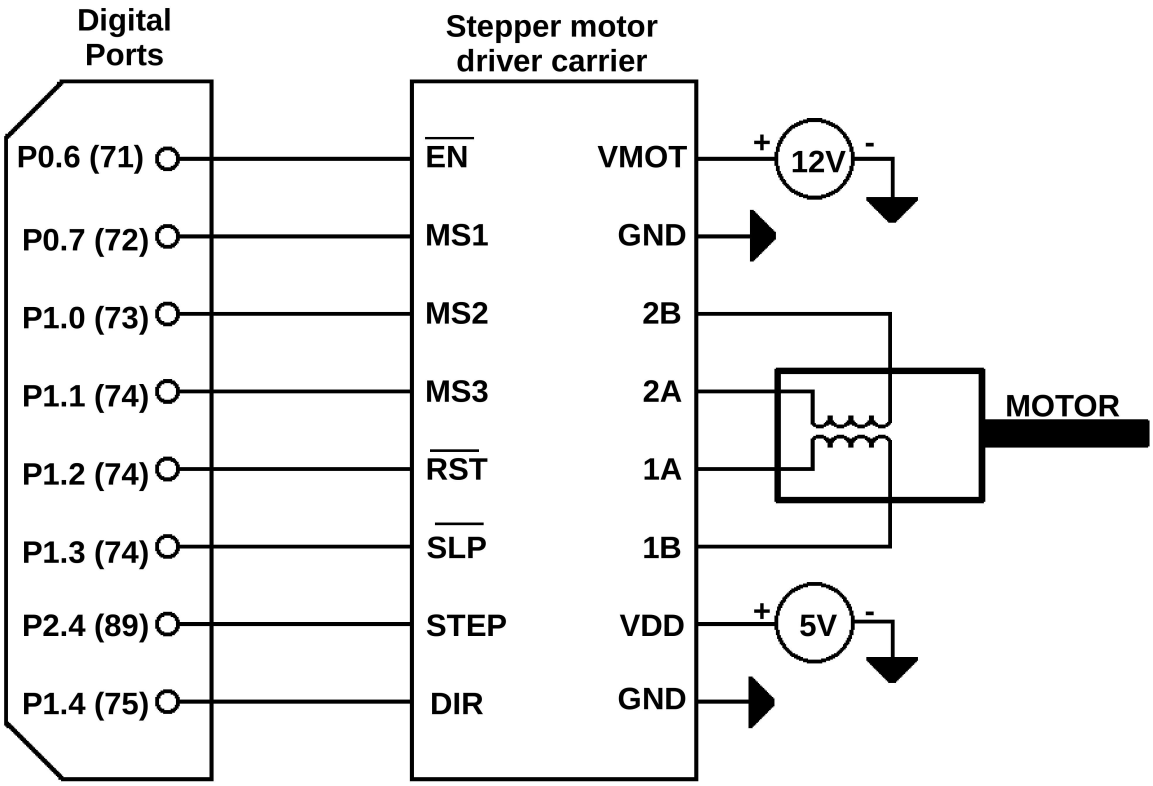

Supplementary Figure 1. Motor driving conceptual schematic. A4988 stepper motor driver carrier chip allows the control of the motor in microstepping mode, minimizing effects of mechanical vibration on the biological sample. The original step size of 0.0031 mm is divided by 16. Voltage regulators has been used for the 5V (UA7805C, Texas Instruments) digital and 12V (LM7812C, Fairchild Semiconductor International Inc) analog supplies. A custom Matlab R2008A routine uses NI USB-6221 DAQ module to change TTL value of DIR pin (setting displacement direction), and send a clock signal to STEP pin (adjusting the motor speed). Detailed descriptions of the A4988 pins are in Supplementary Table 1.

Supplementary Table 1. A4988 stepper motor driver carrier chip pins description.

Pin	Description
EN	Enable. 0 = operation mode / 1 = outputs disabled.
MS1,2,3	Microstep selection. 111 for 1/16th step.
RST	Reset. 0 = reset mode / 1 = operation mode.
SLP	Sleep. 0 = sleep mode / 1 = operation mode. (1ms delay to wake up)
STEP	Step control. Low-to-High = 1 step.
DIR	Direction. 0 = forward / 1 = backward
VMOT	12V analog supply (+12V voltage regulator).
1,2,A,B	Coils of the motor
VDD	5V digital supply (+5V voltage regulator)
GND	Ground

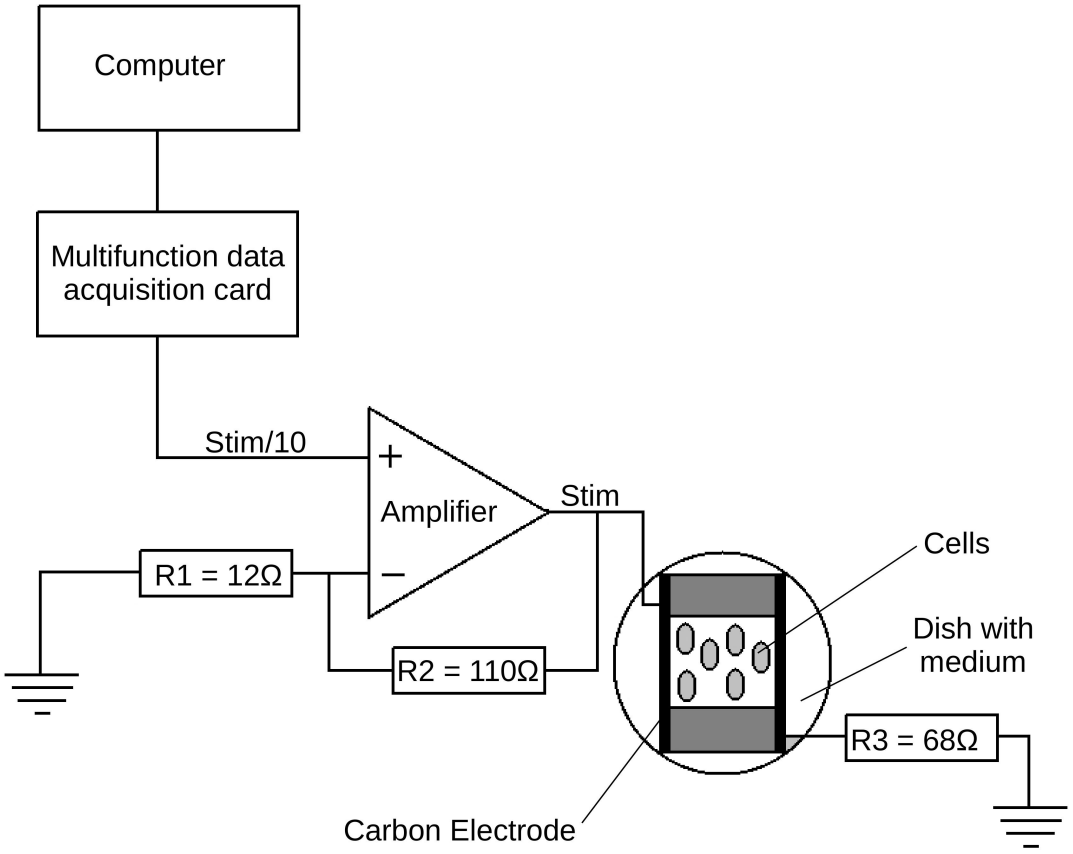

Supplementary Figure 2. Electric field stimulation. A computer-controlled subsystem delivering an electric field has been constructed. The multifunction digital acquisition card NI USB-6221 outputs analog stimulation pulses at 1/10 of target amplitude to bypass its voltage and current limitations. Resistors R1 and R2 are used along with a power amplifier chip (LM675, Texas Instruments) to implement a non-inverting amplifier configuration. The card output voltage (Stim/10) is increased to target level by a gain of 10. The electric field is applied to the cells via a pair of parallel carbon plate electrodes. The system allows voltage amplitude up to 17V. The current is limited to 250 mA by the resistance R3. The controlling software is custom-made in Matlab R2008A.

4.2.3. Characterization of culture membrane deformation

The membrane deformation during uniaxial stretch was characterized to determine the relationship between elongation (in mm) applied to the membrane by the motors displacement and the effective stretch (in %) of the central square culture well. To do so, a digital camera (Dino-Lite, 5 megapixels, AnMo Electronics Corp) was used to take 19 top view pictures of the membrane with different levels of elongation (0 to 9 mm, with a step of 0.5 mm).

Each picture of a series was processed as follows:

(1) conversion from RGB to grayscale;

(2) contrast increase – 1% of image data is saturated at low and high intensities;

(3) offset removal – the average intensity of the image data is subtracted to the intensity of each pixel;

(4) absolute value – each pixel value is replaced with its absolute value;

(5) Prewitt filtering – to detect the edges of the well;

(6) Gaussian filtering (window of 15 × 15 pixels, standard deviation of 1) – to smooth out spatial heterogeneities.

Fig. 1c,d shows the processed images used to detect the borders of the culture well for the first (Δ = 0 mm) and last elongation (Δ = 9 mm). The direction of stretch corresponds to vertical y-axis, while the direction of stretch-induced contraction can be observed in horizontal x-axis.

Each of the vertical lines of Fig. 1e is the result of the horizontal summation of all pixel intensities for each image obtained at different elongation; the points with the highest intensities (closest to 1) are the edges in the elongation direction and allow the calculation of the culture well length. Correspondingly, each of the vertical line of Fig. 1f is the result of the vertical summation of all pixel intensities for each image obtained at different elongation; the points with the highest values are the edges in the contraction direction and allow the calculation of the culture well width. Stretch and contraction amplitude were estimated from the lines in Fig. 1e and Fig. 1f, and are normalized to the dimensions measured at Δ = 0 mm. The linear relationship between stretch and stretch-induced contraction are shown in Fig. 1g,h. Linear regression (solid lines) demonstrates that an elongation of 3.2 mm is required to obtain 20% stretch, which also corresponds to an orthogonal stretch-induced contraction of 5.8%.

4.2.4. Cell isolation

All animal handling procedures were concordant with the Canadian Council on Animal Care guidelines and were approved by the Montreal Heart Institute Animal Research Ethics Committee. Sprague-Dawley rats aged 1–3 days were sacrificed by decapitation. Beating hearts

were removed immediately and kept in cold Ca^{2+}- and Mg^{2+}-free Hank's balanced salt solution. Ventricular muscle was excised and tissue was minced on ice into 1–3mm pieces. The mixture was subjected to purified enzymatic digestion using a Neonatal Cardiomyocytes Isolation System (Worthington Biochemical). Isolated cells (enriched cardiomyocytes) were counted at a density of 3×10^6 cells/mL.

4.2.5. Cell culture

After isolation, cells were plated at a density of ~68000 cells per membrane fibronectin-coated well. Cells were grown in an incubator (37 °C, 5% CO_2) for 5 days in phenol-free Dulbecco's modified Eagle's medium (DMEM, 319-050-CL, Wisent, St-Bruno, Canada) with 1% penicillin/streptomycin (P/S, 450-201-EL, Wisent) and 10% foetal bovine serum (FBS, SH30396.03, Fisher Scientific).

4.2.6. Optical mapping

The fast responding membrane potential dye Di-8-ANEPPS (61012(BT), Biotium Inc) was used to stain the cells for fluorescence imaging experiments. To prepare the solution, 5 mg of Di-8-ANEPPS was dissolved in 5 mL of pure DMSO (Dimethyl sulfoxide). A 20% solution of pluronic acid (F-127, ThermoFisher Scientific) in pure DMSO was also prepared. Then 45µL of the dissolved dye and 2.5 µL of pluronic acid were added to 5 mL of DMEM (with neither

FBS nor P/S). Cultured monolayers were loaded with 45 µL/well of staining DMEM-dye-pluronic solution and incubated for 25 min. The dye was then washed out with DMEM and replaced with fresh DMEM (with neither FBS nor P/S). Removal of P/S is important as it has been shown to block stretch-activated channels [34]. Mapping experiments were performed with a homemade setup (Supplementary Fig. 3) based on a high-speed EMCCD camera system (iXon3 860, 128 × 128 pixels, Andor Technology Ltd).

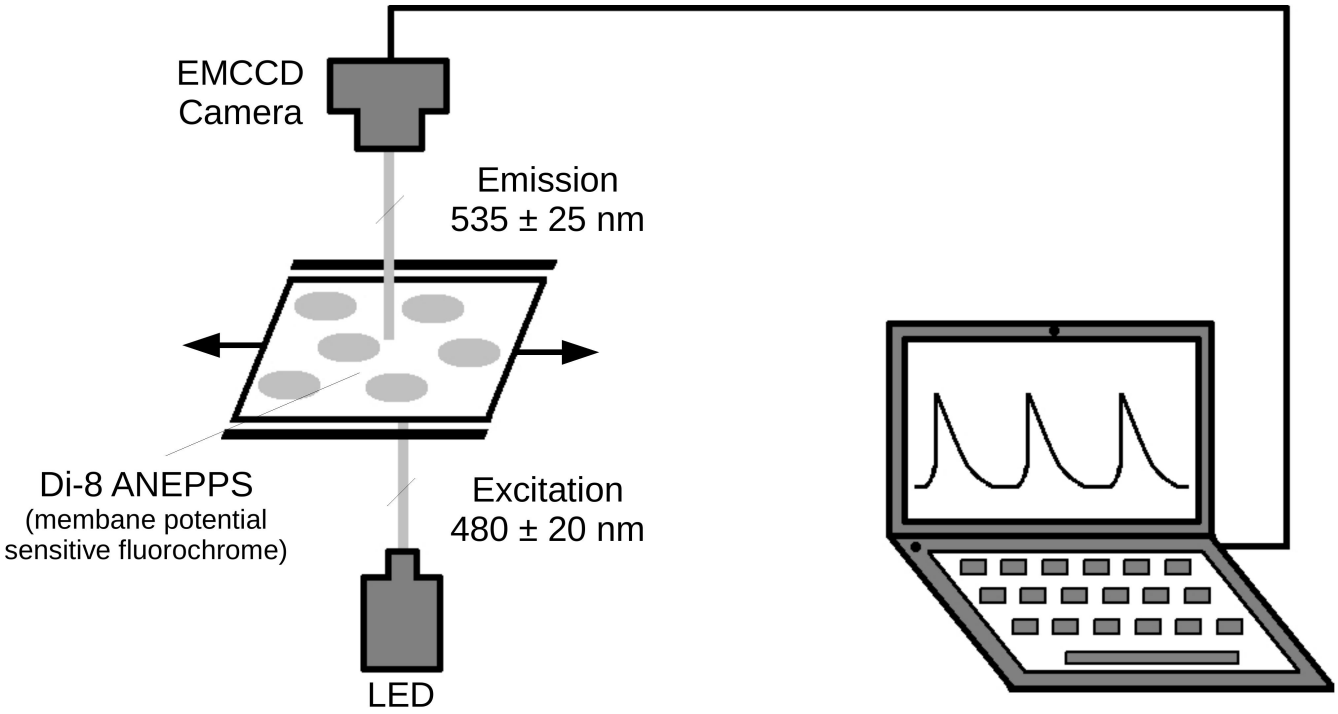

Supplementary Figure 3. Conceptual overview of the experimental setup. The 2 black arrows represent uniaxial stretch of the biological pacemaker patch. The 2 parallel black solid lines on both sides of the patch in the orthogonal direction to stretch represent electric field stimulation. The cells (gray spots) are loaded with Di-8-ANEAPS and stretch is applied with or without electric field stimulation. The dye is excited with a LED whose wavelength spectrum is constraint by a bandpass optical filter (480 ± 20 nm). The emission light from the cardiomyocytes is recorded with a EMCCD camera whose field of view is protected from

undesirable light noise with another bandpass optical filter (535 ± 25 nm).

The dye was excited with a LED (M505F1, Thorlabs). The bandpass filters used for excitation and emission were $\lambda_{excitation} \approx 480 \pm 20$ nm (Chroma Technology) and $\lambda_{emission} \approx 535 \pm 25$ nm (Semrock), respectively. The system was set (lenses and distance adjustments) to have a pixel size of ~0.096 mm yielding a field of view of 12.24x12.24 mm². The acquisition frame rate was 512 Hz for all experiments.

4.2.7. Experimental protocol

A visual summary of the protocol can be found as supplementary Fig. 4.

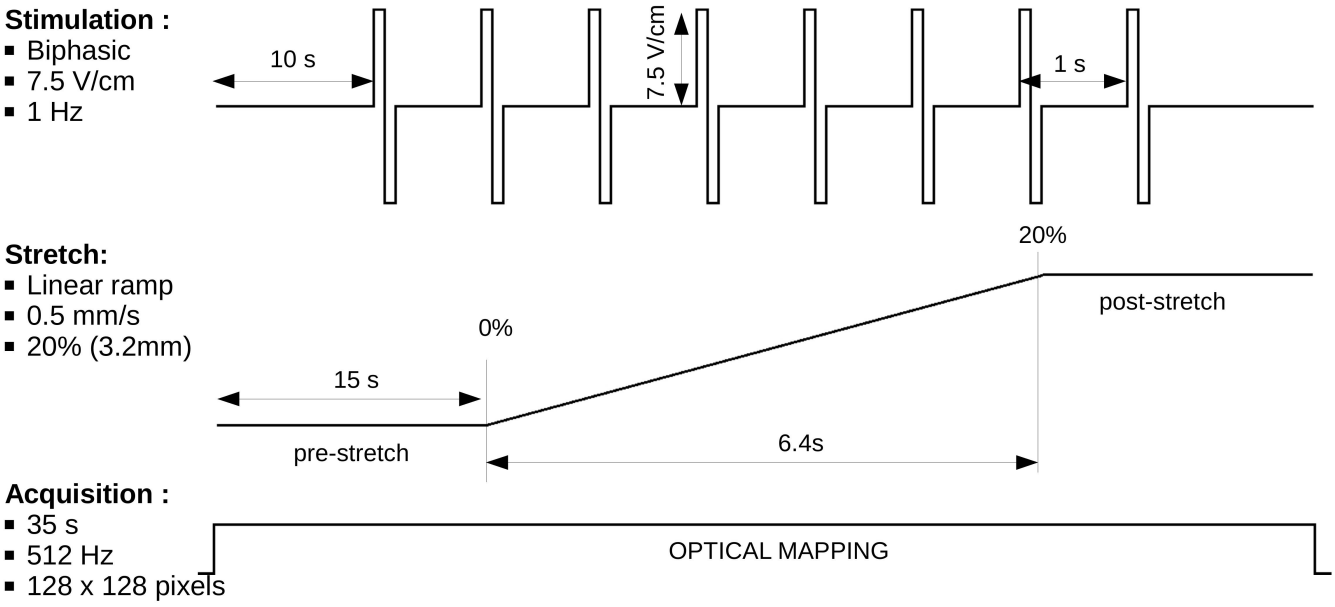

Supplementary Figure 4. Although available protocols are flexible, specific ones are applied in this project. All acquisitions last 35 s and have a sampling rate of 512 Hz. The stretch protocol follows a ramp : after a delay of 15 s, 3.2 mm elongation (20% stretch) is gradually

applied at constant speed (0.5mm/s), and then the stretch state is maintained until the end of acquisition. When required, electric field biphasic stimulation (7.5V/cm amplitude, 5 ms pulse width, and 1 Hz frequency) is applied after a delay of 10 s, and lasts 15 s.

Data were recorded during pre-stretch and post-stretch phases. Acquisition duration was set to 35 s. Elongation of 3.2 mm (20% stretch) was applied after a delay of 15 s, at a constant speed of 0.5 mm/s over a period of 6.4 s. A stretch of 20% was chosen as it has been widely used in the litterature [35], [36]. The elongation was then held until the end of acquisition (remaining 13.6 s). Electrical stimulation, when applied, was biphasic to minimize charge accumulation near the electrodes, with a 7.5 V/cm amplitude, 5 ms pulse width, and 1 Hz frequency. It was started after a delay of 10 s after the beginning of acquisition and lasted 15 s.

Every membrane with cultured cardiomyocytes underwent 6 sequential data acquisition protocols as follows: (1) free running acquisition; (2) stretch; (3) unstretch; (4) electrical stimulation; (5) stretch with electrical stimulation; (6) unstretch with electrical stimulation. Detailed procedures and rationales are presented in Supplementary Table 2.

Supplementary Table 2. Experimental protocols: description and rationales. Detailed description of each experimental protocol are presented with their corresponding rationales.

Protocol	Description	Rationales
Auto	* free running acquisition for 35s	* assess intrinsic variability of the biopacemaker * assess electrophysiological effect of fluorochromes (compare cycle lengths with videomicroscopy and fluorochrome) * assess effect of substrate stiffness
Stretch	* start acquisition * wait 15s delay before stretch * apply 3.2 mm stretch at 0.5 mm/s (6.4 s duration) * stop acquisition after 35 s	* assess effect of stretch on automaticity (autonomous rhythm and spatial characteristics of electrical activations)
Unstretch	* start acquisition * wait 15s delay before reverse stretch * apply 3.2 mm reverse stretch at 0.5 mm/s (6.4 s duration) * stop acquisition after 35 s	* assess if stretch and reverse stretch follow the same electrophysiological path (linearity? hysteresis? memory?)
Electrical stimulation	* start acquisition * wait 10s delay before stimulation * apply stimulation (amplitude 7.5 V/cm, frequency 1Hz, pulse duration 5 ms, stimulation duration 15 s) * stop acquisition after 35 s	* assess stimulation thresholds * assess maximum capture rate
Unstretch + Electrical stimulation	* start acquisition * apply 15 s electrical stimulation after 10 s delay * apply previously described stretch after 15 s delay * stop acquisition after 35 s	* assess effect of stretch on post-stimulation recovery time * assess effect of stretch on action potential morphology (ex.: action potential durations)
Unstretch + Electrical stimulation	* start acquisition * apply 15 s electrical stimulation after 10 s delay * apply previously described reverse stretch after 15 s delay * stop acquisition after 35 s	* assess if stretch and relax follow the same electrophysiological path (linearity? hysteresis? memory?)

4.2.8. Data Analysis and calculation of variables

A custom software was implemented in Matlab. Two-dimensional matrix of pixels at every time point was first spatially filtered (gaussian lowpass filter, window of 7 × 7 pixels, standard deviation of 2.5) [37]. Temporal filtering was then applied using a 5-sample bidirectional window moving average.

After the filtering process, a mask was applied to exclude the pixels without action potentials (APs). Baseline wandering was first corrected by removing very low frequency ([0 – 0.5 Hz]) components of the signal. Then composite discrimination value for each pixel was calculated using the following equation:

$$Discrimination\ value = A \times S \times P \times C \quad (1)$$

A: relative amplitude of the pixel signal (A = maximum value – minimum value)

S: standard deviation of the pixel signal

P: maximum power of the pixel signal frequency spectrum (the spectrum is calculated using fast Fourier transform)

C: area under the pixel signal curve

The highest value of each component of the equation is found when the signal has APs instead of background noise.

A typical discrimination map of all 128×128 pixels is shown in Fig. 3a with their corresponding value depicted as a grayscale (black: highest score, white: lowest score).

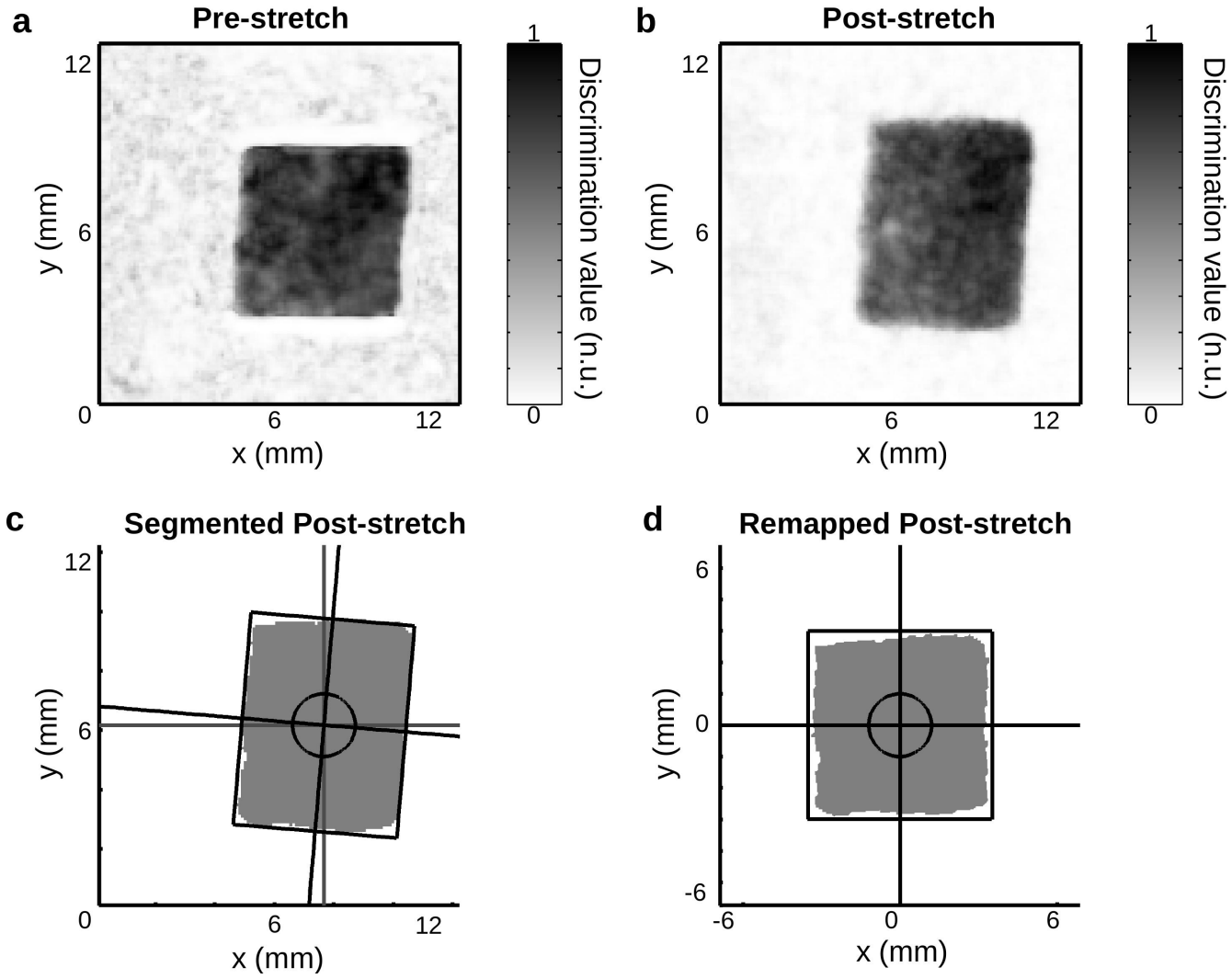

Figure 3. Remapping algorithm. a, Discrimination map before stretch. Pixels with action potentials have much higher score than background noise. **b,** Discrimination map after stretch. **c,** Contour, centroid, and deviation angle detection. The gray area is obtained with Chen-Vese contour detecting algorithm, and is fitted with a rectangle to approximate the culture well border. The centroid (black circle) of the rectangle is the origin of the stretcher device coordinates system (in black). A $\theta = 4.76^{o}$ deviation (for this sample) is estimated with respect to the camera coordinates system (dark gray). **d,** Outcome of the remapping algorithm. The stretcher device coordinates system is straight. The centroid is translated to (0,0). And the map is rescaled (20% vertically and 5.8% horizontally) according a rigid affine transformation to fit pre-stretch proportions. Contrary to post-stretch, pre-stretch maps are not rescaled, but undergoes coordinates straightening and centroid translation to (0,0) as well.

For each AP, the activation time (t_{act}) was identified at the maximum fluorescence change (|*dF/dt*|). The activation map for the ith beat was defined as $M_{tact,i}$ and consisted of estimated activation times at each pixel of the mask. A set of calculations was performed based on the series of activation maps.

* Normalized activation times map for the ith beat ($M_{ntact,i}$ in ms) was obtained when the minimum activation time was subtracted to the activation map:

$$M_{ntact,i} = M_{tact,i} - \min[M_{tact,i}] \tag{2}$$

* Spontaneous cycle length map for the ith beat ($\Delta M_{tact,i}$ in ms) was the map of difference between two sequential activation times maps:

$$\Delta M_{tact,i} = M_{tact,i} - M_{tact,i-1} \tag{3}$$

The spontaneous cycle length for the ith beat ($\Delta t_{act,i}$ in ms) was the median of the corresponding map:

$$\Delta t_{act,i} = \text{median}[\Delta M_{tact,i}] \tag{4}$$

Given N, the number of beats in the recording time window, the average cycle length $\overline{\Delta t}_{act}$ for all beats was defined as:

$$\overline{\Delta t}_{act} = \frac{1}{N-1}\sum_{i=2}^{N} \text{median}[\Delta M_{tact,i}] \tag{5}$$

* Recovery times map ($M_{\tau rec}$ in ms) characterizes the robustness of spontaneous activity. It was estimated by evaluating the time needed for spontaneous activity to resume following electrical stimulation. A matrix of local recovery times corresponded to the time between last stimulated activation and the first spontaneous activation that followed. Therefore:

$$M_{\tau rec} = \max[M_{tact,\,spontaneous}] - \min[M_{tact,\,stimulated}] \tag{6}$$

The recovery time value for a given sample was:

$$\tau_{rec} = \text{median}[M_{\tau rec}] \tag{7}$$

* Synchronization times map for the i[th] beat ($M_{\tau sync,i}$ in s/cm) was a measure of local activation delay and was used as a surrogate to evaluate synchronicity. Synchronized activation would lead to activation delay close to zero. It was calculated as the inverse of the "conduction velocity" according to a previously described method [38] based on the spatial gradient of $M_{tact,i}$. The average synchronization time $\bar{\tau}_{sync}$ for the sample was:

$$\bar{\tau}_{sync} = \frac{1}{N-1}\sum_{i=2}^{N} \text{median}[M_{\tau\, sync,\,i}] \tag{8}$$

* Spontaneous cycle length's beat-to-beat variability (CL_{bbv} in ms) was the interbeat difference between cycle lengths and assessed how cycle lengths changed from one beat to another. The average value was given by:

$$\overline{CL}_{bbv} = \frac{1}{N-2}\sum_{i=3}^{N} \left(\text{median}[\Delta M_{tact,\,i}] - \text{median}[\Delta M_{tact,\,i-1}]\right) \tag{9}$$

* Activation pattern variability (AP_{bbv} in ms) characterized stability of activation pattern and was the average interbeat normalized activation pattern difference. For all beats:

$$\overline{AP}_{bbv} = \frac{1}{N-1}\sum_{i=2}^{N} \text{mean}[M_{ntact,\,i} - M_{ntact,\,i-1}] \tag{10}$$

* Focal position's beat-to-beat variability (FP_{bbv} in mm) evaluated spatial stability of the focal site. The position changes of the first initiation site (centroid of pixel clusters representing the 1[st] percentile of activation times for a given beat) was calculated based on the Euclidean

distance on a beat-to-beat basis. The average was thus calculated with eq. (11):

$$\overline{FP}_{bbv} = \frac{1}{N-1} \sum_{i=2}^{N} \sqrt{\left(x_{focus,i} - x_{focus,i-1}\right)^2 + \left(y_{focus,i} - y_{focus,i-1}\right)^2} \quad (11)$$

4.2.9. Remapping stretched to non-stretched culture well

Remapping the post-stretch maps to pre-stretch positions allowed direct pre- vs. post-stretch spatial comparison, otherwise impossible because of the stretch-induced deformation. The complete process is illustrated in Fig. 3. The Chen-Vese [39] image segmentation method was used to determine the contour of the mask (described in Section 4.2.8). The area corresponding to the mask was then fitted with a rectangle. The angle (θ) between the camera axis and elongation axis of the stretcher system was estimated from the rectangle fit (see Supplementary Fig. 5). Maps were rotated (if $\theta \neq 0^{o}$) and centered based on the fitted rectangle centroid.

Following the linear relationships shown in Fig. 1g,h, the culture well was assumed to have undergone a rigid affine transformation from pre-stretch to post-stretch state as estimated in Section 4.2.3: 20% elongation in the direction of stretch and 5.8% contraction in the direction that was orthogonal to stretch, when the membrane underwent 3.2 mm elongation. These values were applied to the post-stretch coordinates, to remap them to the pre-stretch coordinates.

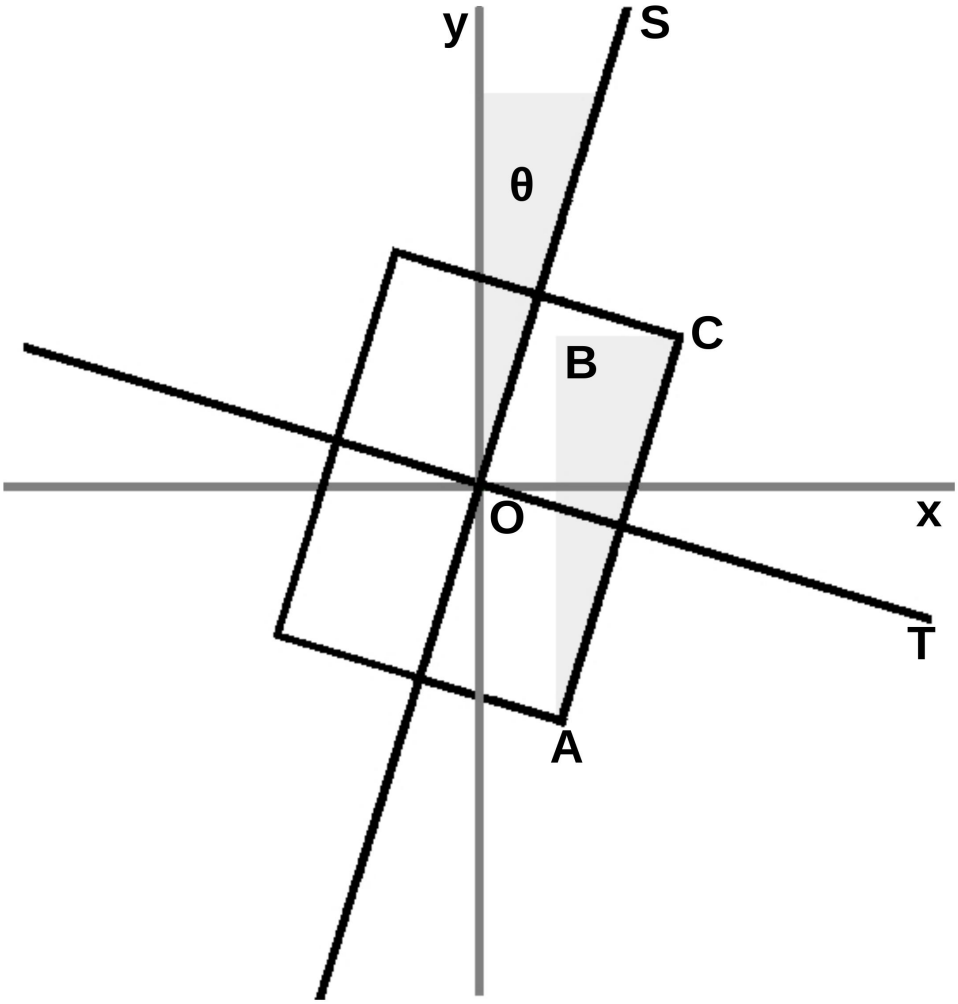

Supplementary Figure 5. Calculation of the deviation angle of the stretcher device frame regarding the recording camera frame. The frame SOT of the stretch device (black) may not be strictly aligned with the frame xOy of the camera (gray). The deviation angle θ = SÔy (light gray) is calculated with the side of the well (black rectangle) which is parallel to the stretch axis OS. ABC is a right triangle because AB is the projection of AC over Oy axis. According to euclidean geometry, SÔy is equal to BÂC since Oy and OS are parallel to AB and AC respectively. BÂC is calculated with basic trigonometry as sin-1(AB/AC). Therefore, the deviation angle is θ = SÔy = BÂC = $\sin^{-1}$(AB/AC).

Cubic interpolation was used to reconstruct the 128×128 activation maps regarding the realigned and stretch-based remapped coordinate system. Then all space-related variables

(AP_{bbv}, FP_{bbv}, and τ_{sync}) were recalculated using the reconstructed activation maps, as previously described in Section 4.2.8. Pre-stretch maps were also reconstructed, but only for realignment, i.e. rotation and centroid-based centering. Pre- and post-stretch maps may not totally overlap (see Supplementary Fig. 6) because the mask contour is not exactly the same for both conditions. Due to shadow projections of the culture well sides, some pixels selected at the border by the mask in pre-stretch may not have been selected in post-stretch and *vice versa*.

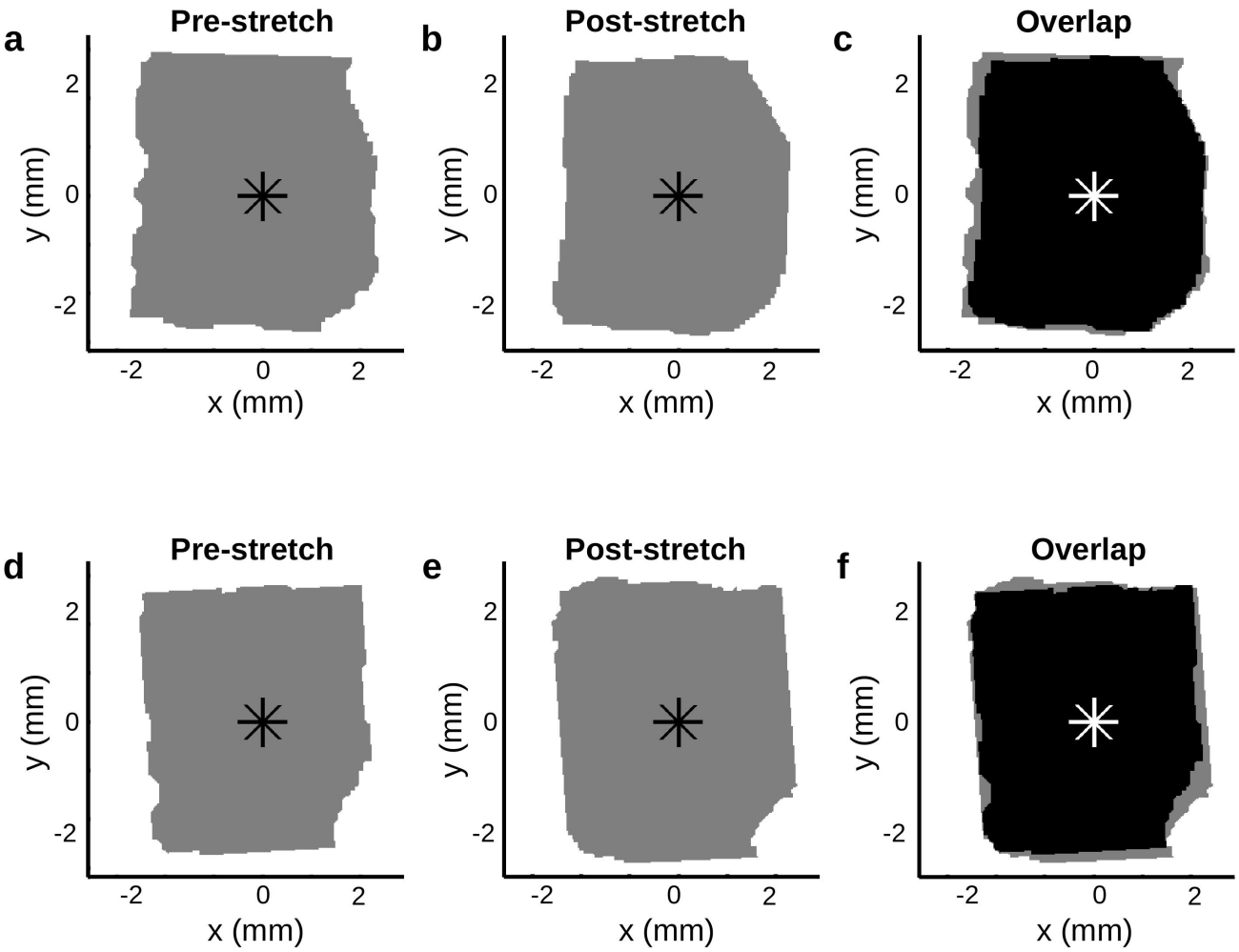

Supplementary Figure 6. Remapping algorithm validation. a,d, Left panels show the area occupied by activation map in pre-stretch for 2 samples. Stars are centroids.. **b,e,** Middle panels

display the area occupied by activation map in post-stretch, after remapping, for the same 2 samples. **c,f,** Overlap of pre- and post-stretch. Black surface exposes the common areas.

4.3. Results

The proposed evaluation method and system was used to show the interests of the approach on evaluating MEF effects on monolayer spatial-temporal spontaneous activity. A set of 14 membranes has been studied using the 6-step acquisition protocol described in Section 4.2.7.

4.3.1. Occurrence of spontaneous activity

According to the experimental protocol (see Supplementary Fig. 4), the pre-stretch and post-stretch recording time windows were respectively [0 s – 15 s] and [21.4 s – 35 s], while constant velocity elongation occurred during the [15 s – 21.4 s] window. A sample was said to be active in pre-stretch or post-stretch if at least two APs were detected within the pre-stretch or post-stretch acquisition window. In pre-stretch, 8 samples were active and 6 samples were inactive. Interestingly, all 14 samples were active in post-stretch, which was a 75% increase compared to pre-stretch level. 20% stretch significantly increased the occurrence of spontaneous activity (Fisher exact test: $p < 0.05$ when comparing pre-stretch vs. post-stretch). Details can be found in Supplementary Table 3.

Supplementary Table 3. Fisher test on occurrence of spontaneous activity pre-stretch vs. post-stretch. A sample is active if there are at least 2 action potentials during the recording time window. The sample is inactive if there is 1 or no action potential during the recording. There is a significant difference ($p < 0.05$) in pre-stretch/post-stretch ratio between active and inactive samples, i.e. the higher number of active samples in post-stretch is effectively due to the applied 20% stretch.

	Pre-stretch	**Post-stretch**	Marginal row totals
Active	8	14	22
Inactive	6	0	6
Marginal column totals	14	14	28 (grand total)
The Fisher exact test statistic value is 0.016. The result is significant at $p < 0.05$			

4.3.2. Time-dependent effects of stretch

An optical trace of APs is shown in Fig. 4a with the pre-stretch, stretching and post-stretch windows. A clear decrease of cycle length Δt_{act} in post-stretch compared to pre-stretch state was found. The exact values of Δt_{act} are illustrated in Fig. 4c. The locations of post-stimulation recovery times τ_{rec} without and with stretch are illustrated in Fig. 4b,d, for one sample. Fig. 4e shows $\overline{\Delta t_{act}}$ for all 8 samples that were active in pre-stretch along with post-strech, and there was a significant decrease in $\overline{\Delta t_{act}}$ from 3916±899 ms to 1469±213 ms with 20% stretch (Kruskal-Wallis test: $p = 0.0117$, $n=8$). Results shown in Fig. 4e demonstrates that the chronotropic response due to stretch was inversely proportional to $\overline{\Delta t_{act}}$ in pre-stretch. The beat-to-beat variability of cycle length $\overline{CL_{bbv}}$ in Fig. 4g was significantly decreased from 590±216 ms to 111±39 ms with 20% stretch (Kruskal-Wallis test: $p = 0.0372$, $n=7$). The recovery time (Fig. 4h) τ_{rec} without and with 20% stretch was significantly decreased from 2345±293 ms to 1202±72 ms (Kruskal-Wallis test: $p = 0.0209$, $n=4$).

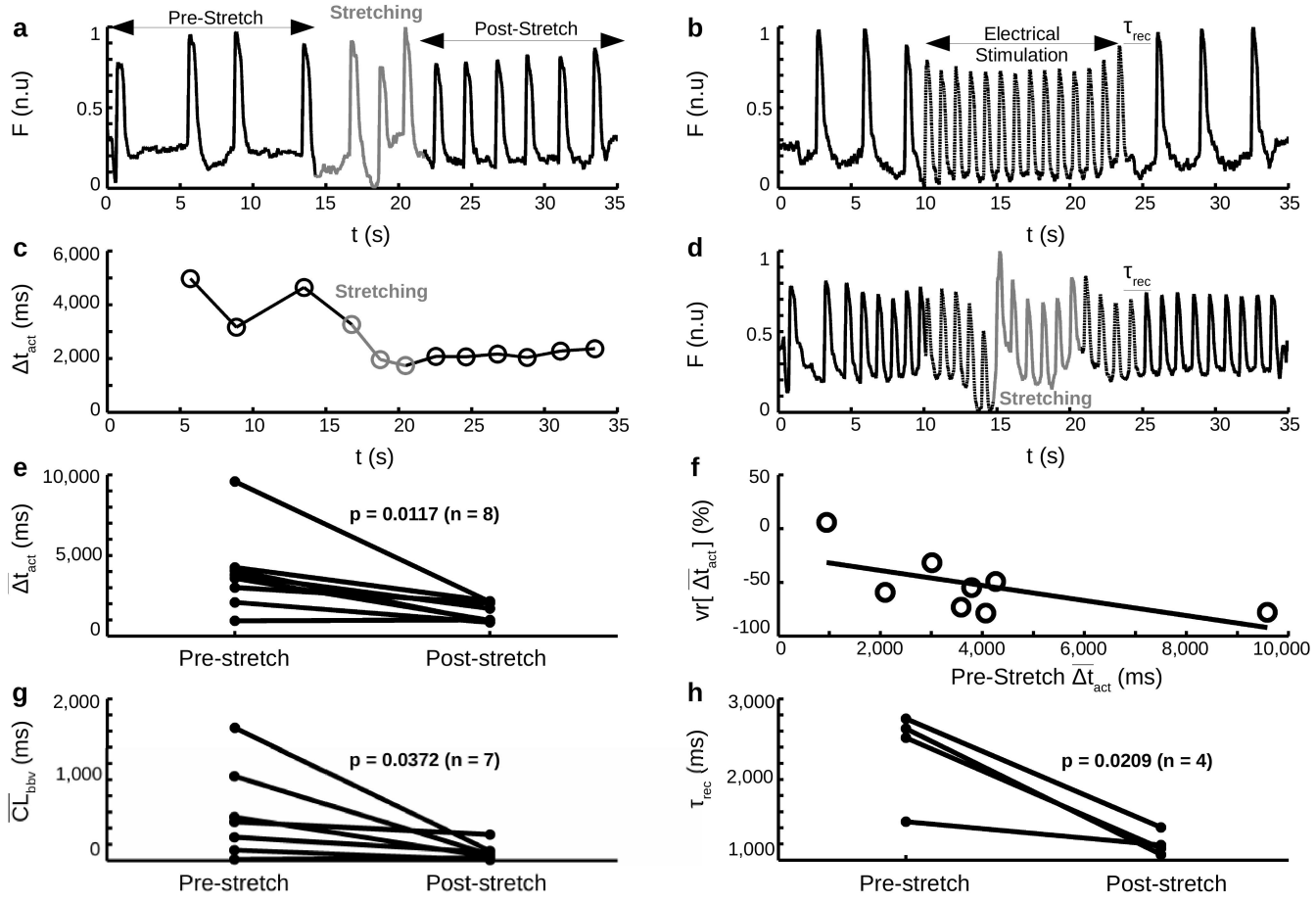

Figure 4. Time-dependent effects of stretch. a,c, Optical trace of APs and the corresponding series of cycle lengths. The gray section highlights the time window inside which stretch movement occurs. Thus pre-stretch state is before the gray section and post-stretch state after. An important decrease is observed both in cycle length (Δt_{act}) and beat-to-beat variability of cycle lengths ($\overline{CL}_{bbv}$). b,d, electrical stimulation with 1 Hz frequency is applied during the dashed section of the APs trace. Post-stimulation recovery time (τ_{rec}) is defined as the time interval between the last stimulation-induced AP and the first following autonomous AP. A decrease in recovery time with stretch is observed. e, For 8 samples active both in pre- and post-stretch, $\overline{\Delta t}_{act}$ usually decreases (7 out of 8 samples) in post-stretch compared to pre-stretch. Indeed, $\overline{\Delta t}_{act}$ decreases significantly with stretch (Kruskal-Wallis test: p = 0.0117, n=8). Each

dot corresponds to equation (5). f, Percentage variations (empty dots) of Δt_{act} in post-stretch compared to pre-stretch are plotted vs. Δt_{act} in pre-stretch. Linear regression (solid line) shows that the chronotropic response in post-stretch is inversely proportional to Δt_{act} in pre-stretch. g, $\overline{CL}_{bbv}$ is usually smaller in post-stretch (6 out of 7 samples), i.e. application of stretch may stabilize Δt_{act}. As a matter of fact, $\overline{CL}_{bbv}$ significantly decreases with stretch (Kruskal-Wallis test: $p = 0.0372$, $n=7$). Each dot corresponds to equation (9). h, Stretch also induces decrease of τ_{rec} for all 4 samples, and the observed decrease is significant (Kruskal-Wallis test: $p = 0.0209$, $n=4$). Each dot corresponds to equation (7). The number of samples varies because results are available only when calculations are application. For instance, 4 samples displayed post-stimulation spontaneous activity both in pre- and post-stretch; so τ_{rec} calculations are applicable only for those 4 samples.

4.3.3. Spatial effects of stretch

We defined the focal site or focus as the spatial position of the first initiation site of a spontaneous activation. The focus position or focal site activity might be stable or might change on a beat-to-beat basis. Changes between foci over time (termed here as focal switch) is a hallmark of spatiotemporal instability [30]. An example of spatiotemporal dynamics is shown in Fig. 5. The optical trace of APs in Fig. 5a clearly shows longer Δt_{acts} and temporal instability in pre-stretch followed by shorter Δt_{acts} and more stable activity in post-stretch. A series of nine beats were labeled with Roman numbers on the trace, with the corresponding grayscale activation times maps in Fig. 5b (darkest spot corresponds to focal site). Pre-stretch beats had a stable focus in the middle-right portion of the culture.

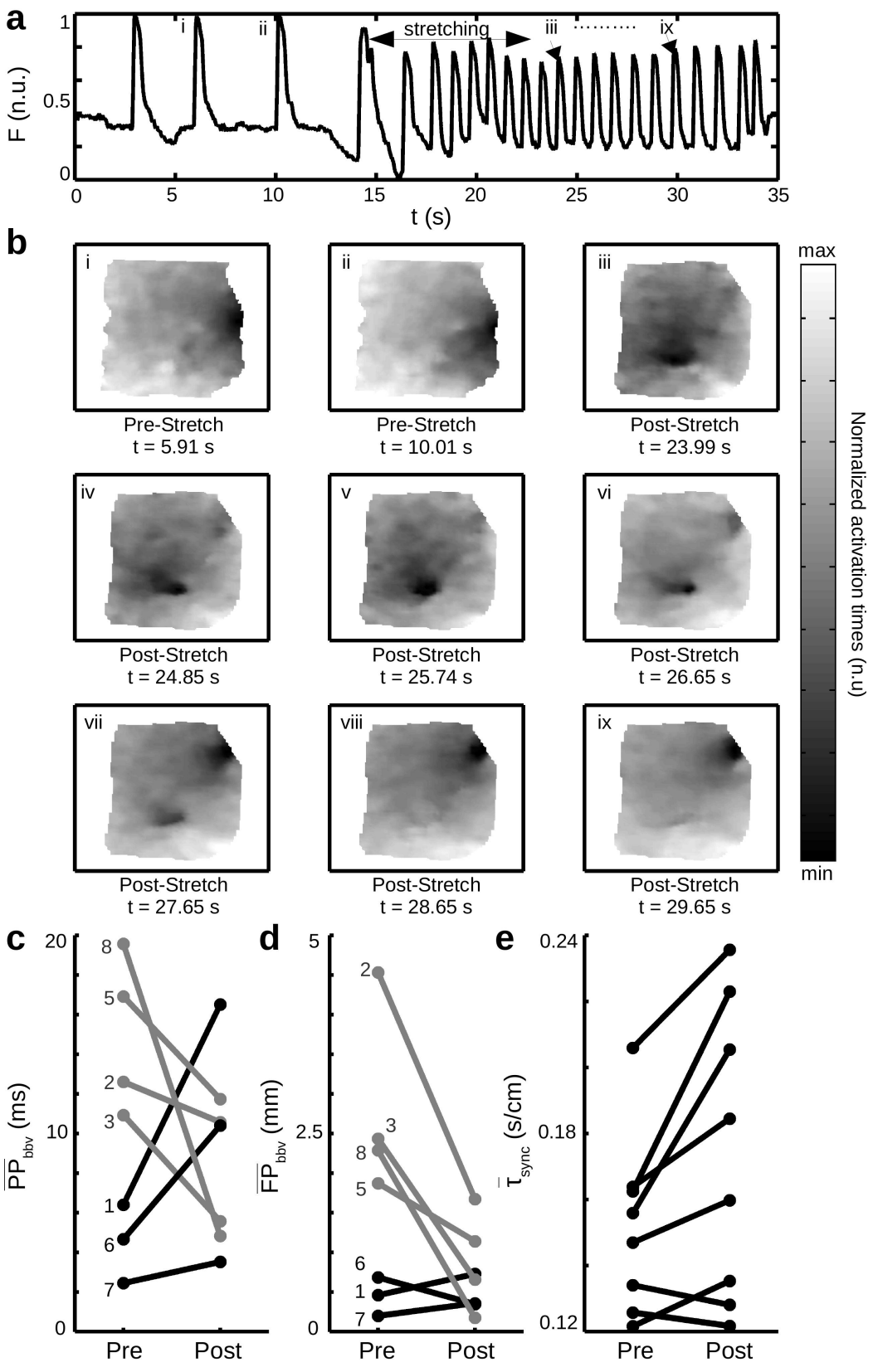

Figure 5. Spatial effect of stretch. a, Optical trace of APs. A series of 9 beats are labeled in

roman numbers. **b,** Series of 9 activation maps related to the 9 labeled beats. Foci are the darkest spots and the corresponding times are written at the bottom of each map. The first 2 activations belong to pre-stretch, and the remaining to post-stretch. Focal switch happens during the transition from pre- to post-stretch (ii to iii), and once again during post-stretch time window (vi to viii). **c,** Activation pattern beat-to-beat variability $\overline{AP}_{bbv}$ is displayed for pre-stretch and post-stretch. When samples are unstable in pre-stretch (gray), i.e. display at least 1 focal switch, stretch significantly decreases $\overline{AP}_{bbv}$ (Kruskal-Wallis test: p = 0.0433, n=4). Conversely, when samples are already stable in pre-stretch (black), changes in post-stretch weren't significant. Each dot is related to equation (10). **d,** Focal position beat-to-beat variability $\overline{FP}_{bbv}$: pre-stretch vs. post-stretch. When samples are unstable in pre-stretch (gray), stretch significantly decreases $\overline{FP}_{bbv}$ (Kruskal-Wallis test: p = 0.0209, n=4). When samples are already stable in pre-stretch, no significant changes were observed in post-stretch. Each dot is related to equation (11). **e,** Synchronization times $\bar{\tau}_{sync}$, significantly increases with stretch, independently of stability (Kruskal-Wallis test: p =0.0391, n=8). Each dot is related to equation (8). All post-stretch values are obtained after remapping. The number of samples varies from panel to panel because results are available only when calculations are applicable. The number of samples varies because results are available only when calculations are application. For instance, sample 4 didn't have enough beats in pre-stretch to perform $\overline{AP}_{bbv}$ and $\overline{FP}_{bbv}$ calculations: 2 instead of the minimum of 3.

Stretching the membrane led to a switch of focus to the center of the culture for four beats. In the 4th beat in post-stretch (labeled vi), a top-right focus started to appear (black region in the map that co-exists with the center focus). Two foci were seen on the beat labeled vii, with following beats only showing the top-right single focus.

All focal events for all 8 samples that show spontaneous activity both in pre-stretch and post-stretch are summarized in Table 1.

Table 1. Focal events. A focal site is the first initiation site of electrical activation. A focal switch happens when the position of the focal changes between activations. For the 8 samples active both in pre-stretch and post-stretch, the number of focal sites occuring during pre-stretch and post-stretch varies between 1 and 3. The number of focal switches is highly variable, ranging from no switch (# focal switches = 0) to a maximum of 3 switches. There usually is a focal switch (yes) during the transition, i.e. from the last activation of pre-stretch to the first activation of post-stretch (5 out of 8 samples).

	# Focal site		**# Focal switches**	
Sample #	during pre-stretch	during post-stretch	during pre-stretch (nb of APs)	during post-stretch (nb of APs)
1	1	2	0 (3)	1 (12)
2	3	2	3 (4)	3 (7)
3	2	3	2 (4)	3 (15)
4	1	1	0 (2)	0 (6)
5	2	2	3 (5)	1 (6)
6	1	2	0 (14)	1 (15)
7	1	1	0 (4)	0 (8)
8	3	1	3 (6)	0 (12)

Samples demonstrated high variability in the number of foci and focal switches: (1) 25% of samples had no focal switch before or after stretch, (2) 25% of samples went from no focal switch in pre-stretch to at least one focal switch in post-stretch, (3) 12.5% of samples went from at least 1 focal switch in pre-stretch to no focal switch in post-stretch, (4) and 37.5% had variable numbers of focal switches in pre-stretch and post-stretch. To evaluate if stretch changed spatial stability, we first defined the density of focal switches as:

$$Density_{switch} = \frac{\#\text{ focal switches}}{\#\text{ interval between APs}} = \frac{\#\text{ focal switches}}{\#\text{ APs - 1}} \quad (12)$$

Then we compared pre-stretch vs. post-stretch dynamics for samples showing spatial instability in pre-stretch, i.e. samples having at least one focal switch in pre-stretch (n = 4; samples 2, 3, 5, 8 in Table 1). We found that on average the density of focal switch in pre-stretch (0.75±0.09) was significantly higher compared to post-stretch condition (0.23±0.10) (Kruskal-Wallis test: p = 0.0209, n = 4). This result means that 20% stretch decreased spatial instability of focal events, when pre-stretch activity is unstable. Changes of densities were not significant when samples were already stable in pre-stretch (Kruskal-Wallis test: p = 0.1306, n=4).

$\overline{AP}_{bbv}$ in pre-stretch vs. post-stretch after remapping is displayed in Fig. 5c. Pre-stretch condition was compared to post-stretch for samples showing spatial instability in pre-stretch (gray samples in Fig. 5c). $\overline{AP}_{bbv}$ in pre-stretch 15.0±2.0 ms was significantly higher compared to post-stretch condition 8.2±1.7 ms (Kruskal-Wallis test: p = 0.0433, n=4). Therefore, 20% stretch decreased beat-to-beat variability in activation patterns when samples were unstable in pre-stretch. When samples were stable in pre-stretch (black samples in Fig. 5c), $\overline{AP}_{bbv}$ did not change significantly after stretch (Kruskal-Wallis test: p = 0.2752, n = 3). $\overline{AP}_{bbv}$ (Fig. 5c) and focal switches (Table 1) are intimately related, but are not interchangeable. Focal switch is obviously a change of activation pattern but a change of pattern is not necessarily a focal switch. The three lowest $\overline{AP}_{bbv}$ in pre-stretch unsurprisingly corresponded to three samples without focal switch (samples 1, 6, and 7), but having no focal switch did not lead to the same value of $\overline{AP}_{bbv}$. The sharp increase in $\overline{AP}_{bbv}$ of sample 1 from pre-stretch to post-stretch was, unsurprisingly again, related to the situation with no focal switch in pre-stretch and one focal switch in post-stretch. However, in sample 3, pre-stretch condition had higher $\overline{AP}_{bbv}$ despite having less focal switches than in post-stretch. So when a sample exhibit focal switches in the

two conditions, $\overline{AP}_{bbv}$ is able to evaluate changes in activation patterns that could, for example, occur due to partial waveblock. Furthermore, samples 2, 5, 8 in pre-stretch had decreasing densities of focal switch (1, 0.75, and 0.6 respectively), but they had increasing values of $\overline{AP}_{bbv}$. Fig. 1d shows the $\overline{FP}_{bbv}$ in pre-stretch and post-stretch after remapping. When samples were unstable before application of stretch (gray samples in Fig. 1d), $\overline{FP}_{bbv}$ in pre-stretch 2.8±0.6 mm significantly decreased in post-stretch condition 0.9±0.3 mm (Kruskal-Wallis test: p = 0.0209, n=4). So, 20% stretch decreased beat-to-beat variability in focal positions when samples are unstable in pre-stretch. When samples were stable in pre-stretch (black samples in Fig. 1d), $\overline{FP}_{bbv}$ did not change significantly (Kruskal-Wallis test: p = 0.8273, n=4) after stretch.

Fig. 1e presents the synchronization times τ_{sync} for pre-stretch and post-stretch after remapping. On average, an increase of τ_{sync} was found with 0.15±0.01 s/cm in pre-stretch compared to 0.17±0.02 s/cm (Kruskal-Wallis test: p=0.0391, n=8); 6 out of 8 samples had an increased $\bar{\tau}_{sync}$ in post-stretch. Independently of focal stability, 20% stretch increased synchronization times. Interestingly, when the same pre- vs. post-stretch comparison was done without remapping, no significant change was observed (Kruskal-Wallis test: p=0.15, n=8) because $\bar{\tau}_{sync}$ was systematically underestimated (0.165±0.014 s/cm) because of increased post-stretch dimension. In fact, assuming no change in cell to cell activation delay by stretch (same activation pattern), the total delay for all cells to activate would be the same. With the increased dimension induced by stretch, the synchronization time should decrease because it would take the same time to activate a larger distance (in the direction of stretch). Remapping was remarkably useful to isolate effects of stretch from effects of purely increased dimension.

4.3.4. Focusing on the transition from pre-stretch to post-stretch

In order to focus on the most acute effects of 20% stretch, the last activation in pre-stretch state was compared to the first activation in post-stretch after remapping. These activations were happening right before and right after the stretching phase (see Fig. 4a) and are thus separated in time by the duration of the movement to get to the 20% stretch amplitude. The data are presented in Table 2.

Table 2. Transition from pre-stretch to post-stretch with 20% stretch at a rate of 3.72%/s. The last activation in pre-stretch is compared with the first activation in post-stretch after remapping, for the 8 samples active before and after stretch. Stretch usually leads to smaller cycle length (negative value of percentage variation vr[Δt_{act}] for 7 out of 8 samples). The lower values of activation pattern changes and focal position changes in sample 4, 6, and 7 indicate absence of focal switch during the transition from pre-stretch to post-stretch (see Table 1). The percentage variation of synchronization time along the stretch axis vr[$\tau_{sync,y}$] is always positive and almost always bigger (7 out of 8 samples) compared to the orthogonal axis vr[$\tau_{sync,x}$].

Sample #	**vr[Δt_{act}] (%)**	**AP_{bbv} (ms)**	**FP_{bbv} (mm)**	**# Focal switch**	**vr[$\tau_{sync,x}$] (%)**	**vr[$\tau_{sync,y}$] (%)**
1	-79.1	26.3	2.7	1	8.0	47.4
2	-55.2	14.4	4.5	1	-39.3	49.3
3	-83.1	23.1	5.8	1	-6.1	27.1
4	-79.7	6.5	0.7	0	-20.4	1.2
5	-36.5	25.5	4.9	1	1.7	61.3
6	9.1	10.1	0.5	0	-17.2	13.4
7	-42.6	5.3	0.4	0	3.0	15.3
8	-59.0	31.9	3.0	1	76.1	18.6
Mean±SEM	-53±11	18±4	3±1	62.5%	1±12%	29±8

Unsurprisingly, the cycle length represented by Δt_{act} usually decreased (7 out of 8 samples) with

a resulting -53±11% on average. The lower values of activation pattern change and focal position change in samples 4, 6, and 7 were due to absence of focal switches during the transition from pre-stretch to post-stretch (see Table 1). Calculating the correlation coefficient R between activation pattern changes AP_{bbv} and focal position changes FP_{bbv} resulted in R = 0.66 (p=0.073). A focal switch was found in 62.5% of samples (5 out of 8) during the transition from pre- to post-stretch. No correlation could be found between the percentage of variations of synchronization times in the direction of stretch $vr[\tau_{sync,y}]$ and the direction orthogonal to stretch $vr[\tau_{sync,x}]$ (R = 0.21, p=0.618). However, changes in $vr[\tau_{sync,y}]$ 29±8% was significantly higher than changes in $vr[\tau_{sync,x}]$ 1±12% (Kruskal-Wallis test: p=0.0274, n=8). Interestingly, the correlation R = 0.7 (p = 0.0537) was obtained between $vr[\tau_{sync,y}]$ and FP_{bbv}, indicating a relationship between a change in focal site and decreased synchronization.

4.3.5. Post-stretch activity properties with and without spontaneous activity in pre-stretch

The results presented in the previous sections were for cases where spontaneous activity was occurring in both pre-stretch and post-stretch states. Although all 14 samples were active in post-stretch, only 8 of them were active in pre-stretch, while the 6 remaining did not show any spontaneous activity before application of stretch. Here we divided the samples in 2 groups: (1) samples with signal in pre-stretch (n = 8), and (2) samples without signal in pre-stretch (n = 6). Fig. 6 presents the average data measured in both groups. In general, all measured variables were lower in post-stretch when no spontaneous activity was found in pre-stretch. This downward tendency is observed with varying amplitudes. For time-dependent variables: $\overline{\Delta t}_{act}$

was 1468±213 ms compared to 965±69 ms (34% lower, p=0.15) and $\overline{CL}_{bbv}$ was 111±37 ms vs. 48±18 ms (57% lower, p=0.25). For spatial variables: $\overline{AP}_{bbv}$ was 8.7±1.5 ms compared to 6.6±1.4 ms (24% lower, p =0.44) while $\overline{FP}_{bbv}$ was 0.65±0.19 mm vs. 0.41±0.12 mm (37% lower, p=0.36). When using a threshold of 1 mm for $\overline{\mathrm{FP}}_{\mathrm{bbv}}$, we found that 2 (over 8 samples) were satisfying this criterion in the group with spontaneous activity in pre-stretch while no sample (over 6 samples) was satisfying this criterion in the group not having spontaneous in pre-stretch.

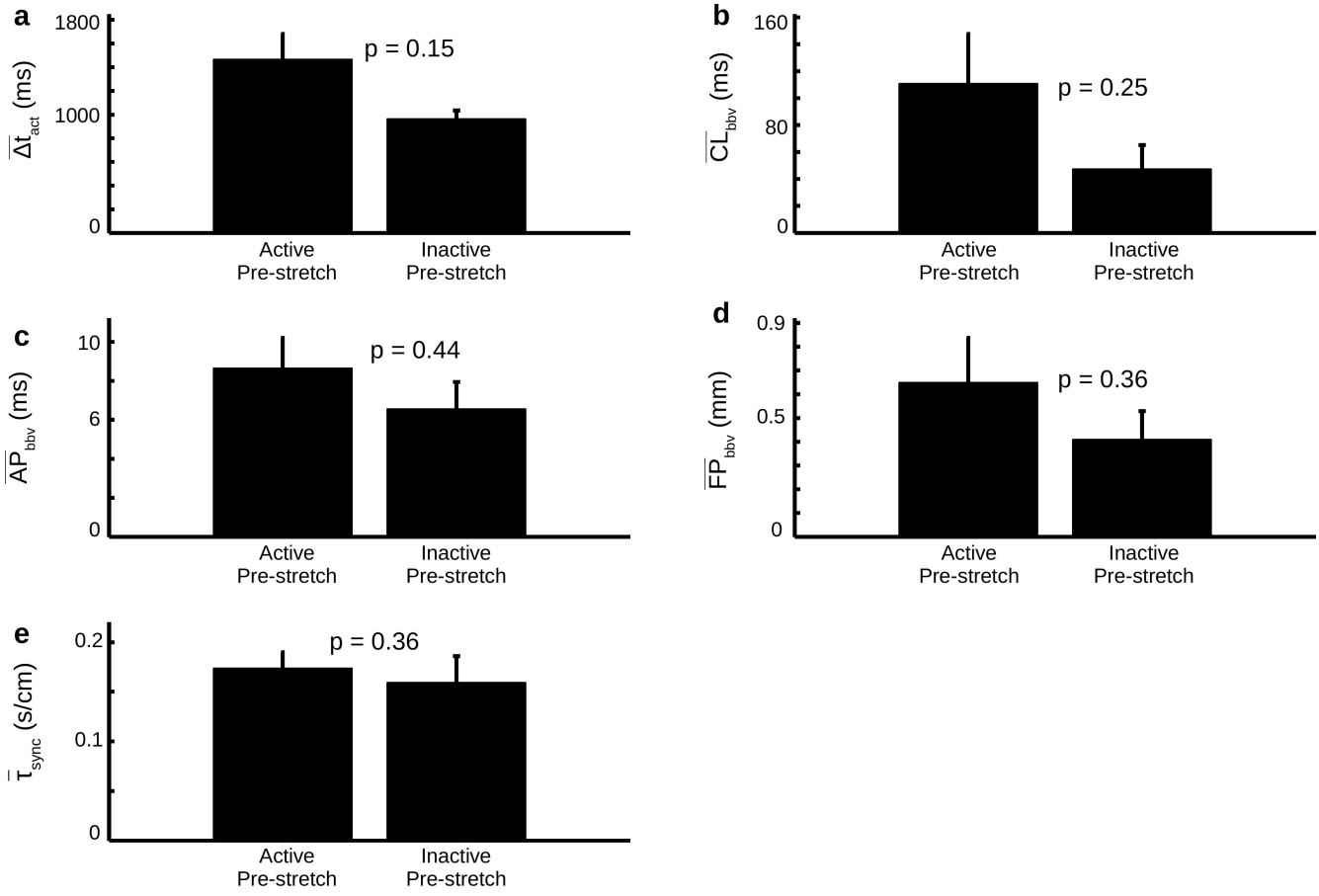

Figure 6. Comparison between cases with (n=8) and without (n=6) spontaneous activity in pre-stretch. The 14 active samples in post-stretch were divided in 2 groups depending on the presence (n = 8) or absence (n = 6) of signal in pre-stretch. Bar graphs of averages are

displayed with SEM. An unexpected drop in all variables are observed. The decrease is strong for $\overline{\Delta t}_{act}$ and $\overline{CL}_{bbv}$, less pronounced for $\overline{AP}_{bbv}$ and $\overline{FP}_{bbv}$, and fairly light for $\bar{\tau}_{sync}$. This striking result need further investigations with more sample and statistical analysis to understand underlying mechanisms.

4.4. Discussion & Conclusion

In this study, we proposed a method to characterize the effects of uniaxial stretch on the spontaneous activity of biological pacemaker monolayer cultures. To our knowledge, this project is the first to:

(1) introduce a remapping approach which opens the possibility to compare pre-stretch and post-stretch changes in space;

(2) quantify the enhancing and stabilizing effects of stretch on occurrence of automaticity and spontaneous rate respectively;

(3) demonstrate in monolayer cultures the inverse proportionality between the basal pre-stretch autonomous rhythm and the amplitude of the positive chronotropic effect in post-stretch;

(4) test the effect of stretch on the robustness of autonomous rhythm versus electrical stimulation;

(5) investigate effects of stretch on spatial characteristics of electrical activation, notably the activation pattern changes and focal activity.

A PDMS membrane with a clear-bottom culture well was designed. Widely used in cardiac stretch studies, PDMS was chosen for its biocompatibility and the possibility of easily adjusting its Young's modulus to fit physiologically relevant values [40]. The choice of

dimensions of the culture well resulted from empirical testing, which led to the following minimal requirements: (1) the depth must prevent cells from flowing out in the seeding process; (2) the bottom area must cover a field of view large enough to allow spatial signal analysis of electrical activation; (3) the area must be small enough to stay within the field of view of the camera in post-stretch state; (4) the well size must be sufficiently small compared to the size of the whole membrane to reduce stretch-induced non-linear (curved) deformation of the borders.

Stepper motors were selected to drive the stretcher device because they are cheap and easier to control than other types of devices like pump [41] or shape-memory alloy [42]. Rotary motors combined with external rotation to linear motion conversion apparatus (like engaged gears, cam-shafts, or timing-belt pulleys) [41] have been avoided offering the simplest design possible. A stepper motor driver carrier chip was used to implement microstepping and divide the original step size of the motor by 16 (from 3.1 µm to 0.2 µm equivalent to a an increase stretch of 0.0013%) in order to minimize rapid change in deformation and mechanical vibrations. Uniaxial stretch has been preferred over biaxial method to accommodate the need for simultaneous electric field stimulation, implemented with two parallel carbon electrodes occupying a free axis that would otherwise be also used for stretch. Carbon electrodes were selected since this material is biocompatible and demonstrates better current injection characteristics than other common materials like titanium [43].

The experimental protocol was designed to extract the maximum amount of information from the same optical mapping acquisition while minimizing the detrimental effects of several constraints, including:

(1) photobleaching of the dye: the total acquisition time is limited to 35 s to prevent a rapid deterioration of the signal;

(2) intrinsic biological variability: pre- vs. post-stretch comparisons are done in the same recording and not between different membranes;

(3) confusing causal relationship: the effect of stretch on automaticity is assessed before any electrical stimulation, since the latter may itself influence spontaneous activity.

This study is the first to provide quantitative data on uniaxial stretch of monolayers increasing occurrence of spontaneous activity and stabilizing autonomous rhythm. Those results were qualitatively described in a previous study in isolated SAN node of cat [27] Enhanced occurrence of automaticity with stretch may be explained by the stretch-induced raise of MDP [24],[44], which brings membrane potential closer to the threshold and increases chance to generate APs. Stretch has also been shown to increase the slope of slow diastolic depolarization in guinea pigs pulmonary veins spontaneous activity [45]. Stabilizing effect may come from the fact that both I_f and I_{CaL} currents, two major ionic current contributing to the membrane clock of cardiac automaticity [46] have their respective channels sensitive to stretch [47]–[49]. Microdomain calcium signalling is also sensitive to stretch [50]. Those results, combined with the decrease of recovery time with stretch, strongly suggest that a basal physiological stretch may be an important aspect to take into consideration when transplanting the BP patch into the myocardium. It is also interesting to notice that samples under the same experimental conditions in pre-stretch may have important distinct behaviors such as exhibiting or not spontaneous activity. It is believed that the neonatal ventricular cardiomyocyte monolayer contains at least two populations of cells: quiescent and autonomous cardiomyocytes [51]. In a

previous simulation study [17], we have shown that the density and spatial distribution of autonomous cells, *a priori* unknown, may lead to non-negligible intrinsic variability of the macroscopic behavior, including occurrence of automaticity.

The positive chronotropic response of autonomous activity in tissue to stretch has been widely demonstrated on isolated heart [22], isolated atrium [22],[52],[53] and isolated SAN node [24], [26],[27],[54]. Tissue preparations, namely isolated SAN of cats and rabbits [24] and isolated right atrium of rats [26], have also been used to demonstrate the inverse proportionality between the basal pre-stretch autonomous rhythm and the amplitude of the positive chronotropic effect in post-stretch. In this study, we have shown that spontaneous activity in neonatal cardiomyocytes monolayer cultures exhibit similar behavior. It is encouraging to realize how monolayer cultures can replicate behaviors originally obtained in tissue, including response to adrenergic and cholinergic stimulations [30],[55]. This leads us to hypothesize that the BP may eventually recapitulate and integrate the different modulators of native SAN.

Monolayer cultures are valuable models to palliate respective limitations of single cells and whole hearts studies. Setups that axially stretch isolated cells with carbon fibers glued to both ends and measure the electrophysiological response in patch clamp experiments [56] still offer unparalleled experimental control (direct application of stimuli and direct measurements); but the translation of the results to whole heart is debatable. Quantifying stretch applied to *ex vivo* hearts or the transformation of this stretch into effective stimuli for MEC is a challenge, considering the heart complex microstructure [57]. Heart anatomical heterogeneity also makes it difficult to assess specific effects of stretch on specific cell populations. Therefore, a monolayer is a good tradeoff between experimental control of single cell and physiological

relevance of whole heart experiments. It offers better experimental control (on the applied stimulus and the measured response) then whole heart while allowing interesting spatial measurements of multicellular networks (focal activity, activation pattern, synchronization, etc.).

In our experiments, a majority of BP monolayers, both in pre-stretch and post-stretch states, had changes in focal positions, a marker of spatio-temporal instability. Foci switch has been shown to occur more often on PDMS (soft substrate) than glass (hard substrate) [30]. When automaticity was unstable (i.e. acquisition with at least one focal switch) in pre-stretch, stretch had a spatial stabilizing effect, as attested in post-stretch by the significant decrease of focal switch densities, and beat-to-beat variability in activation patterns and focal positions. It is interesting to see that stretch may play a spatial stabilizing role, as it does for temporal autonomous rhythm. Synchronization time, τ_{sync}, significantly increases with stretch, highlighting that in a monolayer consisting of spontaneous and resting cell populations, stretch does not favor BP synchronization. Instead, an increased synchronization time corresponds to an increased intercellular activation delay, which is in accordance with decreased conduction slowing shown to occur in stretched monolayers [28],[58],[59]. As such, stretch-induced decreased period of activity is not followed by an increased overall spontaneous activity for all cells that would lead to more synchronized activation. Since conduction slowing with stretch is not affected by SACs blockade [28], the observed results may due to stretch-induces increase of membrane capacitance [28], or stretch-accelerated inactivation of Nav channels [60] (related to Na^+ current) which would reduce availability of sodium current, decreasing membrane excitability, a key factor in conduction velocity [61]. Those results could also be due to partial

inactivation of Na^+ channels leading to lower maximum upstroke velocity of APs because of increased MDP [62].

The proposed remapping algorithm allowed direct spatial comparison between the last activation before stretch and the first activation after stretch, and hence estimate the most acute effect of stretch. However, the approach remains limited leaving out the time interval during which active deformation is done (the time needed to go from 0% to 20% stretch). It was also interesting to see that response to stretch was not the same depending on the presence or absence of spontaneous activity in pre-stretch. All post-stretch variables displayed a downward tendency for samples without spontaneous activity in pre-stretch. This may be due to increase availability of calcium in the sarcoplasmic reticulum when there is no activity in pre-stretch. In fact, positive chronotropic response of autonomous activity to stretch is reduced by decreasing the calcium content of sarcoplasmic reticulum (block of SERCA pump) [63]. This aspect would need clarification in a future study.

In conclusion, the method presented here characterizes spatiotemporal effects of uniaxial stretch on the spontaneous activity of beating cardiac monolayers. It opens the way for numerous other studies, notably assessments of acute effects of stretch speed (rate at which the stretch is applied), overstretch (stretching beyond physiological limits), or cyclic stretch. Investigation of acute mechano-electric coupling in BPs made of human stem cell-derived cardiomyocytes or nodal cells seems [64] a logical follow up for the project.

4.5. References

[1] M. Semelka, J. Gera, and S. Usman, “Sick sinus syndrome: a review,” *Am. Fam. Physician*,

vol. 87, no. 10, pp. 691–696, May 2013.

[2] H. Dobrzynski, M. R. Boyett, and R. H. Anderson, “New Insights Into Pacemaker Activity,” *Circulation*, vol. 115, no. 14, pp. 1921–1932, Apr. 2007.

[3] A. C. Blank, P. Loh, and M. A. Vos, “106 - Atrioventricular Block,” in *Cardiac Electrophysiology: From Cell to Bedside (Sixth Edition)*, D. P. Zipes and J. Jalife, Eds. Philadelphia: W.B. Saunders, 2014, pp. 1043–1049.

[4] P. J. Wang and D. L. Hayes, “117 - Implantable Pacemakers,” in *Cardiac Electrophysiology: From Cell to Bedside (Sixth Edition)*, D. P. Zipes and J. Jalife, Eds. Philadelphia: W.B. Saunders, 2014, pp. 1167–1177.

[5] G. Gregoratos *et al.*, “ACC/AHA Guidelines for Implantation of Cardiac Pacemakers and Antiarrhythmia Devices: Executive Summary,” *Circulation*, vol. 97, no. 13, pp. 1325–1335, Apr. 1998.

[6] G. M. Morris and M. R. Boyett, “Perspectives — biological pacing, a clinical reality?,” *Ther. Adv. Cardiovasc. Dis.*, vol. 3, no. 6, pp. 479–483, Dec. 2009.

[7] F. V. Y. Tjong and V. Y. Reddy, “Permanent Leadless Cardiac Pacemaker Therapy: A Comprehensive Review,” *Circulation*, vol. 135, no. 15, pp. 1458–1470, Apr. 2017.

[8] E. W. Lau, “Technologies for Prolonging Cardiac Implantable Electronic Device Longevity,” *Pacing Clin. Electrophysiol.*, vol. 40, no. 1, pp. 75–96, Jan. 2017.

[9] J. D. Meyers, P. Y. Jay, and S. Rentschler, “Reprogramming the conduction system: Onward toward a biological pacemaker,” *Trends Cardiovasc. Med.*, vol. 26, no. 1, pp. 14–20, Jan. 2016.

[10] G. Gregoratos, “Indications and recommendations for pacemaker therapy,” *Am. Fam.*

Physician, vol. 71, no. 8, pp. 1563–1570, Apr. 2005.

[11] M. Brignole *et al.*, “2013 ESC Guidelines on cardiac pacing and cardiac resynchronization therapyThe Task Force on cardiac pacing and resynchronization therapy of the European Society of Cardiology (ESC). Developed in collaboration with the European Heart Rhythm Association (EHRA),” *Eur. Heart J.*, vol. 34, no. 29, pp. 2281–2329, Aug. 2013.

[12] M. L. Bakker *et al.*, “T-box transcription factor TBX3 reprogrammes mature cardiac myocytes into pacemaker-like cells,” *Cardiovasc. Res.*, vol. 94, no. 3, pp. 439–449, Jun. 2012.

[13] Y.-F. Hu, J. F. Dawkins, H. C. Cho, E. Marbán, and E. Cingolani, “Biological pacemaker created by minimally invasive somatic reprogramming in pigs with complete heart block,” *Sci. Transl. Med.*, vol. 6, no. 245, p. 245ra94, Jul. 2014.

[14] N. Kapoor, W. Liang, E. Marbán, and H. C. Cho, “Transcription factor-driven conversion of quiescent cardiomyocytes to pacemaker cells,” *Nat. Biotechnol.*, vol. 31, no. 1, pp. 54–62, Jan. 2013.

[15] A. Ruhparwar *et al.*, “Transplanted fetal cardiomyocytes as cardiac pacemaker,” *Eur. J. Cardio-Thorac. Surg. Off. J. Eur. Assoc. Cardio-Thorac. Surg.*, vol. 21, no. 5, pp. 853–857, May 2002.

[16] A. N. Plotnikov *et al.*, “Xenografted Adult Human Mesenchymal Stem Cells Provide a Platform for Sustained Biological Pacemaker Function in Canine Heart,” *Circulation*, vol. 116, no. 7, pp. 706–713, Aug. 2007.

[17] J. E. Duverger, J. Boudreau-Béland, M. D. Le, and P. Comtois, “Multicellular

automaticity of cardiac cell monolayers: effects of density and spatial distribution of pacemaker cells," *New J. Phys.*, vol. 16, no. 11, p. 113046, 2014.

[18] P. Kohl, F. Sachs, and M. R. Franz, Eds., *Cardiac Mechano-Electric Coupling and Arrhythmias*. Oxford University Press, 2011.

[19] J. S. Neves, A. M. Leite-Moreira, M. Neiva-Sousa, J. Almeida-Coelho, R. Castro-Ferreira, and A. F. Leite-Moreira, "Acute Myocardial Response to Stretch: What We (don't) Know," *Front. Physiol.*, vol. 6, 2016.

[20] H. Yang *et al.*, "Dynamic Myofibrillar Remodeling in Live Cardiomyocytes under Static Stretch," *Sci. Rep.*, vol. 6, Feb. 2016.

[21] T. A. Quinn and P. Kohl, "Mechano-sensitivity of cardiac pacemaker function: Pathophysiological relevance, experimental implications, and conceptual integration with other mechanisms of rhythmicity," *Prog. Biophys. Mol. Biol.*, vol. 110, no. 2–3, pp. 257–268, Oct. 2012.

[22] J. R. Blinks, "Positive chronotropic effect of increasing right atrial pressure in the isolated mammalian heart," *Am. J. Physiol.*, vol. 186, no. 2, pp. 299–303, Aug. 1956.

[23] P. J. Cooper, M. Lei, L.-X. Cheng, and P. Kohl, "Selected Contribution: Axial stretch increases spontaneous pacemaker activity in rabbit isolated sinoatrial node cells," *J. Appl. Physiol.*, vol. 89, no. 5, pp. 2099–2104, Nov. 2000.

[24] K. A. Deck, "[EFFECTS OF STRETCH ON THE SPONTANEOUSLY BEATING, ISOLATED SINUS NODE]," *Pflugers Arch. Gesamte Physiol. Menschen Tiere*, vol. 280, pp. 120–130, Jul. 1964.

[25] C. M. Brooks, H. H. Lu, G. Lange, R. Mangi, R. B. Shaw, and K. Geoly, "Effects of

localized stretch of the sinoatrial node region of the dog heart," *Am. J. Physiol.*, vol. 211, no. 5, pp. 1197–1202, Nov. 1966.

[26] C. J. Barrett, C. P. Bolter, and S. J. Wilson, "The intrinsic rate response of the isolated right atrium of the rat, Rattus norvegicus," *Comp. Biochem. Physiol. A. Mol. Integr. Physiol.*, vol. 120, no. 3, pp. 391–397, Jul. 1998.

[27] G. Lange, H. H. Lu, A. Chang, and C. M. Brooks, "Effect of stretch on the isolated cat sinoatrial node," *Am. J. Physiol.*, vol. 211, no. 5, pp. 1192–1196, Nov. 1966.

[28] E. R. Pfeiffer *et al.*, "Caveolae in Ventricular Myocytes are Required for Stretch-Dependent Conduction Slowing," *J. Mol. Cell. Cardiol.*, vol. 0, pp. 265–274, Nov. 2014.

[29] "FreeCAD: An open-source parametric 3D CAD modeler." [Online]. Available: https://www.freecadweb.org/. [Accessed: 02-Jun-2017].

[30] J. Boudreau-Béland, J. E. Duverger, E. Petitjean, A. Maguy, J. Ledoux, and P. Comtois, "Spatiotemporal Stability of Neonatal Rat Cardiomyocyte Monolayers Spontaneous Activity Is Dependent on the Culture Substrate," *PLoS ONE*, vol. 10, no. 6, Jun. 2015.

[31] N. Annabi *et al.*, "Hydrogel-coated microfluidic channels for cardiomyocyte culture," *Lab. Chip*, vol. 13, no. 18, pp. 3569–3577, Aug. 2013.

[32] A. J. Zollinger and M. L. Smith, "Fibronectin, the extracellular glue," *Matrix Biol. J. Int. Soc. Matrix Biol.*, vol. 60–61, pp. 27–37, Jul. 2017.

[33] J. E. Duverger, J. Béland, A. Maguy, M. M. Adegbindin, and P. Comtois, "Fluorescence-based system for measurement of electrophysiological changes in stretched cultured cardiomyocytes," *Conf. Proc. Annu. Int. Conf. IEEE Eng. Med. Biol. Soc. IEEE Eng. Med. Biol. Soc. Annu. Conf.*, vol. 2011, pp. 35–38, 2011.

[34] F. Gannier, E. White, A. Lacampagne, D. Garnier, and J. Y. Le Guennec, “Streptomycin reverses a large stretch induced increases in [Ca2+]i in isolated guinea pig ventricular myocytes,” *Cardiovasc. Res.*, vol. 28, no. 8, pp. 1193–1198, Aug. 1994.

[35] J. Sadoshima, L. Jahn, T. Takahashi, T. J. Kulik, and S. Izumo, “Molecular characterization of the stretch-induced adaptation of cultured cardiac cells. An in vitro model of load-induced cardiac hypertrophy.,” *J. Biol. Chem.*, vol. 267, no. 15, pp. 10551–10560, May 1992.

[36] T. Yamazaki *et al.*, “Mechanical stress activates protein kinase cascade of phosphorylation in neonatal rat cardiac myocytes.,” *J. Clin. Invest.*, vol. 96, no. 1, pp. 438–446, Jul. 1995.

[37] J. I. Laughner, F. S. Ng, M. S. Sulkin, R. M. Arthur, and I. R. Efimov, “Processing and analysis of cardiac optical mapping data obtained with potentiometric dyes,” *Am. J. Physiol. - Heart Circ. Physiol.*, vol. 303, no. 7, pp. H753–H765, Oct. 2012.

[38] P. V. Bayly, B. H. KenKnight, J. M. Rogers, R. E. Hillsley, R. E. Ideker, and W. M. Smith, “Estimation of conduction velocity vector fields from epicardial mapping data,” *IEEE Trans. Biomed. Eng.*, vol. 45, no. 5, pp. 563–571, May 1998.

[39] T. F. Chan and L. A. Vese, “Active contours without edges,” *IEEE Trans. Image Process. Publ. IEEE Signal Process. Soc.*, vol. 10, no. 2, pp. 266–277, 2001.

[40] A. L. Thangawng, R. S. Ruoff, M. A. Swartz, and M. R. Glucksberg, “An ultra-thin PDMS membrane as a bio/micro-nano interface: fabrication and characterization,” *Biomed. Microdevices*, vol. 9, no. 4, pp. 587–595, Aug. 2007.

[41] Y. Lei and Z. Ferdous, “Design considerations and challenges for mechanical stretch

bioreactors in tissue engineering," *Biotechnol. Prog.*, vol. 32, no. 3, pp. 543–553, May 2016.

[42] Y. Iwadate and S. Yumura, "Cyclic stretch of the substratum using a shape-memory alloy induces directional migration in Dictyostelium cells," *BioTechniques*, vol. 47, no. 3, pp. 757–767, Sep. 2009.

[43] N. Tandon, C. Cannizzaro, E. Figallo, J. Voldman, and G. Vunjak-Novakovic, "Characterization of electrical stimulation electrodes for cardiac tissue engineering," *Conf. Proc. Annu. Int. Conf. IEEE Eng. Med. Biol. Soc. IEEE Eng. Med. Biol. Soc. Annu. Conf.*, vol. 1, pp. 845–848, 2006.

[44] R. Kaufmann and U. Theophile, "Automatie-fördernde Dehnungseffekte an Purkinje-Fäden, Papillarmuskeln und Vorhoftrabekeln von Rhesus-Affen," *Pflüg. Arch. Für Gesamte Physiol. Menschen Tiere*, vol. 297, no. 3, pp. 174–189, Sep. 1967.

[45] S. Hamaguchi, K. Hikita, Y. Tanaka, Y. Tsuneoka, I. Namekata, and H. Tanaka, "Enhancement of Automaticity by Mechanical Stretch of the Isolated Guinea Pig Pulmonary Vein Myocardium," *Biol. Pharm. Bull.*, vol. 39, no. 7, pp. 1216–1219, 2016.

[46] O. Monfredi, V. A. Maltsev, and E. G. Lakatta, "Modern Concepts Concerning the Origin of the Heartbeat," *Physiology*, vol. 28, no. 2, pp. 74–92, Mar. 2013.

[47] W. Lin, U. Laitko, P. F. Juranka, and C. E. Morris, "Dual Stretch Responses of mHCN2 Pacemaker Channels: Accelerated Activation, Accelerated Deactivation," *Biophys. J.*, vol. 92, no. 5, pp. 1559–1572, Mar. 2007.

[48] B. Calabrese, I. V. Tabarean, P. Juranka, and C. E. Morris, "Mechanosensitivity of N-type calcium channel currents.," *Biophys. J.*, vol. 83, no. 5, pp. 2560–2574, Nov. 2002.

[49] G. L. Lyford *et al.*, “α1C (CaV1.2) L-type calcium channel mediates mechanosensitive calcium regulation,” *Am. J. Physiol. - Cell Physiol.*, vol. 283, no. 3, pp. C1001–C1008, Sep. 2002.

[50] P. Schönleitner, U. Schotten, and G. Antoons, “Mechanosensitivity of microdomain calcium signalling in the heart,” *Prog. Biophys. Mol. Biol.*, Jun. 2017.

[51] W. Guo, K. Kamiya, J. Cheng, and J. Toyama, “Changes in action potentials and ion currents in long-term cultured neonatal rat ventricular cells,” *Am. J. Physiol.*, vol. 271, no. 1 Pt 1, pp. C93-102, Jul. 1996.

[52] S. Chiba, “Pharmacologic Analysis of Stretch-Induced Sinus Acceleration of the Isolated Dog Atrium,” *Jpn. Heart J.*, vol. 18, no. 3, pp. 398–405, 1977.

[53] S. J. Wilson and C. P. Bolter, “Do cardiac neurons play a role in the intrinsic control of heart rate in the rat?,” *Exp. Physiol.*, vol. 87, no. 6, pp. 675–682, Nov. 2002.

[54] C. P. Bolter, “Effect of changes in transmural pressure on contraction frequency of the isolated right atrium of the rabbit,” *Acta Physiol. Scand.*, vol. 156, no. 1, pp. 45–50, Jan. 1996.

[55] A. Jones, D. Edwards, and A. Williams, “Characterisation of cardiomyocytes derived from human induced pluripotent stem cells as monolayers,” *The Lancet*, vol. 387, p. S56, Feb. 2016.

[56] G. Iribe, M. Helmes, and P. Kohl, “Force-length relations in isolated intact cardiomyocytes subjected to dynamic changes in mechanical load,” *Am. J. Physiol. - Heart Circ. Physiol.*, vol. 292, no. 3, pp. H1487–H1497, Mar. 2007.

[57] P. Kohl, “14 - Cardiac Stretch–Activated Channels and Mechano-Electric Coupling,” in

Cardiac Electrophysiology: From Cell to Bedside (Sixth Edition), D. P. Zipes and J. Jalife, Eds. Philadelphia: W.B. Saunders, 2014, pp. 139–149.

[58] E. R. Pfeiffer, J. R. Tangney, J. H. Omens, and A. D. McCulloch, "Biomechanics of Cardiac Electromechanical Coupling and Mechanoelectric Feedback," *J. Biomech. Eng.*, vol. 136, no. 2, pp. 0210071–02100711, Feb. 2014.

[59] Y. Zhang, R. B. Sekar, A. D. McCulloch, and L. Tung, "Cell cultures as models of cardiac mechanoelectric feedback," *Prog. Biophys. Mol. Biol.*, vol. 97, no. 2–3, pp. 367–382, 2008.

[60] C. E. Morris and P. F. Juranka, "Nav Channel Mechanosensitivity: Activation and Inactivation Accelerate Reversibly with Stretch," *Biophys. J.*, vol. 93, no. 3, pp. 822–833, Aug. 2007.

[61] A. G. Kléber and Y. Rudy, "Basic Mechanisms of Cardiac Impulse Propagation and Associated Arrhythmias," *Physiol. Rev.*, vol. 84, no. 2, pp. 431–488, Apr. 2004.

[62] N. H. L. Kuijpers, H. M. M. ten Eikelder, P. H. M. Bovendeerd, S. Verheule, T. Arts, and P. A. J. Hilbers, "Mechanoelectric feedback leads to conduction slowing and block in acutely dilated atria: a modeling study of cardiac electromechanics," *Am. J. Physiol. - Heart Circ. Physiol.*, vol. 292, no. 6, pp. H2832–H2853, Jun. 2007.

[63] A. Arai, I. Kodama, and J. Toyama, "Roles of Cl- channels and Ca2+ mobilization in stretch-induced increase of SA node pacemaker activity," *Am. J. Physiol. - Heart Circ. Physiol.*, vol. 270, no. 5, pp. H1726–H1735, May 1996.

[64] S. I. Protze *et al.*, "Sinoatrial node cardiomyocytes derived from human pluripotent cells function as a biological pacemaker," *Nat. Biotechnol.*, vol. 35, no. 1, pp. 56–68, Jan. 2017.

CHAPITRE 5 : DISCUSSION & CONCLUSION

Le but de cette thèse était d'étudier les effets de deux phénomènes sur l'activité spontanée du stimulateur cardiaque biologique: (1) la répartition spatiale des cardiomyocytes autonomes, et (2) le couplage mécano-électrique.

5.1. La répartition spatiale des cardiomyocytes avec activité spontanée induirait en partie la variabilité intrinsèque du stimulateur cardiaque biologique

La présente thèse est la première à démontrer que la répartition spatiale des cardiomyocytes autonomes, *a priori* inconnue, pourrait induire une variabilité intrinsèque non négligeable de l'activité spontanée du stimulateur cardiaque biologique. La variabilité intrinsèque, définie comme la différence de performance observée expérimentalement entre des SCB développés précisément dans les mêmes conditions, peut affecter négativement le taux de succès des implantations chez le patient.

L'originalité de notre première étude se décline dans les points suivants:

(1) La répartition spatiale aléatoire des cardiomyocytes autonomes au sein d'une monocouche cardiaque a été mathématiquement définie et caractérisée dans un modèle continue 2D en associant une variable de densité D_{aut} à une variable stochastique d'homogénéité spatiale p_{thr}.

(2) Le modèle démontre l'existence d'une plage de valeurs de D_{aut} et p_{thr} pour laquelle il n'y a pas d'activité autonome. En d'autres termes, la répartition spatiale des cardiomyocytes autonomes, inconnue dans la plupart des études visant à développer le SCB, pourrait aléatoirement remettre en cause l'occurrence même de l'automaticité.

(3) Le modèle démontre aussi que la période autonome T peut varier de plus de 30% en

fonction de D_{aut}, et que le temps total de synchronisation $t_{act,tot}$ peut varier d'un ordre de grandeur (plus de 10x) en fonction de p_{thr}. Cela signifierait qu'en plus de pouvoir remettre en cause la présence de l'automaticité, la répartition spatiale des cardiomyocytes autonomes pourraient, aléatoirement et de manière non négligeable, affecter les performances du SCB.

L'algorithme de répartition spatiale aléatoire décrit dans cette thèse s'inspire de différents travaux réalisés dans des domaines non reliés à la cardiologie, notamment l'adsorption[196], la compétition inter-espèce [197] et l'agrégation chimique [198]. La monocouche cardiaque excitable basée sur le modèle de FitzHugh-Nagumo est également bien connue et largement utilisée [199]–[201]. La nouveauté qu'amène la thèse consiste donc à introduire, pour la première fois, l'algorithme de répartition spatiale aléatoire dans le domaine cardiaque. Tout en ne remettant pas en cause la répartition aléatoire selon une loi uniforme en vigueur dans le domaine de la fabrication du SCB, les deux variables combinées (D_{aut}, p_{thr}) ont permis une caractérisation spatiale sans équivalent tant du côté théorique qu'expérimental. En effet, les méthodes expérimentales actuelles ne permettent pas de dissocier à la cellule près un cardiomyocyte autonome d'un cardiomyocyte non autonome en culture, et encore moins *in situ*. Dans de précédents modèles mathématiques, les cellules sont réparties aléatoirement sans aucune variable permettant la caractérisation post-répartition, ou uniquement une variable densité [150], [202], [203]. Mais la densité seule ne suffit pas à définir la répartition spatiale. Deux monocouches ayant le même D_{aut} mais des p_{thr} très différents peuvent démontrer des activités spontanées très dissemblables. Utiliser uniquement la densité comme variable de caractérisation expose le modèle à des écarts de comportement qu'il sera impossible

d'expliquer. D_{aut} donne une idée de la densité globale, mais il est important de ne pas négliger l'effet de la «densité locale» ou «granularité»; et c'est cet information supplémentaire que p_{thr} amène. La taille maximale des sous-groupes (*cluster*) de cardiomyocytes autonomes interconnectés ($S_{cluster}$) et le nombre de ces sous-groupes varient de manière hautement non-linéaire en fonction de D_{aut} et p_{thr}. Ces relations complexes pourraient expliquer le lien entre l'arrangement des cellules à l'échelle microscopique et la variabilité intrinsèque à l'échelle macroscopique; cet aspect sera d'ailleurs couvert en détail dans notre deuxième étude.

Le modèle de FitzHugh-Nagumo a été préféré au modèle de cellule ventriculaire de rats néonataux [204] pour économiser en puissance de calcul et parce qu'un modèle plus réaliste ne répondrait pas nécessairement mieux aux besoins du projet. En effet, la plupart des modèles ont été ajustés pour une seule série expérimentale; leur robustesse et la sensibilité de leurs paramètres ne sont en général pas évaluées au moment de leur conception. Cette faiblesse dans le processus d'ajustement fait en sorte que des modèles de PA différents décrivant une même espèce animale peuvent donner des résultats très discordants [205]. De plus, il arrive que des combinaisons très différentes de paramètres d'un même modèle donnent le même potentiel d'action [206], [207]. Quand une telle situation se présente, le modèle est dit non identifiable, et sa fiabilité prédictive est remise en doute. La plupart des modèles de haute dimension ne sont pas identifiables [208]. Dans ces conditions, la dimension d'un modèle n'est pas nécessairement corrélée avec sa capacité à prédire adéquatement les phénomènes biologiques. Un modèle de basse dimension, capturant les détails physiologiques essentiels d'un point vue phénoménologique, peut donner de meilleurs résultats tout en étant moins gourmand en puissance de calcul. D'ailleurs un modèle 2D de FHN démontre qualitativement les mêmes

propriétés qu'un modèle 2D de Luo-Rudy Phase 1 (LR1, cellules ventriculaire) [108]. Ceci dit, au-delà de la connectivité intercellulaire, la propagation du potentiel d'action dépend également des propriétés de la membrane cellulaire [209]; un modèle de FHN donnera donc toujours une vue incomplète du phénomène. Pour fin de simplicité, uniquement deux populations de cellules ont été considérées: les cardiomyocytes autonomes et les cardiomyocytes non autonomes. La présence de cellules passives (les fibroblastes par exemples) et/ou de régions non conductrices (dommage dans la monocouche ou dépôt de collagène) aurait rendu notre modèle plus réaliste. Mais une autre étude théorique a clairement démontré que ces autres populations avaient des effets non négligeables sur l'activité autonome de la monocouche cardiaque [151]. Le choix de conception consistant à les ignorer offre donc l'avantage de bien isoler les variables à l'étude. La nécessité de bien isoler les variables explique aussi le choix de ne considérer que des monocouches où les cardiomyocytes sont fortement couplés. De fait, des monocouches cardiaques faiblement couplées peuvent émerger des activités asynchrones et de la réentrée [120], [150], [202], [203], [210]. Le coefficient de diffusion utilisé a donc été choisi de telle sorte que ces activités atypiques soient évitées.

L'effet de D_{aut} et p_{thr} sur l'occurrence et la période de l'automaticité s'explique bien dans le cadre de la propagation électrotonique. En effet, si les cardiomyocytes autonomes sont des «sources de courant» et les cardiomyocytes non autonomes des «puits de courant», il devient évident que plus un sous-groupe contient des cardiomyocytes autonomes, plus il a de chance d'émettre un potentiel d'action qui se propagera. Plus D_{aut} est grand, plus les sous-groupes autonomes sont grands et plus l'automaticité a de chance d'apparaître et d'être rapide (T↓). La tendance est inversée avec p_{thr}. Plus p_{thr} est grand, plus les sous-groupes autonomes sont petits (puisque les

cardiomyocytes autonomes sont répartis de manière plus homogène) et moins l'automaticité a de chance d'apparaître et d'être rapide (T↑). Ces résultats rendent possibles l'émission d'hypothèses éclairées concernant les défauts de performances observés dans les récents essais d'implantation du SCB, notamment des rythmes autonomes trop faibles [95], [211]. Ainsi, la faiblesse systématique du rythme pourrait, en partie, être expliquée par un D_{aut} systématiquement trop petit ou un p_{thr} systématiquement trop grand.

5.2. La force de l'automaticité et l'anisotropie linéaire structurelle moduleraient la variabilité intrinsèque du stimulateur cardiaque biologique, sans toutefois l'éliminer.

La présente thèse est aussi la première à démontrer que la force de l'automaticité et l'anisotropie linéaire structurelle pourraient moduler la variabilité intrinsèque du stimulateur cardiaque biologique, sans toutefois l'éliminer.

L'originalité de notre deuxième étude, se décline dans les points qui suivent:

(1) La répartition spatiale aléatoire et bivariable (D_{aut},p_{thr}) des cardiomyocytes autonomes au sein d'une monocouche cardiaque a été mathématiquement redéfinie et recaractérisée dans un modèle semi-discret 2D mettant en valeur la force de l'automaticité et l'anisotropie.

(2) Le modèle démontre que la force de l'automaticité augmente substantiellement les chances de voir apparaître de l'activité spontanée, diminue la variabilité de la longueur de cycle $\overline{\mathrm{CL}}$ et du temps local de synchronisation $\overline{\mathrm{T}}_{\mathrm{sync}}$ pour des répartitions spatiales semblables (i.e. pour les différentes monocouches ayant les mêmes valeurs de D_{aut} et p_{thr}), et augmente la proportion de sites d'initiation situés au centre. Par contre, la variabilité est augmentée pour les répartitions

spatiales dissemblables (i.e. pour les différentes monocouches n'ayant pas les mêmes valeurs de D_{aut} et p_{thr}).

(3) Le modèle démontre aussi que l'anisotropie structurelle linéaire, contrairement à la force de l'automaticité, n'influence pas les chances de voir apparaître l'activité spontanée, augmente la variabilité de $\overline{CL}$ et de $\overline{T}_{sync}$ pour des répartitions spatiales semblables et dissemblables, et diminue la proportion de sites d'initiation situés au centre.

(4) La variabilité intrinsèque n'est cependant en aucun cas éliminée, puisque qu'il subsiste une proportion de couples (D_{aut},p_{thr}) pour laquelle il n'y a pas d'automaticité, et que de grandes disparités de performances (en $\overline{CL}$ et $\overline{T}_{sync}$) existent encore pour des valeurs éloignées de D_{aut} et p_{thr}.

La mise à jour du couple (D_{aut},p_{thr}) comme une des origines plausibles de la variabilité intrinsèque du SCB a immédiatement soulevé une remarquable question: comment peut-on éliminer ou contourner la variabilité intrinsèque tout en ignorant la répartition spatiale des cardiomyocytes autonomes? Étant donné que le contrôle *in situ* de le répartition spatiale des cardiomyocytes autonomes n'est pas envisageable à court et moyen terme, il reste deux principales options: (a) soit le SCB est conçu et testé *ex vivo* pour ensuite être implanté au patient; (b) soit les méthodes de fabrication actuelles s'accompagnent de procédés supplémentaires destinés à minimiser les effets de la variabilité intrinsèque. C'est pour investiguer la deuxième option que deux nouvelles variables ont été introduites: la force de l'automaticité et l'anisotropie structurelle linéaire.

Le modèle de Luo-Rudy Phase 1 (LR1) de potentiel d'action cardiaque ventriculaire [108] a été repris pour représenter les cardiomyocytes non autonomes. Un courant de biais entrant (I_{bias}) a été ajouté pour générer l'automaticité et ainsi représenter les cardiomyocytes autonomes, tel qu'effectué ailleurs dans la littérature [150], [203]. Pour modéliser l'anisotropie structurelle linéaire, un modèle de micro-structure 2D semi-discret précédemment publié a été utilisé [212]. Ce modèle assigne aléatoirement (loi normale) un ensemble de nœuds à chaque cardiomyocyte de la monocouche. L'anisotropie a été créée en augmentant le ratio moyen longueur sur largeur des cellules, et en ajustant la distribution des jonctions communicantes de telle sorte à démontrer des vitesses de conductions longitudinales et transversales équivalentes à celles mesurées expérimentalement dans des cultures anisotropes de cardiomyocytes ventriculaires de rats néonataux. Comme pour la première étude, l'originalité consiste ici à appliquer l'algorithme de répartition spatiale au modèle de microstructure semi-discret 2D. Des monocouches cardiaques isotropes ou anisotropes, aux densités D_{aut} et distributions spatiales p_{thr} variées, ont été générées. La valeur de I_{bias} a été ajustée de sorte à répartir les monocouches en quatre groupes distincts:

* ISO-2.6 – monocouches isotropes a automaticité faible (I_{bias} = 2.6 μA/cm^2)

* ANISO-2.6 – monocouches anisotropes a automaticité faible (I_{bias} = 2.6 μA/cm^2)

* ISO-3.5 – monocouches isotropes a automaticité forte (I_{bias} = 3.5 μA/cm^2)

* ANISO-3.5 – monocouches anisotropes a automaticité forte (I_{bias} = 3.5 μA/cm^2)

Un tel arrangement n'a pas de précédent théorique, ni d'équivalent expérimental. Similairement à la première étude, des simplifications ont été établies afin de bien isoler les variables, et ses simplifications viennent aussi avec leur lot de limitations. Un partie des points faibles de la

première étude reste valide, notamment: (a) l'utilisation de seulement deux populations ce cellules à l'exclusion des autres et (b) l'évitement de la propagation asynchrone ou de la réentrée, au profit d'une simple propagation focale. De plus, pour une monocouche donnée, la valeur de I_{bias} est la même pour tous les cardiomyocytes autonomes; en d'autres termes, les cardiomyocytes autonomes sont identiques, ce qui n'est certainement pas le cas expérimentalement mais néanmoins nous permet de bien isoler l'effet de la force de l'automaticité. Enfin, comme le modèle de FHN, le modèle de LR1 ne récapitule pas nécessairement toute la complexité électrophysiologique observée expérimentalement, mais reste une bonne option théorique (il est identifiable) et pratique (économie de temps de calcul).

La caractérisation de la répartition spatiale donne des résultats remarquablement similaires à notre première étude. C'est d'autant plus surprenant que les deux modèles sont assez dissemblables (l'un est continu et l'autre semi-discret) et que le nombre de voisins n'est pas le même (huit pour le premier, six en moyenne pour le deuxième). La similarité de la caractérisation entre les deux géométries (isotrope et anisotrope) est tout aussi remarquable. Des investigations plus poussées seraient nécessaires pour expliquer comment l'algorithme de répartition spatiale transcende les structures.

Dans la première étude, l'existence d'une plage de valeurs de (D_{aut},p_{thr}) sans automaticité a été mise en lumière. La deuxième étude se distingue nettement par un investigation beaucoup plus poussée de l'occurrence de l'automaticité. L'espace des valeurs de (D_{aut},p_{thr}) possède en effet trois zones: (a) une zone où l'automaticité apparaît de manière certaine (i.e. dans toutes les

simulations); (b) une zone où l'automaticité apparaît de manière incertaine et (c) une zone sans automaticité. L'automaticité apparaît optimalement pour des valeurs croissantes de D_{aut} et des valeurs décroissantes de p_{thr}. En d'autre terme, plus il y a de cardiomyocytes autonomes (grand D_{aut}) et plus ces cardiomyocytes autonomes s'interconnectent au même endroit (petit p_{thr}), plus on a de chance de voir apparaître l'automaticité. D'ailleurs, il faut des D_{aut} encore plus grands et des p_{thr} encore plus petits pour être certain d'avoir de l'automaticité.

Pour pousser l'analyse encore plus loin, les zones d'automaticité ont été séparées par des courbes de transition constituées au fait des valeurs de (D_{aut},p_{thr}) aux frontières entre les différentes zones. Ces courbes ont systématiquement la forme sigmoïdale observée dans notre première étude. Cette curieuse forme a pu être reliée à la microstructure des monocouches. En dessous de la ligne de transition D_{aut} = 0.5, la ligne de transition dépend principalement de $S_{cluster}$ (taille moyenne du plus grand sous-groupe interconnecté de cardiomyocytes autonomes). Au-dessus de la ligne de transition D_{aut} = 0.5, une nouvelle caractéristique entre en jeu: la porosité (la proportion de cardiomyocytes non autonomes au sein du sous-groupe interconnecté de cardiomyocytes autonomes). L'automaticité ne peut apparaître quand les sous-groupes de cardiomyocytes sont trop poreux (porosité > 35%). D'un point de vue électrotonique, les cardiomyocytes autonomes ont trop de cellules à dépolariser dans leur propre sous-groupes, et n'ont plus la force entraînante nécessaire pour dépolariser l'ensemble de la monocouche. Ainsi, l'apparition macroscopique de l'automaticité est intimement reliée à la structure microscopique de la monocouche. Ce résultat renforce la plausibilité de notre hypothèse associant la variabilité intrinsèque à la répartition spatiale. Il indique aussi la résolution que devrait avoir une

éventuelle méthode optique de caractérisation spatiale expérimentale. Cette résolution devrait être presque de la taille d'une cellule, puisqu'un sous-groupe autonome ne peut être juste considéré dans son ensemble, à cause de la porosité. Devant une tel défi technique, éliminer ou contourner la variabilité intrinsèque paraît de plus en plus être l'option la plus viable.

Accroître la force de l'automaticité augmente systématiquement l'occurrence de l'activité spontanée, i.e. augmente du nombre de couples (D_{aut},p_{thr}) démontrant de l'automaticité (certaine ou incertaine). Cette relation est très bien connue puisqu'elle est à la base même du développement de SCB par manipulation de canaux ioniques [83]–[85]. Mais nous disposons maintenant d'une possible explication microstructurelle du succès des ces méthodes: plus l'automaticité est forte, plus l'activité spontanée peut apparaître dans des conditions microstructurelles difficiles. La force de l'automaticité permet, électrotoniquement, de «gagner du terrain» sur la taille maximale $S_{cluster}$ et sur la porosité: l'activité spontanée apparaît pour des $S_{cluster}$ de plus en plus petits et des sous-groupes autonomes de plus en plus poreux. C'est pour ces mêmes raisons que la proportion de sites d'initiation situés au centre augmente. La force de l'automaticité diminue aussi la variabilité pour des répartitions spatiales semblables (par exemple mean[σ_{CL}]). Cette stratégie semble donc gagnante, mais n'est pas sans conséquence. Par exemple, les périodes autonomes les plus faibles de retrouvent systématiquement pour les monocouches les plus poreuses, ce qui a pour effet d'augmenter la disparité des performances pour des répartitions spatiales dissemblables. Il est donc possible que ce qui est gagné au niveau de l'occurrence de l'automaticité soit reperdu au niveau de la variabilité des performances. D'un point de vue expérimental, cela signifierait que la force de l'automaticité ne

doit pas nécessairement être recherchée à tout prix. De plus, il existe irréductiblement un ensemble de couples (D_{aut},p_{thr}) sans automaticité. La force de l'automaticité pourrait moduler la variabilité intrinsèque, mais ne semble pas être en mesure de l'éliminer.

L'anisotropie commence à être utilisée dans le domaine du SCB [213], et une partie de notre projet consiste à tester son effet sur l'activité autonome des monocouches cardiaques en général et la variabilité intrinsèque en particulier. Comparativement à la force de l'automaticité, l'anisotropie structurelle linéaire n'a aucune influence sur les chances de voir apparaître l'automaticité et augmente la variabilité des performances tant pour les répartitions semblables que dissemblables. L'anisotropie structurelle linéaire aggraverait donc la variabilité intrinsèque et serait contre-indiquée, mais cette conclusion est à nuancer selon plusieurs points de vue. Premièrement, dans notre projet, l'anisotropie a été définie de manière totalement indépendante de la force de l'automaticité, exclusivement à partir du ratio longueur sur largeur des cellules et de la distribution des jonctions communicantes. Mais expérimentalement, l'anisotropie peut moduler la dynamique calcique [214], [215]. Ainsi, même si l'anisotropie est sans effet ou est délétère d'un point de vue strictement structurelle, elle peut quand même influencer la force de l'automaticité et indirectement démontrer d'autres propriétés. Deuxièmement, notre projet étudie le SCB isolé et non dans sa destination finale, qui est le milieu *in vivo*. Un brevet allègue clairement que l'adéquation d'alignement entre les cardiomyocytes du SCB et les cardiomyocytes du myocarde améliore la fonction autonome [213]. D'autres investigations théoriques et expérimentales sont clairement nécessaires pour mieux aborder cette question.

Il peut paraître intéressant de maximiser la densité D_{aut} de cardiomyocytes autonomes. De fait,

si tous les cardiomyocytes sont autonomes, p_{thr} n'aura plus aucun effet. Mais la réalité est un peu plus compliquée. L'architecture du nœud SA natif indique avec insistance que, dans une optique biomimétique, le SCB aura besoin de diversité cellulaire. Si toutes les cellules sont identiques, le SCB s'arrêtera net à la première stimulation vagale. D'ailleurs, même les populations de cellules passives et de régions isolantes, non considérées dans notre projet, pourraient être nécessaires, comme c'est le cas dans le nœud SA.

5.3. L'étirement uniaxial physiologique joue un rôle de stabilisateur spatial et temporel pour le stimulateur cardiaque biologique

La présente thèse est finalement la première caractériser spatialement les effets de l'étirement uniaxial sur le SCB en monocouche.

L'originalité de notre troisième étude s'énonce ainsi:

(1) Une approche de re-cartographie a été introduite, et permet la comparaison spatiale directe pré- vs post-étirement.

(2) L'augmentation de l'occurrence de l'automaticité et la stabilisation de la période autonome en post-étirement, dues à l'étirement, ont été quantifiées.

(3) La proportionnalité inverse entre la période autonome en pré-étirement et la réponse chronotrope à l'étirement a été démontrée pour la monocouche cardiaque.

(4) L'effet de l'étirement uniaxial sur la robustesse de l'automaticité vis-à-vis de la stimulation électrique a été testée.

(5) Les effets de l'étirement uniaxial sur les caractéristiques spatiales de l'activation électrique,

notamment l'activité focale et les changements dans les patrons de propagation, ont été investigués en détail.

La présence hypothétiquement irréductible de la variabilité intrinsèque nous oblige à considérer de développement *ex vivo* du SCB comme une alternative viable aux méthodes *in vivo*. Le processus s'accomplirait désormais en deux temps: (a) le SCB est d'abord développé et testé *ex vivo* et (b) ensuite il est implanté au patient. Cette méthode présente l'avantage évident de pouvoir sélectionner parmi un ensemble de SCB développés celui qui répond aux performances souhaitées, contournant ainsi la variabilité intrinsèque. Mais ladite variabilité n'est pas le seul phénomène pouvant affecter, positivement ou négativement, les performances post-implantation du SCB. Le couplage mécano-électrique en est un autre.

Des cardiomyocytes ventriculaires de rats néonataux ont été mis en culture dans le bassin central d'une membrane de PDMS (polydiméthylsiloxane) claire et étirable, conformément à ce qui a été réalisé dans la littérature [216]. Notre étude nous a permis d'établir empiriquement les règles qui doivent être respectées pour obtenir une membrane évitant les écueils expérimentaux les plus courants: (a) le bassin central doit être suffisamment profond pour éviter l'échappement des cellules durant le processus d'ensemencement; (b) la surface du fond du bassin doit couvrir un champ de vision suffisamment grand de la caméra pour avoir un nombre de pixels rendant possible l'analyse spatiale; (c) la surface du fond du bassin doit également être suffisamment petite pour se maintenir au complet dans le champs de vision de la caméra durant tout le processus d'étirement; (d) la taille du puits doit enfin être assez petit comparativement à la taille de la membrane pour éviter la déformation non-linéaire de ses bords en post-étirement.

Des puits de 10 mm × 10 mm × 0.5 mm et de 4 mm × 4 mm × 1 mm ont d'abord été conçus et testés avant d'aboutir à la version finale de 6 mm × 6 mm × 1 mm. Le point (d) a été déterminant dans la caractérisation de la membrane. C'est l'absence de courbure dans les bords qui a rendu possible l'approximation de la déformation de la membrane par une transformation affine rigide, aboutissant la relation linéaire entre l'élongation appliquée par les moteurs (en mm) et l'étirement de la membrane (en %). Cette relation linéaire ne varie pas pour des membranes identiques. Mais il est important de souligner que le processus de caractérisation doit être repris en cas de changement de taille de la membrane ou du puits. L'algorithme de re-cartographie utilise la relation linéaire issue de la caractérisation pour ré-assigner à chaque pixel en post-étirement la position qui a été occupée en pré-étirement. Cet algorithme est le premier à permettre une comparaison directe entre la dernière activation en pré-étirement et la première activation post-étirement. En d'autre terme, elle permet de visualiser l'effet le plus aigü en post-étirement. Cependant, l'algorithme de re-cartographie n'est pas une méthode de correction de mouvement, et de ce fait, ne permet pas de visualiser le comportement l'échantillon durant le déplacement nécessaire pour atteindre le niveau d’étirement. Ce qui se passe après la fenêtre de pré-étirement et avant la fenêtre de post-étirement n'est pas analysable et constitue une limitation du projet, ainsi qu'une suite logique. Il existe en effet des algorithmes de correction de mouvement, basés notamment sur la méthode de flot optique et appliqués au cœur entier [217]. Il serait intéressant de les adapter aux monocouches cardiaques.

L'étirement de monocouches cardiaques est un procédé très courant en recherche, mais est surtout employé au niveau chronique. Beaucoup de systèmes d'élongation ont ainsi été

développés afin d'être utilisés au sein de bioréacteurs [218] dans des protocoles étalés sur plusieurs jours. Les principes d'ingénierie reliés à ces systèmes peuvent être repris dans le cadre aigu. Notre processus de conception a été guidé par deux idées centrales: la biocompatibilité et la simplicité. Les choix de matériaux comme le PDMS pour la membrane [219] ou le carbone pour les électrodes de stimulation électrique [220] ont évidemment été guidées par la biocompatibilité. Quant aux moteurs pas-à-pas, ils ont été choisis parce qu'ils sont simples à contrôler, par rapport à d'autres actuateurs comme les pompes [218] et les alliages à mémoire de forme [221]. La simplicité a également été à la base de notre module de stimulation électrique (convertisseur numérique-analogique associé à un amplificateur). Le résultat final met en lumière un système efficace, adapté aux cellules, facile à contrôler et à répliquer. Mais nos choix de conception ne sont pas dépourvus de limitations. L'étirement uniaxial par exemple a été sélectionné afin d'accommoder la présence des deux électrodes de carbone sur l'axe orthogonal à l'élongation, de part et d'autre de la membrane. Mais étirer dans un seul axe ne rend pas totalement compte des contraintes mécaniques réelles que va subir le SCB dans le myocardium.

L'analyse de l'occurrence de l'automaticité a offert une illustration saisissante de la variabilité intrinsèque introduite dans les deux précédents projets. Sur les 14 membranes à l'étude, préparées dans des conditions identiques, six ne démontraient pas d'automaticité en pré-étirement. Le maintient permanent d'une concentration de 10% de sérum de veau dans le milieu de culture, connu pour accroître la force de l'automaticité en augmentant l'amplitude du courant entrant I_{CaL} [222], n'a pas éliminé la variabilité intrinsèque. La disparité des performances en

pré-étirement est également une illustration de la variabilité intrinsèque. Par exemple la période autonome varie d'un ordre de grandeur, de 9,584 ms à 946 ms. L'étirement a eu pour effet d'augmenter significativement l'occurrence de l'automaticité (à 100% des échantillons à l'étude), et de réduire sensiblement la variabilité de la période autonome (de 2,167 ms à 851 ms). L'analyse de l'occurrence de l'automaticité est une première par son aspect quantitatif et par le fait qu'elle concerne une monocouche. À ce sujet, une précédente étude, qualitative, a été réalisée sur le nœud SA isolé de chat [187].

L'étirement diminue la période autonome, et joue un rôle de stabilisateur du rythme, i.e. il réduit significativement la variabilité de la période autonome d'un battement à l'autre. L'effet chronotrope en post-étirement est un phénomène bien connu dans les cellules autonomes isolées [193], le tissu [189] et même le cœur entier [183], mais encore jamais démontré chez les monocouches cardiaques. Le rôle de stabilisateur du rythme a quant à lui déjà été qualitativement décrit dans le tissu [187], mais c'est la première fois qu'il est quantifié dans une monocouche. L'étirement augmente aussi significativement la robustesse de l'automaticité vis-à-vis d'un perturbateur externe comme la stimulation électrique en diminuant le temps de récupération, i.e. le temps nécessaire pour revenir à l'activité autonome après le dernier battement stimulé. Du côté spatial, l'étirement diminue significativement l'instabilité des patrons de propagation et des positions des sites d'initiation, sans créer d'instabilité dans les échantillons déjà stables. Dans l'ensemble, ces résultats semblent indiquer qu'un étirement physiologique de base, en augmentant le potentiel diastolique minium, pourrait être bénéfique aux performances du SCB. Cette idée a déjà été proposée de manière qualitative [187] et

nécessite plus d'investigation sur les comportements à long terme et sur la manière de préserver l'élongation de base du SCB un fois implanté *in vivo*. Il est également intéressant de remarquer que les monocouches récapitulent des réponses obtenues originellement dans du tissu. Ce fait fonde de grands espoirs sur la capacité d'un SCB en feuillet à remplacer la fonction du tissu sinusal natif. L'étirement augmente aussi significativement le temps de synchronisation local et cet augmentation a lieu principalement dans la direction de l'élongation. Cette «anisotropie fonctionnelle» provoquée par l'étirement est assez remarquable et ne doit pas être confondue avec la véritable anisotropie structurelle. Le temps de synchronisation augmente dans le sens de «anisotropie fonctionnelle», alors qu'il diminue dans le sens de l'anisotropie structurelle. Des études plus poussées sont nécessaire pour bien définir ce phénomène.

Enfin, la comparaison directe entre le dernier battement en pré-étirement et le premier battement en post-étirement montre essentiellement que les effets temporels de l'étirement (diminution de la période autonome) se manifestent depuis le début, i.e. que la phase transitoire de la réponse post-étirement est inexistante ou trop courte pour être détectée par notre analyse. Il est également possible que cette période transitoire se retrouve au contraire au début du mouvement d'étirement, dans la fenêtre non analysée.

Notre méthode ne donnera pas toutes les réponses sur le sort mécano-électrique du SCB *in situ*, mais propose des résultats suffisamment convaincant pour comprendre que l'étirement est un facteur important dont il faut tenir dans le cadre du développement du SCB. Le comportement *in vitro* de la monocouche cardiaque ne correspondra pas nécessairement à son comportement *in vivo*. Mais bien maîtrisé (étirement physiologique basal), l'étirement peut contribuer à l'amélioration des performances.

5.4. Conclusion

Dans le cadre du traitement de la bradycardie, le stimulateur cardiaque biologique (SCB) représente une alternative potentiellement viable palliant aux limitations des stimulateurs cardiaques électroniques (SCE). Mais le chemin vers la translation au patient est encore long. Les équipes développant les SCE sont au courant de leurs faiblesses et développent des appareils de plus en plus performants. Quand aux SCB, la plupart des recherches sont encore à un niveau fondamental. L'expérience la plus prometteuse a été réalisée dans un modèle porcin, en tandem avec un pacemaker électronique [95]. Le but dans un premier temps ne serait donc pas de remplacer le SCE, mais d'en être moins dépendant. La combinaison d'un SCB stable à long terme et d'un SCE, sans électrode [223] et peu gourmand en énergie, semble être gagnante. Mais à ce stade des recherches, les SCB implantés *in vivo* sont lents et leurs effets se dissipent en quelques semaines tout au plus [95], [211].

Nous nous sommes intéressés à l'origine spatiale de la variabilité intrinsèque observée expérimentalement et aux effets du couplage mécano-électrique sur les performances du SCB. Nos deux premières études nous ont d'abord amenés à conclure que la répartition spatiale des cardiomyocytes autonomes pourraient induire une variabilité intrinsèque non négligeable, qui ne peut être éliminée ou contournée par la force de l'automaticité et/ou l'anisotropie structurelle linéaire. La recommandation a donc été faite de recourir à des méthodes de développement *ex vivo* permettant une évaluation pré-implantation des performances. Mais ces méthodes

amèneront bien sûr leur lot de défis, l'un des plus prévisibles étant l'implantation au patient; amener un tissu vivant par cathéter dans le myocarde est un processus qui s’avérera beaucoup plus risqué qu'une «simple» injection de cellules ou de virus. Notre dernière étude a mis en lumière l'effet stabilisateur de l'étirement uniaxial physiologique sur l'activité spontanée du SCB en monocouche. Une méthode novatrice de caractérisation expérimentale a été conçue et validée. Les résultats mettent en lumière l'effet bénéfique que pourrait avoir un étirement physiologique de base appliquée au SCB, pré- et post-implantation.

L'origine spatiale de la variabilité intrinsèque et les effets de l'étirement sont deux phénomènes importants qui ont mérité d'être le sujet de cette thèse. Des études plus poussées sur ces phénomènes sont encore nécessaires, et apporteront sans aucun doute une meilleure compréhension des défis reliés au développement du SCB et au succès de son implantation au patient.

BIBLIOGRAPHIE

[1] M. E. Silverman and A. Hollman, “Discovery of the sinus node by Keith and Flack: on the centennial of their 1907 publication,” *Heart*, vol. 93, no. 10, pp. 1184–1187, Oct. 2007.

[2] Madhero88, *English: A graphical representation of the Electrical conduction system of the heart showing the Sinoatrial node, Atrioventricular node, Bundle of His, Purkinje fibers, and Bachmann's bundle*. 2013.

[3] O. Monfredi, V. A. Maltsev, and E. G. Lakatta, “Modern Concepts Concerning the Origin of the Heartbeat,” *Physiology*, vol. 28, no. 2, pp. 74–92, Mar. 2013.

[4] M. Baruscotti, A. Bucchi, and D. Difrancesco, “Physiology and pharmacology of the cardiac pacemaker (‘funny’) current,” *Pharmacol. Ther.*, vol. 107, no. 1, pp. 59–79, Jul. 2005.

[5] H. F. Brown, D. DiFrancesco, and S. J. Noble, “How does adrenaline accelerate the heart?,” *Nature*, vol. 280, no. 5719, pp. 235–236, Jul. 1979.

[6] D. DiFrancesco, “The cardiac hyperpolarizing-activated current, if. Origins and developments,” *Prog. Biophys. Mol. Biol.*, vol. 46, no. 3, pp. 163–183, 1985.

[7] S. Herrmann, J. Stieber, G. Stöckl, F. Hofmann, and A. Ludwig, “HCN4 provides a ‘depolarization reserve’ and is not required for heart rate acceleration in mice,” *EMBO J.*, vol. 26, no. 21, pp. 4423–4432, Oct. 2007.

[8] K. Yanagihara and H. Irisawa, “Inward current activated during hyperpolarization in the rabbit sinoatrial node cell,” *Pflugers Arch.*, vol. 385, no. 1, pp. 11–19, May 1980.

[9] J. C. Denyer and H. F. Brown, “Pacemaking in rabbit isolated sino-atrial node cells during Cs+ block of the hyperpolarization-activated current if.,” *J. Physiol.*, vol. 429, no. 1, pp. 401–409, Oct. 1990.

[10] M. E. Mangoni and J. Nargeot, “Genesis and Regulation of the Heart Automaticity,” *Physiol. Rev.*, vol. 88, no. 3, pp. 919–982, Jul. 2008.

[11] R. Wilders, “Computer modelling of the sinoatrial node,” *Med. Biol. Eng. Comput.*, vol. 45, no. 2, pp. 189–207, Feb. 2007.

[12] A. Noma and H. Irisawa, “Contribution of an electrogenic sodium pump to the membrane potential in rabbit sinoatrial node cells,” *Pflugers Arch.*, vol. 358, no. 4, pp. 289–301, Aug. 1975.

[13] M. E. Mangoni *et al.*, “Bradycardia and Slowing of the Atrioventricular Conduction in Mice Lacking CaV3.1/α1G T-Type Calcium Channels,” *Circ. Res.*, vol. 98, no. 11, pp. 1422–1430, Jun. 2006.

[14] N. Hagiwara, H. Irisawa, and M. Kameyama, “Contribution of two types of calcium currents to the pacemaker potentials of rabbit sino-atrial node cells.,” *J. Physiol.*, vol. 395, pp. 233–253, Jan. 1988.

[15] H. Satoh, “Role of T-type Ca2+ channel inhibitors in the pacemaker depolarization in rabbit sino-atrial nodal cells,” *Gen. Pharmacol.*, vol. 26, no. 3, pp. 581–587, May 1995.

[16] M. E. Mangoni *et al.*, “Functional role of L-type Cav1.3 Ca2+ channels in cardiac pacemaker activity,” *Proc. Natl. Acad. Sci.*, vol. 100, no. 9, pp. 5543–5548, Apr. 2003.

[17] M. E. Mangoni, B. Couette, L. Marger, E. Bourinet, J. Striessnig, and J. Nargeot, “Voltage-dependent calcium channels and cardiac pacemaker activity: from ionic currents to genes,” *Prog. Biophys. Mol. Biol.*, vol. 90, no. 1–3, pp. 38–63, Apr. 2006.

[18] I. Kodama, M. R. Nikmaram, M. R. Boyett, R. Suzuki, H. Honjo, and J. M. Owen, “Regional differences in the role of the Ca2+ and Na+ currents in pacemaker activity in the sinoatrial node,”

Am. J. Physiol. - Heart Circ. Physiol., vol. 272, no. 6, pp. H2793–H2806, Jun. 1997.
[19] J. Hüser, L. A. Blatter, and S. L. Lipsius, “Intracellular Ca2+ release contributes to automaticity in cat atrial pacemaker cells,” *J. Physiol.*, vol. 524, no. Pt 2, pp. 415–422, Apr. 2000.
[20] Y. K. Ju and D. G. Allen, “The distribution of calcium in toad cardiac pacemaker cells during spontaneous firing,” *Pflugers Arch.*, vol. 441, no. 2–3, pp. 219–227, Dec. 2000.
[21] V. A. Maltsev and E. G. Lakatta, “Normal heart rhythm is initiated and regulated by an intracellular Calcium clock within pacemaker cells,” *Heart Lung Circ.*, vol. 16, no. 5, pp. 335–348, Oct. 2007.
[22] V. A. Maltsev, T. M. Vinogradova, and E. G. Lakatta, “The Emergence of a General Theory of the Initiation and Strength of the Heartbeat,” *J. Pharmacol. Sci.*, vol. 100, no. 5, pp. 338–369, 2006.
[23] T. M. Vinogradova, Y.-Y. Zhou, V. Maltsev, A. Lyashkov, M. Stern, and E. G. Lakatta, “Rhythmic Ryanodine Receptor Ca2+ Releases During Diastolic Depolarization of Sinoatrial Pacemaker Cells Do Not Require Membrane Depolarization,” *Circ. Res.*, vol. 94, no. 6, pp. 802–809, Apr. 2004.
[24] M. Shigekawa and T. Iwamoto, “Cardiac Na+-Ca2+ Exchange,” *Circ. Res.*, vol. 88, no. 9, pp. 864–876, May 2001.
[25] L. Sanders, S. Rakovic, M. Lowe, P. A. D. Mattick, and D. A. Terrar, “Fundamental importance of Na+–Ca2+ exchange for the pacemaking mechanism in guinea-pig sino-atrial node,” *J. Physiol.*, vol. 571, no. 3, pp. 639–649, Mar. 2006.
[26] A. E. Lyashkov *et al.*, “Calcium Cycling Protein Density and Functional Importance to Automaticity of Isolated Sinoatrial Nodal Cells Are Independent of Cell Size,” *Circ. Res.*, vol. 100, no. 12, pp. 1723–1731, Jun. 2007.
[27] G. M. Wahler, “Developmental increases in the inwardly rectifying potassium current of rat ventricular myocytes,” *Am. J. Physiol. - Cell Physiol.*, vol. 262, no. 5, pp. C1266–C1272, May 1992.
[28] A. Méry, F. Aimond, C. Ménard, K. Mikoshiba, M. Michalak, and M. Pucéat, “Initiation of Embryonic Cardiac Pacemaker Activity by Inositol 1,4,5-Trisphosphate–dependent Calcium Signaling,” *Mol. Biol. Cell*, vol. 16, no. 5, pp. 2414–2423, May 2005.
[29] S. Viatchenko-Karpinski *et al.*, “Intracellular Ca2+ oscillations drive spontaneous contractions in cardiomyocytes during early development,” *Proc. Natl. Acad. Sci.*, vol. 96, no. 14, pp. 8259–8264, Jul. 1999.
[30] H. Matsuura, T. Ehara, W.-G. Ding, M. Omatsu-Kanbe, and T. Isono, “Rapidly and slowly activating components of delayed rectifier K+ current in guinea-pig sino-atrial node pacemaker cells,” *J. Physiol.*, vol. 540, no. Pt 3, pp. 815–830, May 2002.
[31] K. Ono and H. Ito, “Role of rapidly activating delayed rectifier K+ current in sinoatrial node pacemaker activity,” *Am. J. Physiol. - Heart Circ. Physiol.*, vol. 269, no. 2, pp. H453–H462, Aug. 1995.
[32] K. Ono, S. Shibata, and T. Iijima, “Properties of the delayed rectifier potassium current in porcine sino-atrial node cells,” *J. Physiol.*, vol. 524, no. Pt 1, pp. 51–62, Apr. 2000.
[33] E. E. Verheijck, A. C. G. van Ginneken, J. Bourier, and L. N. Bouman, “Effects of Delayed Rectifier Current Blockade by E-4031 on Impulse Generation in Single Sinoatrial Nodal Myocytes of the Rabbit,” *Circ. Res.*, vol. 76, no. 4, pp. 607–615, Apr. 1995.
[34] M. Baruscotti, D. DiFrancesco, and R. B. Robinson, “A TTX-sensitive inward sodium current contributes to spontaneous activity in newborn rabbit sino-atrial node cells.,” *J. Physiol.*, vol. 492, no. Pt 1, pp. 21–30, Apr. 1996.
[35] M. Baruscotti, R. Westenbroek, W. A. Catterall, D. DiFrancesco, and R. B. Robinson, “The

newborn rabbit sino-atrial node expresses a neuronal type I-like Na+ channel.," *J. Physiol.*, vol. 498, no. 3, pp. 641–648, Feb. 1997.
[36] M. Lei *et al.*, "Requirement of neuronal- and cardiac-type sodium channels for murine sinoatrial node pacemaking," *J. Physiol.*, vol. 559, no. Pt 3, pp. 835–848, Sep. 2004.
[37] S. K. G. Maier *et al.*, "An unexpected requirement for brain-type sodium channels for control of heart rate in the mouse sinoatrial node," *Proc. Natl. Acad. Sci. U. S. A.*, vol. 100, no. 6, pp. 3507–3512, Mar. 2003.
[38] G. Lande, S. Demolombe, A. Bammert, A. Moorman, F. Charpentier, and D. Escande, "Transgenic mice overexpressing human KvLQT1 dominant-negative isoform. Part II: Pharmacological profile," *Cardiovasc. Res.*, vol. 50, no. 2, pp. 328–334, May 2001.
[39] M. A. Laflamme and C. E. Murry, "Heart Regeneration," *Nature*, vol. 473, no. 7347, pp. 326–335, May 2011.
[40] M. Rubart and D. P. Zipes, "Mechanisms of sudden cardiac death," *J. Clin. Invest.*, vol. 115, no. 9, pp. 2305–2315, Sep. 2005.
[41] D. P. Zipes and H. J. J. Wellens, "Sudden Cardiac Death," *Circulation*, vol. 98, no. 21, pp. 2334–2351, Nov. 1998.
[42] N. V. Munshi and E. N. Olson, "Improving cardiac rhythm with a biological pacemaker," *Science*, vol. 345, no. 6194, pp. 268–269, Jul. 2014.
[43] W. C. Members *et al.*, "ACC/AHA/HRS 2008 Guidelines for Device-Based Therapy of Cardiac Rhythm Abnormalities," *Circulation*, vol. 117, no. 21, pp. e350–e408, May 2008.
[44] H. Dobrzynski, M. R. Boyett, and R. H. Anderson, "New Insights Into Pacemaker Activity," *Circulation*, vol. 115, no. 14, pp. 1921–1932, Apr. 2007.
[45] C. Melzer *et al.*, "Predictors of chronotropic incompetence in the pacemaker patient population," *EP Eur.*, vol. 8, no. 1, pp. 70–75, Jan. 2006.
[46] "Diagnosis and Treatment of Sick Sinus Syndrome - American Family Physician." [Online]. Available: http://www.aafp.org/afp/2003/0415/p1725.html. [Accessed: 21-Apr-2017].
[47] D. P. Zipes *et al.*, "Guidelines for clinical intracardiac electrophysiological and catheter ablation procedures," *J. Am. Coll. Cardiol.*, vol. 26, no. 2, pp. 555–573, Aug. 1995.
[48] K. B. Keller and L. Lemberg, "The Sick Sinus Syndrome," *Am. J. Crit. Care*, vol. 15, no. 2, pp. 226–229, Mar. 2006.
[49] H. Holm *et al.*, "A rare variant in MYH6 is associated with high risk of sick sinus syndrome," *Nat. Genet.*, vol. 43, no. 4, pp. 316–320, Mar. 2011.
[50] D. W. Benson *et al.*, "Congenital sick sinus syndrome caused by recessive mutations in the cardiac sodium channel gene (*SCN5A*)," *J. Clin. Invest.*, vol. 112, no. 7, pp. 1019–1028, Oct. 2003.
[51] S. A. Jones, M. R. Boyett, and M. K. Lancaster, "Declining Into Failure," *Circulation*, vol. 115, no. 10, pp. 1183–1190, Mar. 2007.
[52] Y.-H. Yeh *et al.*, "Funny Current Downregulation and Sinus Node Dysfunction Associated With Atrial Tachyarrhythmia," *Circulation*, vol. 119, no. 12, pp. 1576–1585, Mar. 2009.
[53] A. Elvan, K. Wylie, and D. P. Zipes, "Pacing-Induced Chronic Atrial Fibrillation Impairs Sinus Node Function in Dogs," *Circulation*, vol. 94, no. 11, pp. 2953–2960, Dec. 1996.
[54] P. B. Sparks, S. Jayaprakash, J. K. Vohra, and J. M. Kalman, "Electrical Remodeling of the Atria Associated With Paroxysmal and Chronic Atrial Flutter," *Circulation*, vol. 102, no. 15, pp. 1807–1813, Oct. 2000.
[55] J. M. Mangrum and J. P. DiMarco, "The Evaluation and Management of Bradycardia," *N. Engl. J. Med.*, vol. 342, no. 10, pp. 703–709, Mar. 2000.
[56] G. Y. Oudit, V. Korley, P. H. Backx, and P. Dorian, "Lithium-induced sinus node disease at therapeutic concentrations: Linking lithium-induced blockade of sodium channels to impaired

pacemaker activity," *Can. J. Cardiol.*, vol. 23, no. 3, pp. 229–232, Mar. 2007.
[57] A. C. Blank, P. Loh, and M. A. Vos, "106 - Atrioventricular Block," in *Cardiac Electrophysiology: From Cell to Bedside (Sixth Edition)*, D. P. Zipes and J. Jalife, Eds. Philadelphia: W.B. Saunders, 2014, pp. 1043–1049.
[58] D. S. Park and G. I. Fishman, "The Cardiac Conduction System," *Circulation*, vol. 123, no. 8, pp. 904–915, Mar. 2011.
[59] P. J. Wang and D. L. Hayes, "117 - Implantable Pacemakers," in *Cardiac Electrophysiology: From Cell to Bedside (Sixth Edition)*, D. P. Zipes and J. Jalife, Eds. Philadelphia: W.B. Saunders, 2014, pp. 1167–1177.
[60] Npatchett, *English: Locations of cardiac pacemaker leads*. 2016.
[61] C. P. Lau, D. C. W. Siu, and H. F. Tse, "Implantable Sensor for Rate Adaptation and Hemodynamic Monitoring," *Clin. Card. Pacing Defibrillation Resynchronization Ther. 4th Ed*, 2011.
[62] Grupa Robocza Europejskiego Towarzystwa Kardiologicznego ds. stymulacji serca i resynchronizacji we współpracy *et al.*, "[Guidelines in cardiac pacing and resynchronization therapy]," *Kardiol. Pol.*, vol. 65, no. 12, pp. 1449-1487; discussion 1488-1489, Dec. 2007.
[63] R. Kay, M. Estioko, and I. Wiener, "Primary sick sinus syndrome as an indication for chronic pacemaker therapy in young adults: Incidence, clinical features, and long-term evaluation," *Am. Heart J.*, vol. 103, no. 3, pp. 338–342, Mar. 1982.
[64] E. Alt, R. Völker, A. Wirtzfeld, and K. Ulm, "Survival and Follow-up After Pacemaker Implantation: A Comparison of Patients With Sick Sinus Syndrome, Complete Heart Block, and Atrial Fibrillation," *Pacing Clin. Electrophysiol.*, vol. 8, no. 6, pp. 849–855, Nov. 1985.
[65] D. B. Shaw, R. R. Holman, and J. I. Gowers, "Survival in sinoatrial disorder (sick-sinus syndrome).," *Br. Med. J.*, vol. 280, no. 6208, pp. 139–141, Jan. 1980.
[66] G. Härtel and T. Talvensaari, "Treatment of sinoatrial syndrome with permanent cardiac pacing in 90 patients," *Acta Med. Scand.*, vol. 198, no. 5, pp. 341–347, Nov. 1975.
[67] O. Edhag and A. Swahn, "Prognosis of patients with complete heart block or arrhythmic syncope who were not treated with artificial pacemakers. A long-term follow-up study of 101 patients," *Acta Med. Scand.*, vol. 200, no. 6, pp. 457–463, 1976.
[68] T. L. Donmoyer, R. W. DeSanctis, and W. G. Austen, "Experience with Implantable Pacemakers Using Myocardial Electrodes in the Management of Heart Block," *Ann. Thorac. Surg.*, vol. 3, no. 3, pp. 218–227, Mar. 1967.
[69] M. C. Hindman *et al.*, "The clinical significance of bundle branch block complicating acute myocardial infarction. 1. Clinical characteristics, hospital mortality, and one-year follow-up.," *Circulation*, vol. 58, no. 4, pp. 679–688, Oct. 1978.
[70] E. Donoso, L. N. Adler, and C. K. Friedberg, "Unusual forms of second-degree atrioventricular block, including Mobitz Type-II block, associated with the Morgagni-Adams-Stokes syndrome," *Am. Heart J.*, vol. 67, no. 2, pp. 150–157, Feb. 1964.
[71] R. C. Dhingra, P. Denes, D. Wu, R. Chuquimia, and K. M. Rosen, "The Significance of Second Degree Atrioventricular Block and Bundle Branch Block," *Circulation*, vol. 49, no. 4, pp. 638–646, Apr. 1974.
[72] G. A. Lamas *et al.*, "Ventricular Pacing or Dual-Chamber Pacing for Sinus-Node Dysfunction," *N. Engl. J. Med.*, vol. 346, no. 24, pp. 1854–1862, Jun. 2002.
[73] H. Masumoto *et al.*, "Long-term clinical performance of AAI pacing in patients with sick sinus syndrome: a comparison with dual-chamber pacing," *EP Eur.*, vol. 6, no. 5, pp. 444–450, Jan. 2004.
[74] J. A. Jarcho, "Resynchronizing Ventricular Contraction in Heart Failure," *N. Engl. J. Med.*, vol. 352, no. 15, pp. 1594–1597, Apr. 2005.

[75] J. C. Nielsen *et al.*, “A comparison of single-lead atrial pacing with dual-chamber pacing in sick sinus syndrome,” *Eur. Heart J.*, vol. 32, no. 6, pp. 686–696, Mar. 2011.
[76] J. S. Healey *et al.*, “Cardiovascular Outcomes With Atrial-Based Pacing Compared With Ventricular Pacing,” *Circulation*, vol. 114, no. 1, pp. 11–17, Jul. 2006.
[77] G. A. Lamas, K. A. Ellenbogen, and M. D. With the Assistance of Charles H. Hennekens, “Evidence Base for Pacemaker Mode Selection,” *Circulation*, vol. 109, no. 4, pp. 443–451, Feb. 2004.
[78] C. Leclercq and J. M. Hare, “Ventricular Resynchronization,” *Circulation*, vol. 109, no. 3, pp. 296–299, Jan. 2004.
[79] J. D. Burkhardt and B. L. Wilkoff, “Interventional Electrophysiology and Cardiac Resynchronization Therapy,” *Circulation*, vol. 115, no. 16, pp. 2208–2220, Apr. 2007.
[80] J. D. Meyers, P. Y. Jay, and S. Rentschler, “Reprogramming the conduction system: Onward toward a biological pacemaker,” *Trends Cardiovasc. Med.*, vol. 26, no. 1, pp. 14–20, Jan. 2016.
[81] L. M. Baddour, Y.-M. Cha, and W. R. Wilson, “Clinical practice. Infections of cardiovascular implantable electronic devices,” *N. Engl. J. Med.*, vol. 367, no. 9, pp. 842–849, Aug. 2012.
[82] G. Gregoratos, “Indications and recommendations for pacemaker therapy,” *Am. Fam. Physician*, vol. 71, no. 8, pp. 1563–1570, Apr. 2005.
[83] J. Miake, E. Marbán, and H. B. Nuss, “Biological pacemaker created by gene transfer,” *Nature*, vol. 419, no. 6903, pp. 132–133, Sep. 2002.
[84] A. Bucchi *et al.*, “Wild-Type and Mutant HCN Channels in a Tandem Biological-Electronic Cardiac Pacemaker,” *Circulation*, vol. 114, no. 10, pp. 992–999, Sep. 2006.
[85] J. Qu *et al.*, “Expression and Function of a Biological Pacemaker in Canine Heart,” *Circulation*, vol. 107, no. 8, pp. 1106–1109, Mar. 2003.
[86] A. Ruhparwar *et al.*, “Transplanted fetal cardiomyocytes as cardiac pacemaker,” *Eur. J. Cardio-Thorac. Surg. Off. J. Eur. Assoc. Cardio-Thorac. Surg.*, vol. 21, no. 5, pp. 853–857, May 2002.
[87] A. N. Plotnikov *et al.*, “Xenografted Adult Human Mesenchymal Stem Cells Provide a Platform for Sustained Biological Pacemaker Function in Canine Heart,” *Circulation*, vol. 116, no. 7, pp. 706–713, Aug. 2007.
[88] Y. Shiba *et al.*, “hESC-Derived Cardiomyocytes Electrically Couple and Suppress Arrhythmias in Injured Hearts,” *Nature*, vol. 489, no. 7415, pp. 322–325, Sep. 2012.
[89] J. J. H. Chong *et al.*, “Human Embryonic Stem Cell-Derived Cardiomyocytes Regenerate Non-Human Primate Hearts,” *Nature*, vol. 510, no. 7504, pp. 273–277, Jun. 2014.
[90] S. M. Chambers and L. Studer, “Cell Fate Plug and Play: Direct Reprogramming and Induced Pluripotency,” *Cell*, vol. 145, no. 6, pp. 827–830, Jun. 2011.
[91] M. Ieda *et al.*, “Direct Reprogramming of Fibroblasts into Functional Cardiomyocytes by Defined Factors,” *Cell*, vol. 142, no. 3, pp. 375–386, Aug. 2010.
[92] Y.-J. Nam *et al.*, “Reprogramming of human fibroblasts toward a cardiac fate,” *Proc. Natl. Acad. Sci. U. S. A.*, vol. 110, no. 14, pp. 5588–5593, Apr. 2013.
[93] M. L. Bakker *et al.*, “T-box transcription factor TBX3 reprogrammes mature cardiac myocytes into pacemaker-like cells,” *Cardiovasc. Res.*, vol. 94, no. 3, pp. 439–449, Jun. 2012.
[94] N. Kapoor, W. Liang, E. Marbán, and H. C. Cho, “Transcription factor-driven conversion of quiescent cardiomyocytes to pacemaker cells,” *Nat. Biotechnol.*, vol. 31, no. 1, pp. 54–62, Jan. 2013.
[95] Y.-F. Hu, J. F. Dawkins, H. C. Cho, E. Marbán, and E. Cingolani, “Biological pacemaker created by minimally invasive somatic reprogramming in pigs with complete heart block,” *Sci. Transl. Med.*, vol. 6, no. 245, p. 245ra94, Jul. 2014.
[96] A. L. Hodgkin and A. F. Huxley, “A quantitative description of membrane current and its

application to conduction and excitation in nerve," *J. Physiol.*, vol. 117, no. 4, pp. 500–544, Aug. 1952.
[97] W. A. Catterall, I. M. Raman, H. P. C. Robinson, T. J. Sejnowski, and O. Paulsen, "The Hodgkin-Huxley Heritage: From Channels to Circuits," *J. Neurosci.*, vol. 32, no. 41, pp. 14064–14073, Oct. 2012.
[98] E. Izhikevich and R. FitzHugh, "FitzHugh-Nagumo model," *Scholarpedia*, vol. 1, no. 9, p. 1349, 2006.
[99] R. FitzHugh, "Impulses and Physiological States in Theoretical Models of Nerve Membrane," *Biophys. J.*, vol. 1, no. 6, pp. 445–466, Jul. 1961.
[100] B. Van der Pol, "A theory of the amplitude of free and forced triode vibrations," *Radio Rev.*, vol. 1, no. 1920, pp. 701–710, 1920.
[101] J. Nagumo, S. Arimoto, and S. Yoshizawa, "An active pulse transmission line simulating nerve axon," *Proc. IRE*, vol. 50, no. 10, pp. 2061–2070, 1962.
[102] D. Noble, "A modification of the Hodgkin—Huxley equations applicable to Purkinje fibre action and pacemaker potentials," *J. Physiol.*, vol. 160, no. 2, pp. 317–352, Feb. 1962.
[103] D. Noble, A. Garny, and P. J. Noble, "How the Hodgkin–Huxley equations inspired the Cardiac Physiome Project," *J. Physiol.*, vol. 590, no. 11, pp. 2613–2628, Jun. 2012.
[104] H. Irisawa and A. Noma, "Pacemaker Mechanisms of Rabbit Sinoatrial Node Cells," in *Cardiac Rate and Rhythm*, L. N. Bouman and H. J. Jongsma, Eds. Springer Netherlands, 1982, pp. 35–51.
[105] M. Courtemanche, R. J. Ramirez, and S. Nattel, "Ionic mechanisms underlying human atrial action potential properties: insights from a mathematical model," *Am. J. Physiol. - Heart Circ. Physiol.*, vol. 275, no. 1, pp. H301–H321, Jul. 1998.
[106] G. W. Beeler and H. Reuter, "Reconstruction of the action potential of ventricular myocardial fibres," *J. Physiol.*, vol. 268, no. 1, pp. 177–210, Jun. 1977.
[107] R. L. Winslow, J. Rice, S. Jafri, E. Marbán, and B. O'Rourke, "Mechanisms of Altered Excitation-Contraction Coupling in Canine Tachycardia-Induced Heart Failure, II," *Circ. Res.*, vol. 84, no. 5, pp. 571–586, Mar. 1999.
[108] C. H. Luo and Y. Rudy, "A model of the ventricular cardiac action potential. Depolarization, repolarization, and their interaction.," *Circ. Res.*, vol. 68, no. 6, pp. 1501–1526, Jun. 1991.
[109] K. H. W. J. ten Tusscher, D. Noble, P. J. Noble, and A. V. Panfilov, "A model for human ventricular tissue," *Am. J. Physiol. - Heart Circ. Physiol.*, vol. 286, no. 4, pp. H1573–H1589, Apr. 2004.
[110] J. L. Puglisi and D. M. Bers, "LabHEART: an interactive computer model of rabbit ventricular myocyte ion channels and Ca transport," *Am. J. Physiol. - Cell Physiol.*, vol. 281, no. 6, pp. C2049–C2060, Dec. 2001.
[111] S. V. Pandit, R. B. Clark, W. R. Giles, and S. S. Demir, "A Mathematical Model of Action Potential Heterogeneity in Adult Rat Left Ventricular Myocytes," *Biophys. J.*, vol. 81, no. 6, pp. 3029–3051, Dec. 2001.
[112] V. E. Bondarenko, G. P. Szigeti, G. C. L. Bett, S.-J. Kim, and R. L. Rasmusson, "Computer model of action potential of mouse ventricular myocytes," *Am. J. Physiol. - Heart Circ. Physiol.*, vol. 287, no. 3, pp. H1378–H1403, Sep. 2004.
[113] C. E. Clancy and Y. Rudy, "Linking a genetic defect to its cellular phenotype in a cardiac arrhythmia," *Nature*, vol. 400, no. 6744, pp. 566–569, Aug. 1999.
[114] T. J. Hund and Y. Rudy, "Rate Dependence and Regulation of Action Potential and Calcium Transient in a Canine Cardiac Ventricular Cell Model," *Circulation*, vol. 110, no. 20, pp. 3168–3174, Nov. 2004.
[115] J. J. Saucerman, L. L. Brunton, A. P. Michailova, and A. D. McCulloch, "Modeling β-

Adrenergic Control of Cardiac Myocyte Contractility in Silico," *J. Biol. Chem.*, vol. 278, no. 48, pp. 47997–48003, Nov. 2003.
[116] C. H. Luo and Y. Rudy, "A dynamic model of the cardiac ventricular action potential. I. Simulations of ionic currents and concentration changes.," *Circ. Res.*, vol. 74, no. 6, pp. 1071–1096, Jun. 1994.
[117] J. L. Greenstein and R. L. Winslow, "An Integrative Model of the Cardiac Ventricular Myocyte Incorporating Local Control of Ca2+ Release," *Biophys. J.*, vol. 83, no. 6, pp. 2918–2945, Dec. 2002.
[118] N. Wiener and A. Rosenblueth, "The mathematical formulation of the problem of conduction of impulses in a network of connected excitable elements, specifically in cardiac muscle," *Arch. Inst. Cardiol. Mex.*, vol. 16, no. 3, pp. 205–265, Jul. 1946.
[119] G. K. Moe, W. C. Rheinboldt, and J. A. Abildskov, "A COMPUTER MODEL OF ATRIAL FIBRILLATION," *Am. Heart J.*, vol. 67, pp. 200–220, Feb. 1964.
[120] G. Bub, A. Shrier, and L. Glass, "Spiral wave generation in heterogeneous excitable media," *Phys. Rev. Lett.*, vol. 88, no. 5, p. 058101, Feb. 2002.
[121] M. Gerhardt, H. Schuster, and J. J. Tyson, "A cellular automation model of excitable media including curvature and dispersion," *Science*, vol. 247, no. 4950, pp. 1563–1566, Mar. 1990.
[122] C. R. H. Barbosa, "Simulation of a plane wavefront propagating in cardiac tissue using a cellular automata model," *Phys. Med. Biol.*, vol. 48, no. 24, pp. 4151–4164, Dec. 2003.
[123] J. Greenberg and S. Hastings, "Spatial Patterns for Discrete Models of Diffusion in Excitable Media," *SIAM J. Appl. Math.*, vol. 34, no. 3, pp. 515–523, May 1978.
[124] J. M. Smith and R. J. Cohen, "Simple finite-element model accounts for wide range of cardiac dysrhythmias.," *Proc. Natl. Acad. Sci. U. S. A.*, vol. 81, no. 1, pp. 233–237, Jan. 1984.
[125] S. F. Roberts, J. G. Stinstra, and C. S. Henriquez, "Effect of Nonuniform Interstitial Space Properties on Impulse Propagation: A Discrete Multidomain Model," *Biophys. J.*, vol. 95, no. 8, pp. 3724–3737, Oct. 2008.
[126] M. S. Spach, J. F. Heidlage, E. R. Darken, E. Hofer, K. H. Raines, and C. F. Starmer, "Cellular Vmax reflects both membrane properties and the load presented by adjoining cells," *Am. J. Physiol.*, vol. 263, no. 6 Pt 2, pp. H1855-1863, Dec. 1992.
[127] M. S. Spach, J. F. Heidlage, P. C. Dolber, and R. C. Barr, "Electrophysiological Effects of Remodeling Cardiac Gap Junctions and Cell Size," *Circ. Res.*, vol. 86, no. 3, pp. 302–311, Feb. 2000.
[128] J. Stinstra, S. Roberts, J. Pormann, R. MacLeod, and C. Henriquez, "A Model of 3D Propagation in Discrete Cardiac Tissue," *Comput. Cardiol.*, vol. 33, pp. 41–44, 2006.
[129] E. J. Vigmond and L. J. Leon, "Computationally efficient model for simulating electrical activity in cardiac tissue with fiber rotation," *Ann. Biomed. Eng.*, vol. 27, no. 2, pp. 160–170, Apr. 1999.
[130] M. Potse, B. Dubé, J. Richer, A. Vinet, and R. M. Gulrajani, "A comparison of monodomain and bidomain reaction-diffusion models for action potential propagation in the human heart," *IEEE Trans. Biomed. Eng.*, vol. 53, no. 12 Pt 1, pp. 2425–2435, Dec. 2006.
[131] B. J. Roth, "Frequency locking of meandering spiral waves in cardiac tissue," *Phys. Rev. E*, vol. 57, no. 4, pp. R3735–R3738, Apr. 1998.
[132] C. S. Henriquez, "Simulating the electrical behavior of cardiac tissue using the bidomain model," *Crit. Rev. Biomed. Eng.*, vol. 21, no. 1, pp. 1–77, 1993.
[133] B. J. Roth, "Mechanisms for electrical stimulation of excitable tissue," *Crit. Rev. Biomed. Eng.*, vol. 22, no. 3–4, pp. 253–305, 1994.
[134] P. J. Hunter, A. J. Pullan, and B. H. Smaill, "Modeling total heart function," *Annu. Rev. Biomed.*

Eng., vol. 5, pp. 147–177, 2003.
[135] S. D. Unudurthi, R. M. Wolf, and T. J. Hund, “Role of sinoatrial node architecture in maintaining a balanced source-sink relationship and synchronous cardiac pacemaking,” *Front. Physiol.*, vol. 5, Nov. 2014.
[136] V. V. Fedorov *et al.*, “Structural and Functional Evidence for Discrete Exit Pathways That Connect the Canine Sinoatrial Node and Atria,” *Circ. Res.*, vol. 104, no. 7, pp. 915–923, Apr. 2009.
[137] V. V. Fedorov *et al.*, “Optical mapping of the isolated coronary-perfused human sinus node,” *J. Am. Coll. Cardiol.*, vol. 56, no. 17, pp. 1386–1394, Oct. 2010.
[138] V. V. Fedorov, A. V. Glukhov, and R. Chang, “Conduction barriers and pathways of the sinoatrial pacemaker complex: their role in normal rhythm and atrial arrhythmias,” *Am. J. Physiol. - Heart Circ. Physiol.*, vol. 302, no. 9, pp. H1773–H1783, May 2012.
[139] N. T, A. OV, Z. H, and E. IR, “Structure/Function Relationship in the Sinus and Atrioventricular Nodes,” *Pediatr. Cardiol.*, vol. 33, no. 6, pp. 890–899, Aug. 2012.
[140] I. ten Velde *et al.*, “Spatial Distribution of Connexin43, the Major Cardiac Gap Junction Protein, Visualizes the Cellular Network for Impulse Propagation From Sinoatrial Node to Atrium,” *Circ. Res.*, vol. 76, no. 5, pp. 802–811, May 1995.
[141] D. Sánchez-Quintana, J. A. Cabrera, J. Farré, V. Climent, R. H. Anderson, and S. Y. Ho, “Sinus node revisited in the era of electroanatomical mapping and catheter ablation,” *Heart*, vol. 91, no. 2, pp. 189–194, Feb. 2005.
[142] C. J. H. J. Kirchhof, F. I. M. Bonke, M. A. Allessie, and W. J. E. P. Lammers, “The influence of the atrial myocardium on impulse formation in the rabbit sinus node,” *Pflüg. Arch.*, vol. 410, no. 1–2, pp. 198–203, Sep. 1987.
[143] I. Kodama and M. R. Boyett, “Regional differences in the electrical activity of the rabbit sinus node,” *Pflugers Arch.*, vol. 404, no. 3, pp. 214–226, Jul. 1985.
[144] H. Zhang, A. V. Holden, and M. R. Boyett, “Gradient Model Versus Mosaic Model of the Sinoatrial Node,” *Circulation*, vol. 103, no. 4, pp. 584–588, Jan. 2001.
[145] H. Masumiya, Y. Oku, and Y. Okada, “Inhomogeneous distribution of action potential characteristics in the rabbit sino-atrial node revealed by voltage imaging,” *J. Physiol. Sci.*, vol. 59, no. 3, pp. 227–241, May 2009.
[146] J. G. C. Ponard, A. A. Kondratyev, and J. P. Kucera, “Mechanisms of Intrinsic Beating Variability in Cardiac Cell Cultures and Model Pacemaker Networks,” *Biophys. J.*, vol. 92, no. 10, pp. 3734–3752, May 2007.
[147] P. Kuklik and J. J. Żebrowski, “Reentry wave formation in excitable media with stochastically generated inhomogeneities,” *Chaos Interdiscip. J. Nonlinear Sci.*, Jul. 2005.
[148] S. Rohr, J. P. Kucera, V. G. Fast, and A. G. Kléber, “Paradoxical Improvement of Impulse Conduction in Cardiac Tissue by Partial Cellular Uncoupling,” *Science*, vol. 275, no. 5301, pp. 841–844, Feb. 1997.
[149] J. P. Fahrenbach, R. Mejia-Alvarez, and K. Banach, “The relevance of non-excitable cells for cardiac pacemaker function,” *J. Physiol.*, vol. 585, no. 2, pp. 565–578, Dec. 2007.
[150] A. K. Kryukov *et al.*, “Synchronization phenomena in mixed media of passive, excitable, and oscillatory cells,” *Chaos Interdiscip. J. Nonlinear Sci.*, vol. 18, no. 3, p. 037129, Sep. 2008.
[151] T. K. Shajahan, B. Borek, A. Shrier, and L. Glass, “Scaling properties of conduction velocity in heterogeneous excitable media,” *Phys. Rev. E Stat. Nonlin. Soft Matter Phys.*, vol. 84, no. 4 Pt 2, p. 046208, Oct. 2011.
[152] S. Zlochiver, V. Muñoz, K. L. Vikstrom, S. M. Taffet, O. Berenfeld, and J. Jalife, “Electrotonic Myofibroblast-to-Myocyte Coupling Increases Propensity to Reentrant Arrhythmias in Two-Dimensional Cardiac Monolayers,” *Biophys. J.*, vol. 95, no. 9, pp. 4469–4480, Nov. 2008.

[153] D. M. Bers, “16 - Excitation-Contraction Coupling,” in *Cardiac Electrophysiology: From Cell to Bedside (Sixth Edition)*, D. P. Zipes and J. Jalife, Eds. Philadelphia: W.B. Saunders, 2014, pp. 161–169.
[154] P. Kohl, F. Sachs, and M. R. Franz, Eds., *Cardiac Mechano-Electric Coupling and Arrhythmias*. Oxford University Press, 2011.
[155] A. C. Nobrega, J. W. Williamson, and J. H. Mitchell, “Left ventricular volumes and hemodynamic responses at onset of dynamic exercise with reduced venous return,” *J. Appl. Physiol.*, vol. 79, no. 5, pp. 1405–1410, Nov. 1995.
[156] O. Frank, “On the dynamics of cardiac muscle,” *Am. Heart J.*, vol. 58, no. 2, pp. 282–317, Aug. 1959.
[157] S. W. Patterson and E. H. Starling, “On the mechanical factors which determine the output of the ventricles,” *J. Physiol.*, vol. 48, no. 5, pp. 357–379, Sep. 1914.
[158] E. Schott, “On ventricular standstill (Adam-Stokes attacks) together with other arrhythmias of temporary nature,” *Dtsch Arch Klin Med*, vol. 131, pp. 211–29, 1920.
[159] F. Meola, “La commozione toracica,” *Gior Internaz Sci Med*, vol. 1, pp. 923–37, 1879.
[160] F. Riedinger, *Über Brusterschütterung*. FCW Vogel, 1882.
[161] F. Guharay and F. Sachs, “Stretch-activated single ion channel currents in tissue-cultured embryonic chick skeletal muscle.,” *J. Physiol.*, vol. 352, pp. 685–701, Jul. 1984.
[162] W. Lin, U. Laitko, P. F. Juranka, and C. E. Morris, “Dual Stretch Responses of mHCN2 Pacemaker Channels: Accelerated Activation, Accelerated Deactivation,” *Biophys. J.*, vol. 92, no. 5, pp. 1559–1572, Mar. 2007.
[163] P. Kohl, C. Bollensdorff, and A. Garny, “Effects of mechanosensitive ion channels on ventricular electrophysiology: experimental and theoretical models,” *Exp. Physiol.*, vol. 91, no. 2, pp. 307–321, Mar. 2006.
[164] D. R. Van Wagoner and M. Lamorgese, “Ischemia Potentiates the Mechanosensitive Modulation of Atrial ATP-Sensitive Potassium Channels a,” *Ann. N. Y. Acad. Sci.*, vol. 723, no. 1, pp. 392–395, Jun. 1994.
[165] C. E. Morris, “Pacemaker, potassium, calcium, sodium: stretch modulation of the voltage-gated channels,” in *Cardiac Mechano-Electric Coupling and Arrhythmias*, P. Kohl, F. Sachs, and M. R. Franz, Eds. Oxford University Press, 2011, pp. 42–49.
[166] B. Calabrese, I. V. Tabarean, P. Juranka, and C. E. Morris, “Mechanosensitivity of N-type calcium channel currents.,” *Biophys. J.*, vol. 83, no. 5, pp. 2560–2574, Nov. 2002.
[167] G. L. Lyford *et al.*, “α1C (CaV1.2) L-type calcium channel mediates mechanosensitive calcium regulation,” *Am. J. Physiol. - Cell Physiol.*, vol. 283, no. 3, pp. C1001–C1008, Sep. 2002.
[168] C. E. Morris and P. F. Juranka, “Nav Channel Mechanosensitivity: Activation and Inactivation Accelerate Reversibly with Stretch,” *Biophys. J.*, vol. 93, no. 3, pp. 822–833, Aug. 2007.
[169] D. G. Allen and J. C. Kentish, “The cellular basis of the length-tension relation in cardiac muscle,” *J. Mol. Cell. Cardiol.*, vol. 17, no. 9, pp. 821–840, Sep. 1985.
[170] S. C. Calaghan and E. White, “The role of calcium in the response of cardiac muscle to stretch,” *Prog. Biophys. Mol. Biol.*, vol. 71, no. 1, pp. 59–90, 1999.
[171] H. E. D. J. ter Keurs, “The interaction of Ca2+ with sarcomeric proteins: role in function and dysfunction of the heart,” *Am. J. Physiol. - Heart Circ. Physiol.*, vol. 302, no. 1, pp. H38–H50, Jan. 2012.
[172] J. Gamble, P. B. Taylor, and K. A. Kenno, “Myocardial stretch alters twitch characteristics and Ca2+ loading of sarcoplasmic reticulum in rat ventricular muscle,” *Cardiovasc. Res.*, vol. 26, no. 9, pp. 865–870, Sep. 1992.
[173] G. Iribe and P. Kohl, “Axial stretch enhances sarcoplasmic reticulum Ca2+ leak and cellular

Ca2+ reuptake in guinea pig ventricular myocytes: experiments and models," *Prog. Biophys. Mol. Biol.*, vol. 97, no. 2–3, pp. 298–311, Jul. 2008.
[174] G. Iribe *et al.*, "Axial Stretch of Rat Single Ventricular Cardiomyocytes Causes an Acute and Transient Increase in Ca2+ Spark Rate," *Circ. Res.*, vol. 104, no. 6, pp. 787–795, Mar. 2009.
[175] A. Arai, I. Kodama, and J. Toyama, "Roles of Cl- channels and Ca2+ mobilization in stretch-induced increase of SA node pacemaker activity," *Am. J. Physiol. - Heart Circ. Physiol.*, vol. 270, no. 5, pp. H1726–H1735, May 1996.
[176] S. Belmonte and M. Morad, "'Pressure–flow'-triggered intracellular Ca2+ transients in rat cardiac myocytes: possible mechanisms and role of mitochondria," *J. Physiol.*, vol. 586, no. 5, pp. 1379–1397, Mar. 2008.
[177] D. G. Allen and J. C. Kentish, "Calcium concentration in the myoplasm of skinned ferret ventricular muscle following changes in muscle length.," *J. Physiol.*, vol. 407, no. 1, pp. 489–503, Dec. 1988.
[178] Y. Yaniv *et al.*, "Beat to beat Ca2+-dependent regulation of sinoatrial nodal pacemaker cell rate and rhythm," *J. Mol. Cell. Cardiol.*, vol. 51, no. 6, pp. 902–905, Dec. 2011.
[179] L. Bao, F. Sachs, and G. Dahl, "Connexins are mechanosensitive," *Am. J. Physiol. - Cell Physiol.*, vol. 287, no. 5, pp. C1389–C1395, Nov. 2004.
[180] E. Perozo, A. Kloda, D. M. Cortes, and B. Martinac, "Physical principles underlying the transduction of bilayer deformation forces during mechanosensitive channel gating," *Nat. Struct. Biol.*, vol. 9, no. 9, pp. 696–703, Sep. 2002.
[181] F. A. Bainbridge, "The influence of venous filling upon the rate of the heart," *J. Physiol.*, vol. 50, no. 2, pp. 65–84, Dec. 1915.
[182] T. A. Quinn and P. Kohl, "Mechano-sensitivity of cardiac pacemaker function: Pathophysiological relevance, experimental implications, and conceptual integration with other mechanisms of rhythmicity," *Prog. Biophys. Mol. Biol.*, vol. 110, no. 2–3, pp. 257–268, Oct. 2012.
[183] J. R. Blinks, "Positive chronotropic effect of increasing right atrial pressure in the isolated mammalian heart," *Am. J. Physiol.*, vol. 186, no. 2, pp. 299–303, Aug. 1956.
[184] S. Chiba, "Pharmacologic Analysis of Stretch-Induced Sinus Acceleration of the Isolated Dog Atrium," *Jpn. Heart J.*, vol. 18, no. 3, pp. 398–405, 1977.
[185] S. J. Wilson and C. P. Bolter, "Do cardiac neurons play a role in the intrinsic control of heart rate in the rat?," *Exp. Physiol.*, vol. 87, no. 6, pp. 675–682, Nov. 2002.
[186] K. A. Deck, "[EFFECTS OF STRETCH ON THE SPONTANEOUSLY BEATING, ISOLATED SINUS NODE]," *Pflugers Arch. Gesamte Physiol. Menschen Tiere*, vol. 280, pp. 120–130, Jul. 1964.
[187] G. Lange, H. H. Lu, A. Chang, and C. M. Brooks, "Effect of stretch on the isolated cat sinoatrial node," *Am. J. Physiol.*, vol. 211, no. 5, pp. 1192–1196, Nov. 1966.
[188] C. P. Bolter, "Effect of changes in transmural pressure on contraction frequency of the isolated right atrium of the rabbit," *Acta Physiol. Scand.*, vol. 156, no. 1, pp. 45–50, Jan. 1996.
[189] C. J. Barrett, C. P. Bolter, and S. J. Wilson, "The intrinsic rate response of the isolated right atrium of the rat, Rattus norvegicus," *Comp. Biochem. Physiol. A. Mol. Integr. Physiol.*, vol. 120, no. 3, pp. 391–397, Jul. 1998.
[190] R. Kaufmann and U. Theophile, "Automatie-fördernde Dehnungseffekte an Purkinje-Fäden, Papillarmuskeln und Vorhoftrabekeln von Rhesus-Affen," *Pflüg. Arch. Für Gesamte Physiol. Menschen Tiere*, vol. 297, no. 3, pp. 174–189, Sep. 1967.
[191] B. F. Hoffman and P. F. Cranefield, *Electrophysiology of the heart*. New York: McGraw-Hill, 1960.
[192] P. Kohl, "14 - Cardiac Stretch–Activated Channels and Mechano-Electric Coupling," in

Cardiac Electrophysiology: From Cell to Bedside (Sixth Edition), D. P. Zipes and J. Jalife, Eds. Philadelphia: W.B. Saunders, 2014, pp. 139–149.
[193] P. J. Cooper, M. Lei, L.-X. Cheng, and P. Kohl, "Selected Contribution: Axial stretch increases spontaneous pacemaker activity in rabbit isolated sinoatrial node cells," *J. Appl. Physiol.*, vol. 89, no. 5, pp. 2099–2104, Nov. 2000.
[194] W. Craelius, V. Chen, and N. El-Sherif, "Stretch activated ion channels in ventricular myocytes," *Biosci. Rep.*, vol. 8, no. 5, pp. 407–414, Oct. 1988.
[195] P. J. Cooper and P. Kohl, "Species- and Preparation-Dependence of Stretch Effects on Sino-Atrial Node Pacemaking," *Ann. N. Y. Acad. Sci.*, vol. 1047, no. 1, pp. 324–335, Jun. 2005.
[196] J. W. Evans, "Random and cooperative sequential adsorption," *Rev. Mod. Phys.*, vol. 65, no. 4, pp. 1281–1329, Oct. 1993.
[197] G. Korniss and T. Caraco, "Spatial dynamics of invasion: the geometry of introduced species," *J. Theor. Biol.*, vol. 233, no. 1, pp. 137–150, Mar. 2005.
[198] F. Family, P. Meakin, and T. Vicsek, "Cluster size distribution in chemically controlled cluster–cluster aggregation," *J. Chem. Phys.*, vol. 83, no. 8, pp. 4144–4150, Oct. 1985.
[199] M. Aguilar-Shardonofsky, E. J. Vigmond, S. Nattel, and P. Comtois, "In Silico Optimization of Atrial Fibrillation-Selective Sodium Channel Blocker Pharmacodynamics," *Biophys. J.*, vol. 102, no. 5, pp. 951–960, Mar. 2012.
[200] B. Borek, T. K. Shajahan, J. Gabriels, A. Hodge, L. Glass, and A. Shrier, "Pacemaker interactions induce reentrant wave dynamics in engineered cardiac culture," *Chaos Woodbury N*, vol. 22, no. 3, p. 033132, Sep. 2012.
[201] P. Comtois and S. Nattel, "Impact of tissue geometry on simulated cholinergic atrial fibrillation: a modeling study," *Chaos Woodbury N*, vol. 21, no. 1, p. 013108, Mar. 2011.
[202] G. Bub, A. Shrier, and L. Glass, "Global organization of dynamics in oscillatory heterogeneous excitable media," *Phys. Rev. Lett.*, vol. 94, no. 2, p. 028105, Jan. 2005.
[203] O. I. Kanakov, G. V. Osipov, C.-K. Chan, and J. Kurths, "Cluster synchronization and spatio-temporal dynamics in networks of oscillatory and excitable Luo-Rudy cells," *Chaos Woodbury N*, vol. 17, no. 1, p. 015111, Mar. 2007.
[204] T. Korhonen, S. L. Hänninen, and P. Tavi, "Model of Excitation-Contraction Coupling of Rat Neonatal Ventricular Myocytes," *Biophys. J.*, vol. 96, no. 3, pp. 1189–1209, Feb. 2009.
[205] J. Cooper, G. R. Mirams, and S. A. Niederer, "High-throughput functional curation of cellular electrophysiology models," *Prog. Biophys. Mol. Biol.*, vol. 107, no. 1, pp. 11–20, Oct. 2011.
[206] T. Banyasz, B. Horvath, Z. Jian, L. T. Izu, and Y. Chen-Izu, "Sequential dissection of multiple ionic currents in single cardiac myocytes under action potential-clamp," *J. Mol. Cell. Cardiol.*, vol. 50, no. 3, pp. 578–581, Mar. 2011.
[207] E. Marder, "Variability, compensation, and modulation in neurons and circuits," *Proc. Natl. Acad. Sci.*, vol. 108, no. Supplement 3, pp. 15542–15548, Sep. 2011.
[208] B. B. C. B. Hui, S. Dokos, and N. H. Lovell, "Parameter Identifiability of Cardiac Ionic Models Using a Novel CellML Least Squares Optimization Tool," in *2007 29th Annual International Conference of the IEEE Engineering in Medicine and Biology Society*, 2007, pp. 5307–5310.
[209] A. G. Kléber and Y. Rudy, "Basic Mechanisms of Cardiac Impulse Propagation and Associated Arrhythmias," *Physiol. Rev.*, vol. 84, no. 2, pp. 431–488, Apr. 2004.
[210] B. E. Steinberg, L. Glass, A. Shrier, and G. Bub, "The role of heterogeneities and intercellular coupling in wave propagation in cardiac tissue," *Philos. Trans. R. Soc. Lond. Math. Phys. Eng. Sci.*, vol. 364, no. 1842, pp. 1299–1311, May 2006.
[211] S. Chauveau *et al.*, "0406 : Keratinocyte-derived cardiomyocytes provide in vivo biological pacemaker function," *Arch. Cardiovasc. Dis. Suppl.*, vol. 8, no. 3, p. 257, Apr. 2016.

[212] V. Jacquemet and C. S. Henriquez, “Loading effect of fibroblast-myocyte coupling on resting potential, impulse propagation, and repolarization: insights from a microstructure model,” *Am. J. Physiol. - Heart Circ. Physiol.*, vol. 294, no. 5, pp. H2040–H2052, May 2008.
[213] P. H. Campbell, A. W. Feinberg, J. A. Goss, K. K. Parker, and C. M. Ripplinger, “Anisotropic biological pacemakers and av bypasses,” WO2012048242 A1, 12-Apr-2012.
[214] T. Pong *et al.*, “Hierarchical architecture influences calcium dynamics in engineered cardiac muscle,” *Exp. Biol. Med. Maywood NJ*, vol. 236, no. 3, pp. 366–373, Mar. 2011.
[215] K. B. Walsh and G. E. Parks, “Changes in cardiac myocyte morphology alter the properties of voltage-gated ion channels,” *Cardiovasc. Res.*, vol. 55, no. 1, pp. 64–75, Jul. 2002.
[216] L. Lu *et al.*, “Design and validation of a bioreactor for simulating the cardiac niche: a system incorporating cyclic stretch, electrical stimulation, and constant perfusion,” *Tissue Eng. Part A*, vol. 19, no. 3–4, pp. 403–414, Feb. 2013.
[217] P. Khwaounjoo, S. L. Rutherford, M. Svrcek, I. J. LeGrice, M. L. Trew, and B. H. Smaill, “Image-based motion correction for optical mapping of cardiac electrical activity,” *Ann. Biomed. Eng.*, vol. 43, no. 5, pp. 1235–1246, May 2015.
[218] Y. Lei and Z. Ferdous, “Design considerations and challenges for mechanical stretch bioreactors in tissue engineering,” *Biotechnol. Prog.*, vol. 32, no. 3, pp. 543–553, May 2016.
[219] A. L. Thangawng, R. S. Ruoff, M. A. Swartz, and M. R. Glucksberg, “An ultra-thin PDMS membrane as a bio/micro-nano interface: fabrication and characterization,” *Biomed. Microdevices*, vol. 9, no. 4, pp. 587–595, Aug. 2007.
[220] N. Tandon, C. Cannizzaro, E. Figallo, J. Voldman, and G. Vunjak-Novakovic, “Characterization of electrical stimulation electrodes for cardiac tissue engineering,” *Conf. Proc. Annu. Int. Conf. IEEE Eng. Med. Biol. Soc. IEEE Eng. Med. Biol. Soc. Annu. Conf.*, vol. 1, pp. 845–848, 2006.
[221] Y. Iwadate and S. Yumura, “Cyclic stretch of the substratum using a shape-memory alloy induces directional migration in Dictyostelium cells,” *BioTechniques*, vol. 47, no. 3, pp. 757–767, Sep. 2009.
[222] J. P. Gomez, D. Potreau, J. E. Branka, and G. Raymond, “Developmental changes in Ca2+ currents from newborn rat cardiomyocytes in primary culture,” *Pflugers Arch.*, vol. 428, no. 3–4, pp. 241–249, Oct. 1994.
[223] F. V. Y. Tjong and V. Y. Reddy, “Permanent Leadless Cardiac Pacemaker Therapy: A Comprehensive Review,” *Circulation*, vol. 135, no. 15, pp. 1458–1470, Apr. 2017.